On the combustion of solid biomass fuels for large scale power generation

Investigations on the combustion behaviour of single particles of pulverised biomass fuel

Patrick Edward Mason

Submitted in accordance with the requirements for the degree of
Doctor of Philosophy

The University of Leeds
School of Chemical and Process Engineering

JULY 2016

The candidate confirms that the work submitted is his own and that appropriate credit has been given where reference has been made to the work of others.

Acknowledgements

In undertaking the research presented in this report, the author gratefully acknowledges the following assistance:

Guidance and support from my supervisory team: *Professor Jenny Jones; Professor Alan Williams; Dr Leilani Darvell* at The University of Leeds and *Professor Mohamed Pourkashanian* at The University of Sheffield*;*

Training provided for the use of analytical equipment and laboratory hardware: *Simon Lloyd; Dr Leilani Darvell; Dr Adrian Cunliffe; Dr Bijal Gudka; Stuart Micklethwaite; Sara Dona (The University of Leeds);Dr Phil Davies (TA Instruments); Matthew Clavey (Thermal Vision Research);*

Preparation of ash samples for XRF analysis: *Peinong Xing.*

Performing flame oxygen concentration measurements: *Eirini Karagianni.*

Machining, fitting and other laboratory technical support: *Ed Woodhouse, Chris Day, Gurdev Boghal.*

Design and build of photometer amplifier circuit: *Dr Iain Mosely, Converter Technology Ltd, Reading.*

Provision of various samples of fuels: *Paul Straker and James Ashman (Drax Power); Susan Weatherstone (Eon); Ricky Chaggar (SSE); Carly Whittaker (Rothamstead Research).*

Cellulose fibre and lignin analyses – *IBERS Analytical Laboratory, Aberystwyth University.*

Elemental analysis of coal samples - *Environmental Scientifics Group Ltd, Bretby.*

General support, assistance and comradery as fellow PhD students in the field of biomass combustion: *Dr Paula McNamee; Ben Dooley; Eddy Mitchell; Dr Farooq Atiku; Yee Sing Chin, Dougie Phillips and Aidan Smith.*

Colleagues in the Future Conventional Power Research Consortium: *Dr Juan Riaza, Dr Hannah Chalmers, Dr David Waldron and Professor Simon Hogg*

Funding for research activities was provided through Research Councils UK Energy Programme (EPSRC) grant reference EP/K02115X/1. This was part of the *Future Conventional Power Research Consortium,* a multi-disciplinary and cross-institutional research project focussing on the use of conventional thermal power stations in the context of a low-carbon UK energy economy.

For financial support, the author is very grateful the University of Leeds for the award of a Postgraduate Student Scholarship.

Special thanks to my wife, Irene for inspiring me to study for a PhD, supporting my decision to do so full-time, and providing the essential encouragement needed during the process to convince me that I could achieve it.

Abstract

Biomass is classed as a renewable resource. Depending on the means of production, it can be sustainable and can provide net benefits regarding CO_2 emissions by displacing fossil fuels as an energy source. A significant biomass energy conversion technology is combustion in conventional thermal power stations. This can be implemented in large scale plants such as those which dominated electricity generation throughout the 20th century. While these power stations were generally fuelled by the erstwhile ‘King Coal’, the technology is not exclusive to it. Coal consumption can be displaced in these types of plants by either co-firing biomass with coal or full conversion to biomass.

Currently, in the UK, the vast majority of the biomass fuel consumed for power generation is imported pelletized forestry wood. However, sustainability and domestic energy security concerns have created interest in using other resources including energy crops such as short rotation coppice willow and miscanthus, agricultural by-products such as wheat straw and olive residue. The variation in the properties of these fuels presents a number of technical challenges which conventional power plant must overcome to achieve ‘fuel flexibility’. Along with other technical challenges regarding the operation of conventional thermal power plant, these formed the basis of the Research Councils UK funded consortium grant (EPSRC, 2012) entitled *Future Conventional Power*. As a consortium partner in this project, the University of Leeds led research tasks associated with fuel flexibility. Much of the research presented in this thesis was based on the objectives set out in the *Future Conventional Power* project and was financially supported though this grant.

Two particular challenges provide the incentive for the investigations presented in this thesis and can be summarised as:

- assessing the variability in fuel combustion behaviour and control of burn-out efficiency for different fuels
- understanding the behaviour of potassium during the combustion of biomass fuels to aid in the prediction of ash behaviour, emissions and associated operational problems

Both these points were addressed with a series of experimental studies. In addition, a model of the combustion of single particles was developed for validating and interpreting the results.

A range of fourteen solid biomass fuels, typical of those likely to be used in large scale power plant, were selected for the experimental studies. The composition and fundamental characteristics of these fuels, obtained by standard analytical techniques, are presented.

In the first experimental study, single particles were exposed to a methane flame, simulating biomass combustion in a furnace. Measurements of ignition delay, volatile burning time and char burn-out time were undertaken using high speed image capture. Particle surface temperatures were measured by infra-red thermal imaging. Analysis of the data identified correlations between the biomass fundamental characteristics, particle size, and the observed combustion profiles. Empirical expressions for the duration of each combustion stage are obtained from the data. From these, a “burn-out” index is derived which provides a useful indication of the relative milling requirements of different fuels for achieving effective burn-out efficiency.

A similar experimental method was used in the second study in which the gas-phase potassium release patterns from single particles of various biomass fuels were measured by use of flame emission spectroscopy. The observed potassium release patterns for the various fuel samples are presented. The release patterns revealed qualitative differences between different fuel types. Relationships between the initial potassium content, peak rate of release and the fractions of potassium released at each stage of combustion were identified. These were subsequently used for comparing with results of modelled potassium release.

A third experimental study investigated the variation in thermal conductivity between different types of solid biomass using a technique and apparatus developed specifically for the study. The results showed variation of thermal conductivity between different types of biomass which had been similarly homogenised and densified. The thermal conductivity of small particles of each fuel was derived. The resulting data provides useful values for thermal

modelling of biomass particles and is used subsequently in a combustion model.

Elements of each of the experimental studies were used in a detailed model of single particle combustion. In this, the particle was modelled as a series of concentric spherical layers which enabled calculation of internal mass diffusion and heat transfer. Devolatilisation and char oxidation were approximated with single step reaction kinetics. A volatilisation and diffusion mechanism was adopted to simulate the release of gas-phase potassium from the particle. The output from the model was compared and validated using data from the experimental studies. The modelling produced confirming evidence that the assumed mechanisms for gas-phase potassium release were valid and provided a tool for future investigation of the subject.

Table of Contents

List of Tables

List of Figures

List of Symbols and Abbreviations

Symbol	Description	Dimensions
A	frequency factor for kinetic reaction rate	s^{-1}
$\mathcal{A}$	cross-sectional area	m^2
a, b	coefficients in regression functions	
B	pre-exponential coefficient of vapour pressure function	$N . m^{-2}$
C	specific heat capacity	$J . kg^{-1} . K^{-1}$
D	diameter of equivalent spherical particle	m
E	activation energy for kinetic reaction rate	$J . mol^{-1}$
F	Thermal conductivity to density coefficient	$W.m^2.kg^{-1}.K^{-1}$
G	coefficient of relative mass diffusivity	dimensionless
H	enthalpy of reaction / phase change	$J . kg^{-1}$
h	heat transfer coefficient	$W. m^{-2}. K^{-1}$
i	index number of layer: $i = 1\ to\ N$	dimensionless
L	length	m
M	proportion of moisture in particle by mass	dimensionless
m	mass	kg
N	number of layers in particle model	dimensionless
P	pressure	$N . m^{-2}$
Q	heat flux	W
R	Gas constant (= 8.31446)	$J . K^{-1} . mol^{-1}$
Δr	radial thickness of modelled concentric layer	m
S	surface area	m^2
T	temperature	K
t	time	s
U	velocity	$m . s^{-1}$
V	volume	m^3
W	specific energy (energy per unit mass)	$J . kg^{-1}$

α	coefficient relating solid-phase to gas-phase mass of potassium	
β	coefficient of potassium entrainment in devolatilisation	
Γ	mass diffusion coefficient	$m^2 . s^{-1}$
γ	proportion of gas in particle by volume	dimensionless
ε	emissivity	dimensionless
η	order of reaction	dimensionless
κ	thermal diffusivity	$m^2 . s^{-1}$
λ	thermal conductivity	$W. m^{-1}. K^{-1}$
ρ	density	$kg . m^{-3}$
σ	Stefan-Boltzmann constant (= $5.67x10^{-8}$)	$J . s^{-1} . m^{-2} . K^{-4}$
σ	standard deviation	dimensionless
τ	characteristic time constant	s
υ	kinematic viscosity	$m^2 . s^{-1}$
Φ	mass concentration	$kg . m^{-3}$
ζ	coefficient of moisture evaporation	$s . K^{-1}$
χ	conversion fraction	dimensionless
Ω	coefficient of energy of comminution	$J . kg^{-1} . m$
Nu	Nusselt number	dimensionless
Re	Reynolds number	dimensionless
Pr	Prandtl number	dimensionless
C, H, N, O S, Cl, K etc.	standard chemical symbols for elements (also used to indicate mass fractions)	

subscripts:

s	relating to surface of spherical particle
i	property of layer i
p	property of entire particle
w	property of moisture fraction
d	property of dry (moisture free) fraction
vol	property of volatile fraction
$char$	property of char fraction

ash	property of ash fraction
gas	property of gas surrounding particle
0	initial condition
$conv$	relating to convective heat transfer
rad	relating to radiative heat transfer
$cond$	relating to conductive heat transfer
gr	gross value
net	net value
ar	relating to sample 'as received'
O_2	relating to molecular oxygen (gas)
K	relating to potassium (all species)
KOH	relating to potassium hydroxide
KCl	relating to potassium chloride
cv	constant volume
cp	constant pressure
eq	condition at equilibrium
tc	relating to thermocouple
ins	relating to insulation
S	relating to sample

abbreviations:

AAS	atomic absorption spectroscopy
d.a.f.	dry ash-free (measurement basis)
EDX	energy-dispersive x-ray spectroscopy
GCV	gross calorific value
MTOE	million tonnes of oil equivalent (energy)
wt%	percentage by weight
XRF	X-ray fluorescence spectroscopy

Other, non-mathematical abbreviations and acronyms are defined in the text where first cited or as appropriate in the context.

Chapter 1
Use of solid biomass fuels for large scale power generation

1.1 Introduction

Combustion of biomass is not a new technology. Indeed, it is arguably one of the oldest, with evidence of controlled fire being used by early hominids dating back hundreds of thousands of years (Berna et al., 2012). With such a long history of experience in burning wood and other biomass materials, it is a valid question then to ask “why do we not already know all there is to know about burning biomass?”. There are two key points to make in answer to this. Firstly, the terms “biomass” and even” wood” cover materials which are hugely variable in many significant aspects relevant to their use as fuel, particularly in power generation applications. Secondly, the technologies used to burn biomass also vary considerably. The large-scale boilers which are the context of this research were originally developed for use with coal, not biomass, so the experience in this particular area is not as extensive as many other energy technologies or fuels. The questions which this research thesis sets out to answer are related to these two points.

Before these questions are set out explicitly in later chapters, it is useful to provide some context explaining why solid biomass fuels are being considered for large scale power generation and clarification of the meaning of the terms “solid biomass fuel” and “large scale power generation” .

1.2 Renewable Energy

1.2.1 The demand for renewable energy

In 2014, the Intergovernmental Panel on Climate Change (IPCC) completed publication of the fifth assessment report on climate change. The report covers numerous and extensive scientific studies on the pertinent aspects of the possible causes (i.e. greenhouse gases) and effects (i.e. global warming) regarding climate change. The first key point made in the summary document is:

> *"Human influence on the climate system is clear, and recent anthropogenic emissions of green-house gases are the highest in history. Recent climate changes have had widespread impacts on human and natural systems."* (IPCC, 2015)

This was a re-iteration of the conclusions of previous reports but was supported with more convincing evidence and analysis. This served to reinforce the consensus among governments worldwide to act on reducing greenhouse gas emissions. In fact, many governments have committed to such measures since signing up to the 1997 Kyoto Protocol Treaty and subsequent agreements of the United Nations Framework Convention on Climate Change (UNFCCC). The latest of these was the 2015 Paris Agreement which set out proposed action on climate change mitigation from 2020 onwards. The focus of these agreements and treaties has been to reduce global greenhouse gas (GHG) emissions and, in particular, carbon dioxide (CO_2) emissions.

Anthropogenic CO_2 emissions arise primarily from conversion of fossil-fuels for energy. Currently world primary energy consumption is overwhelmingly dependent on fossil fuels, be it consumed in the transport sector (mainly petroleum oil), in buildings sector (mainly natural gas and oil) or the industrial sector (coal, natural gas and oil). Electricity generation is a means of converting from one energy vector to a another vector which is subsequently delivered to the various consumption sectors. As one of the main users of primary energy, electricity generation can also be considered as a consumption sector in itself. Historically (through the twentieth century) electricity was generated mainly from burning coal. This was the case on a global basis but it was particularly the case in the UK where abundant domestic supplies of coal were produced. Part 3 of the IPCC Fifth Assessment Report assessed climate change mitigation measures and included the following statement concerning electricity generation:

> *"Electricity production is the largest single sector emitting fossil fuel CO_2 at present and in baseline scenarios of the future. A variety of mitigation options exist in the electricity sector, including renewables (wind, solar energy, biomass, hydro, geothermal), nuclear, and the possibility of fossil*

or biomass with CCS. The electricity sector plays a major role in mitigation scenarios with deep cuts of GHG emissions." (IPCC, 2014)

The use of renewable energy as a means of "decarbonising" electricity generation has been regarded as a key GHG reduction strategy for many of the governments which have signed up to the various UNFCCC agreements. Since unilateral action by individual states on energy matters is tempered by the pressures to maintain economic advantage through low energy prices, internationally agreed legislation has been important in implementing these strategies. One significant commitment in this regard has been the agreement by European Union (EU) member states to enforce renewable energy strategies through legislation. The resulting EU renewable energy directive 2009/28/EC (EU, 2009) "*on the promotion of the use of energy from renewable sources*" set a target for 20% of energy consumed in the EU by 2020 to be from renewable sources. The individual targets set for each member state were weighted depending on existing energy dependencies and other economic factors.

1.2.2 UK renewable energy targets

The EU renewable energy target agreed by the United Kingdom of Great Britain and Northern Ireland (UK) was to achieve 15% of final consumption of energy from renewable sources by 2020. This was embodied in the National Renewable Energy Action Plan for the United Kingdom. The aims, if not the means, of reducing greenhouse gas emissions had already been set out in the Climate Change Act (UK_Government, 2008) which set a target for an 80% reduction on 1990 levels in net CO_2 and equivalent greenhouse gas emissions by 2050. Accompanying this legislation, specific policy targets (DTI, 2006) called for an increase in the proportion of electricity generated from renewable sources with a target of 20% by 2020.

Support and incentives for renewable power generation were already in place since 2002 in the form of the renewable obligation scheme and this continued as a key mechanism for implementing the EU renewable energy target.

By 2012, the UK Government produced the "UK Bioenergy Strategy" (DECC, 2012) which was developed as a cross-departmental guide to policy development. In this document, the principle of the conversion of existing large-

scale coal-fired power stations to biomass was presented as a key in the transition away from coal up to 2030. The document states:

> *"use of sustainable biomass as a transitional fuel to reduce carbon emissions from current coal power generation is an important decarbonisation pathway."* (DECC, 2012)

However, there was not any longer-term support for new large-scale biomass power generation past 2030 unless accompanied by carbon capture and sequestration (CCS). Nevertheless, the incentives for biomass conversion continue as part of the "Electricity Markets Reform" (DECC, 2013) introduced in the 2013 Energy Act. The reforms include discontinuation of the renewable obligation scheme and introduction of contracts-for-difference (CfD) for low-carbon, large-scale generation projects. The CfD strike prices set for biomass conversion and dedicated CHP biomass were £105/MWh and £125/MWh respectively. For comparison, the strike price offered offshore wind was £155/MWh and the price agreed for Hinkley Point C Nuclear power station was £92.50/MWh

In addition to the GHG reduction plans, other legislation (UK_Government, 2007) concerning limitations on emissions of nitrogen oxides (NOx) and sulphur dioxide had been introduced in 2007 as a result of the EU large combustion plant directive 2001/80/EC (EU, 2001). These regulations placed direct pressure on large coal-fired power stations to take action to reduce nitrogen oxides (NO_x) and sulphur dioxide (SO_2) emissions beyond 2015 or cease operation. A combination of the incentives from the renewable obligation scheme and the constraints of the large combustion plant regulations led many power station operators in the UK to introduce co-firing of biomass with coal. The displacement of high sulphur and nitrogen coal with biomass was one means of controlling emissions to within limits.

Overall, UK energy policy appears to be supportive of biomass combustion for electricity generation. However, confidence in the long-term reliability of UK government support in this area is likely to have been undermined by direction changes and lack of clarity in renewable energy policy. For example, in 2014 tacit support for conversion of one of the units at Drax to 100% biomass in the

form of a contract-for-difference failed to materialise and led to a legal challenge – which Drax subsequently lost (The_Guardian, 2014).

1.2.3 Biomass as a renewable energy resource

In the context of legislation and regulations in the UK and EU, biomass energy is classed as a renewable resource and a means towards “decarbonising” energy consumption. However, unlike other renewable resources such as wind, solar and hydro, biomass combustion does emit carbon dioxide to the atmosphere. The reason it is classed alongside other renewables is that, on a certain timescale, it is considered as being virtually “carbon neutral”. That is, the total quantity of carbon released as CO_2 upon combustion is balanced in the natural carbon cycle (Priestley, 1777) by conversion by photosynthesis from CO_2 back into biomass.

The validity of the “carbon neutral” assumption depends on the harvested biomass being replaced by a new growth on an on-going basis. The time scale over which the carbon released as CO_2 is returned to biomass depends mainly on the harvest rotation period of the crop or forest. Certain “energy crops”, once established may have annual harvests, short rotation coppice may have a period of 3-5 years, short rotation forestry up to 20 years and traditional forestry from 50 to 100 years. Further to this, as with other renewable energy technologies, there are associated energy inputs for implementing the technology. For biomass there are energy expenditures for cultivation, harvesting, processing and transportation. Additional indirect greenhouse gas emissions may result in the use of nitrogen fertiliser which not only uses energy to produce but can also contribute to increased N_2O emissions, a significant greenhouse gas itself.

Since the “carbon neutrality” of biomass has been hailed as one of its main benefits as an energy source, this has led to the validity of the premise being questioned (Zanchi et al., 2012, Bracmort, 2013). The CO_2 emissions benefits depend on many factors, not least the type of biomass under consideration. In order to adequately address the issue of the carbon-cycle balances of biomass energy, one approach has been to undertake life-cycle assessments which account, as far as practical, for all the inputs and outputs in a given bioenergy system (Adams et al., 2013).

In an overview of the carbon emissions benefits of biomass, Zanchi et al. (Zanchi et al., 2012) examined the balance of total forest carbon stock including tree biomass, litter and soil organic matter for three harvesting scenarios and compared this against a fossil fuel reference scenario. The effectiveness of a bioenergy system in reducing CO_2 emissions compared to the replaced fossil fuel system is used to evaluate the carbon-neutrality of the system with different production scenarios. Whereas new forest plantation gives an initial credit to the carbon balance, Zanchi et al. suggest that additional fellings from existing managed forest may take over 200 years to achieve carbon neutrality. However, the claim that timescales are too long to meaningfully achieve atmospheric carbon reductions can be misleading. The claim may be valid if a single harvest area is considered in isolation but if an established managed forest is considered, the reduction in carbon stock during harvesting is minor in relation to the whole. A sustainably managed forest can maintain a significant carbon stock while providing an annual harvest of biomass for timber, paper and/or energy use (Matthews et al., 2012).

It is necessary then that claims of carbon neutrality and classification of bioenergy as renewable should be qualified with an account of the long-term sustainability of feedstocks and the life-cycle timescales for the replacement biomass to re-absorb to CO_2 emissions released during production and consumption.

The “UK Bioenergy Strategy” report (DECC, 2012), addresses the issue of forest management by referring to The UK Forestry Standard (Forestry_Commission, 2011) and government procurement policy. Although this does not address directly how private power generation companies will source biomass on the open market, an agreed strategy for sourcing wood pellets has been developed by a joint initiative of major European power companies including Eon, Drax, RWe, GDF Suez, Dong, Vattenfall and Eggborough (IWPB, 2012b) .

The use of energy crops and agricultural by-products also raises concerns over land-use change and displacement of food production either direct or indirect. Overall, the technical, economic and environmental considerations with regards energy crops are more complex compared to existing managed sustainable

forestry. Assessment of the likely impacts of new energy crops and forestry are highly dependent on specific situations so can only be undertaken meaningfully on a case by case basis.

Life cycle assessments (LCA) of energy crops and forestry can give an indication of the overall environmental impact of cultivation, processing and transportation of solid biomass fuels. There is much variation in reported greenhouse gas impacts of biomass fuel production from published LCA calculations. As noted in a report by the UK Supergen Bioenergy Hub (Adams et al., 2013), the main reasons for these variations are: (i) Variations in the cultivation practices and production methods for similar types of crops; (ii) Uncertainties from insufficient knowledge of greenhouse gas impacts from certain processes such as N_2O emissions from cultivated soils; (iii) Methodological variations such as differing system boundary definitions.

A published example LCA for Miscanthus, willow, wheat straw and rape straw (Borzecka-Walker et al., 2011) suggests that energy for production of these crops is in the order of 3% to 18% of the energy value of the crop. The IPCC Special Report on Renewable Energy Sources (IPCC, 2012) presents data on life-cycle emissions for biomass fuels in the order of 0.05 tonnes of CO_2 equivalent per GJ(e). When compared to coal, at around 0.4 tonnes per GJ(e), the equivalent CO_2 “saving” is in the order of 0.35 tonnes per GJ(e). Other analyses (Cherubini et al., 2009) present figures for the equivalent CO_2 “saved” by use of biomass crops when compared to electricity production from coal in the order of 0.11 tonnes per GJ(e). The uncertainty in such LCA calculations has been highlighted in analyses by Röder et al. (Röder et al., 2015) wherein the CO_2 equivalent determined for wood pellet delivered to power stations ranges from 0.04 to 0.37 tonnes per GJ(e). The former of these figures is consistent with the analyses cited above but the latter figure indicates that, in some cases, the CO_2 emissions saving is marginal. A UK Government report (Stephenson and Mackay, 2014) to assess the potential greenhouse gas impacts from the use of imported wood pellet from the USA gives similar figures, concluding that a figure of 0.055 tonnes per GJ(e) may be possible with respect to the UK demand by 2020.

Forecasting the carbon neutrality of forestry for bioenergy systems is clearly not straightforward and assessing the net avoidance in atmospheric CO_2 emissions will probably only be meaningful in retrospect. Despite this, in accounting for the carbon footprint of bioenergy, various UK and European guidance and regulations make the “carbon neutral” assumption. This assumption continues to be challenged (Johnson, 2009, Haberl et al., 2012) and a more accurate means of calculating emissions, carbon–stock changes and effects of land use change continue to be necessary to avoid accusations of being “dirtier than coal” (RSPB et al., 2013).

1.3 Power generation from Biomass

1.3.1 Biomass for power generation globally

The global energy consumption of biomass for electricity generation by 2012 was approximately 4EJ/y (EIA, 2015). Comparison of this with estimated forestry biomass production (25EJ/y) and estimated overall biomass consumption (55EJ/y) indicates that current levels of biomass power generation are small relative to the overall consumption and the resource. An inference of this numerical comparison is that a modest increase in biomass power generation from current levels is quite feasible without being disruptive to existing markets and production methods. However, if the aim is to displace a significant proportion of existing fossil fuel power generation (149EJ/y) and provide new power generation by 2050 considerable additional resources would be required. Exploitation of additional biomass resources on this scale are likely to have strong effects on markets and production methods and it would be important to anticipate this and manage changes effectively to avoid detrimental environmental effects and economic reactions.

An examination of the trends in biomass power generation over the past decade or so can give some indication of possible future deployment of biomass power generation. **Figure 1-1** shows the data for power generation output (in TWh) from biomass and wastes between 2000 and 2012 for the top 5 world economies and the world total (EIA, 2015). The data shows that there was a steady rate of growth globally from 2000 to 2010. This growth appears to result mainly from the trend in European countries. The global growth rate since 2010

has accelerated even though the European trend seems to have stalled since the increased growth in countries such as China and Brazil has contributed to the global trend. The global trend over the past decade, has averaged growth of about 20TWh per year. A simple linear extrapolation of this trend to 2050 would lead to over 1100TWh of generation requiring around 11EJ of primary energy from biomass. The World Energy Council (WEC) projections for electricity generation (WEC, 2013) suggest that 2500-2800 TWh could be possible by 2050 requiring 25-28EJ of primary energy from biomass. This is not insubstantial – and could contribute around 5% of the total world electricity demand by 2050 (WEC, 2013). It is feasible that power generation from biomass can make a contribution to the displacement of fossil fuels in the next decades albeit alongside other renewable energy sources and nuclear power.

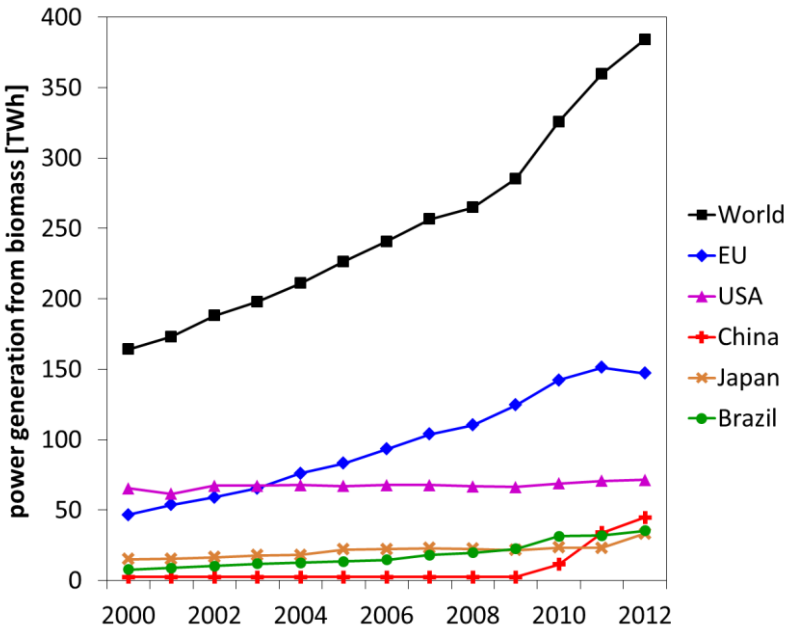

Figure 1-1 – growth in biomass electricity generation globally and in main global economies

Source data: (EIA, 2015)

1.3.2 Biomass for power generation in the UK

By 2012, the United Kingdom was the sixth largest generator of electricity from biomass with just over 14TWh generated equivalent to about 0.15EJ of primary energy (**Table 1-1**). However, this was set to increase rapidly up to 27TWh by 2015 – equivalent to 0.32EJ of primary energy (DECC, 2015). This increase

was almost entirely as result of the full conversion to biomass firing of two 660MWe units at Drax power station in North Yorkshire.

Table 1-1 – World electricity generation from biomass and wastes in 2012

	Electricity generation [TWh]	*Primary Energy [EJ]*	*Primary Energy [MTOE]*
United States	71.4	0.73	17.5
China	44.7	0.46	11.0
Germany	44.6	0.46	11.0
Brazil	35.2	0.36	8.6
Japan	33.2	0.34	8.2
United Kingdom	14.2	0.15	3.5
Italy	12.5	0.13	3.1
Sweden	11.6	0.12	2.8
Finland	11.0	0.11	2.7
Poland	10.1	0.10	2.5
rest of world	95.5	0.98	23.5
TOTAL	384	3.95	94.3

Source: (EIA, 2015) Note: primary energy to electricity generation 0.35 conversion factor

1.3.2.1 The role of Biomass in UK electricity sector

As previously discussed in 1.2.2 the targets for CO_2 reduction set out in UK legislation include an increase in the proportion of electricity generated from renewable sources with a target of 20% by 2020.

To put this target in context, the proportion of electricity generated by fuel type in the UK is shown in **Figure 1-2**. This shows that the proportion of electricity generation from renewable energy sources did steadily increase over the period from 2004 to 2014 reaching around 14% by 2014. This appears to be on course to reach the 2020 target. Beyond 2020, controls on CO_2 emissions in line with the 2050 target of 80% reductions on the 1990 levels will require ongoing deployment of renewable energy technologies to achieve this.

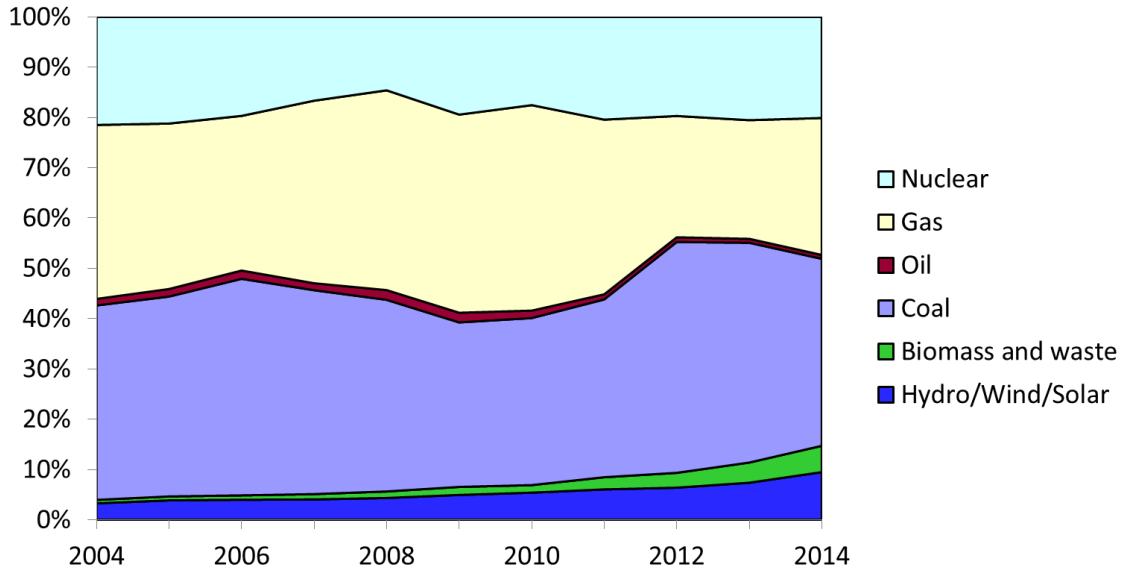

Figure 1-2 - Percentage shares of fuel for electricity generation in UK, 2004 to 2014

Source data:(DECC, 2015)

In seeking to move away from dependence on fossil fuels (or “decarbonising”), there are a number of alternative energy resources available for electricity generation which are classed as renewable by UK government: hydro; solar; wind; bio-energy. Added to these, conventional nuclear power generation is classed as a low-carbon power source although not a renewable one.

Hydroelectricity contributed about around 4.4TWh to UK electricity production which accounted for almost all renewable production in 1990. While hydroelectric generation has not changed much in the meantime, all the other renewable energy technologies have grown considerably since 2000. By 2014, total renewable electricity production was over 60TWh or 14% of total UK electricity supplied (DECC, 2015). Wind power accounts for over half of the increase but most of the rest has been from bioenergy sources (9% of UK total in 2014). A time history of this development is illustrated in **Figure 1-3**.

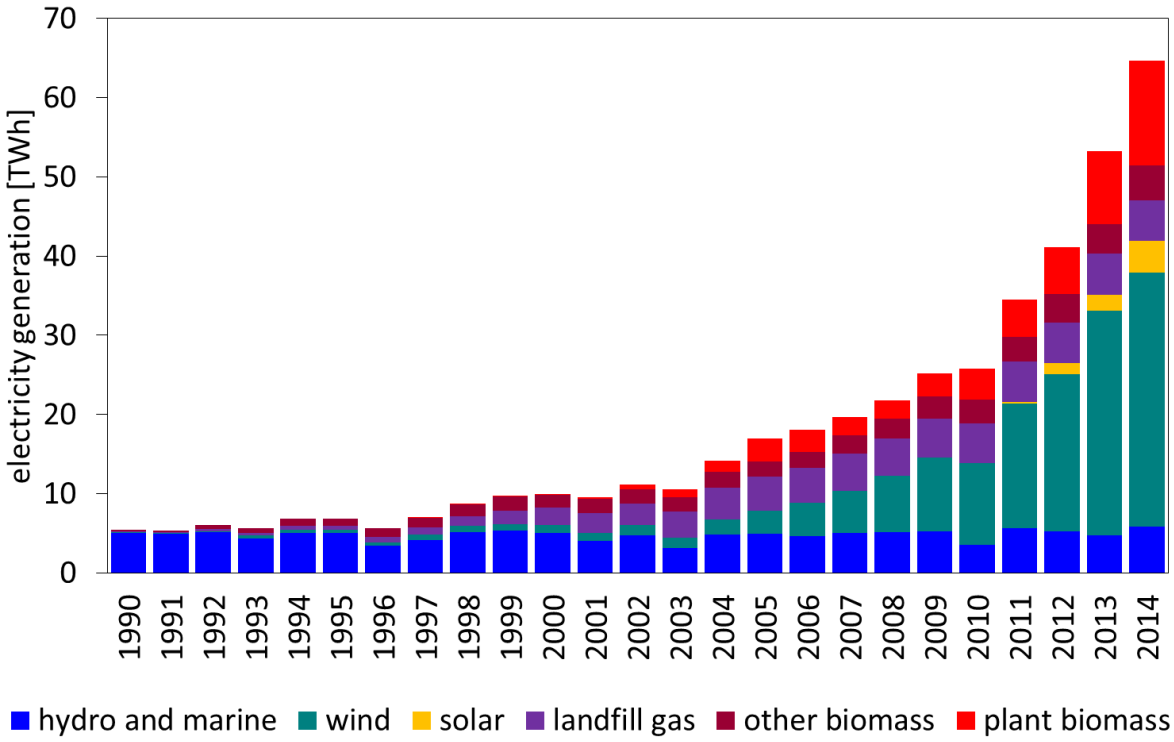

Figure 1-3 - Energy generated from renewable sources in the UK.
Source data:(DECC, 2015)

Recent policy towards the use of biomass for electricity generation is set out in the 2012 cross-departmental "UK Bioenergy Strategy" report (DECC, 2012). Biomass is identified as an important means to:

> "*deliver genuine carbon reductions that help meet UK carbon emissions objectives to 2050 and beyond*" and "*use of wood and energy crops for bioenergy is a good carbon reduction option compared to alternative uses of the resource in certain circumstances*". (DECC, 2012)

There is also recognition of the wider question of sustainability of biomass production and impacts on land use change and food production. The report agrees with the recommendation from the Committee on Climate Change (CCC) that:

> "*Support for biomass power generation ... should be focused on co-firing and conversion of existing coal power plants. Any support for new dedicated biomass generation should be limited to small-scale … new large-scale dedicated biomass should be limited to a very small number of projects*".

The current strategy is therefore that biomass in large scale electricity generation in the UK is likely to be as "*transitional"* technology.

However, there is another significant advantage in the use of so-called 'conventional' thermal power stations. Wind and solar power generation are temporally de-coupled from the electrical energy demand. As more of these sources are introduced onto the electricity grid, there is still a need to maintain adequate demand-side controlled and rapidly despatched power to account for variations in the availability of those sources. Conventional thermal power stations are able to fulfil this role. Full 'decarbonisation' of the UK electricity sector may be achievable if this conventional power generation were to be fuelled by biomass.

1.3.2.2 Biomass Electricity Generation Capacity and Production in UK

In the UK statistics (DECC, 2015), electricity from bioenergy accounted for over 15TWh or 4.4% of total electricity supply in 2012. However, the classification "bioenergy" encompasses a number of differing technologies including generation from landfill gas. The use of non-waste plant biomass in electricity generation has grown more from less than 0.5 TWh in 2000 to 5.9 TWh in 2012. Since 2010, biomass co-fired with coal has accounted for about 2 TWh per year with dedicated plant biomass increasing rapidly to account for 4TWh in 2012.

To put this in some perspective, statistics issued by the US Dept. of Energy (EIA, 2014) indicates that around 40 TWh of electricity was produced from wood biomass and 20TWh from waste biomass in the USA in 2013. The total electricity production in the period was 4058 TWh. Biomass therefore accounts for only about 1.5% of the electricity production in the USA.

The electricity generating capacity from solid biomass (i.e. not including landfill gas power stations) in the UK in early 2014 was around 1.1GW. More than half of this capacity was a result of the first stage conversion of Drax power station. The remainder of the capacity was from co-firing in other coal fired power stations (~ 90MW) and smaller dedicated combined heat and power (CHP) plants ranging from 2MW to 50MW. Of this, 75MW capacity was from plant burning poultry litter and 55MW from plant using industrial wastes (paper and food). Most of the capacity is from plant burning woody biomass (Biomass_Enery_Centre, 2014).

Biomass combustion for electricity power generation has therefore been a significant contributor towards reaching the UK's targets for decarbonisation of electricity generation. The technology is likely to remain key in the strategy for achieving the Climate Change Act targets for 2050.

The current contribution of bioenergy to power generation is admittedly small. Nevertheless, the forecast is that at least 8% of UK primary energy can be from bioenergy use by 2020 and up to 12% by 2050. Of this, the power generation target for biomass by 2020 is between 20 and 40 TWh. Electricity generation from co-firing and conversion of large scale plant is projected to exceed 20TWh/yr by 2020 - in addition to energy from waste and landfill ((DECC, 2012)fig.8 p.44). Beyond 2020, the use of biomass for electricity is expected to fall as the technologies for other energy users become a priority – In particular, the issue of providing alternative fuels for the transport sector is considered to become more dominant.

1.4 Solid Biomass Fuels

1.4.1 Types of solid biomass fuel

"Biomass" as a generic class of material covers an enormous variety of substances derived from living/ recently living organisms. Although some smaller scale combustion applications use animal wastes and sewage sludge as fuel, by far the largest energy resource globally is plant-based biomass. In large scale combustion applications, the range of materials used as fuels is somewhat narrower and is mainly ligno-cellulosic solids, principally wood and large herbaceous plants.

There are many existing and potential biomass fuel feedstocks from dedicated crops grown primarily as a fuel source through to waste materials and by-products of forestry and agriculture. Many of these are identified and discussed in published reports assessing biomass fuel resources (Gaur and Reed, 1995, Thornley et al., 2008).

In identifying and assessing biomass fuel resources it is helpful to sub-divide the types of fuels into categories defined by either origin or properties. With regards specifically to solid biofuels, an assessment of the trade in the different feedstocks is possible by considering certain trade categories for which

statistics are published by either the World Trade Organisation or the European Union (Lamers et al., 2012). Trade categories include: agricultural residues; industrial residues; forestry products. The European (CEN) Standard for *solid biofuels - fuel specifications and classes* (Standard, 2010) sets out a more detailed hierarchical categorisation for solid biofuels based on the biological origin with the high-level categories being: woody biomass; herbaceous biomass; fruit biomass.

1.4.1.1 Woody biomass

Woody biomass is that which is obtained from trees, bushes and shrubs. Production for fuel use can be from dedicated forestry or coppicing but it is also available from by-products as residues from commercial timber production and from waste as used-wood from construction and demolition.

Forestry

Traditional forestry for the production of wood for construction, furniture products, paper and other non-fuel uses is a well-established and very large scale global industry. Sustainably managed forests remove no more biomass in a harvest than the mass which will be replenished in growth in the time-scale of subsequent harvests. The tree species grown in sustainably managed forests are often fast growing softwoods such as pine, larch, spruce and fir. The time scales for regeneration of conventional forestry depends on many factors including climate, species and soil. A forestry harvesting cycle may be as short as 40 years but can range up to 150 years. Much shorter timescales than this are possible. Short rotation forestry (SRF) rotation cycles are typically 8-20 years. Tree species suited to SRF include alder, ash, birch, sycamore, poplar, eucalyptus and southern beech. For most tree species, the yields are generally around ~5-8 dry tonnes per hectare per year. Eucalyptus SRF can deliver typically 15 and even up to 30 dry tonnes per hectare per year. For this reason, eucalyptus is already widely grown in SRF for the purposes of paper production. Depending on completion for existing markets, it is therefore a likely source of fuel for power generation. (Thornley et al., 2008)

Short Rotation Coppice

Coppicing is a well-established, indeed ancient, means of woodland management whereby some tree species are cut back to the root stock and allowed to regrow in a repeating cycle ranging from a few years to several decades. Short-rotation coppice (SRC) generally refers to coppice cycles of five years or less and, naturally, requires fast-growing high-yield species. Suitable species include willow (*Salix* spp.) and poplar (*Populus* spp.). The practice of short rotation coppicing is specific to larger scale energy crops and as such would be a likely feedstock for power generation plant. SRC can yield approximately 10 dry tonnes per hectare per year (Thornley et al., 2008). However, the production of SRC requires use of agricultural land and is therefore in direct competition with farming for food production. Furthermore, SRC requires application of fertilisers which have an energy cost and environmental impact. (Keoleian and Volk, 2005).

Waste wood

Waste wood arises from various activities including the construction and demolition industries, commercial packaging, furniture manufacture and municipal solid wastes. Waste wood is of variable quality and is categorised accordingly (Standard, 2012). The cleaner, uncontaminated wood is generally recycled either as particle-board or as animal bedding. The lower grade waste is available as a fuel feedstock although some treated woods are classed as hazardous waste and must be disposed at special facilities.

1.4.1.2 Herbaceous Biomass

Herbaceous biomass it that which is obtained from plants that have a non-woody stem. This includes by-products from agricultural food crops and certain species of grass which are grown as dedicated energy crops.

Miscanthus and other giant grasses

Miscanthus [*Miscanthus giganteus*] is a hybrid perennial grass which can be grown in Europe and North America. It is propagated from rhizome (the hybrid seed is sterile) and grows up to 3.5m high. Crops can take at least 3 years to become established with yields from 10 to 25 dry tonnes per hectare per year or even higher depending on irrigation and climate (Lewandowski et al., 2000).

Switchgrass [*Panicum virgatum*] is a native species of the North American prairies often cultivated there for animal feed. Although it can take up to 3 years to establish from seed, thereafter, it grows up to 2.5m high annually and can yield up to 15 dry tonnes per hectare per year (McLaughlin and Adams Kszos, 2005).

Reed Canary Grass [*Phalaris arundinacea*] is a European native species which grows in wet habitats. It can be propagated from seed and can grow to about 2m high. Yields may be as low as 6-7 dry tonnes per hectare per year but the crops may be grown on marginal agricultural land (Kukk et al., 2011).

Agricultural Straws

Straw is a by-product from cereal crops (e.g. wheat, barley or oats) or from oil-seed crops (e.g. rape or linseed). There are other markets for straw (e.g. traditional animal bedding) and it is generally traded in bale form of varying sizes. Yields are roughly between 3 and 4 dry tonnes per hectare although since it is a by-product, the economics of production are dominated by the primary use of the crop.

Sugar Cane Bagasse

Sugar cane [*saccharum officinarum x saccharum spontaneum*] is a hybrid grass cultivated for its very high sucrose content. The largest production of sugar cane in the world is in Brazil where much of it is used for production of ethanol as transport fuel. The fibrous ligno-cellulosic residue left over from milling and cane-juice extraction is called bagasse. In most sugar cane mills, the bagasse is used as fuel to raise steam and power for the sugar processing. Some varieties of sugar cane have very high yields of bagasse and are known as “energy cane”. Energy cane can yield over 60 dry tonnes per hectare per year leading to the possibility of its use primarily as an energy crop (Matsuoka et al., 2014).

1.4.1.3 Fruit Biomass

Fruit biomass is that which is obtained from the parts of a plant which are from or hold seeds including nut shells. Since virtually all fruit production is for food use, it is only the non-consumable residues which are available as fuel

feedstocks. Many of these have little potential for alternative use so are economically attractive as fuel.

Olive residues

Olive residue is the waste left over from the production of olive oil. After the olive fruits have been pressed, the stones and fibre can be formed into a cake or pellet. Around 10-12 million tonnes of olives are harvested each year in the EU resulting in around 2 million tonnes of olive residue (EUROSTAT, 2015).

Other fruit and nut residues

Palm kernels are a by-product of palm oil production which is derived from the fruit of the African oil palm *Elaeis guineensis*. The residue fibre and shells are formed into a cake known as palm kernel expeller or PKE. As a waste by-product, it can be used as an animal feed but much of it is available as a low-cost biomass fuel. Production is mainly in Malaysia and Indonesia. The shells of nuts such as peanuts, pistachio and cashew are also waste by-products which are used as biomass fuels.

1.4.2 Biomass energy resources

1.4.2.1 The global biomass energy potential

Estimates of potential availability of biomass for energy to the year 2050 are highly variable. An assessment of the overall global bioenergy resource undertaken by Smeets et al. (Smeets et al., 2007) gives wide ranging estimates with a mid-range figure of 910 EJ/yr. Figures of this scale indicate the size of the possible resource but the practicalities and economics of exploiting it lead others to much more modest estimates. In a contrasting report, Haberl et al (Haberl et al., 2013) suggest 250EJ/yr to be a practical biophysical limit based on limitations in agriculture and sustainability. In accordance with this, an assessment which focuses on forestry being the main realistic large scale resource, Parikka (Parikka, 2004) makes an much lower estimate at 100EJ as the possible sustainable global biomass energy potential. The global potential of renewable energy sources assessed by De Vries et al. (deVries et al., 2007) takes into account economic factors and gives an estimate of 212EJ/yr for biofuel production by 2050. This is similar to the International Energy Agency (IEA) 2009 report on bioenergy (IEA, 2009) which suggests that a supply of

between 200 and 500 EJ/yr by 2050 could be possible. An extensive review of many more published estimates including some of those mentioned above are presented in a UK Energy Research Centre report (Slade et al., 2011). The mid-range values derived from the macro-analysis give upper and lower estimates of 100 to 600 EJ/yr respectively with an average estimate at 300 EJ/yr. A summary of the estimates is presented in **Table 1-2**.

Table 1-2 - Biomass energy potential availability by 2050

Reference	*Forecast biomass energy potential 2050 [EJ]*
(Smeets et al., 2007)	350-1471
(Haberl et al., 2013)	250
(Parikka, 2004)	100
(deVries et al., 2007)	212
(IEA, 2009)	200-500
(Slade et al., 2011)	100-600

1.4.2.2 Current global biomass energy resources

Woody biomass from forestry is currently the largest practically and commercially obtainable resource for solid fuel supplies. An estimate of its availability may be made with reference to the United Nations Food and Agriculture Organisation (FAO) statistical databases on wood production and forestry resources which are available online (FAOSTAT, 2015). The production data for globally traded biomass materials from forestry include figures for industrial roundwood, fuel wood, wood chips and wood residues. Fuel wood, wood chips and wood residues can be considered as available for energy use but only a fraction of the industrial roundwood can be considered. The premium wood (i.e. the large-diameter roundwood) from such production has high market value and is more likely to be traded for non-fuel use. However, there is a significant amount of residue wood left from the extraction of the premium wood, This includes the smaller diameter branches and bark in the forest and the trimmings and sawdust at the primary mills. According to a study by Parikka (Parikka, 2004) around 70% of the total global wood harvest is available for energy use. Taking this into account, the FAO wood production data can be used to estimate the potential energy value. Using a conversion

factor of ~19GJ/dry tonne (Lamers *et al.* 2012), the resulting estimates for biomass energy from forestry since 2000 are presented in **Figure 1-4** which shows little variation around an average of around 25 EJ per year.

Since most other biomass fuels are not traded in the same way as forestry products (or indeed, as oil, gas and coal) statistics on production are not readily available and inference from related agricultural statistics and other sources has to be used to draw estimates. Using such methods, an analysis by Haberl et al. (Haberl et al., 2013) states an estimated rate of consumption of 55EJ of bioenergy per year for 2012-2013.

Comparing this figure with the estimated potential resources in **Table 1-2** suggests that overall production in forestry and energy crops would need to at least double by 2050 to realise even the lowest of the estimates (+100EJ). This would likely require considerable and rapid increases in forestry, primarily, but also changes in and expansion of agricultural land use for energy crops.

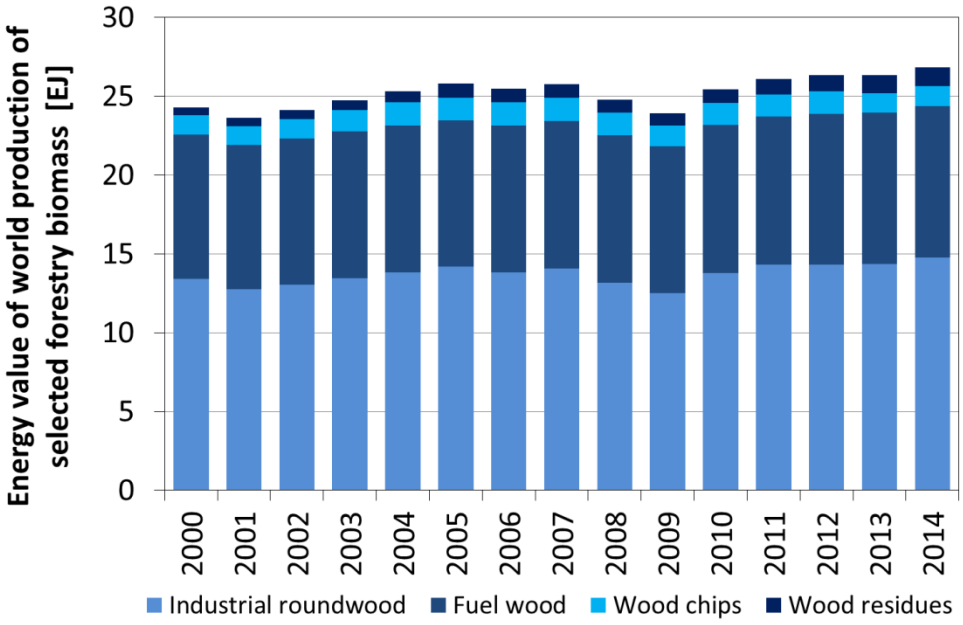

Figure 1-4 - Biomass energy available from world production of forestry 2000 to 2014

Source:(FAOSTAT, 2015)

1.4.2.3 Current global bioenergy consumption

To put these figures in perspective: world fossil fuel consumption from 2012 to 2014 was around 465 EJ (BP, 2015). Clearly there is potential for biomass to

displace a significant proportion of fossil fuel energy consumption even at the lower end of the estimates.

Almost a third of global fossil fuel consumption (146EJ) is attributed to the transportation sector which is still almost entirely dependent on liquid petroleum products. The development of liquid biofuels to displace the liquid fossil fuels is therefore a priority for many countries in the context of bioenergy research. In the USA, Brazil and Europe there is currently significant production of biofuels for transport use. In 2013, world production of liquid biofuels amounted to around 2.5EJ energy equivalent (EIA, 2015): between 1 and 2% of world liquid fossil fuel production.

Global electricity generation in 2012 was over 21,000 TWh (EIA, 2015) and of this, about 14,500 TWh were generated from fossil fuels and only 384TWh were generated from biomass (including wastes). An estimate of the primary energy input for electricity generation can be made assuming a conversion efficiency of around 0.35 (similar to that of a typical coal power station). The total fossil fuel consumption on this basis for 2012 is estimated at 149 EJ. This is almost a third of the total fossil fuel consumption – a similar proportion to that of the transportation sector. In the case of electricity generation, the dominant fossil fuel input globally is coal. Displacing fossil fuels from power generation may be achieved in many ways including expansion of the deployment of wind, solar, hydroelectric and nuclear generation. However, solid fuel fired thermal generation plant such as existing coal power stations remain an effective means of providing large-scale (>500MW) and controllable power. A relatively straight forward means of exploiting bioenergy resources and displacing fossil fuels is the use solid biomass for “conventional” power generation. The world electricity generation from biomass and wastes in 2012 was 384 TWh accounting for 4 EJ of primary energy input (EIA, 2015).

In sectors other than transportation and power generation, the main use of biomass is for domestic and commercial heating. Taking the estimate of total bioenergy consumption of 55EJ per year by Haberl et al. and accounting for biofuel in transportation (2.5EJ) and biomass for power generation (4EJ), the remainder of 48.5EJ gives an indication of the scale of consumption for heating (although some of this will be energy use in industrial processes).

1.4.2.4 UK biomass supply

The analysis of energy production and consumption on a global scale has given some perspective on the potential of biomass power generation for displacing fossil fuels. However, simple comparison of figures masks many practicalities of economics and logistics. Since more detailed figures are available for the UK, a view of the situation regarding biomass resources on an individual country basis is possible and provides a different perspective.

Domestic production

SRC willow production in the UK in 2010 was around 16 thousand tonnes but this dropped to only 7 thousand tonnes by 2014. Miscanthus production in 2010 was at about 24 thousand tonnes and this level has remained steady through to 2014 (DEFRA, 2015). In energy terms, this represents an average production of about 0.5PJ per year from UK energy crops.

In the same period, over 4 million tonnes of waste wood arose per year of which about a quarter was available as biomass fuel (DEFRA, 2012) representing between 20 and 25PJ of energy per year.

About 12 million tonnes of agricultural straws are produced in Great Britain annually (J Copeland, 2008) of which around 200 thousand tonnes (~3PJ) were used for power generation from 2010 to 2013 rising to about 440 thousand tonnes (~7PJ) in 2014.

Wood pellet production in the UK grew steadily from 118 thousand tonnes (~2PJ) in 2009 to 354 thousand tonnes (~6PJ) in 2014: a three-fold increase over 5 years.

Imports

Before 2009, wood pellet imports to the UK were small enough not to be categorised as a separate wood product in published statistics. Since then there has been a large and rapid increase in imported wood pellet rising to over 4.1 million tonnes (62 PJ) by 2014 (Forestry_Commission, 2016). As solid biomass fuel, this exceeds by far the combined domestic production as outlined above. The increase is almost entirely as a result of biomass co-firing and conversion at coal-fired power stations.

The statistics for UK domestic production and net imports of solid biomass fuels are presented in **Figure 1-5**. This illustrates clearly that domestic production became a smaller proportion of the total since 2013. While domestic production has risen, possibly in response to increased demand, it appears to be only making a slight difference compared to the large quantity of imported wood pellet. While this suggests that the UK is dependent on imports for biomass supply, it is worth putting this in the context of the existing situation regarding coal in the UK: in 2014, 85% of the UK coal supply was from imports. Imported solid biomass fuel is displacing imported solid fossil fuel.

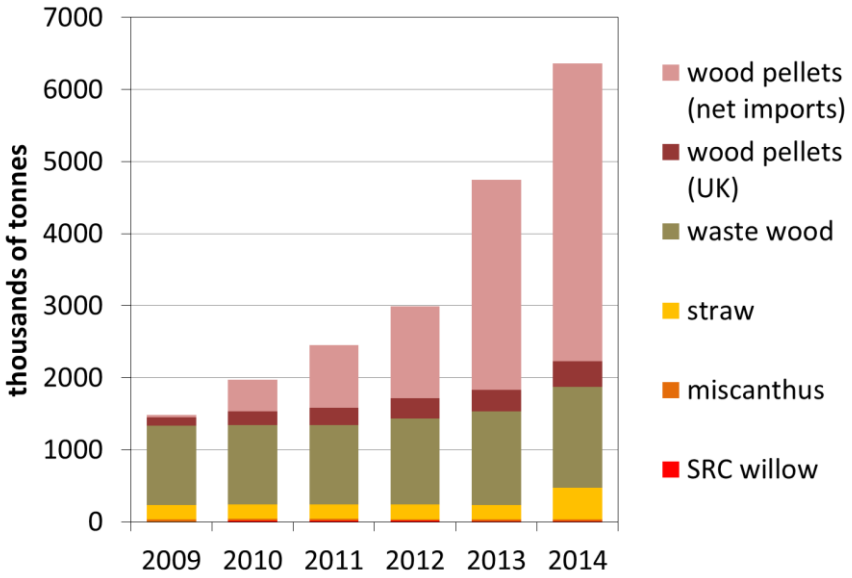

Figure 1-5 – Supply of solid biomass fuels in the UK 2009-2014. Sources: (Forestry_Commission, 2016, DEFRA, 2015, DEFRA, 2012, J Copeland, 2008)

1.4.3 Processing biomass for solid fuel use

1.4.3.1 Processing for transportation

Bulk, raw biomass requires processing before it can be usefully used as fuel. At the very least the material must be converted to manageable particle sizes for transportation. Further particle size reduction is usually required before insertion into a burner/furnace.

For processing of forestry residues and smaller wood, the material may be converted to wood chips in a cutting mill. This can be performed on site using a mobile wood chipper which then enables ease of transport off site.

Alternatively, for larger scale operations, the bulk wood may be transported to a processing plant for conversion. Wood for paper manufacture, for example, is transported as whole-stem roundwood and processing occurs at the paper mill to ensure production of clean uncontaminated chips. Horizontal feed disk chippers are typically used in such facilities which can process tree-length logs to produce chips in the 12-25mm size range with an energy consumption of between 25-50MJ/tonne. (Biermann, 1996).

Rather than cutting using blades to breakdown biomass material, alternative means such as impact comminution can be used using hammer-mills. Comparison between the two methods (Spinelli et al.) suggests that, depending on feedstock type, cutting comminution requires on average 24% less energy per unit of product and produced better quality of wood chip product.

For bulk transport in shipping and by rail, wood chips are not ideal. The size and geometry of the chips prevents good compaction in volume and leads to a low energy density of the load. Wood chips are also difficult to handle since they do not flow well in hoppers and chutes. It is more common that wood is milled to smaller particle sizes (a few millimetres) and then compressed into pellets by forcing through a die. The process of pelletisation raises the temperature of the biomass sufficiently to partially dry it. The particles also bind together by the application of heat and pressure which partially decomposes some of the lignin in the material which then acts as an adhesive. Since there is significant processing of the raw wood to make the pellets, there is an energy requirement for production which can be up to 10% of the fuel energy of the pellet (UseWoodFuelScotland, 2014).

Pellets flow better than wood chips and this allows the material to be handled in a similar manner to grains or aggregates. However, a drawback of wood pellets is that they are fragile and can produce quantities of dust as they are moved in handling. Wood pellets are also water absorbent and if exposed to rain, they will swell up and disintegrate. Transport solutions must therefore ensure that pellets are enclosed and protected from moisture. Because of the added convenience for transportation, pelletisation is also applied to other non-woody biomass including straws and olive residues.

A major advantage of pelletisation is the increase in energy density that is achieved. The bulk density of wood pellets is around 650 kg/m^3. For pellets with low moisture content and with a net calorific value of 17 MJ/kg, the energy density is 11GJ/m^3. The bulk density of wood chips is around 250 kg/m^3. Wood chips may have much higher moisture content and even with moisture content similar to pellets, the energy density is not likely to be much more than 4GJ/m^3. The bulk density of baled straw or miscanthus is even lower at about 180 kg/m^3 and the moisture content of bales can be around 25% leading to energy densities as low as 2GJ/m^3 (UK_Forest_Research, 2015). Since transport costs are more closely a function of volume, the cost of transporting wood chips or bales can be 2-3 times higher for the same energy value (EUBIA, 2009).

In recognition that pellets are the preferred form in which to transport solid biomass fuels, there have been moves to standardise the products. European Standard EN 14961-1 includes a standard specification of properties for wood pellets. UK industry standards also exist such as the IWPB (Initiative Wood Pellets Buyers) wood pellet specifications (IWPB, 2012a).

1.4.3.2 Pre-treatments

Moisture content reduces the net calorific value of a fuel. Like many properties of biomass materials, moisture content is highly variable and depends on initial conditions of the harvested material, storage conditions and size of particles. Many feedstocks generally require some form of drying before being transported let alone being used as fuels. Forestry wood, for example, usually spends a period of natural drying after felling to remove much of the moisture form the living wood. Energy crops and agricultural residues such as straw are also subjected to a certain degree of natural drying although this can be affected by adverse weather conditions.

Further drying of the biomass can be achieved by use of sheltered storage of the chipped/cut product and use of either natural or forced air flow across or through the material. A higher degree of drying can be achieved by passing the product through an oven or furnace although this clearly has an energy cost.

An extension of this process is to subject the biomass to a higher temperature in an inert atmosphere such that the material undergoes partial pyrolysis –i.e. not only is virtually all the moisture driven off, but some of the carbohydrate

content is broken down. Depending on the degree of pyrolysis, some low-calorific-value volatile matter may be extracted in the gas phase leaving a fuel with higher fixed carbon content. Other heavier hydrocarbon products such as tars and oils give the product different physical properties including a reduced tendency to absorb and contain moisture. This treatment process is known as torrefaction *(Bridgeman et al., 2008)* .

Pelletisation also reduces the moisture content as a result of the heat and pressure applied to the material in the process. When pelletisation is combined with torrefaction, the products of pyrolysis can also act as adhesive to bind the biomass particles together producing a stronger pellet less prone to subsequent moisture absorption. In addition to the significant reduction in moisture content, the resulting product has a higher energy density (Bridgeman et al., 2008). Furthermore torrefied pellets are also more friable than raw biomass so the material can be milled to small and more consistent particle sizes with grindability more similar to coal (Bridgeman et al., 2010).

A similar process which involves partial pyrolysis is “steam exploding” of wood (Lam, 2011). This process involves “cooking” the wood in a pressure vessel such that the wood structure contains pressurised steam. If the pressure in the vessel is released suddenly, the force with which internal pockets of steam expand causes the cellulosic structure to “explode”. At the same time, partial pyrolysis of the lignin and other carbohydrates leads to production of heavy hydrocarbons. The resulting mixture is similar to a fibre-composite material with the exploded cellulose fibres forming a more homogeneous and less anisotropic structure held together by a hydrocarbon glue (Suzuki et al., 1998). The material is much more hydrophobic than simple torrefied pellets and can even withstand being stored without protection against rain.

1.4.3.3 Biomass fuel storage

The majority of the solid biomass fuel delivered to large power stations is in the form of pellets. To ensure continuity of supply to the boilers, it is necessary to keep a certain reserve of fuel in storage on site. This acts as a buffer to irregular delivery patterns and possible disruption to transport links. The quantity stored depends on, among various other business considerations, logistical risks in the supply chain, operational requirements of the plant and the technical

practicalities of bulk storage. For example, for a power station with an average continuous output of 500MW and a thermal efficiency of 38% , the thermal input requirement would be 1316MW. Assuming ideal combustion and a net calorific value of the fuel as 17MJ/kg, the fuel requirement for one hour of operation would be around 280 tonnes. The storage requirement for one week of operation would be almost 50,000 tonnes. Storage of such a large quantity of biomass pellets must address the issue of protection from moisture ingress and avoidance of self-ignition.

Biomass pellets will swell and disintegrate if exposed to moisture and so must be protected from rain and other moisture ingress. Unlike coal, biomass pellets must therefore be stored under cover. For quantities in the order of 50,000 tonnes a structure with a capacity of over 100,000 cubic metres may be required. A self-supporting concrete dome with a diameter of 50-60 meters would be a possible solution. The bulk storage of biomass leads to the phenomenon of self-heating whereby biological and chemical decomposition results in exothermic processes occurring inside the mass of material. Since the material is thermally insulating, the resulting heat dissipates poorly and the temperature of the biomass internal to the mass increases. This can lead to further thermal decomposition, release of volatile matter and, if unchecked, self-ignition of the fuel. To counteract this problem, very large bulk storage may require the mass of pellets to be forcibly ventilated to remove heat. Since forcing air into a self-heated mass of material can stimulate more exothermic oxidation and increase the risk of self-ignition, it is necessary to use inert gas (nitrogen) for this purpose (Energy_Institute, 2016).

1.4.3.4 Milling biomass fuels

Pellets are the usual form in which solid biomass fuel is delivered to power generation plants. The dimensions of pellets can range from 5 – 12mm diameter and from 5 – 30 mm in length. In the pelletisation process, the constituent material of the pellet has usually been milled to a particle size much less than this. Wood pellets are typically made up of particles no larger than 3mm long. Pellets can be broken down into their constituent particles in subsequent impact milling at the combustion plant.

In plant where biomass is co-fired with coal, mixing the pellets with the coal in the coal-pulverisation plant is possible. A common type of coal pulverisation mill is a rotating ball mill in which large (0.5-1.0m diameter) steel balls and raw fuel are churned in a rotating drum or ring. The coal is pulverised by impact (crushing) between the ball and drum/ring. When small amounts (e.g. 5%) of biomass are added, the material can be broken up in the same mill. However, since biomass is typically fibrous, soft and lacking friability, it behaves in a very different manner to coal and larger quantities of biomass are more suited to dedicated mills.

If the original particle size distribution achieved in a cutting mill prior to making the pellets is suited to the combustion plant, the use of impact mills the same as or adapted from coal mills may be adequate for producing a particle size distribution suitable for the boiler. However, if further reduction in the top particle size is necessary, such an approach may not be optimal. Reduction of the top particle size by impact milling can be more energy intensive than cutting milling and may even be quite ineffective in mills designed for coal pulverisation. For milling these solid biomass fuels further, the use of a hammer-mill or cutting mill is more appropriate. Esteban and Carrasco (Esteban and Carrasco, 2006) evaluated the use of hammer-mills for grinding wood biomass with differing process strategies concluding that two-stage grinding (the larger fraction passing through the first stage being separated and passed through a second stage) was most effective for achieving a consistent particle size distribution.

Clearly, there is an energy requirement for milling whether this is in the pelletisation plant or the combustion plant. For the most efficient use of the fuel, this energy requirement should be minimised. The energy input is related to the scale of the size reduction – i.e. the smaller the particle size required, the more energy the process will consume. The nature of the biomass material and the moisture content also play a role in the energy requirement.

Temmerman et al. (Temmerman et al., 2013) made a study of the energy use for different biomass types which relates the particle size reduction and moisture content to energy requirement using an approximation based on the Von Rittinger theory of milling (Lynch and Rowland, 2005). The relation given by this study, converted to standard units, is:

$$W_{1-2} = \Omega\, M \left(\frac{1}{x_2} - \frac{1}{x_1}\right) \qquad \textbf{(1-1)}$$

Where:
W_{1-2} is the energy per unit mass required to reduced particle size from x_1 to x_2 [J/kg]
Ω is a characteristic constant for the material
M is the moisture fraction of the material
x_1 is the initial particle size [m]
x_2 is the ultimate particle size [m]

Values of Ω for various woods are given as: Beech, 1840; Oak, 3074; Pine, 3474; Spruce, 4266. For example, in order to reduce chipped pine with 15% moisture from 12mm size down to <1mm size, the energy requirement would be predicted as 478 MJ/tonne (133 kWh/tonne).
Adding the energy required for chipping the harvested wood to 12mm size (50 MJ/tonne) (Biermann, 1996) the total energy required for comminution to pulverized fuel is around 530 MJ/tonne. For a net calorific value of the fuel at around 17MJ/kg, the process of size reduction represents about 3% of the energy value of the fuel.

The pulverised fuel in the mill is extracted by an air stream (the primary air flow) through the mill which entrains the smaller particles and carries them in ducting/pipe to the combustion chamber. Only the particles under certain size and mass limits are extracted in this way. Larger particles are retained by gravity and further separation by screening on the outlet of the mill. Although the particles are then limited by a “top size” , the particle size distribution of the pulverized fuel can remain wide with the smallest fraction being fine dust (<50μm).

The challenge of achieving a consistent and uniform particle size distribution is one of the aspects of controlling effective and efficient combustion in boilers.

1.5 Large Scale Combustion Plant for Electricity Generation

1.5.1 Large scale generation plant

The technology employed for electricity generation from biomass varies depending on the physical scale of the plant and access and logistics of delivery of the fuel. An IEA report on bioenergy (IEA, 2009) presents a comparison of the capital costs and production costs of the various technologies. The principal power conversion technologies presented are:

a) Dedicated combustion of biomass in conventional thermal plant
b) Co-firing of biomass in existing coal-fired conventional thermal plant
c) Biomass integrated gasification (BIG) to fuel a combined cycle gas-turbine
d) Anaerobic digestion (AD) to produce methane for the operation of an internal combustion engine (the technology most widely used in landfill gas power stations)

The latter technology is restricted to small scale power generation. The larger AD installations in the UK are rated for peak output of no more than 3MWe. Gasification plant are generally larger, but few exceed 50MWe and the largest in the world (in 2015), in Vaasa Finland, has a peak output of 140MWe. Biomass-fuelled power generation plant with power output capacities greater than this generally employ solid fuel combustion to raise steam to drive turbines – so called conventional thermal power. The design of these types of plant are based on coal-fired technology or are actually coal-fired plant that have been converted or adapted. The typical capacity of this type of power station is between 1 to 4 GWe.

Many such plant in The Netherlands, Sweden, Finland and the UK have co-fired biomass with coal for many years since this is a simple and low risk means of using biomass fuel in existing operational coal plant without the need for major re-design of components or infrastructure investment. There are broadly two principal types of boiler designs in modern large scale solid fuel power stations: fluidised bed (FB) and pulverised fuel (PF). The proliferation of the two types is different from country to country. In the UK, most of the large scale power stations built in the 1960s and 70s by the Central Electricity Generating Board

(CEGB) are PF type. In other parts of Europe including Scandinavia, Belgium and The Netherlands, fluidised bed technologies are more common (EUBIA, 2015).

1.5.2 Pulverised fuel boilers

Since the current development of biomass combustion for large scale power generation in the UK has been based on co-firing or conversion of existing coal plant, it has been by default that pulverised fuel plant is the principal technology currently in operation for biomass power generation. This is the context for much of the remainder of this study, so it is useful to present here an overview of the plant and processes in a typical pulverised fuel power station. A schematic of a typical pulverised fuel power station is presented in **Figure 1-6**.

1.5.2.1 Combustion

The pulverised fuel and air mixture is introduced into the combustion chamber via a series of burner nozzles on the side of the boiler structure. The burners are constructed such that additional secondary air can be introduced simultaneously to control the fuel-air ratio inside the combustion chamber. The nozzle size and the mass flow rate of the fuel-air mixture will determine the velocity of the mixture into the chamber. The nozzle design may also include vanes or fins to introduce a rotational velocity (swirl) to the flow as it enters the chamber. The fuel-air mixture is thus introduced into the lower part of the boiler. Heat transfer to the fuel particles is by convection from the surrounding hot combustion gases but mainly through radiation from other combusting particles and the boiler heat transfer surfaces. As the particle heats up, the volatile matter in the fuel is vaporised and, being mixed with the primary air, combusts as a volatile flame. The remaining char particle, still entrained in the flow of gases in the chamber continues to heat up and combusts at a slower rate. The combustion process is affected by the temperature and the concentration of oxygen at the different zones of the boiler. The fuel-air ratio in the primary zone of the boiler will affect the temperature of the volatile flame. In pulverised coal furnaces, the flame temperature is typically in the range of 1700K to 1900K (Gang and Yong, 2006). Biomass, having a lower calorific value to coal, has lower flame temperatures typically in the range 1600K to 1800K (Williams et al., 2001, Ma et al., 2007). Maximum flame temperatures are obtained near to the

optimal stoichiometric mix of air and fuel. At lower air ratios, the flame temperature is reduced. Adjusting the air-fuel ratio in the primary combustion zone is a means of controlling the temperature of the flame. While higher boiler temperatures can be advantageous for heat transfer and thermal efficiency, higher combustion temperatures can increase nitrogen oxide emissions and exacerbate ash melting in the furnace so control of the combustion temperature is important. Where fuel-rich mixtures are introduced in to the boiler, the incompletely burned products from the primary zone subsequently combust with secondary air. In some cases, tertiary air can be introduced into the combustion chamber after the main combustion stage (Nussbaumer, 2003). Moisture content of the fuel also affects the flame temperature, reducing the maximum by up to 100K for each 10% moisture by weight (Salzmann and Nussbaumer, 2001). Ideally, the particles of pulverised fuel should have combusted completely by the time the entrained particle reaches the back of the boiler (the shorter “leg” of the boiler in **Figure 1-6**) thus having released all its thermal energy to the combustion chamber. The efficiency of the plant at converting the fuel energy to steam and thence electricity is dependent on achieving a high level of “burn-out” in this way. Burn-out of pulverised biomass fuel is one of the issues considered in investigations in later chapters.

Heat transfer to the steam raising part of the boiler is mainly through the combustion chamber walls which are constructed as a water jacket surrounding the main chamber. The steam raised passes out of the steam drum at the top of the boiler at high pressure (over 150 bar) or even super critical pressure (>220 bar). The temperature of the steam may be raised even further by passing within the combustion chamber in a series of tubes called “super-heaters” (steam super-heater in **Figure 1-6**). Large scale power stations generally have units with at least 500MW rated electrical output. On this scale, the steam turbines are typically staged with a high pressure stage followed by reheat of the steam by an additional pass through the boiler (steam reheater in **Figure 1-6**) and return to an intermediate pressure stage and low pressure stage turbine in series. The super-heater tubes and steam reheater tubes form a large surface area inside the combustion chamber and require their surfaces to be in good condition and unimpeded by deposits such as to afford effective heat transfer.

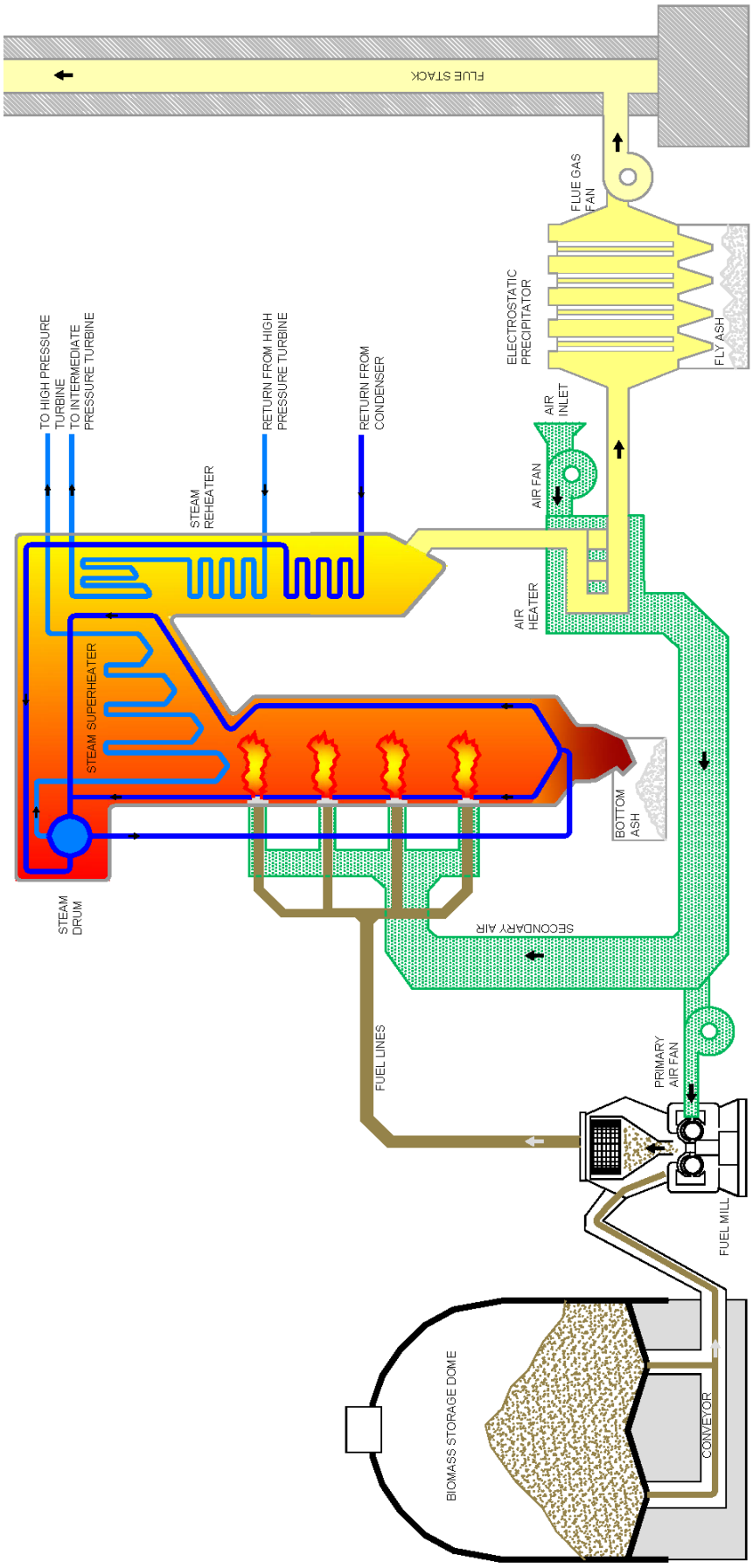

Figure 1-6 – Diagram of a large scale pulverised biomass-fuel power station showing the principal components of combustion plant (excluding steam turbines and electrical plant)

1.5.3 Ash, fouling and slagging

If complete combustion of the coal or biomass is achieved, the carbon and hydrogen pass out of the boiler as carbon dioxide and steam while the inorganic part of the fuel burned forms other substances. The substances which pass out in the gas phase (sulphur dioxide and nitrogen oxides) are discussed in the following section on emissions. The substances which form condensed phase materials are ash. The ash in the combustion chamber behaves differently and causes different issues depending on which part of the boiler it ends up in.

The fraction of ash which falls to the bottom of the chamber by gravity is called bottom ash and can usually be removed regularly with the boiler in operation. However, certain composition of ash at certain temperatures can lead to the material melting together in an amorphous, sometimes vitreous mass known as slag (slagging). Other solid ash can deposit on the heat transfer tubes. Again, with certain composition and temperature, the ash partially melts and becomes sticky such that it adheres to the surfaces and impedes the heat transfer (fouling). Ideally, that part of the ash that is not collected in the bottom of the chamber but which is light enough to be entrained in the gas flow, passes out of the chamber completely. The exhaust gases can be treated to remove this “fly ash” by the use of an electrostatic precipitator (ESP). The efficiency of the ESP is related to the electrical properties of the ash particles which, again is related to the ash composition.

The melting behaviour of the ash is a complex function of the ash composition but one particular element, potassium, which is present in biomass has a strong influence on the melting point and this will be one of the issues considered in investigations in later chapters.

1.5.4 Emissions

In addition to contributing to a reduction of CO_2 emissions, biomass energy can deliver some advantages over coal combustion with regards to other polluting emissions. While coal-fired electricity power stations are increasingly able to tackle the issues of sulphur dioxide (SO_2) and nitrogen oxides (NO_x) emissions with the adoption of, albeit costly, “clean coal” technologies, biomass combustion can have less of a tendency to produce these pollutants and their

use can allow large scale power generation to continue operations while complying with emissions limiting regulations.

In the EU, a major incentive for operators to convert to the use of biomass in existing large scale conventional power stations has not been necessarily the need to reduce CO_2 emissions but, primarily, compliance with the restrictions on pollutant emissions imposed by the regulatory limits introduced in EU Directive 2001/80/EC (EU, 2001). This legislation entitled "*on the limitation of emissions of certain pollutants into the air from large combustion plants*" requires reductions in overall emissions of NO_x and SO_2 with respect to 1980 levels. In the UK, the means of implementing this has been the National Emissions Reduction Plan (NERP) (UK_Government, 2007). This has placed specific limits on very large existing power plant (>500MW_{th}): For example the NO_x emissions limits for Drax and Eggborough power stations in Yorkshire, UK will drop from nearly 500 mg/m^3 for the period 2008-2015 to just over 200 mg/m^3 from January 2016.The likely means of compliance for power plant such as these was envisaged (in NERP) to be the introduction of low-NO_x burners together with selective catalytic reduction plant. However, the economics of fitting such technology to existing plant appeared to be unattractive compared to an alternative solution: that is, conversion to fuel which results in lower NO_x. Since many solid biofuels ostensibly satisfy this requirement, some power station operators made plans for full conversion to biomass fuel by 2016. To date, only Drax in North Yorkshire has successfully implemented full conversion which could make them viable as power generators well past 2020 (Mason, 2015).

1.6 Conclusion

1.6.1 Context

The aim of this first chapter has been to provide a contextual background about the use of biomass fuels in large scale power generation.

The question of why biomass as a fuel resource is important has been answered in terms of its potential to provide renewable, sustainable and flexible power generation as part of the primary energy mix. While there are large variations in the predicted usable resources, it is feasible that up to 5% of global electricity production could be derived from biomass by 2050. This has been recognized both in the UK and globally in response to the necessity to control CO_2 emissions from fossil fuels and mitigate their influence on climate change.

In order for the deployment of the technology to be effective in this respect, the fuel resources must be sustainable and economically viable. The current and potential biomass fuel supply has been discussed and it is contended that there is scope for biomass power generation to make significant impact in displacing fossil fuels. This has then led to an explanation of the meaning of what is “solid biomass fuel” with identification of the types of biomass which are currently being used and also those which have potential in future developments.

While there are many technologies for converting biomass fuels to electricity, the context of this study is large scale power generation with a particular focus on pulverized fuel combustion plant. An overview of this technology has been presented. Some of the operational issues associated with the technology include control over the efficiency of achieving full burn-out of the fuel inside the furnace and control over the behaviour of the resulting ash.

1.6.2 Research and knowledge gaps

Three areas where there are gaps in knowledge of biomass combustion have been identified:

1) Particle size and burn-out efficiency

Effective control of burn-out efficiency has been identified as one of the key issues with respect to the operation of pulverized fuel (p.f.) boilers with solid biomass fuel. While there is extensive knowledge and experience of the

combustion behaviour of pulverized coal, experience of burning biomass in the same plant is comparatively limited. The difficulties in reducing biomass fuels to particle sizes as small as p.f. coal is challenging and energy-consuming. There is therefore an incentive for operators to aim for the largest particle size possible while still achieving good burn-out. The relationships between particle size and burn–out in the context of p.f. have not been addressed in detail in the literature. Furthermore, there is little, if any information presented to quantify the variations in these relationships for different biomass fuels.

2) Potassium transformations during combustion

Fouling, slagging and corrosion in boiler plant are significant issues for large combustion plant operators. It is recognised that the ash from most biomass fuels is different in composition to most coals. In particular, biomass contains higher proportions of potassium which affects ash behaviour and can stimulate corrosion mechanisms. However, the phase transformations and species transformations of potassium during the combustion of biomass are not understood sufficiently to allow accurate prediction of how and where potassium might end up. Deeper understanding of potassium transformations during biomass combustion is therefore important.

3) Thermal conductivity of solid biomass fuels

While there are considerable data in the literature on the thermal properties of various woody materials, there is little information on the thermal conductivity of herbaceous biomass or other non-woody biomass materials. This is important information required for modelling and analysing solid fuel combustion.

1.6.3 Thesis aims and overview

Having provided a contextual background and identified certain gaps in knowledge, the aims of the research presented in this thesis can be set out. Two particular challenges relevant to the combustion of biomass in large scale power generation, provide the incentive for investigation. These can be summarised as:

- assessing the variability in fuel combustion behaviour and control of burn-out efficiency for different fuels

- understanding the behaviour of potassium during the combustion of biomass fuels to aid in the prediction of ash behaviour and associated emissions

In addition, the need for data on the thermal properties of a wider range of solid biomass fuels has been identified. In this case, the challenge is the means of taking measurements on small quantities of very variable materials.

In tackling these challenges, each chapter addresses a specific research question. These are set out below along with a brief overview of the chapter content.

Chapter 2

What are the characteristics of solid biomass fuels as used in large scale power generation and how do these characteristics compare to each other and to other fuels?

Details are presented of the composition and fundamental characteristics of the solid biomass fuels selected for experimental study. This includes description of the analytical methods used for fundamental characterisation and means of interpreting the data. The analytical results are presented alongside a discussion and comparison of the fuel properties.

Chapter 3

What are the relationships between particle size/shape/mass and the time required for full combustion (burn-out efficiency) in certain high-temperature conditions?

A detailed description is presented of an experimental method to determine the relationship between particle size and duration for burn-out in a high-temperature flame environment. A large data set is obtained from three fuel samples for detailed analysis. Empirical expressions to describe the relationship between particle mass and characteristic combustion times are derived from the data. A further ten fuels are examined using the same method. The chapter includes an introduction (including literature review), methodology, results and analysis.

Chapter 4

What are the relationships between potassium content and the patterns of gas-phase potassium release during combustion of biomass fuels and how does this vary between different types of fuel?

A detailed description is presented of an experimental method for examining the patterns of gas-phase potassium release from a particle of biomass as it combusts in a furnace-like environment. Thirteen fuels are examined using the method. The chapter includes an introduction (including literature review), methodology, results and analysis.

Chapter 5

How does the thermal conductivity of different types of biomass fuel vary?

A detailed description is presented of an experiment for measuring the effective thermal conductivity of various biomass materials. Measurements are presented for fourteen different biomass fuel materials. The chapter includes an introduction (including literature review), methodology, results and analysis.

Chapter 6

What insights into the combustion of biomass at high temperature can be inferred from modelling based on experimental results of single particle combustion and potassium release?

A model is presented of a single particle of biomass in the same combustion environment as that of the experiments described in chapters 3 and 4. Each element of the model is described with appropriate references and justifications. The completed model is used to validate assumptions and interpret the results of the experiments. A brief review of the literature on modelling gas-phase potassium release in biomass combustion is included in the introduction.

Chapter 2
Fundamental characterisation of solid biomass fuels

2.1 Solid biomass fuel samples

In preparation for the investigations on combustion behaviour of solid biomass fuels covered in later chapters, samples of a range of solid biomass fuels were selected for study. The samples were selected on the following criteria:

a. To be representative of fuels which are typically used or considered for use in large scale power generation plant.
b. To have diversity in the types of materials (within the limits of criterion a.) to allow comparison across the range of fuel properties and characteristics.

To obtain fuels which were known to be used as fuels in operational power plant, many of the samples were sourced from power station operators directly. Some samples were obtained from harvests of research-trial crops from Rothamsted Research agricultural research institution. The quantity and form of the samples was determined by the availability from the various suppliers. Three coal samples were selected for comparison. The full selection of samples is summarised in **Table 2-1**.

All materials were prepared using similar processing to provide consistent samples for the appropriate analyses in accordance with the methods described in European Standard EN14780 (Standard, 2011a). Where division of the sample was required for extracting a sub-sample, this was achieved using cone-and-quartering technique or using a riffle. Materials received in raw or pelletised form were reduced to <2mm top particle size using a Retzsch SM100 cutting mill. This coarse, milled material was used for producing ash samples and for proximate analysis (i.e. moisture, volatile matter and ash content). A fraction of all materials were further milled using a liquid nitrogen impact mill (Spex 6770 freezer mill) and the entire fraction (~10-20g per material) passed through a 90μm sieve. These finely milled samples was used in thermo-gravimetric analysis, elemental analysis and calorimetric analysis. For other experiments and analyses where large particle sizes were required, the as-received materials were used and cut to the appropriate sizes.

Table 2-1 - Solid fuel samples

Sample name	*Description*	*Form supplied*
Willow A	a short rotation coppice willow energy crop from the United Kingdom	pellet
Willow B	research-trial short rotation coppice willow energy crop from the United Kingdom	wood-chips & hammer milled
Wood pellet A	"white" wood pellet originating from United Kingdom	pellet
Wood pellet B	"white" wood pellet originating from North America	pellet
Wood pellet C	mixed forestry wood pellet originating from North America	pellet
Pine	pine wood from UK forestry (including bark)	milled in various particle size fractions
Eucalyptus	eucalyptus wood from north America	wood chips
Wheat straw A	wheat crop harvest in Yorkshire, UK	loose straw
Wheat straw B	research-trial wheat crop harvest in United Kingdom	loose straw & hammer milled
Rape straw	oilseed rape crop harvest in Yorkshire, UK	loose straw
Miscanthus A	miscanthus energy crop from the United Kingdom	whole harvested plants
Miscanthus B	research-trial miscanthus crop from the United Kingdom	hammer milled
Steam exploded wood pellet	"black-pellet" from a producer of steam-exploded wood pellets in the USA	pellet
Olive residue	from Mediterranean olive residue waste	pellet
Coal A	from El Cerrejón mine, Colombia	milled
Coal B	from Kellingley colliery, Yorkshire, UK	lump
Coal C	from Pittsburgh, USA (Pittsburgh #8)	milled

2.2 Experimental and Analytical Methods

2.2.1 Proximate analysis

Proximate analysis is the determination of the composition of a fuel in terms of the following constituents:

- Moisture
- Volatile matter
- Fixed carbon
- Ash

2.2.1.1 Moisture content

The moisture content of a fuel sample is the amount of water, removable by oven drying, that is contained within the material. It is defined here (and is used consistently throughout other chapters) as a proportion of the gross sample mass:

$$M = \frac{m_w}{m_w + m_d} \quad \textbf{(2-1)}$$

where:

M is the mass fraction of moisture in the sample

m_w is the mass of moisture in the sample

m_d is the mass of the dry (moisture-free) sample

The standard procedure for determining moisture content of solid biomass fuels is defined in EN 14774-3 (Standard, 2009a). The method entails heating a milled sample (~1g) of the fuel in a laboratory oven to 105°C for an extended period (>3 hours) and measuring the mass loss. This method was used to determine the “as received” moisture content of the fuel samples.

Since the moisture level is affected by the freezing process, the moisture in the finely-milled samples processed in the freezer-mill were measured separately using a similar heating profile in a thermo-gravimetric analyser (TA Instruments TGA Q5000).

2.2.1.2 Volatile matter content

As a ligno-cellulosic material is heated, the complex organic components (cellulose, hemicellulose and lignin) thermally break down to produce a wide range of simpler organic compounds. These may be light hydrocarbons or

heavier tars depending on the heating rate and temperature at which they form. Higher temperatures favour gas formation as the volatiles break down further to species such as CO, CO_2, H_2O, CH_4 and H_2. The process of thermal conversion of the solid fuel into volatile products is *pyrolysis.* The volatile release itself is referred to as *devolatilisation.* When devolatilisation is complete, a solid residue remains which is composed of the carbon-enriched char and the ash components. Since the devolatilisation process is dependent somewhat on heating rates and temperatures, evaluating the volatile content with replicability requires that these conditions are reasonably consistent in each test.

The standard procedure for determining volatile content of solid biomass fuels is defined in EN 15148 (Standard, 2009d). The method entails rapid heating of a milled sample (~1g) held in a loosely-lidded crucible placed in a furnace at 900°C for 7 minutes. The volatile matter in the sample is taken to be the mass loss of the sample adjusted to account for moisture content. This method was used to determine the volatile content of each fuel sample. The volatile content is defined as:

$$vol_d = \frac{m_{vol}}{m_d} \qquad \textbf{(2-2)}$$

where:

vol_d is the dry basis mass fraction of volatile content

m_{vol} is the mass of volatile matter in the sample

2.2.1.3 Ash content

If a biomass fuel is fully combusted, the volatile organic components and the carbon are all oxidised and transfer to the gas-phase. Ash is the unburned solid phase residue left over at the end of the process. It mainly consists of oxidised inorganic components. However, depending on the temperature and atmosphere during combustion, there may be small quantities of unburned carbon in ash also.

The standard procedure for determining ash content of a biofuel sample is defined in standard EN 14775 (Standard, 2009b). The method entails heating a milled sample (~1g) in a furnace with a suitable air flow to an initial temperature of 250°C for one hour and then to 550°C for a further two hours. The mass of ash in the sample is the mass of the remaining residue in the crucible. This

method was used to determine the ash content of each fuel sample. The ash content is defined as:

$$ash_d = \frac{m_{ash}}{m_d} \quad \textbf{(2-3)}$$

where:
ash_d is the dry basis mass fraction of ash in the sample
m_{ash} is the mass of ash in the sample

2.2.1.4 Fixed carbon content

The 'fixed carbon' in a biomass material refers to the quantity of material remaining in the sample, excluding the ash content, after the devolatilisation process. While the material may still include some heavier organic molecules, it is predominantly non-volatile carbon hence the term 'fixed carbon'.

The fixed carbon content is derived as:

$$char_d = 1 - vol_d - ash_d \quad \textbf{(2-4)}$$

where:
$char_d$ is the dry basis mass fraction of char (fixed carbon)

2.2.2 Molecular analysis

The three principal molecular components of ligno-cellulosic biomass are cellulose, hemicellulose and lignin. The proportions of each of these can be determined from a series of digestions and filtrations (Goering and Soest, 1970).

Analytical methods for determining the three components of fibrous biomass are defined in international standards: ISO 13906 (Standard, 2008);ISO 16472 (Standard, 2006b) and; ASTM D1106 (Standard, 2013).

The non-fibrous matter can be extracted from the sample by use of a neutral detergent to produce a residue of 'neutral detergent fibre' (NDF) consisting of the hemicellulose, cellulose and part of the lignin. An acid detergent can dissolve out the hemicellulose but leave the acid detergent fibre (ADF) which consists of cellulose and the NDF part of the lignin. The hemicellulose content is determined by the difference between the NDF and ADF content. That part of the lignin in the ADF can be extracted as acid detergent lignin (ADL) such that the cellulose content can be determined as the difference between the ADF and

ADL. The total lignin or ‘Klason lignin’ is determined by a separate extraction by 72% sulphuric acid.

The selected biomass fuel samples were analysed externally, using the above techniques, by the *Institute of Biological, Environmental and Rural Sciences* (IBERS), Aberystwyth University.

2.2.3 Ultimate analysis

Ultimate analysis is the determination of the composition of a fuel in terms of the principal elemental components. In ligno-cellulosic biomass these are carbon, hydrogen and oxygen. Nitrogen and sulphur may also be present in small, but significant quantities. Both of these are important in the context of combustion since their oxide forms are gaseous (i.e. NOx and SO_2) and notable pollutants.

The determination of the principle elemental content (ultimate analysis) can be carried out using proprietary automated organic element (CHNS) analysers. Such analysers perform a controlled combustion at 900°C in an oxygen atmosphere to produce CO_2, H_2O, NO_2 and SO_2. The products pass through a gas-chromatography column and the relative volume fraction of each is measured at the exit of the column by detecting the change in thermal conductivity of the gas. The absolute masses of C, H, N and S in the original sample can then be calculated. The oxygen content is derived by mass difference, accounting for the mass of ash in the sample. The standard procedure for determination of carbon, hydrogen and nitrogen content is defined in EN 15104(Standard, 2011b).

In accordance with the standard method, the analysis was undertaken on duplicate samples using an automated analyser (CE Instruments Flash EA1112). Additional measurements were undertaken independently on samples of pine, eucalyptus and willow pellet using a second analyser (CE Instruments Flash EA2000) for verification of the results from the first analyser. Standard reference materials (B2170 Olive stone and B2276 Oatmeal) were used to check the calibration of the instruments. Proportional quantities of carbon, hydrogen, nitrogen and sulphur were obtained.

2.2.4 Calorific value

The specific energy is also referred to as the calorific value (or heating value) of a fuel. There are two distinct measures of calorific value: gross calorific value (GCV - also referred to as High Heating Value or HHV) and net calorific value (NCV - also referred to as Lower Heating Value or LHV). The difference between the two values is the energy of vaporisation of the moisture after combustion (moisture in fuel + water produced from oxidisation of fuel hydrogen content). The gross value represents the energy release if the water in the combustion products is in liquid phase whereas the net value represents the energy release if the water in the combustion products is in vapour phase. Although the net value is the real useful energy extracted in most applications, the gross figure (or HHV) on a dry basis (excluding the initial moisture in the material) is the usual figure given in fuel characteristic data.

The actual calorific values of different biofuels depend on the chemical composition and the physical density of the material. The calorific value of a fuel sample can be determined in the laboratory using a bomb calorimeter. It is important to distinguish between the different calorific values obtained on net or gross basis on dry or wet basis. The European standard method, EN14918 (Standard, 2009c) for determination of calorific value in solid biofuel defines the various calorific values (in J/kg) as follows:

Gross calorific value at constant volume:

$q_{cv,gr}$ (The value determined in bomb calorimeter)

Gross calorific value at constant volume, dry basis:

$$q_{cv,gr,d} = q_{v,gr} \times \frac{1}{1-M} \quad \textbf{(2-5)}$$

Net calorific value at constant pressure, dry basis:

$$q_{cp,net,d} = q_{cv,gr,d} - 2.122\, H_d - 0.008(O_d + N_d) \quad \textbf{(2-6)}$$

Where: H_d , $O_d$and N_d are respectively, the fractions of hydrogen, oxygen and nitrogen by mass in the dry sample

Net calorific value at constant pressure, in sample with moisture content :

$$q_{\mathrm{cp,net,w}} = q_{\mathrm{cp,net,d}} \times (1 - M) - 2443 \times M \quad \textbf{(2-7)}$$

There are also empirical formulae based on the proportions of the principal elemental constituents. A formula derived empirically with detailed statistical analysis by Friedl et al. (Friedl et al., 2005) can be used as a means of estimating the gross calorific value:

$$GCV = 100 \times \{355(C_d)^2 - 232(C_d) - 2230(H_d) + 5120(C_d \times H_d) + 131(N_d) + 206\} \quad \textbf{(2-8)}$$

The calorific values of the samples were measured using a bomb calorimeter (Parr 6200 Isoperibol Calorimeter) in accordance with EN14918 standard (Standard, 2009c). Calculated values were obtained using the approximation from Friedl et al. (Friedl et al., 2005).

2.2.5 Inorganic content

Evaluation of the inorganic content of fuels can be made by various methods including production and analysis of ash. However, depending on the combustion temperatures and heating rates, ash produced for analysis may include unburned carbon or may lose some more volatile elements (e.g. potassium) to the gas phase in the process (Xing et al., 2016).

Analysis can be made directly on the fuel by digesting the material in acid rather than combusting it so that volatile components are not lost in the process. A standard method for determination of major inorganic elements in solid biofuels is set out in EN15290 standard (Standard, 2011c).

Methods of determining inorganic content in fuels include:

- Wet chemical analysis
- X-ray fluorescence spectroscopy (XRF)
- Energy dispersive x-ray spectroscopy (EDX)

For each of the biomass materials analysed, ash samples were prepared using similar methods as described in section 2.2.1.3. These were further heated at 815°C to remove residual carbon. Each of the methods listed above was employed to evaluate inorganic content of the selected biomass fuels. In most cases, all three methods were used and the results were collated.

Chlorine content of the biomass samples was determined by a separate wet chemical analysis through the laboratory services of the University of Leeds,

Department of Chemistry. Chlorine content relative to the major inorganic elemental content was also measured as part of the EDX analysis (see 2.2.5.3).

2.2.5.1 Wet chemical analysis

A sample of each ash was prepared for wet chemical analysis by acid digestion to form an aqueous solution. Two analytes were produced:

> Solution A – reaction of ash with sodium hydroxide at 650°C to produce sodium silicate which is dissolved in HCl to give silicic acid in solution. The analyte is used only for the determination of silicon content.
> Solution B – acid digestion by hydrofluoric, hydrochloric, sulphuric and nitric acid sequentially.

Evaluation of the quantity of each element in the solution by atomic absorption spectroscopy (AAS), spectrophotometry or titration. The content of ten major inorganic elements was quantified using the analytical methods summarised in **Table 2-2**.

Table 2-2 - Wet chemical analytical methods for major elements of ash

Element	*Analyte*	*measurement method*
Sodium	Solution B	AAS
Magnesium	Solution B	AAS
Aluminium	Solution B + KCl	AAS
Silicon	Solution A + ammonium molybdate + reducing agent to give silicomolybdic complex (blue)	Spectrophotometer @ 650nm
Phosphorous	Solution B + molybdovanadate to give vanadomolybdophosphoric complex (yellow)	Spectrophotometer @ 430nm
Potassium	Solution B	AAS
Calcium	Solution B + triethanolamine	Titration with EDTA
Titanium	Solution B + hydrogen peroxide to give pertitanic complex (yellow)	Spectrophotometer @ 430nm
Manganese	Solution B	AAS
Iron	Solution B	AAS

2.2.5.2 X-ray fluorescence spectroscopy (XRF)

XRF spectroscopy may be used for analysing elemental content in solid-phase samples. The method is based on measurement of the fluorescent x-ray emissions from a sample after it has been irradiated by a primary x-ray source. Each element in the sample can be identified by its characteristic spectra and relative concentrations can be determined from the respective emission intensities.

A sample of each ash was prepared for the XRF analysis by fusing into solid glass discs for insertion in to the XRF spectrometer. The discs consisted of 0.5g of standard or sample (ground to <100 μm), 5.0g of flux and 0.05g lithium bromide. A melt was produced at 1200°C for 12 min in a Pt/Au crucible and was cast as a disc in a mould. The samples were analysed for the elements listed in **Table 2-2** using an X-Thermo ARL Advant XP sequential XRF spectrometer. The measurement method is not fully quantitative and the results show only the relative proportions of the selected elements.

2.2.5.3 Energy dispersive x-ray spectroscopy (EDX)

Energy dispersive x-ray spectroscopy can also be used for analysing elemental content. Similarly to XRF, the method involves the measurement of the x-ray emission spectra from a sample. However, in EDX spectroscopy, the x-ray emissions from the sample are stimulated by an electron beam rather than primary x-ray radiation. EDX is then commonly used with scanning electron microscopes (SEM) where the scanning electron beam stimulates the x-ray emissions.

Samples of each ash for EDX analysis were adhered to a copper substrate support for insertion into a Carl Zeiss EVO MA15 scanning electron microscope (SEM) fitted with an Oxford Instruments AztecEnergy EDX system. The samples were analysed for the elements listed in **Table 2-2** with EDX spectra recorded for at least six different sample sites. The measurement method is not fully quantitative and the results show only the relative proportions of the selected elements.

2.2.5.4 Minor Inorganic content

Biomass fuels also contain inorganic elements, other than those listed in **Table 2-2**, which are present at lower levels and for which the methods described in section 2.2.5 are not sensitive or precise enough. Some of these are of interest because of their toxic pollution potential (e.g. mercury and cadmium) while others can affect ash behaviour (e.g. lead and zinc). For these, a more sensitive means of analysis is necessary. A standard method for determination of minor inorganic elements in solid biofuels is set out in standard EN 15297-20. In accordance with this standard, the biomass fuels were prepared by digestion in concentrated nitric acid together with microwave heating. The resulting acid solution was diluted with deionised water to produce estimated concentrations of the elements of interest in the range 10-1000 parts per billion (ppb). In some cases this required dilutions of the initial analyte by 1000 times. The solutions were then analysed for the measurement of lead and zinc content using a Perkin Elmer ELAN DRC-e inductively-coupled-plasma-mass-spectrometer (ICP-MS) analyser. In an ICP-MS analyser, the sample is ionised in a plasma produced by electromagnetic induction (inductively couple plasma). The ionised sample is then passed through a quadrupole mass analyser which separates the ions on the basis of their mass-to-charge ratio. The concentration of ions is measured by a detector. The method allows detection of concentrations in the order of parts per billion which can be quantified by calibration against analytes with known concentrations.

2.2.6 Thermogravimetric analysis

Thermogravimetric analysis is a method of examining the changes in the solid-phase mass of a sample as it is subjected to a fixed or changing temperature. For the investigation of biomass fuels, measurement of the change in mass of a sample as a function of increasing temperature provides insights into the process of drying and the chemical reaction characteristics and devolatilisation and combustion.

Three aspects of the biomass thermal behaviour were examined by means of thermogravimetric analysis: drying; pyrolysis and char oxidation. A *TA Instruments TGA Q5000* thermo-gravimetric analyser was used for the measurements.

Samples were milled, using the method described in section 2.1, to a top particle size of less than 90μm. Samples of 2-3mg were placed in the TGA analyser sample pans and arranged in a thin, evenly-spread layer. These measures were taken to facilitate good heat transfer and minimise effects of internal heat conduction which may introduce a discrepancy between the apparent measured temperature and actual temperature of the sample (Hayhurst, 2013).

2.2.6.1 Drying

The samples were initially heated at a rate of 10°C/min up to 105°C in a nitrogen gas flow rate of 50 ml/min. The temperature was held at 105°C for 20 minutes ensuring that the rate of mass loss was negligible by the end of this heating stage. The mass loss during this part of the analysis was taken as the mass of moisture released during drying.

2.2.6.2 Pyrolysis

Following the drying phase, the temperature of the sample was increased at a heating rate of 10°C/min to 900°C. The furnace was maintained in a nitrogen atmosphere with a gas flow rate of 50 ml/min. During this part of the analysis, the samples underwent pyrolysis producing a char at the end of the stage. The mass loss and rate of mass loss were recorded to allow examination of the pyrolysis reaction rate(s) as a function of temperature.

2.2.6.3 Char Oxidation

Following the pyrolysis stage, the furnace was allowed to cool to 50°C before the gas flow was changed to air at a flow rate of 50 ml/min. The temperature of the samples was then increased at a heating rate of 10°C/min to 600°C. During this part of the analysis, the char samples underwent oxidation. The mass loss and rate of mass loss were recorded to allow examination of the oxidation reaction rate as a function of temperature.

2.3 Results of analyses

2.3.1 Phyllis2 reference data

Data on the compositional analysis of a wide range of biomass fuels and coals gathered from various laboratories and published literature have been collated by the Energy research Centre of the Netherlands (ECN) and made available online through the Phyllis2 database (Phyllis2, 2013). Data extracted from the database were used for comparison with the measured results of analysis for the fuel samples selected in this study. This was done, primarily, as a check on the measurements to confirm that the values obtained were consistent with those of similar biomass materials analysed elsewhere. Since the database includes data for several thousand samples, it is also a useful indicator of the variability of biomass fuels.

The materials groups selected for comparison with proximate analysis results included: “grass/plant”; “husk/shell/pit”; “straw/stalk/cob/ear”; “untreated wood”. This provided a set of data based on 648 different samples from which mean, median, maximum and minimum values were obtained for each measurement.

2.3.2 Proximate analysis results

The results of the proximate analyses (moisture, volatile content, fixed carbon and ash) of the selected fuel samples are presented in **Table 2-3**. All measurements were duplicated or triplicated. The error bands indicate the 95% confidence range derived from the standard error of the data. The results are also presented graphically in **Figure 2-1** to allow visual comparison between the different fuels.

2.3.2.1 Moisture content

Even for fuel from the same source, moisture content can vary from one extreme to the other and depends on the type of material, age, storage conditions and pre-treatments – including milling and drying processes. To illustrate this variability, moisture content figures from the ECN Phyllis2 online database were examined. The moisture content levels in the database selection range from less than 1% to 95%. The mean level is 20% and median at 10%.

With the exception of two samples, the 'as received' moisture content of the selected fuels was less than 10%. Following the cryo-milling process, most of the biomass samples had moisture contents of 5% ± 2%.

Table 2-3 - Proximate analysis of selected biomass fuel samples

wt%	*moisture content* as received		cryo-milled		*volatile content* dry-basis		*ash content* dry-basis		*fixed carbon* dry-basis	
	%	+/-	%	+/-	%	+/-	%	+/-	%	+/-
willow A	5.6	0.09	5.9	0.42	78.0	0.61	5.4	0.16	16.6	0.77
willow B	3.1	0.08	4.1	0.50	82.0	0.33	1.9	0.07	16.1	0.40
wood pellet A	8.9	0.23	2.7	0.12	84.8	0.17	0.3	0.11	15.0	0.28
wood pellet B	5.5	0.04	4.1	0.02	83.0	0.32	1.0	0.02	16.0	0.34
wood pellet C	6.9	0.08	5.1	0.52	83.8	0.07	1.2	0.09	15.0	0.16
pine	9.5	0.10	4.5	0.37	80.9	0.01	2.0	0.37	17.1	0.38
eucalyptus	8.1	0.06	6.0	0.31	82.6	0.14	0.9	0.04	16.5	0.18
wheat straw A	10.8	0.03	5.5	0.29	73.4	0.23	7.5	0.26	19.1	0.49
wheat straw B	8.1	0.07	5.2	0.04	76.6	0.33	6.4	0.05	17.0	0.38
rape straw	14.3	0.03	7.6	0.56	76.9	0.40	6.3	0.09	16.8	0.49
miscanthus A	7.4	0.05	4.6	0.13	77.6	0.10	4.9	0.14	17.5	0.24
miscanthus B	2.5	0.00	3.7	0.77	83.4	0.13	1.8	0.01	14.8	0.14
S-E pellet	7.2	0.05	4.2	0.02	76.1	0.41	4.2	0.08	19.7	0.49
olive residue	5.9	0.00	4.8	0.04	74.0	0.10	7.6	0.25	18.4	0.35
coal A	5.5	0.01	2.2	0.02	39.5	0.06	1.5	0.06	59.0	0.12
coal B	2.2	0.09	2.2	0.09	30.3	0.00	18.4	0.10	51.3	0.10
coal C	1.6	0.11	1.6	0.11	37.7	0.16	7.6	0.07	54.7	0.23

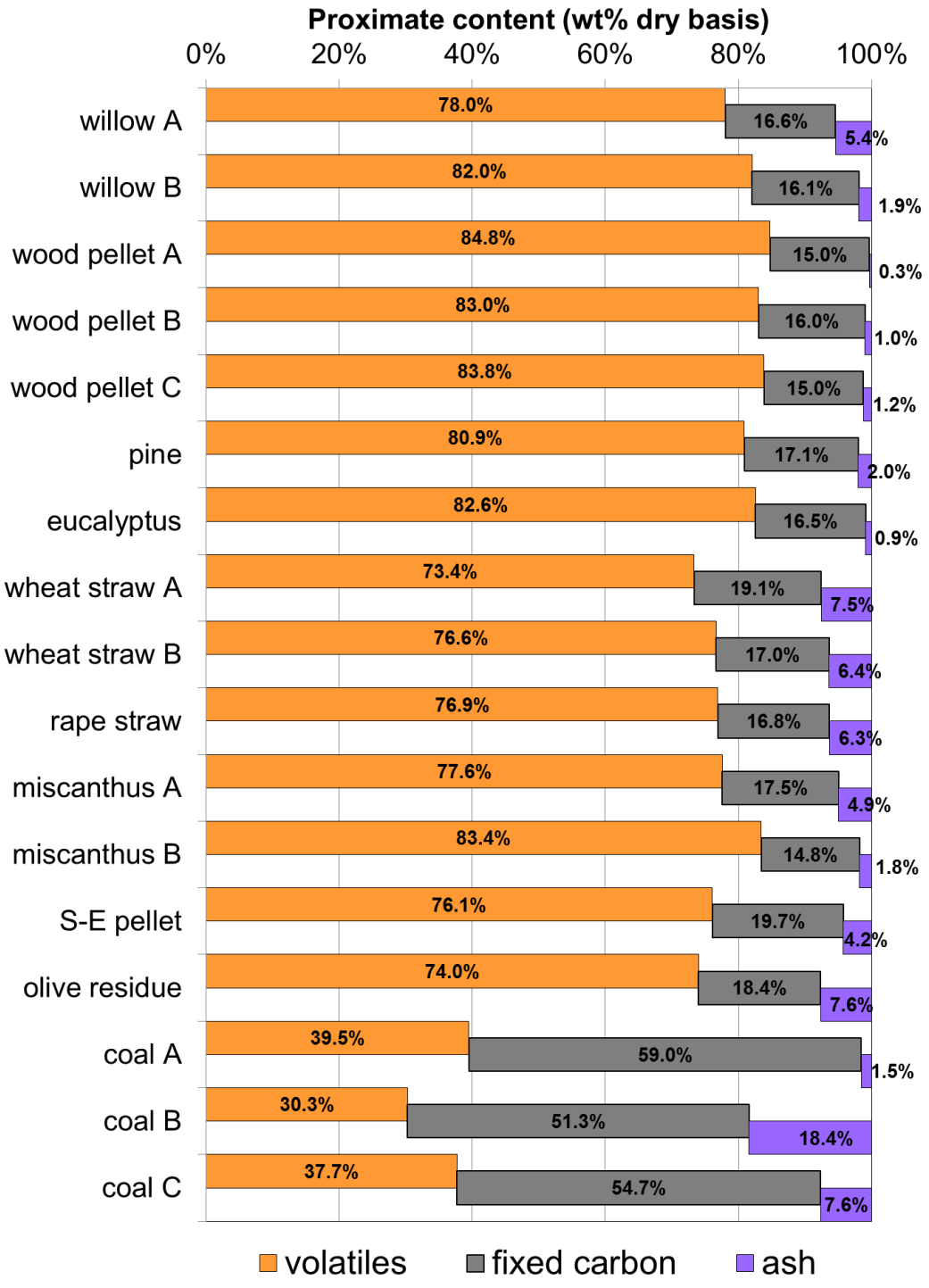

Figure 2-1 – Proximate analyses of selected biomass fuel samples

2.3.2.2 Volatile content

Volatile content figures for 648 biomass samples were obtained from the ECN Phyllis2 online database (Phyllis2, 2013). The volatile content values in the database study have a mean of 81% and a median at 82%.

From the measurements, all the biomass samples have a volatile content in the range 70%-85% (dry basis). It is noted that most of the woody materials have a volatile content exceeding 80% while the herbaceous materials all have lower volatile content. The steam exploded pellets have a lower volatile contents than other wood derived fuels owing to partial pyrolysis during processing (torrefaction). The coal samples have volatile content around half or less of that of the biomass samples.

2.3.2.3 Ash content

A set of values for (550°C) ash content for 157 biomass samples were obtained from the ECN Phyllis2 online database. The ash content values in the database study have a mean at 4.2% and median at 2.9%. The selected biomass samples are consistent with this having a mean average ash content of 3.7% with a median of 3.1%.

It is notable that most of the wood based fuels have low ash content. The steam exploded pellet and willow pellets have higher than expected ash possibly from the inclusion of inert material (e.g. dirt) in the pelletisation process.

2.3.2.4 Fixed carbon

A set of values for fixed carbon content for 648 biomass samples were obtained from the ECN Phyllis2 online database. The fixed carbon content levels in the database study have a mean average at 18.7% and median average at 18.1%.

While carbon in cellulosic biomass varies around 47% +/-3% (see elemental composition analysis section 2.3.4), the proportion of this which is extracted in the volatile content measurement is variable. The usefulness of this measurement is limited since the chemical kinetics are affected by the heating rates experienced and variability in particle size and thermal conductivity will affect the result. With this caveat, the standard method can be taken at face value as a simple means of obtaining a reproducible value which may be used for analysis and for comparison between fuels. In the selected samples, it is notable that most materials are within about +/-10% of the “expected” value. The exceptions are the miscanthus samples for which the measurements are higher than expected. Nevertheless, all the measured values for biomass materials are in a fairly narrow range from about 15% to just less than 20%. The

coal samples, as expected since their volatile contents are considerably lower, have fixed carbon content of 50-60%.

2.3.3 Molecular composition

Woody biomass is a complex mixture of molecules and clearly variable in density, strength and texture. However, the principle organic molecular components are common to all varieties albeit in differing quantities and arrangements.

Wood is made up of xylem tissue. The outer surface of the xylem core is surrounded by a thinner layer of phloem which is the tissue that carries nutrients from the leaves to other parts of the tree. The phloem is in turn covered by a layer of impermeable suberin-containing phellem cells (cork) and finally a layer of hard dead cells (rhytidome). The phloem, phellem and rhytidome together make up the bark. As a tree grows, a new layer of xylem tissue is formed at the interface of the phloem. In older trees, the xylem cells in the inner core can die and accumulate extractives (oils and pigments) giving the wood in the centre a harder texture and darker appearance – this is known as “heartwood”. The living xylem which transports the water through the tree is known as the “sapwood”. (Hon and Shiraishi, 2001)

Cellulose in the form of microfibrils serves to make up the structural framework in the cell walls of wood xylem. Hemicellulose is the substance present between the microfibrils and lignin is the encrusting substance binding the wood cells together and giving rigidity to the cell walls. These three principal molecular components, cellulose, hemicellulose and lignin make up the main bulk of most plant-based biomass materials including woods and grasses which are collectively referred to as ‘lignocellulosic’ materials.

Cellulose is a polysaccharide chain of glucose rings (pyranose) linked via an oxygen which can be represented as $[C_6H_{10}O_5]_n$. The chains form rigid “ribbons” with the CH_2OH group on each ring sited alternately on opposite sides of the chain. The chains can be up to several thousand units in length. Hydrogen bonding between adjacent chains forms the cellulose into fibres (Hon and Shiraishi, 2001).

Hemicellulose is also a polysaccharide consisting of a mixture of pentose and hexose components which can be represented as: $[C_5H_8O_4]_{n1} \cdot [C_6H_{10}O_5]_{n2}$. In contrast to cellulose, the chains formed from these sugars tend to form shorter and rather random, cross-linked and amorphous structures. In wood, the hemicellulose encases and adds strength to the cellulose fibres (Hon and Shiraishi, 2001).

Lignin is a much more complex polymer compound with an irregular and non-homogeneous structure. The sub-units of lignin are coumaryl, sinapyl and coniferyl alcohol. Lignin molecules bind together the fibres of wood as an adhesive. A representative chemical formula is not very useful since the composition of lignin in different plants is so variable. The proportions of CHO in lignin are approximately: $C_{31}H_{34}O_{11}$

In addition to the principal components, biomass can contain many other organic compounds collectively referred to as extractives. Extractives can be subdivided in to those which are water-soluble and those which are soluble in organic solvents. The main groups of wood extractives are:

- Terpenes (phenols, hydrocarbons, lignans)
- Fatty acids (oils, waxes, resins, resin acids and sterols)
- Pigments (phlobaphenes, tannins, stilbenes)
- Carbohydrates (proteins, alkaloids, sugars, starch, pectin)

The results of fibre content analyses for cellulose, hemicellulose and lignin are presented in **Table 2-4** (on a dry ash-free basis). The results are also presented graphically in **Figure 2-2** (including ash content) to allow visual comparison between the different fuels.

The analysis shows the broad similarities between the woody materials which have cellulose:hemicellulose:lignin in (ash free) proportions approximately 50:15:30. The herbaceous materials have proportions nearer to 40:25:20. It is notable that the steam-exploded wood pellet has no detectable hemicellulose – a consequence of the thermal conversion (torrefaction) that the material underwent in the steam-explosion process. The olive residue is substantially different to the other materials, having much less fibrous content overall and a higher proportion of extractives. This is because the fruits and seed of plants

concentrate nutrients and contain higher proportions of oils with other carbohydrates and proteins.

Table 2-4 - Molecular composition of selected biomass fuel samples

wt% d.a.f. basis	*hemicellulose*	*cellulose*	*lignin*	*extractives*
willow A	15.4	55.8	27.7	1.1
willow B	13.3	50.9	27.3	8.5
wood pellet A	15.5	47.7	27.9	8.9
wood pellet B	16.7	47.6	29.3	6.4
wood pellet C	13.3	48.3	30.2	8.2
pine	11.2	56.8	29.9	2.2
eucalyptus	10.6	58.8	30.2	0.5
wheat straw A	26.4	47.1	21.9	4.5
wheat straw B	30.7	45.0	20.9	3.3
rape straw	19.6	47.8	20.5	12.1
miscanthus A	29.8	43.5	23.1	3.5
miscanthus B	29.7	32.8	21.3	16.2
S-E pellet	0.0	44.6	41.3	14.0
olive residue	10.6	22.1	31.5	35.8

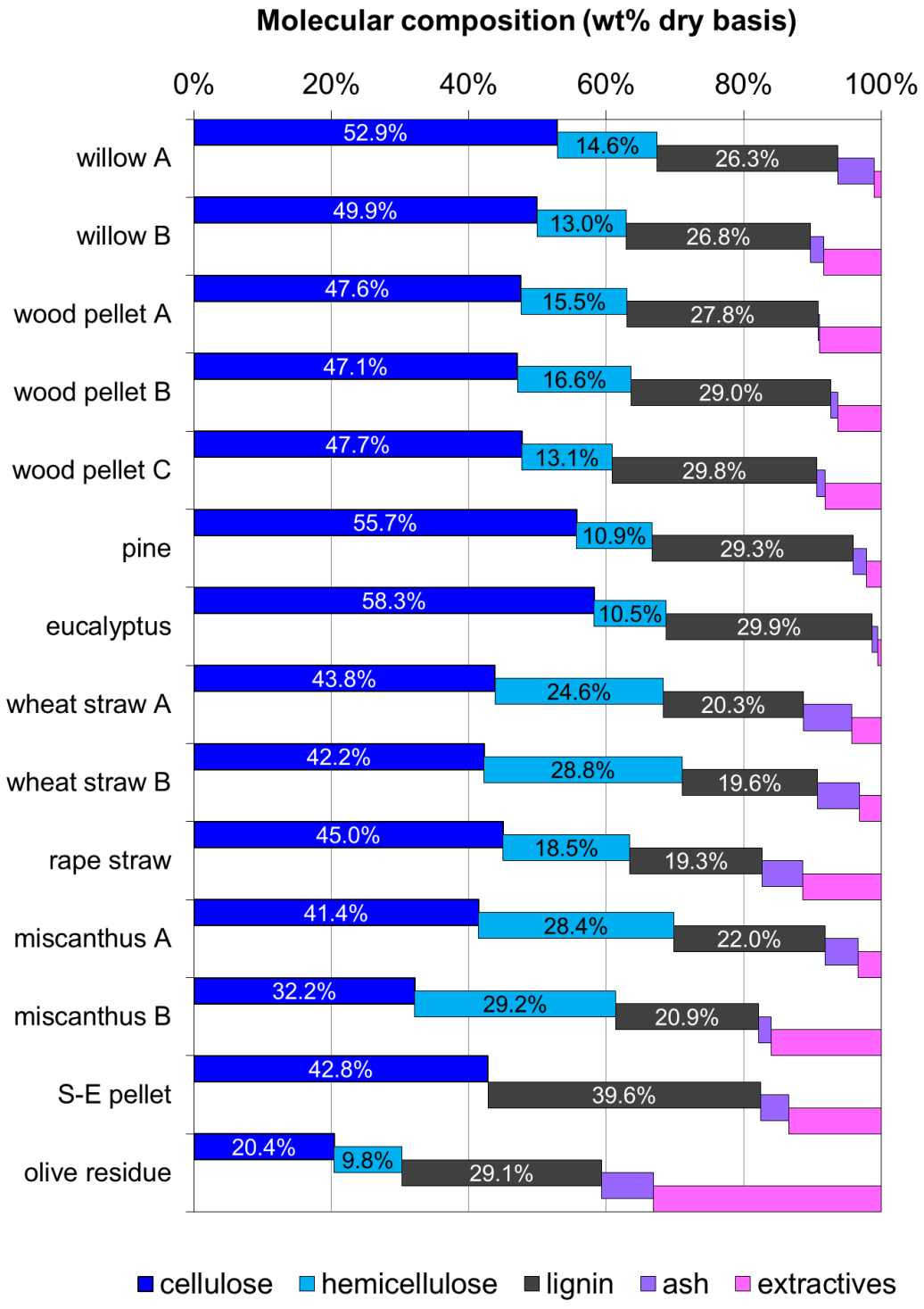

Figure 2-2 - Molecular composition of selected biomass fuel samples

2.3.4 Ultimate analysis

From the analysis of molecular composition, the average mass proportions of cellulose, hemicellulose and lignin in wood are approximately 50:15:30 (%) respectively with the balance (5%) being extractives. From this, the proportion of the principal elements can be estimated from:

$0.5 \times C_6H_{10}O_5 + 0.15 \times C_5H_8O_4 + 0.3 \times C_{31}H_{34}O_{11} + 0.05 \times C_6H_{12}O_6$

This gives an approximate composition by mass of: Carbon 56%; Hydrogen 6%; Oxygen 38%

This will vary depending on proportions of components and quantities of extractives in the in the material. Measured composition by mass of C, H and O for wood reported in literature are generally around: Carbon 50%; Hydrogen 6%; Oxygen 44% (Biermann, 1996).

The results of the analysis are presented in **Table 2-5** on the dry ash free basis. The results are also presented, on dry basis (including ash), graphically in **Figure 2-3** to allow visual comparison between the different fuels.

The analysis shows variation between 43% and 51% carbon (dry basis) in the selected materials with the wood materials having, on average, higher carbon contents than the herbaceous materials. Nitrogen levels range from up to 1.6% (in olive residue) to almost undetectable in some cases (e.g. wood pellet). The error on such low detection levels may be up to 0.5 percentage points which is in the order of 50-100% error margin in most cases. The results obtained indicate lower levels in the wood pellets while the straws have higher levels. The pine wood sample shows the highest level of nitrogen which is unexpected from comparison with the other woods. Out of 49 samples of pine wood and sawdust on the Phyllis2 database, the maximum nitrogen content reported is 0.53% (d.a.f. basis). Sulphur levels were below the detection limit or below the margin of measurement error for all biomass materials.

A useful means of graphically representing the chemical composition of coal developed by Van Krevelen is to plot the H/C ratio to the O/C ratio (van Krevelen, 1950). This can also be useful for comparison of biomass fuels and how they change with processing (such as torrefaction). **Figure 2-4** shows the selected biomass fuels and coals plotted on a Van Krevelen diagram. In this

plot, the order of the materials is generally consistent with their measured calorific value.

Table 2-5 - Principal elemental composition of selected biomass fuels & coals

wt%	C		H		N		S		O	
d.a.f. basis	%	+/-	%	+/-	%	+/-	%	+/-	%	+/-
willow A	49.5	0.56	5.8	0.20	0.5	0.01	0.1	0.09	44.1	0.66
willow B	50.8	1.27	6.0	0.13	0.4	0.03	0.0	0.08	42.7	1.25
wood pellet A	49.2	1.89	6.0	0.05	0.0	0.09	0.1	0.12	44.7	2.05
wood pellet B	50.7	0.23	6.0	0.07	0.1	0.00	0.0	0.00	43.2	0.15
wood pellet C	50.8	0.11	6.1	0.02	0.0	0.00	0.0	0.00	43.1	0.09
pine	47.4	0.70	5.3	0.48	1.3	0.04	0.0	0.04	45.9	1.14
eucalyptus	49.2	0.67	5.6	0.18	0.1	0.05	0.0	0.00	45.1	0.72
wheat straw A	48.6	0.41	6.0	0.08	0.6	0.01	0.1	0.14	44.8	0.64
wheat straw B	48.9	0.25	6.1	0.20	0.6	0.00	0.0	0.00	44.5	0.45
rape straw	48.7	1.97	5.9	0.29	1.1	0.03	0.2	0.07	44.2	2.21
miscanthus A	48.5	1.13	6.0	0.16	0.6	0.01	0.0	0.00	44.9	1.30
miscanthus B	49.2	0.61	6.0	0.07	0.2	0.00	0.0	0.00	44.6	0.68
S-E pellet	52.7	0.65	5.8	0.11	0.2	0.00	0.0	0.00	41.2	0.76
olive residue	52.8	0.19	6.5	0.03	1.6	0.00	0.0	0.07	39.1	0.23
coal A	73.0	3.86	5.2	0.08	2.2	0.21	0.0	1.07	19.6	2.92
coal B	78.2	0.42	5.1	0.19	2.2	0.16	2.1	0.00	12.3	0.34
coal C	76.4	0.66	5.5	0.26	2.8	0.12	0.0	0.00	15.2	0.52

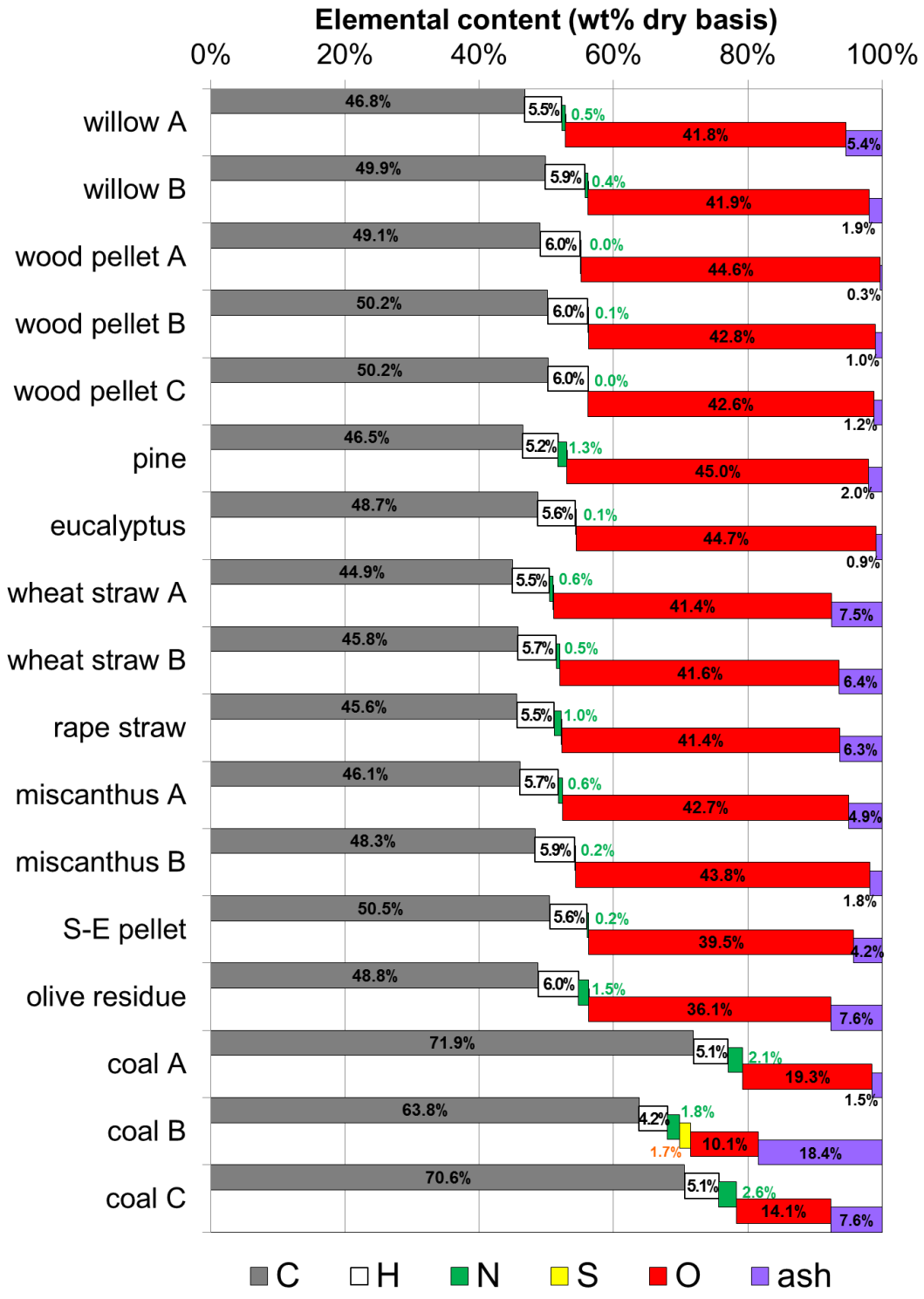

Figure 2-3 - Principal elemental composition of selected biomass fuels & coals

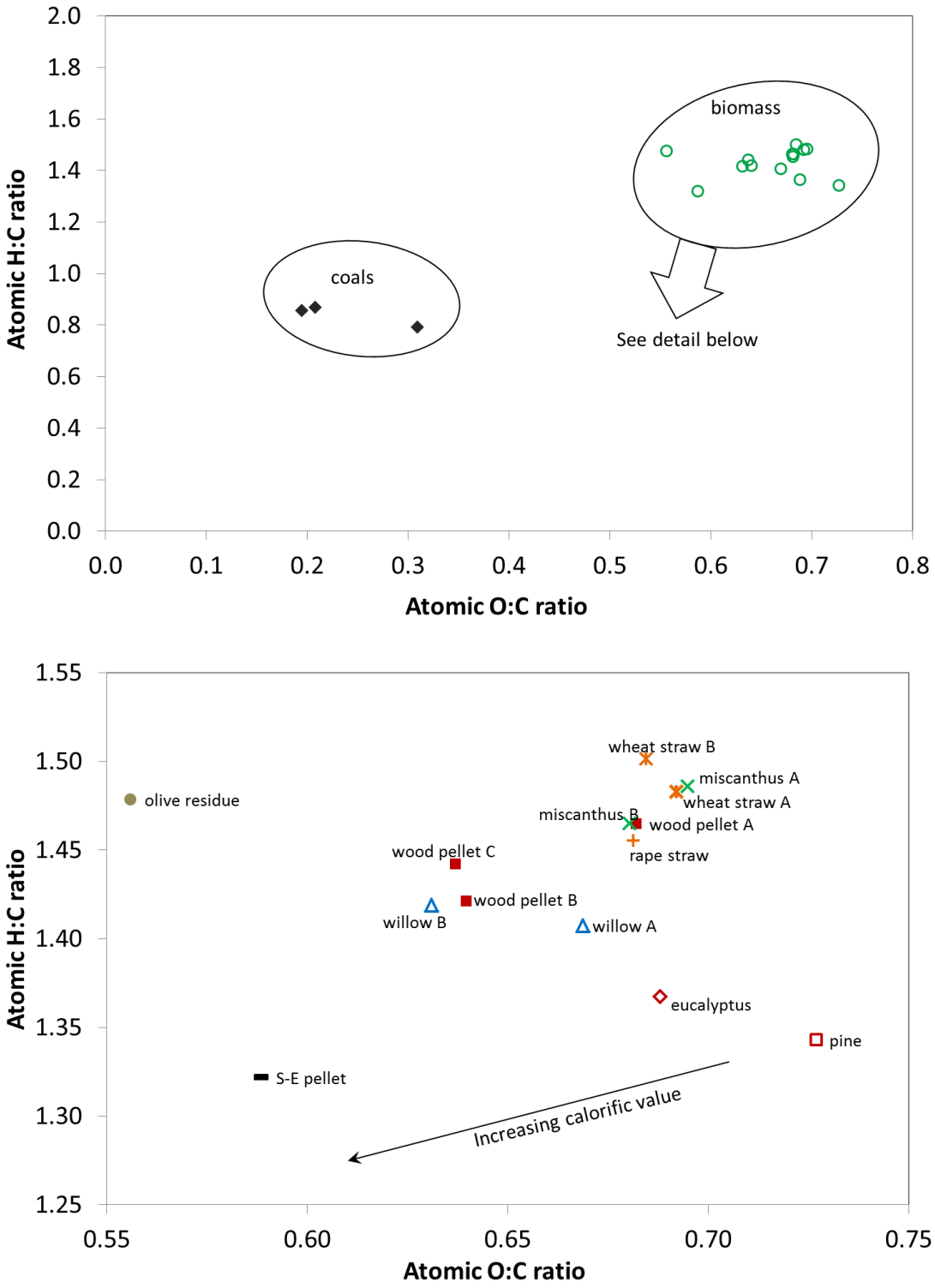

Figure 2-4 – Van Krevelen plot of selected solid biomass materials

2.3.5 Calorific value

The gross calorific values (GCV) of the samples as measured using a bomb calorimeter are presented in **Table 2-6** along with the values calculated from the CHN analysis using the approximation of equation **(2-8)**. The average calorific values for the similar materials taken from the Phyllis2 database (Phyllis2, 2013) have been included to allow comparison with "expected" values. In the absence of data on the black pellets, the value published by the suppliers has been used for comparison. A sample variation error was not evaluated in this case since only one measurement per sample was taken. The estimated error of these measurements is less than 1%, based on the errors of weighing samples.

Table 2-6 - Gross calorific values for selected fuel samples

MJ/kg dry basis	*Measured by calorimeter*	*Derived from CHN data*	*Typical value from Phyllis2*
willow A	18.88	18.49	19.40
willow B	19.76	19.81	19.40
wood pellet A	19.49	19.45	20.00
wood pellet B	20.04	19.93	20.00
wood pellet C	20.32	19.95	20.00
pine	18.59	18.44	20.00
eucalyptus	19.40	19.22	20.00
wheat straw A	18.15	17.80	17.80
wheat straw B	18.08	18.14	17.80
rape straw	18.41	18.12	19.10
miscanthus A	18.82	18.26	19.30
miscanthus B	19.10	19.13	19.30
S-E pellet	19.95	19.94	19.60†
olive residue	20.14	19.53	20.20
coal A	32.70	30.35	30.00
coal B	28.01	25.63	28.00
coal C	32.68	31.51	30.50

†value claimed by supplier

Comparison of calorific values cited in the literature and marketing materials should be treated with care since the basis (dry or dry-ash-free) of the value is not always made clear. The figures presented in **Table 2-6** are the Gross Calorific Value (GCV) on a dry fuel basis ranging from about 18 to 20 MJ/kg. For practical engineering calculations, a dry fuel basis is not necessarily useful since fuel delivered to a burner is rarely dry. However for comparison and analysis purposes it is important to consider the dry basis since variable moisture levels obscure the underlying calorific value of the material.

The accuracy of the approximation derived from CHN data can be assessed by a plot of the calculated values against those measured – as shown in **Figure 2-5**. It can be seen from the figure that there are no severe discrepancies between the measured values and calculated values and the coefficient of determination, $R^2 = 0.92$. The largest discrepancies are only around 3%. Some of this may be accounted for by measurement error and the value calculated from equation **(2-8)** appears to be a reasonable estimate.

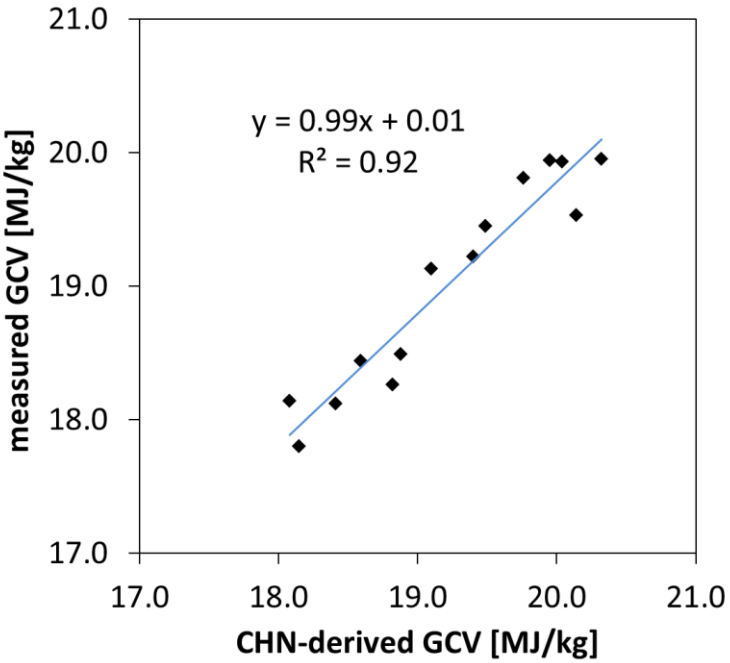

Figure 2-5 - Gross calorific values for selected fuel samples

2.3.6 Inorganic content

Aside from the nitrogen, sulphur and chlorine, much of the inorganic content of fuels ends up as a solid-phase residue after combustion. This residue (ash) may be retained in the furnace (bottom ash) or collected from the flue gas (fly ash). Much of the inorganic content is metals and silicon which form metal oxides or mineral compounds. However, sulphur and chlorine can also be present in significant quantity in many fuels. Sulphur in combustion generally forms sulphur dioxide $SO_{2(g)}$ which passes into the flue gas (and is subject to emissions controls). Sulphur can also form other products such as solid-phase sulphates which may deposit as ash or form fine particulate matter which can also pass into the flue gas (Li et al., 2013). Chlorine can also pass out of the furnace in the gas phase or it can combine with alkali metals and deposit as solid phase chloride salts stimulating corrosion on furnace surfaces (Schofield, 2012). **Table 2-7** presents the results of a wet chemical analysis determination of chlorine.

Table 2-7 - Chlorine content of selected biomass fuels

wt% dry basis	*WCA*	*+/-*
willow A	0.07	0.3
willow B	0.11	0.3
wood pellet C	0.04	0.3
wood pellet A	0.01	0.3
wood pellet B	0.00	0.3
pine	0.13	0.3
eucalyptus	0.00	0.3
wheat straw A	0.26	0.3
wheat straw B	0.61	0.3
rape straw	0.32	0.3
miscanthus A	0.46	0.3
miscanthus B	0.67	0.3
S-E pellet	0.05	0.3
olive residue	0.28	0.3

Figure 2-6 shows data from the analyses for the major inorganic content presented to indicate the relative content (by mols) of the ten principal metals (including silicon). For comparison, data on raw biomasses and coal taken from average values in the Phyllis2 database (Phyllis2, 2013) have been included. The values obtained were taken as the mean values reported for all items in the database classified as “untreated wood”, “straw(stalk/cob/ear)” and “coal” respectively. While these values are based on averages from a database in which there is wide variation, they do indicate how the selected samples compare with the similar fuels. It is important to note that the data are presented in the figure to show the relative proportions of each element, not absolute values. The total content of each element will be related to the total ash content as presented in **Table 2-3.**

Some notable similarities and differences are observable from the figure:

- Biomass fuels (both wood and straw) have higher proportions of potassium, calcium and phosphorous than coal on average.
- Coals have a higher proportion of aluminium and iron than the biomass fuels on average.
- Wood pellets (which have relatively low overall ash content) have more magnesium, titanium and manganese than the other fuels.
- Olive residue is anomalous compared to the other biomass fuels with considerably higher content of potassium than any other inorganic element.

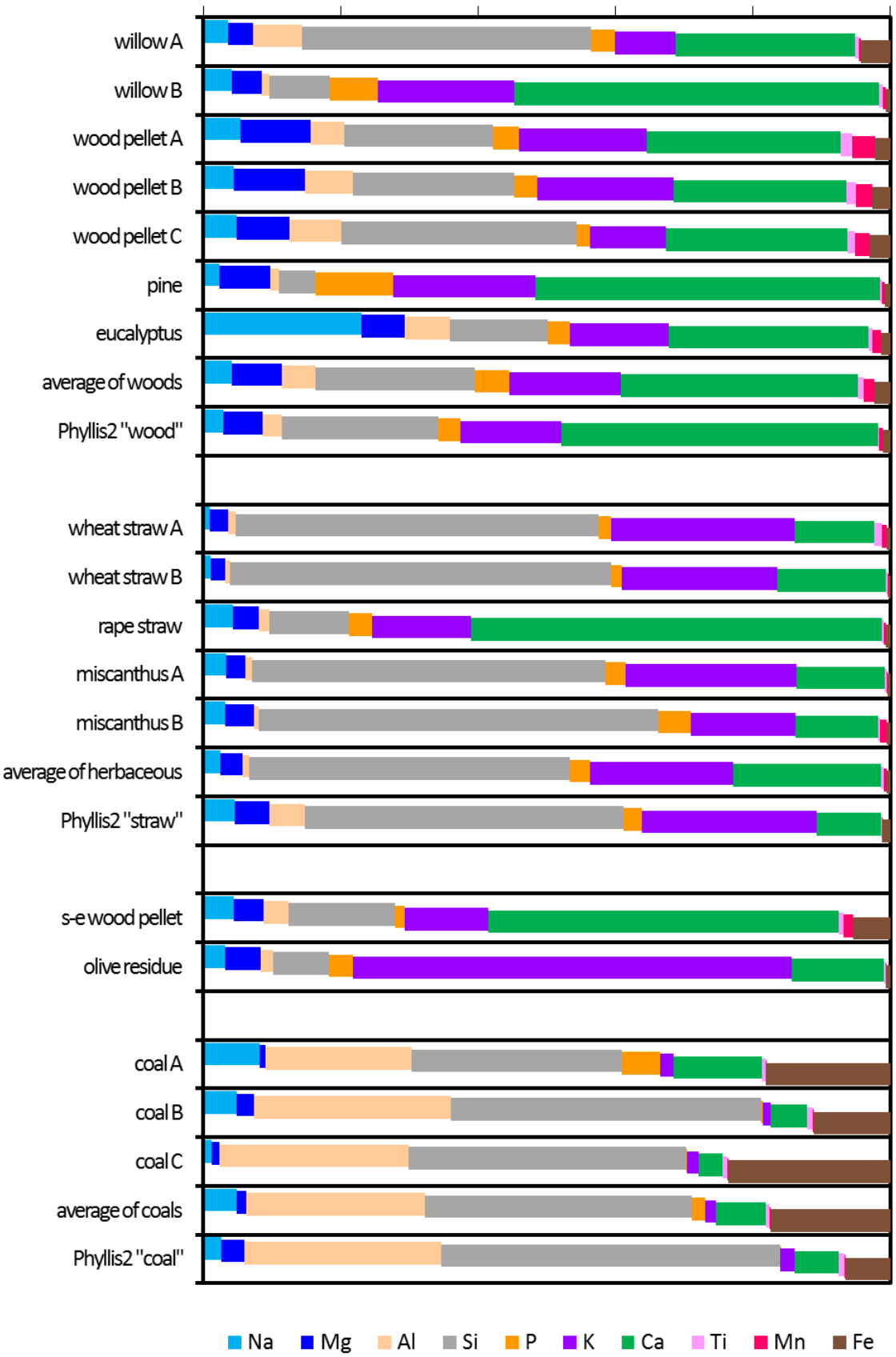

Figure 2-6 – Relative proportions (molar) of major inorganic elements of selected fuels

2.3.7 Ash composition

In furnaces, the fusibility and melting temperatures of the ash are highly significant since the ash may form deposits on the furnace walls and heat transfer surfaces. For steam-raising boilers, this will clearly impede the performance of the system and reduce efficiency. The formation of these deposits in the radiative heat–transfer part of the furnace is known as slagging. The formation of other solid ash deposits on the convective heat transfer surfaces of a boiler (e.g. super-heater tubes) is known as fouling. In the furnace, the inorganic matter in the fuel may go through a number of phase transformations as some of the materials are volatilised and different species are formed at the varying temperatures in different parts of the furnace. Certain minerals may be transported in the vapour, liquid or solid phase and may then be transformed upon contact with other ash particles or the furnace structure.

A detailed survey of the different mineral phases produced in biomass combustion is presented by Vassilev et. al in reference (Vassilev et al., 2013). These mineral phases include:

Silicates – ranging from simple quartz/silica (Si02) to silicates of iron, aluminium, calcium, sodium and potassium. Some of these silicates have relatively low melting points, in particular some eutectic mixtures of potassium silicates (600°C - 980°C) and sodium silicates (≥874°C) as well as potassium aluminosilicate (~695°C) and potassium-magnesium silicate (~685°C).

Oxides and Hydroxides – All the oxides of the metals present may be formed. Most of these oxides have melting temperatures above 1500°C. The hydroxides of sodium and potassium have relatively low melting temperatures (318°C and 380°C respectively).

Phosphates – Biomass can have significant phosphorus content. The minerals listed in ref. (Vassilev et al., 2013) are mainly calcium based with melting temperatures from 1270-2000°C. Some phosphates of potassium can have melting points ranging from 590-800°C.

Sulphates, sulphides, sulphites – A number of sulphur compounds have relatively low melting temperatures. In particular, copper sulphate (200°C) and potassium-sodium sulphate-chloride mixture (515°C).

Carbonates – Potassium calcium carbonate, potassium carbonate, and sodium carbonate (with melting points of 815, 788-904 and 850°C respectively).

Chlorides, chlorates and chlorites – Some biomass fuels have relatively high chlorine content which leads to formation of chlorides including potassium, sodium and calcium all of which have melting temperatures in the region of 800°C. However, eutectic mixtures of KCl and NaCl may have melting points lower than 400°C.

Nitrates – Sodium and potassium nitrates with melting points at 370 and ~330°C respectively.

The mixture of all these minerals together makes a very complex system with many variables contributing to its behaviour. However, some correlations with certain mixtures are apparent regarding ash composition and its tendency to form fouling or slagging deposits in the furnace. An indication of ash melting behaviour is possible by measuring physical changes with respect to temperature. While there are standard tests for determining ash melting characteristic temperatures (Standard, 2006a), it is also possible it use ash composition data to provide an indication of ash behaviour.

The tendency of ash to form a slag has been empirically correlated to the relative proportions of the basic oxide content to the acidic oxide content. The ratio of the relative mass fractions of these oxides in the ash analysis (dry basis) can be used as a rough indication of the slagging propensity with a 'slagging index' (Miller, 2005) given by:

$$slagging\ index = \frac{(Fe_2O_3 + CaO + MgO + K_2O + Na_2O)_d}{(SiO_2 + Al_2O_3 + TiO_2)_d} \quad \textbf{(2-9)}$$

A ratio of basic/acidic <0.5 is a low propensity and >1 is a high propensity.

The tendency to cause fouling is correlated to the content of alkali metals which are released by volatilisation and subsequently condensed on the cooler parts of the furnace. Potassium sulphate, which is common in fly ash, has a melting temperature of 1068°C. With the formation of potassium carbonate and chloride, the fly ash melting temperature can be reduced to 643°C. Further to this, small amounts of sodium can reduce the melting temperature to 609°C.

Fouling propensity has been empirically correlated to the “alkali index” which is given (Miles et al., 1996) by:

$$alkali\ index = \frac{mass\ of\ K_2O\ + Na_2O\ [kg/kg]}{Gross\ Calorific\ Value\ \ [GJ/kg]} \qquad \textbf{(2-10)}$$

Ash alkali index values more than 0.17 indicate a propensity to cause fouling whereas values higher than 0.34 indicate that fouling is almost certain.

These empirical formulae have been derived from coal combustion experience. Directly using them for biomass ash may not be as reliable. Nevertheless, applying the data obtained for the fuel samples analysed for inorganic content can illustrate variability in biomass ash properties. In this analysis, it is assumed that the ash consists of the simple metal oxides of the inorganic elements. The relative content of the 8 main oxides in the ash for the 14 biomass and 3 coals is presented in **Table 2-8**.

From the data in **Table 2-8**, the slagging propensity can be evaluated for each fuel. Along with the measurements of calorific value and ash content, the alkali index can also be evaluated. The results of this analysis are presented in **Table 2-9** and **Figure 2-7**.

Ash melting temperature can also be affected by small amounts of certain metals (so-called ‘minor elements’). Presence of lead (Pb) and zinc (Zn) reduces the melting point further to 196°C. Such low melting points can result in rapid deposition and corrosion (BIOASH, 2007). The lead and zinc content in each of the biomass fuel materials was determined by inductively-coupled plasma mass spectrometry (ICP-MS) of diluted, acid-digested solutions of each sample. The results of this analysis are presented in **Table 2-10**. The measurement error is estimated at +/- 10% based on errors introduced in the considerable dilution of the analytes. The willow samples, pine and steam-exploded wood pellet have zinc contents more than 100 parts per million (ppm) which would suggest an increased propensity of fouling – in **Figure 2-7** this would likely move them into the “high fouling propensity” category.

Table 2-8 - Relative content of 8 main oxides in ash for biomass and coal samples

wt% dry basis	Na_2O	MgO	Al_2O3	SiO_2	K_2O	CaO	TiO_2	Fe_2O_3
willow A	2.9	3.6	7.8	53.3	6.3	21.9	0.6	3.7
willow B	4.1	5.3	1.6	14.1	17.7	55.7	0.7	0.7
wood pellet A	5.0	11.5	6.1	31.2	15.2	26.9	2.0	2.2
wood pellet B	4.0	11.4	8.6	32.8	15.8	23.5	1.4	2.6
wood pellet C	4.0	7.9	8.6	44.7	8.1	22.8	1.2	2.7
pine	2.5	9.8	1.9	8.8	19.7	55.8	0.4	1.0
eucalyptus	21.5	7.1	8.5	20.7	11.9	28.2	0.6	1.4
wheat straw A	0.8	2.6	1.2	65.6	18.7	9.6	1.1	0.4
wheat straw B	0.9	2.0	0.7	67.6	15.6	12.8	0.2	0.2
rape straw	4.0	4.5	2.0	17.2	12.1	59.2	0.3	0.7
miscanthus A	2.6	2.8	1.1	64.5	17.7	10.6	0.3	0.3
miscanthus B	2.5	4.0	0.8	71.6	10.6	9.8	0.3	0.5
s-e wood pellet	4.1	4.9	4.5	22.2	9.8	48.5	0.8	5.3
olive residue	3.3	6.6	2.6	13.2	58.8	14.4	0.4	0.7
coal A	6.8	0.9	24.0	39.7	1.4	11.1	0.5	15.8
coal B	3.6	2.2	28.5	51.7	0.7	4.0	0.7	8.6
coal C	0.9	1.0	28.0	47.1	1.0	2.7	0.7	18.5

Table 2-9 - Slagging and fouling propensity of fuel samples

	slagging index	*slagging propensity*	*GCV* [MJ/kg]	K_2O+Na_2O [g/kg of fuel]	*alkali index*	*fouling propensity*
willow A	0.62	MED.	18.88	4.96	0.26	MED.
willow B	5.11	HIGH	19.76	4.13	0.21	MED.
wood pellet A	1.55	HIGH	20.04	2.44	0.12	LOW
wood pellet B	1.33	HIGH	19.49	0.56	0.03	LOW
wood pellet C	0.84	MED.	20.32	1.20	0.06	LOW
pine	7.98	HIGH	18.59	4.43	0.24	MED.
eucalyptus	2.35	HIGH	19.4	2.94	0.15	LOW
wheat straw A	0.47	LOW	18.15	14.69	0.81	HIGH
wheat straw B	0.46	LOW	18.08	10.49	0.58	HIGH
rape straw	4.13	HIGH	18.41	10.14	0.55	HIGH
miscanthus A	0.52	MED.	18.82	10.03	0.53	HIGH
miscanthus B	0.38	LOW	19.1	2.36	0.12	LOW
s-e wood pellet	2.64	HIGH	19.95	5.87	0.29	MED.
olive residue	5.19	HIGH	20.14	47.5	2.36	HIGH
coal A	0.56	MED.	32.7	1.22	0.04	LOW
coal B	0.24	LOW	28.01	7.94	0.28	MED.
coal C	0.32	LOW	32.68	1.48	0.05	LOW

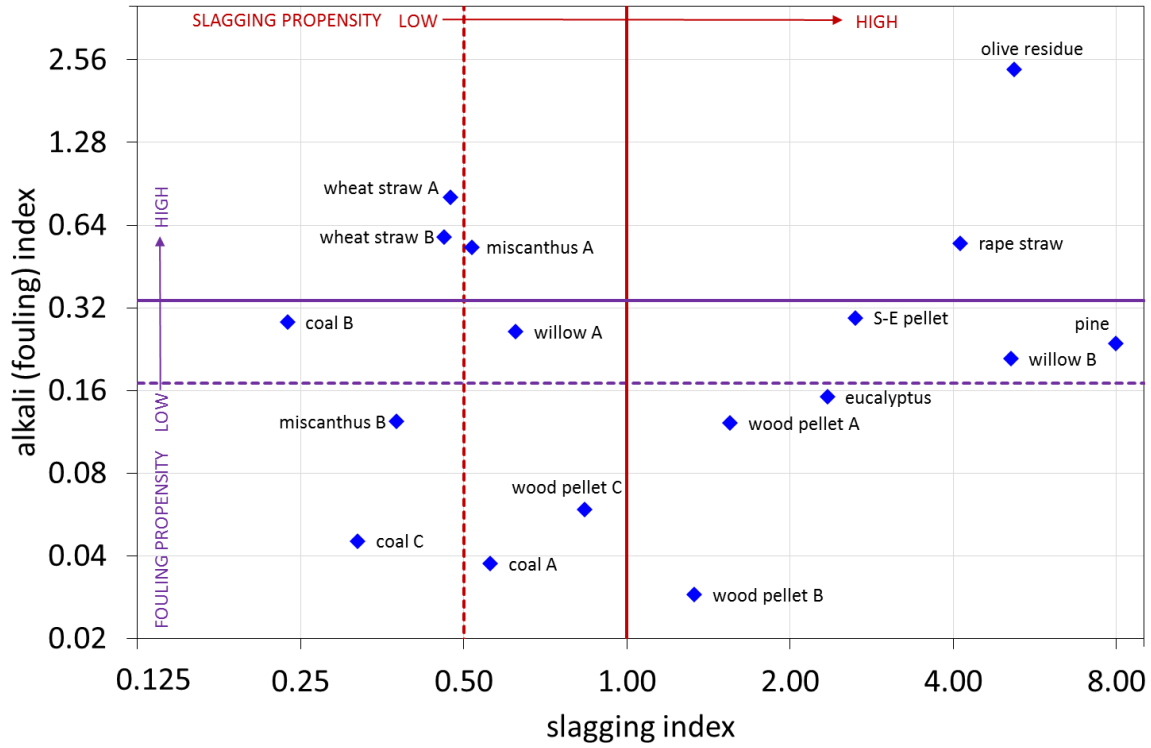

Figure 2-7 - Plot of slagging and fouling propensity for various fuel samples (logarithmic scale)

Table 2-10 - Zinc and lead content in biomass fuel samples

ppm dry basis	*Zn*	*+/-*	*Pb*	*+/-*
willow A	106.8	0.3	51.6	0.3
willow B	152.4	0.3	2.4	0.3
wood pellet A	43.5	0.3	2.8	0.3
wood pellet B	11.4	0.3	3.1	0.3
wood pellet C	13.3	0.3	4.8	0.3
pine	168.0	0.3	6.7	0.3
eucalyptus	7.2	0.3	6.5	0.3
wheat straw A	3.5	0.3	27.4	0.3
wheat straw B	-	0.3	3.9	0.3
rape straw	6.1	0.3	3.9	0.3
miscanthus A	21.8	0.3	2.2	0.3
miscanthus B	32.4	0.3	1.1	0.3
s-e wood pellet	214.6	0.3	1.8	0.3
olive residue	39.2	0.3	2.1	0.3

2.3.8 Thermogravimetric analysis of drying

As a solid fuel particle is introduced into the high temperature environment of a furnace, the first process that starts as it heats up is the loss of moisture: drying. Moisture inside a particle of solid biomass may be either: free water contained in the pores of the structure; adsorbed water bound to surfaces in the particle structure; chemically-bound water in hydrated molecules within the fuel. As the particle is heated up, the free water is evaporated, the adsorbed water is desorbed and evaporated and, finally, the chemically bound water is separated. The drying rate is dependent on the heat transfer within the particle which itself is partly dependent on the moisture content. The diffusion of the water vapour through the particle also affects the evaporation rate at the surface. Drying rate therefore increases fairly rapidly to begin with as the external free water is removed and then levels off as the internal water is driven off. Thereafter the rate of moisture loss decreases as less and less adsorbed and chemically bound water is able to be removed.

In evaluating models for drying wood at low temperatures (<100°C), Hosseinabdi et al. (Hosseinabadi et al., 2012) have presented experimental data showing that, for moisture contents below around 30%, the drying rate is approximately proportional to the moisture content and to the drying temperature. This is the basis for a simplified model of the drying rate for small particles proposed by Peters (Peters, 2003) and adopted in single biomass particle drying by Yang et al.(Yang et al., 2008). The model is of the form:

$$\frac{dm_w}{dt} = \zeta\left(T_p - T_{eq}\right)m_w \qquad \text{for } T_p \geq T_{eq}$$

$$\frac{dm_w}{dt} = 0 \qquad \text{for } T_p < T_{eq} \qquad \textbf{(2-11)}$$

Where:

m_w is the mass of moisture in the particle

T_p is the temperature of the particle at time t

T_{eq} is the temperature with initial moisture at equilibrium (~310K)

ζ is a coefficient derived from the density, specific heat capacity and enthalpy of vaporisation of the water (Peters, 2003)

The total moisture loss and rate of evaporation of the biomass fuel samples were measured using a thermo-gravimetric analyser (TA Instruments TGA

Q5000). Samples of between 3 and 5mg with a particle size <90μm were analysed with a linear heating profile from 25°C to 105°C at 20°C per minute and a nitrogen gas flow rate of 20ml/min. The mass loss and rate of mass loss (i.e. evaporation rate) of an example analysis are shown in **Figure 2-8**.

Equation **(2-11)** was used to replicate the measured data in **Figure 2-8** with a value for $\zeta = 0.00093$ derived empirically. The model provided a good approximation for all samples with moisture content ranging from 2.7% to 6% (refer also **Table 2-3**).

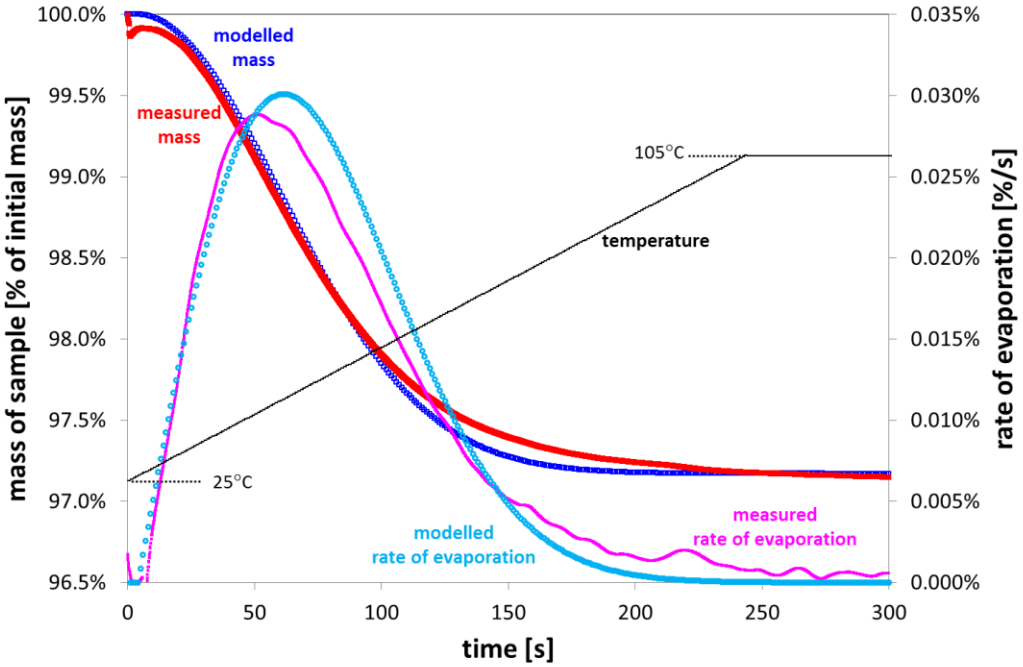

Figure 2-8 - Mass loss and evaporation rate from biomass sample (particle size<90μm) during drying in nitrogen

For larger particles and higher heating rates the internal temperatures in single particles of biomass cannot be assumed to be uniform. A study by Lu and Baxter (Lu and Baxter, 2011) included measurement of internal temperature gradients during drying of particles >10mm diameter. The study reports the temperature at the centre of the particle initially rising to near to the boiling point as the moisture evaporates out. In the meantime, depending on the size of the particle, the surface temperature may rise high enough such that the exterior of the particle starts to devolatilise while the interior is still drying out. At high heating rates and with small particle sizes (e.g. in a pulverised-fuel furnace)

there is very little temporal separation between the drying and the devolatilisation processes (Thunman et al., 2004).

2.3.9 Thermogravimetric analysis of devolatilisation

As the dried particles of fuel are heated further (105 to 600°C) , the organic molecular structures (cellulose, hemicellulose, lignin and other substances) start to undergo pyrolysis and the devolatilisation process begins. The decomposition of organic materials into gaseous products is an endothermic process. While the temperature inside the particle is increased by heat conduction from the surface, energy absorbed in decomposition reactions tend to counteract this. The change from condensed phase to gas phase products also imparts a cooling effect as the enthalpies of vaporisation are also endothermic. In a combustion environment (i.e. in a furnace), the volatile products escape to the surrounding atmosphere which contains some oxygen. With sufficient heat and oxygen the volatile gases combust forming a flame around the particle. The oxygen in the vicinity will vary depending on the mixing of the primary and secondary air and the consumption of oxygen locally by the ongoing combustion.

The pyrolysis process is a complex mixture of many different decomposition reactions occurring in parallel. Different organic molecules break down at differing rates at different temperatures. A detailed examination of the pyrolysis process for lignocellulosic biomass materials can be undertaken by considering the principal organic components: cellulose; hemicellulose; and lignin. A number of experimental studies using TGA have been carried out regarding the pyrolysis behaviour of the individual substances [(Orfao et al., 1999, Raveendran et al., 1996, Yang et al., 2007)]. These do show clearly different pyrolysis behaviours of the different components which help to understand the behaviour of biomass materials with varying proportions of these constituents.

Hemicellulose is the least stable component with decomposition starting at temperatures around 200°C with almost all volatile weight loss taking place below 350°C and with peak rate up to 1.0wt%/°C. The residual char after devolatilisation of hemicellulose accounts for about 30wt%.

Cellulose decomposition starts above 250°C [523K] and is more rapid than that of hemicellulose. Almost all the loss in mass for cellulose occurs below 380°C with a maximum rate around twice that for hemicellulose. The devolatilisation of cellulose results in only around 15wt% of char - much less residual char than hemicellulose.

Lignin is the least reactive component. It decomposes at a lesser rate than either hemicellulose or cellulose and although decomposition can start at below 200°C, devolatilisation continues up to 600°C. Lignin also has the highest residual char which accounts for up to 50wt%.

The selected biomass fuels, being a mixture of these three principal organic components show a thermal decomposition profile which is a superposition of the three. The mass-loss with respect to temperature for each fuel sample undergoing pyrolysis was measured at a heating rate of 10°C/min from 50°C to 900°C. The derivative of (total sample) mass loss with respect to temperature for the willow-A sample is shown in **Figure 2-9**. To illustrate the behaviour of the cellulose, hemi-cellulose and lignin content as described above, the range of the devolatilisation of each is superimposed on the plot.

To model the rate of the reactions during pyrolysis, it is possible to measure the rate of mass loss at different temperatures and heating rates and derive reaction rate equations. This can be done by considering multiple reactions and deriving a reaction rate equation for each one (Scott et al., 2006). The model can be with reduced number of parallel reactions such as: solid→gas; solid→tar and solid→char (Haseli et al., 2011b). The reaction rates of the cellulose, hemicellulose and lignin can also be used to model biomass pyrolysis (Gronli et al., 2002). These analyses and models are important for processes which require detailed knowledge of pyrolysis products e.g. in liquid or gas biofuel production.

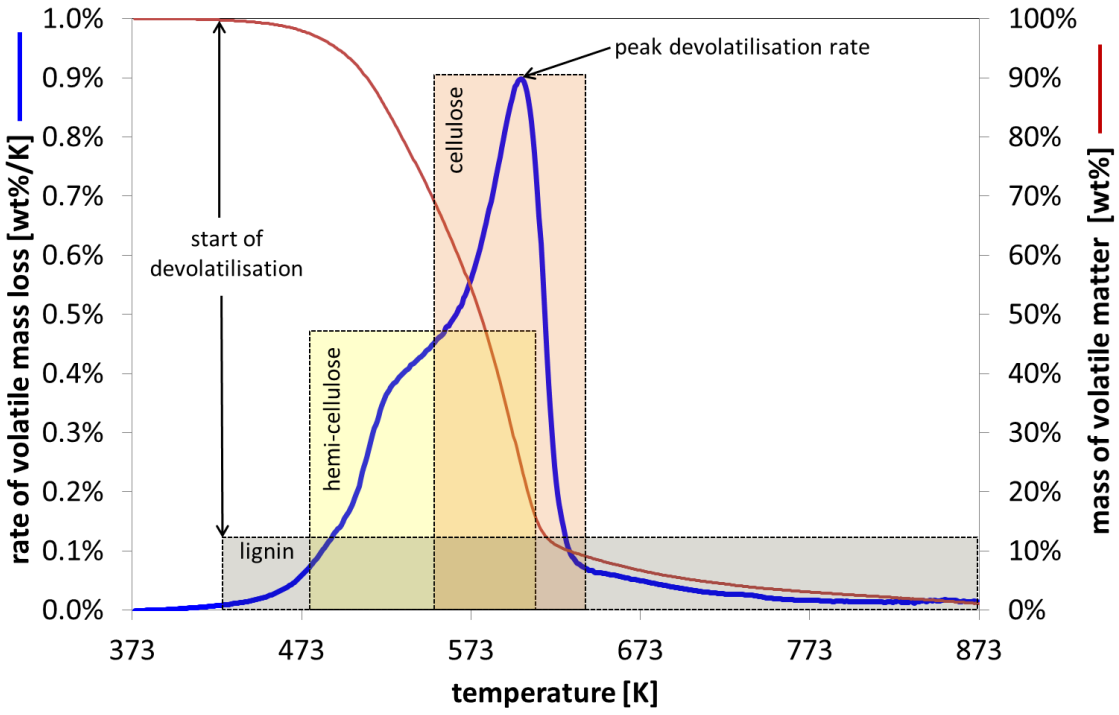

Figure 2-9 – An example of the rate of volatile mass-loss with respect to temperature for a sample of willow undergoing pyrolysis (<90μm particles in nitrogen)

For higher heating rates such as applicable to pulverised fuel furnaces, the apparent devolatilisation reaction rate will be dominated by the initial reaction rate (i.e. That around 180-230°C [450-500K]). The faster devolatilisation reactions at higher temperatures will effectively occur contemporaneously if the temperature of the particle exceeds ~500°C [773K] before the initial reaction has completed. A parallel-reaction model is not necessary in this case and a useful approximation can be obtained by assuming a first-order, single step reaction (Saddawi et al., 2010). The chemical kinetic reaction rate is described by:

$$\frac{dm_{vol}}{dt} = -k_{vol}.m_{vol} \qquad \textbf{(2-12)}$$

Where:

m_{vol} is the mass of volatile material at time t

k_{vol} is the devolatilisation reaction rate coefficient [s^{-1}]

The reaction rate coefficient can be described by the Arrhenius equation as a function of temperature:

$$k_{vol} = A_{vol}\ exp\left(\frac{-E_{vol}}{RT}\right) \quad \textbf{(2-13)}$$

Where:
A_{vol} is the pre-exponential constant or frequency factor [s^{-1}]
E_{vol} is the activation energy [J mol^{-1}]
R is the gas constant (=8.314 J $mol^{-1}K^{-1}$)
T is the temperature (K)

The rate of mass loss during devolatilisation can be measured using thermo-gravimetric analysis. The resulting data can be used to calculate the reaction rate parameters. Rearranging equation **(2-13)** by taking the logarithm of each side gives:

$$\ln k_{vol} = \ln A_{vol} - \frac{E_{vol}}{RT} \quad \textbf{(2-14)}$$

Using the thermo-gravimetric data, k_{vol} can be calculated from equation **(2-14)** for each measured point of temperature. This allows a plot of $\ln k_{vol}$ versus $^1/_T$ to be made. A least-squares linear regression line of the form $y = ax + b$ can be fitted to the plot. The coefficients of the linear equation give the activation energy and pre-exponential constant:

$$E_{vol} = -8.314.a \quad \textbf{(2-15)}$$

$$A_{vol} = e^b \quad \textbf{(2-16)}$$

The data for the selected biomass fuel samples are plotted in this manner in **Figure 2-10**, while those for the selected coal samples are plotted in **Figure 2-11** for comparison. The parameters characterising the devolatilisation kinetics are presented in **Table 2-11**.

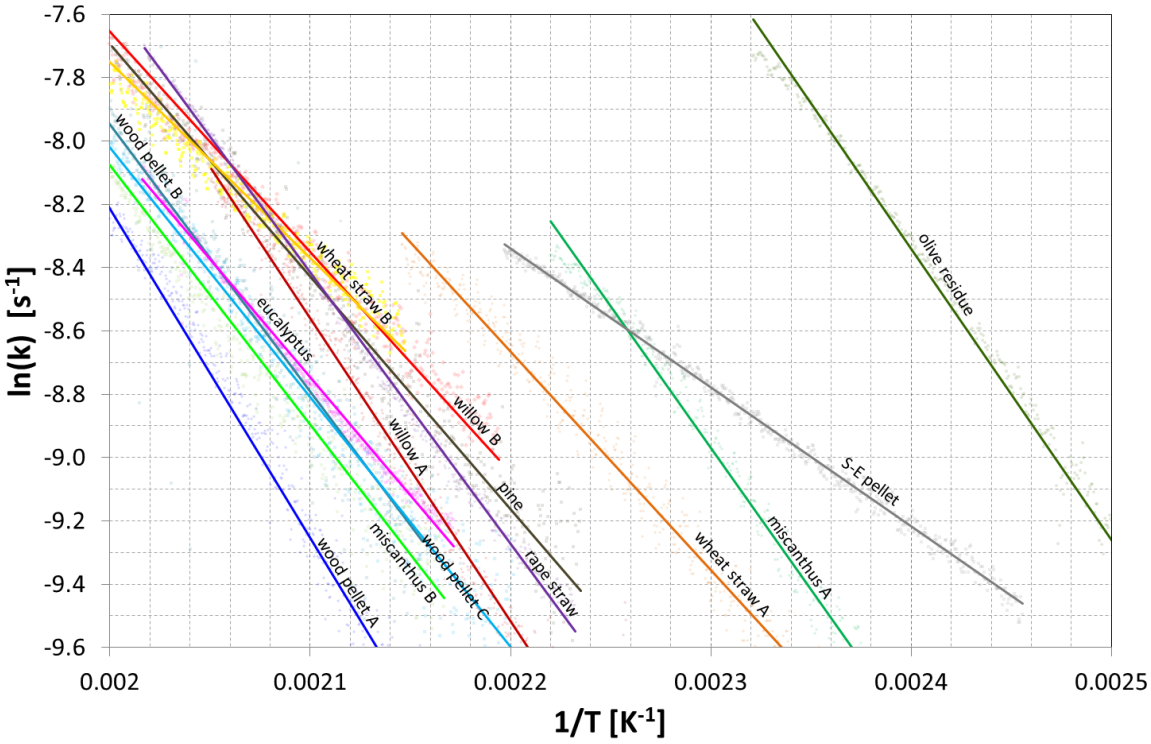

Figure 2-10 - Devolatilisation reaction rate coefficient, k (logarithmic scale) versus reciprocal of temperature (1/T) for biomass fuel samples

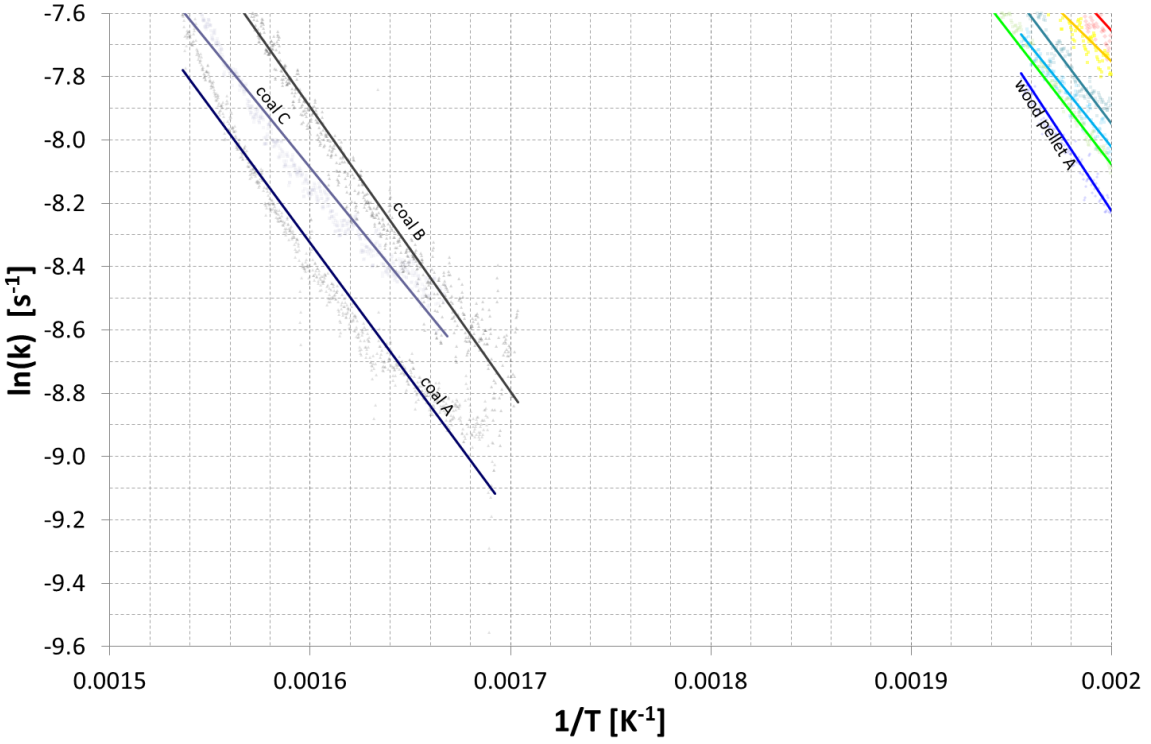

Figure 2-11 - Devolatilisation reaction rate coefficient, k (logarithmic scale) versus reciprocal of temperature (1/T) for coal samples

Table 2-11 - Devolatilisation reactivity for selected fuel samples

Fuel	*reaction rate temperatures* K		*Activation Energy E_{vol}* *kJ mol^{-1}*	*Pre-exponential ln(A_{vol})* s^{-1}	*range of conversion for evaluation* %m_{vol}		*Coefficient of determination* R^2
	start	*peak*			*from*	*to*	
willow A	450	595	80	11.5	1	6	0.970
willow B	450	598	58	6.3	1	8	0.992
wood pellet A	460	606	86	12.4	1	6	0.980
wood pellet B	450	606	71	9	1	8	0.930
wood pellet C	450	605	64	7.3	1	8	0.979
pine	450	597	61	7	1	8	0.986
eucalyptus	450	601	62	7	1	8	0.981
wheat straw A	420	554	59	7	1	6	0.980
wheat straw B	450	566	55	5	1	8	0.981
rape straw	450	591	70	9.3	1	6	0.994
miscanthus A	420	619	76	12	1	8	0.983
miscanthus B	450	599	68	8.3	1	8	0.981
S-E pellet	400	597	37	1.6	1	6	0.994
olive residue	380	547	76	12.9	1	6	0.990
coal A	590	737	71	5.4	5	15	0.730
coal B	580	752	75	6.5	5	13	0.965
coal C	590	697	65	4.4	5	15	0.957

2.3.10 Thermogravimetric analysis of char oxidation

The final stage of combustion is the oxidation of the fixed carbon in the fuel. The removal of volatile material from a fuel particle, in the absence of oxygen (e.g.; in a nitrogen atmosphere) produces a “char” particle which is made of highly porous activated carbon along with the retained inorganic content. In an atmosphere containing oxygen such as inside a furnace, the char is oxidised to CO and CO_2. Although this oxidation reaction proceeds at higher temperatures than the devolatilisation, particles in a furnace can reach char combustion temperatures well before devolatilisation is complete. Consequently, there is not a clear distinction between the end of devolatilisation and the start of char combustion.

The char burn-out requires that oxygen diffuses into the particle where it is adsorbed and reacts with the carbon. The products (CO and CO_2) are then desorbed and diffused out of the particle. The CO may then further burn to CO_2 by a gas phase reaction(Van Loo and Koppejan, 2008).

Some of the principal reactions involved are:

$$C(s) + O_2(g) \Rightarrow CO_2(g) \qquad \textbf{(2-17a)}$$

$$2C(s) + O_2(g) \Rightarrow 2CO(g) \qquad \textbf{(2-17b)}$$

$$C(s) + CO_2(g) \Rightarrow 2CO(g) \qquad \textbf{(2-17c)}$$

$$2CO(g) + O_2(g) \Rightarrow 2CO_2(g) \qquad \textbf{(2-17d)}$$

In modelling the heterogeneous reactions between the solid carbon and the gas phase reactants **(2-17a-c)**, the chemical kinetics, mass transfer of reactants and products, heat generation in the reaction and heat transfer in the particle should all be accounted for (Gremyachkin, 2006). These aspects of the process are dependent on several variables: the reactivity, the particle size; the porosity of the particle structure, internal surface area and the internal heat transfer. Many of these variables change as char combustion proceeds, and the interactions between all of them can be very complicated. Nevertheless, it is possible to model the apparent behaviour using a reduced the number of variables. In the case of char oxidation, a generic gas-solid reaction model (Khawam and Flanagan, 2006) can be expressed as:

$$\frac{dm_{char}}{dt} = -k_{char} \cdot f(\chi) \qquad \textbf{(2-18)}$$

Where:

m_{char} is the mass of char material at time t (excluding ash fraction)

k_{char} is the char reaction rate coefficient [s^{-1}]

χ is the char conversion fraction where $\chi = \frac{m_{char,0} - m_{char}}{m_{char,0}}$

The function $f(\chi)$ in the model reflects how the (isothermal) reaction rate either accelerates, decelerates or remains constant as the char conversion proceeds. In the case whereby the reaction rate is directly proportional to the char conversion the function $f(\chi)$ is:

$$f(\chi) = (1 - \chi) = \frac{m_{char}}{m_{char,0}} \qquad \textbf{(2-19)}$$

Changes in char structures can increase or reduce porosity, internal surface area as the particle burns. For example, the effective surface area will change as the particle shrinks either with a constant density (shrinking core) or a constant volume (decreasing density) or a combination of both. To account for this, equation **(2-19)** can be modified to include an apparent reaction order, m, such that the reaction rate model becomes:

$$f(\chi) = (1-\chi)^m \qquad \textbf{(2-20)}$$

Other gas-solid reaction models include those based on differing physical processes such as 'power law' and 'Avrami-Erofeyev' nucleation models, and 1-D, 2-D or 3-D diffusion models (Khawam and Flanagan, 2006). With specific reference to biomass, models based on the development of the pore structures in wood char have been evaluated in a study by Janse et al. which concludes that the form given in equation **(2-20)** provides an accurate description for chars produced from rapid heating (Janse et al., 1998). In a study by Di Blasi, variations on this form of reaction model were compared for lignocellulosic chars (Di Blasi, 2009) with values of m in the models ranging from 0.4 to 1.8 and m equal to unity or close to unity for many of them. The simple form of first order model given by equation **(2-19)** can be a good choice as a first approximation and has been adopted by others evaluating combustion reaction kinetics of biomass chars – for example (Fisher et al., 2012). For the purposes of a basic comparison of the selected fuels in this study, this first-order (m=1) single step model is used.

The reaction rate of the char oxidation, as a function of temperature, is modelled on Arrhenius reaction kinetics. The char reactivity is characterised by the pre-exponential factor and activation energy and these can be derived in a similar manner as described for the analysis for devolatilisation kinetics with:

$$k_{char} = A_{char}\ exp\left(\frac{-E_{char}}{RT}\right) \qquad \textbf{(2-21)}$$

Where:

k_{char} is the char oxidation reaction rate coefficient[s^{-1}]

A_{char} is the pre-exponential constant or frequency factor [s^{-1}]

E_{char} is the activation energy [J mol^{-1}]

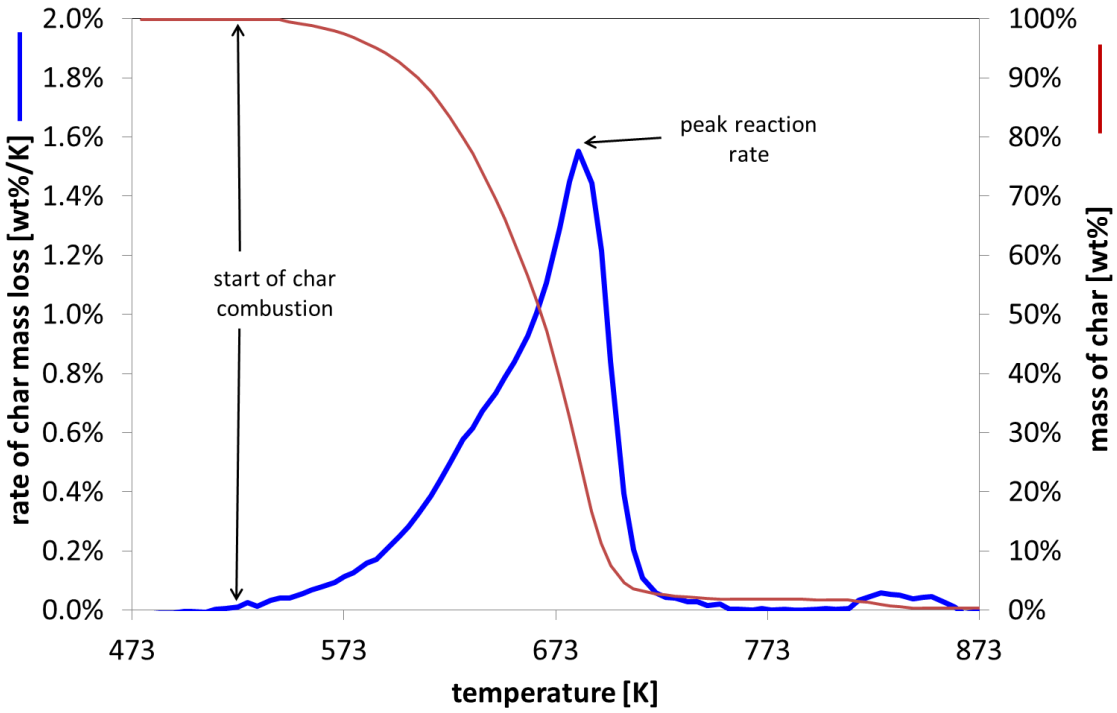

Figure 2-12 – Example of a char mass-loss profile with respect to temperature for a sample of willow char undergoing combustion (<90μm particles in air)

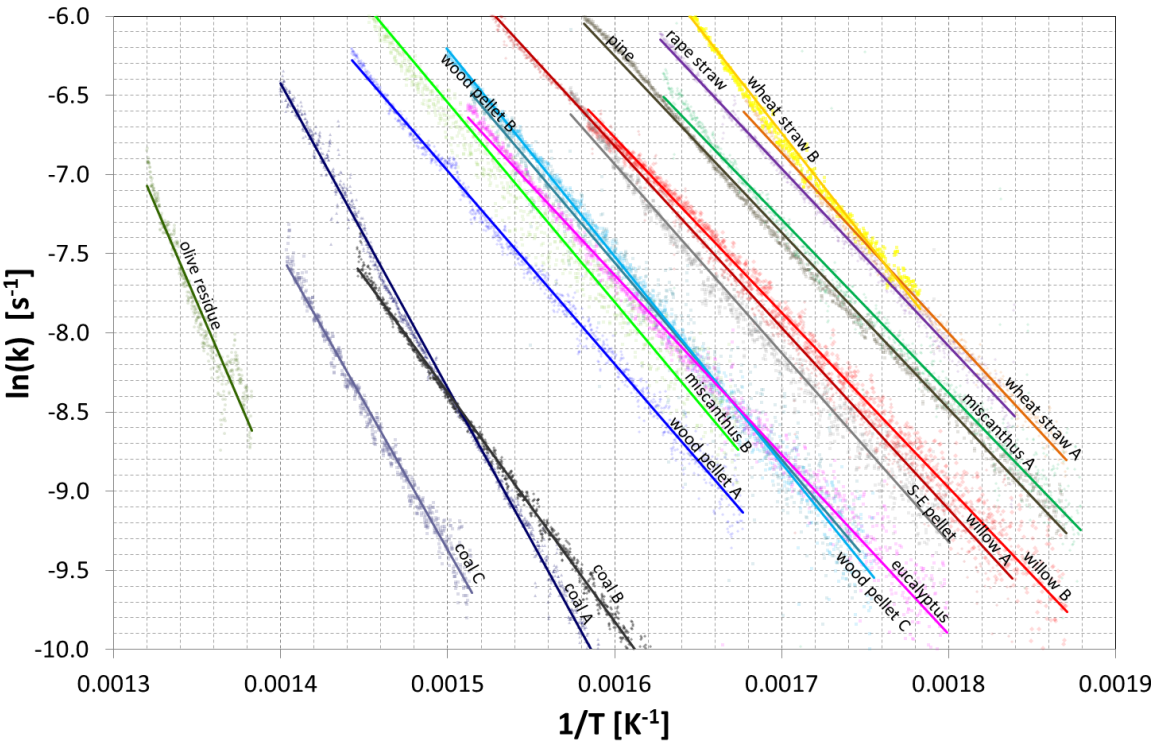

Figure 2-13 – Char combustion reaction rate coefficient, k (logarithmic scale) versus reciprocal of temperature (1/T) for biomass fuels and coals

Figure 2-12 shows, for example, the measurements taken from thermo-gravimetric analysis of willow-char undergoing combustion, with a heating rate of 10°C/min from 200°C to 600°C. The reactivity data for the selected biomass and coal fuel samples are plotted in **Figure 2-13**. The derived parameters characterising the char combustion kinetics are presented in **Table 2-12**. The conversion range for which these are evaluated is no more than 40 percent in order to obtain a good fit to the data (R^2 value).

While this analysis is based on a much simplified mode of the char reaction kinetics (single-step, first-order), the reactivity parameters presented show similarities among most of the biomass materials ($91 < E_{char} < 111$). The notable exception is the olive residue which also has a distinctly different molecular composition compared with the other fuels (see Figure 2-2).

Table 2-12 – Char combustion reactivity for selected fuel samples

Fuel	*reaction rate temperatures* K		*Activation Energy* E_{char} *kJ mol*$^{-1}$	*Pre-exponential* $ln(A_{char})$ s^{-1}	*range of conversion for evaluation* $\%m_{char}$		*Coefficient of determination* R^2
	start	*peak*			*from*	*to*	
willow A	520	682	95	11.5	1	30	0.991
willow B	500	681	92	10.9	1	30	0.981
wood pellet A	580	729	108	13.4	1	35	0.993
wood pellet B	560	700	101	11.3	1	30	0.910
wood pellet C	560	705	108	13.4	1	35	0.991
pine	500	645	92	11.6	1	40	0.996
eucalyptus	540	703	94	10.5	1	30	0.981
wheat straw A	500	623	95	12.5	1	30	0.993
wheat straw B	500	626	111	16.0	1	40	0.991
rape straw	520	631	93	12.1	1	30	0.990
miscanthus A	500	642	91	11.3	1	30	0.922
miscanthus B	550	703	105	12.4	2	30	0.978
S-E pellet	540	670	99	12.1	1	20	0.972
olive residue	700	770	205	25.5	1	20	0.930
coal A	590	738	159	20.4	1	20	0.996
coal B	580	751	120	13.3	1	20	0.996
coal C	610	763	152	18.7	1	20	0.985

2.4 Conclusion

The fundamental characteristics of fourteen biomass samples and the means of determining these characteristics have been presented. The characteristics have been presented graphically and discussed to illustrate the similarities and differences between different types of biomass and also with some coals. This has shown the variability in this small selection of biomass fuels. The variability is not just across different types of plant or wood but also across materials ostensibly of the same type.

The samples were selected as representative of fuels used in large scale power generation, the combustion behaviours of which are the subject of the following chapters. Some or all of the fuels characterised in this chapter are also used in the experimental studies presented in Chapters 3-5. Some of the data presented in this chapter are also used in analyses and discussions in later chapters. In particular, the results of proximate analysis are used in analyses in Chapters 3, 4 and 5 for accounting for moisture and ash content in the fuels.

The thermogravimetric data are referred to in the last chapter in which modelling of the devolatilisation and char oxidation adopt the kinetic parameters derived from TGA as an initial case for the model.

Chapter 3
Flame combustion experiments on single particles of solid biomass

3.1 Introduction

In this chapter, the relationships between particle size/shape/mass and the time required for full combustion (burn-out) are investigated. An experimental method for measuring the duration of various stages of combustion of single particles of biomass is described. A large data set obtained from three fuel samples in this experiment is presented and a further ten fuels are examined using the same method. Empirical expressions to describe the relationship between particle mass and characteristic combustion times are derived from the data.

3.1.1 Pulverized fuel

In large scale pulverized-fuel (p.f.) boilers, the solid particles of biomass (and/or coal) are introduced into a high temperature environment of the combustion chamber. At full load, the flame temperatures may be above 1500°C (1773K) and the particles of fuel are very rapidly heated as they enter the flame. The fuel particles will be entrained in the flow of hot gases in the combustion chamber. While this is designed to be turbulent in the primary combustion zone to promote mixing with the air, there is a net flow of the combustion gases over the upper end of the boiler and then down to the flue gas exit. The entrained particles therefore have a finite period of exposure to the combustion environment – often referred to as the “residence time”. The residence time must be appropriate to allow the particle to completely combust before the remnant ash particle passes out into the flue (and flue gas treatment plant). In a large scale boiler in a power generation plant on full load, the residence time is only a few seconds - typically less than two. If the particle of fuel entering the boiler is small enough, it will completely combust in the initial combustion zone. Larger particles may not “burn-out” until much nearer the back of the boiler (i.e. the flue gas exit) or may even pass through to the flue before fully burning. Very large particles may be so weighty that they fall out of the gas flow altogether

and accumulate in the bottom ash before they have fully combusted. The control of particle size is therefore imperative in achieving efficient “burn-out” and thereby effective conversion of the fuel energy to thermal energy (and ultimately to electrical energy).

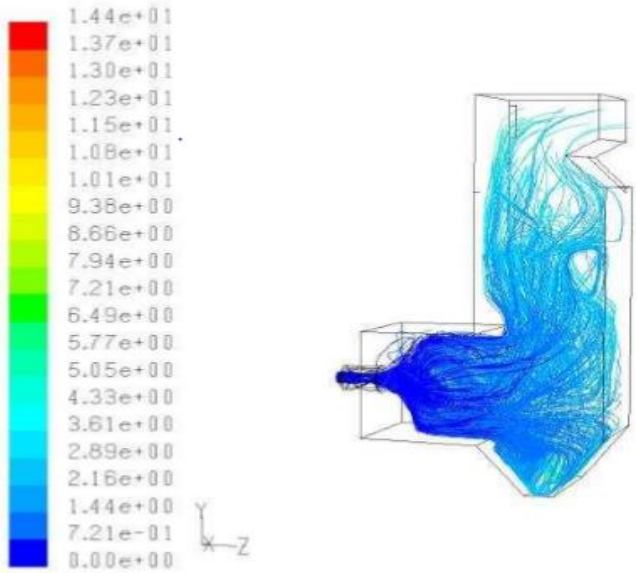

Figure 3-1 –biomass fuel particle trajectories and their respective residence times[s] from a CFD model of a pulverized fuel boiler source:(Darvell et al., 2014)

Whereas coal can be broken-down to <50μm particle sizes through milling, similar milling effort on woody biomass can result in a spread of particle sizes and shapes ranging up to 3mm or so (Van Loo and Koppejan, 2008). Since most solid biomass fuels have around 80% volatile content and generally less than 20% “fixed carbon”, the burning profile differs somewhat from that of coal. Biomass combustion in furnaces designed for pulverised coal therefore needs careful consideration to ensure effective operation. The volatile combustion stage will tend to produce more rapid release of fuel energy in the early part of the furnace (Gubba et al., 2012). Larger particles can extend the period of heat release in this stage but the remaining char will also have an extended burn-out time; this can be at the expense of a high proportion of un-burned char passing through to the ash (Gera et al., 2002) or particles dropping out of suspension unburned in the furnace. Achieving a good balance between milling effort, heat release profile and char burn-out is therefore one of the main challenges for efficient use of biomass in conventional plant.

Achieving a consistent particle size distribution and a small particle “top” size (i.e. maximum particle dimension) is, as discussed in Chapter 1, challenging owing to the fibrous nature of lignocellulosic materials. Furthermore, different types of biomass materials of the same particle size may burn at different rates. It is therefore very useful for the operators of large scale boilers to be sure that the biomass fuel is milled optimally to achieve the maximum practical burn out efficiency without excessive milling effort. Knowledge of the relationship between particle size and burn-out is therefore very important.

3.1.2 Combustion of single particles

The combustion of a particle of biomass fuel placed in a high temperature flame proceeds through a number of different processes: loss of moisture, devolatilisation and char combustion. While these processes are distinct there can be considerable overlap between the end of one process and the start of the next. Nevertheless, it is useful in the analysis of the overall process to distinguish different stages of combustion associated with the predominant individual processes. These stages can be identified as:

ignition delay – the period in which moisture is evaporated from the particle and the particle heats up before the ignition of the first volatile flame

volatile combustion – the period in which the particle is predominantly undergoing devolatilisation and thereby producing a flame from the volatile matter

char combustion – the period in which the devolatilised char particle is predominantly undergoing oxidation reaction

burn-out – the point at which the char ceases to burn so the remaining particle is entirely ash

ash decomposition– if the ash particle is retained in the high temperature combustion environment, there can be volatilisation or other phase transitions of certain inorganic components

For a given fuel in a certain combustion environment, the duration of each stage is dependent on a number of variables including the particle dimensions and shape, moisture/volatile/char content, thermal conductivity and heat capacity

and reaction kinetics. The influence of each of these variables can be investigated by modelling. In order to inform and validate any model, it is necessary to gather relevant empirical data.

Experiments on single particles of biomass have practical limitations in replicating the conditions in a pulverised fuel (p.f.) furnace. Nevertheless, there have been a number of experimental methods documented which examine combustion behaviour of biomass particle dimensions in the order of 1mm (Flower and Gibbins, 2009, Lu et al., 2010, Lu and Baxter, 2011, Gubba et al., 2011, Momeni et al., 2012). These have investigated the influence of variables including particle size and shape, gas temperature and oxygen concentration with the intention of informing and validating models.

Flower and Gibbins (Flower and Gibbins, 2009) developed apparatus in which single particles of biomass were suspended on a wire mesh and heated to 900°C in less than 0.5 seconds using an electrical element radiant heater. Experimental data for the drying, devolatilisation and char burn-out were obtained for European Ash wood with differing moisture contents. Despite having fewer data points this experiment offers one of the more directly comparable sets of results to those presented in this chapter.

Lu et al. (Lu et al., 2010) suspended single particles in an enclosed chamber reactor with a pre-heated air/nitrogen feed and internal heating elements enabling gas temperatures up to 1037°C. Using poplar wood and hardwood sawdust particles in the size range 0.3 – 9.5mm, the experiment focussed on the effects of shape differences on devolatilisation times, demonstrating that shape and aspect ratio differences affect the heat transfer and thereby show measurable differences in pyrolysis rates. Lu and Baxter (Lu and Baxter, 2011) proceeded to directly measure the internal thermal gradients produced in these conditions using thermocouples in the centre and surface of 11mm diameter particles. The data from this were used for validating CFD modelling by Gubba et al. (Gubba et al., 2011).

Momeni at al. (Momeni et al., 2012, Momeni et al., 2013) developed experimental apparatus using a gas burner and mass flow controllers to control the temperature and oxygen concentration in a vertical tube reactor in which single particles were placed for observing the combustion behaviour. The

experiment examined ignition, devolatilisation and char burn-out for cylindrical particles with similar mass (12.5mg) with aspect ratios ranging from 1 to 6 and for gas temperatures ranging from 1200°C to 1600°C (with oxygen concentrations ranging from 5 to 20% for the burn-out tests). In similar experiments Riaza et al. (Riaza et al., 2014) used a drop tube furnace and high speed camera on moving particles milled to <150μm and measured burnout times for various biomass and oxygen concentrations.

Investigation of the relationship between particle size and the duration of each of the principal combustion stages described above is the focus of the experimental study presented in this chapter.

3.2 Description of the experiment

In order to gather data on the duration of each combustion stage with respect to particle size (and shape), it is possible to perform simple visual examination of individual single particles of fuel, whilst they burn in a high temperature flame. By assigning visually observable criteria to the notional start and finish of each stage of combustion, it is possible to make consistent and comparable measurements of the duration of ignition delay, volatile flame combustion and char burn-out.

To facilitate observations and allow a certain degree of accuracy in the measurements, the visual examination can be undertaken by the use of a high-speed video camera. The footage of the particle combustion can then be examined in slow-motion playback and/or stopped on a specific frame to identify the start and end of each process.

The demarcation between each stage may not be clear since, as has been noted, there may be some overlap between the stages. Furthermore, it may not be possible to see the visual signs of the actual start of the volatile flame or the char burn. However, as will be demonstrated, if consistent criteria for defining the start and end of each process by visual inspection are adhered to, the resulting data should also maintain a degree of consistency and be meaningful.

Once the recorded data for the ignition delay, volatile burn and char burn-out have been obtained, they can be plotted against various characteristics such as

size, shape and moisture level to determine correlations and, if possible, establish mathematical relationships for modelling purposes.

3.2.1 Biomass fuel sample selection

There were two phases to the experiment. The first phase examined in detail the relationship between, mass, size and shape with respect to ignition delay, volatile combustion and char combustion for three materials: pine; eucalyptus and willow B. The second phase of experiments examined a further 10 materials but with fewer data points recorded in each experiment.

In the first phase of experiments, a selection of three fuels was examined and data for particles in the size range 0.5mm – 5mm were obtained. The initial sets of three fuels were examined with moisture levels at:

a) “as received” - dried in ambient air in the laboratory;

b) “wet” – with moisture added by soaking the particle in deionised water prior to the test

The fundamental fuel characteristics of the three materials selected for investigation are presented with detailed narrative in Chapter 2 and summarised in the data sheets in appendix A.

To achieve a higher level of statistical confidence in the analysis of the data, in these experiments, at least 100 tests were performed on each material. While not all of the measurements were valid (e.g. some particles dropped off the support before the end of char burn-out), the size of the data set for each set of measurements was at least 80.

In the second phase of experiments with ten different solid biomass fuels, for expediency, the number of measurements was reduced to 28. Again, not all the measurements were valid. However, having established the form of the regression function for fitting the data in the first phase of the experiment, this was taken to be acceptable for fitting the reduced set of data in the second phase. The error range was evaluated in all cases.

3.2.2 Sample preparation

To afford reasonable estimation of particle volume and surface area, a regular particle shape is preferred. Samples were therefore cut to size using a razor

blade such that the fibrous ends of the particle were cut square. Loose fibres were removed. The resulting particle shapes were between a quasi-cuboid shape and a quasi-cylindrical shape as illustrated in **Figure 3-2**.

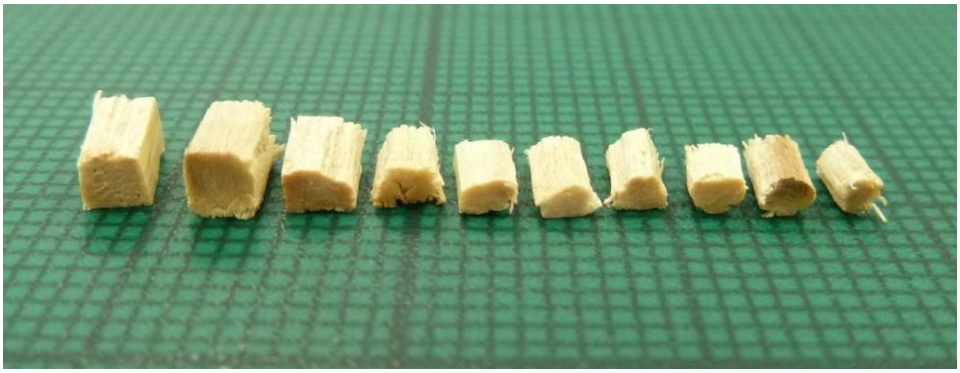

Figure 3-2 - Prepared pine sample particles in the 2-4mm size range

3.2.2.1 Measurement of size and shape

Although the "top-size" of particles in a pulverised fuel furnace is not likely to exceed 3mm, the samples had linear dimensions in the range 0.5 – 5mm. While this range extends above what is likely in a p.f. application, it was necessary to provide enough data for identifying clear relationships while being practical for the scale of the experimental apparatus.

The length, width and height of each cut particle were measured using a micrometer (+/- 0.01mm). While accurate measurement of the length of the particle is facilitated by cutting the ends square, only the principal dimension across the irregular sides of the particle could be measured. The following means of estimating volume and surface area of the particle were employed: (i) Calculate the volume and surface area of the cuboid which encloses the particle as measured; (ii) Calculate the volume and surface area of the ellipsoid cylinder that has the same principal dimensions; (iii) Assume that the actual volume and surface area are between the two values and use the mean as an estimate. The principle is illustrated in **Figure 3-3**.

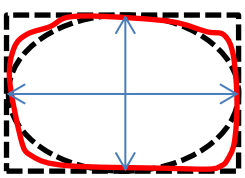

Dashed lines: notional regular-shaped cross-section

Red line: actual particle cross-section

Figure 3-3 - Estimating the cross section of the particle

The mass of each particle was recorded “as received” using an electronic balance with a precision of +/- 0.01 mg. Experimental results were analysed with respect to the dry mass of each particle which was derived using the moisture content measured by standard method EN 14774-3 for the bulk material. The apparent density of the particle was calculated using the dry mass and estimated volume.

3.2.2.2 Controlling the moisture content

The “as received” moisture content of the materials was determined by weighing before and after oven drying in accordance with the standard method for determining moisture content (Standard, 2009a).

In order to investigate the effects of higher moisture content, a sub-set of pine particles was simply immersed in deionised water for a period in excess of 24 hours to allow the moisture to soak into the centre of the particle. This method required the quantity of water in which the particle was immersed to be in excess of the amount absorbed. Although it was attempted to minimise this by sealing the particles in polythene sachets, the excess water unavoidably resulted in some leaching, and therefore, some loss of soluble salts from the particle in this process.

Particles prepared in this way were removed from the water and excess surface water removed with an absorbent paper towel lightly pressed on the surface. The wet mass of the particle was then weighed and the proportion of moisture in the particle determined using an estimated dry mass. Where moisture content is referred to in this context, it is defined as:

$$M = \frac{m_w}{m_w + m_d} \qquad \textbf{(3-1)}$$

where:

M is the mass fraction of moisture in the particle

m_w is the mass of moisture in the particle

m_d is the dry mass of the particle

In the ambient conditions in an air conditioned laboratory, moisture will evaporate from the particle surface rapidly and the particle will dry quickly (in the context of the duration of the experiment). Combustion tests were therefore commenced as soon as possible after removal from immersion and the length

of the delay was recorded and kept consistent as far as reasonably practical. Prior to undertaking the combustion tests on wetted particles, the rate of moisture loss from a particle in ambient air was assessed using the following method:.

(i) Laboratory conditions were recorded as: 23°C ±1°C with 32% relative humidity.

(ii) Selected particles were removed from immersion and excess water removed. They were then placed directly onto a weighing pan open to the ambient air and the mass recorded at timed 1-minute intervals over a period of 20 minutes to 1 hour depending on the rate of moisture loss.

(iii) The resulting mass-loss data plotted against time showed a weak exponential decay as is consistent with several models for drying of particles (Hall, 1987, Hosseinabadi et al., 2012). The data were fitted to least-square regression lines with the function:

$$m_w = m_{w0} \times e^{-t/\tau} \qquad \textbf{(3-2)}$$

where:
m_{w0} is the initial mass of moisture in the particle
τ is a characteristic time constant.

Since particles of different sizes and shapes have different drying rates, a function for estimating the drying rate based on the particle's physical dimensions is required. Since drying rate is related to the relative surface area available for moisture to evaporate, it was assumed it could be derived from a function the particle's surface-area-to-volume ratio. The time constants for each particle determined previously were then plotted against their surface area to volume ratio and a best-fit polynomial function was determined from least-square regression. The resulting function is then a drying time–constant as a function of surface area to volume ratio. This provides a means of modelling the rate of moisture loss for particles of varying sizes and shapes. A comparison of the measured data and the modelled data, for two batches of pine particles (A1-5 and B1-4) is presented in **Figure 3-4**. This analysis provides a guide to how much moisture is likely to be in the particle at the start of the combustion test.

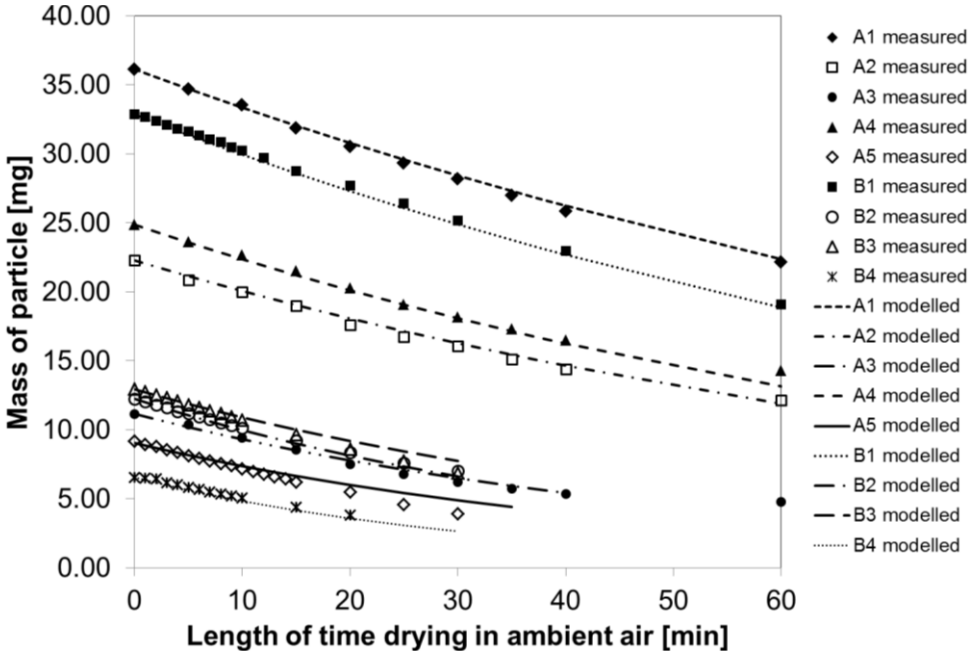

Figure 3-4 - Moisture loss curves for 9 particles of pine of varying sizes

During the single particle combustion experiments, the typical time taken from weighing the particle to the start of combustion was 90 seconds. **Table 3-1** shows that the reduction in the particle moisture content was not more than 3% (of total mass) after 2 minutes exposure.

Table 3-1 - Moisture loss from prepared particles of pine after 2 minutes ambient drying

Sample ref.	volume	Oven dry mass	Initial wet mass	initial moisture content	moisture content after 2 minutes
	mm^3	mg	mg		
A1	36.40	14.32	36.13	60%	60%
A2	22.26	9.89	22.28	56%	55%
A3	10.68	4.53	11.16	59%	58%
A4	24.15	12.16	24.87	51%	50%
A5	8.27	3.40	9.05	62%	61%
B1	27.28	12.21	32.85	63%	62%
B2	9.90	4.73	12.25	61%	60%
B3	11.02	4.01	12.94	69%	68%
B4	6.44	2.84	6.56	57%	54%

3.2.3 Fuel particle support and flame-shield

The experimental method required that the single particles of solid biomass being studied should be suspended in the centre of a methane flame with consistency and with the ability to focus video and thermal imaging cameras on the particle while it is burning. A single particle combustion experimental apparatus was built for the purpose of supporting the particles in a Méker burner flame at a stable and consistent position. The apparatus incorporated a movable protective water-cooled sleeve to shield the particle from the flame prior to exposure. For most biomass samples, the particle was impaled on a steel needle which was, in turn, supported in a twin-bore ceramic tube as shown in **Figure 3-5**. For accuracy of the time measurement, the particle must be exposed to the methane flame in an instant that can be indexed as t=0. This is achieved by protecting the particle in the sleeve while the methane flame is established. The sleeve, which is mounted on linear bearings is then withdrawn rapidly thus exposing the particle to the flame in less than 0.1 seconds. The test rig is shown in **Figure 3-6**.

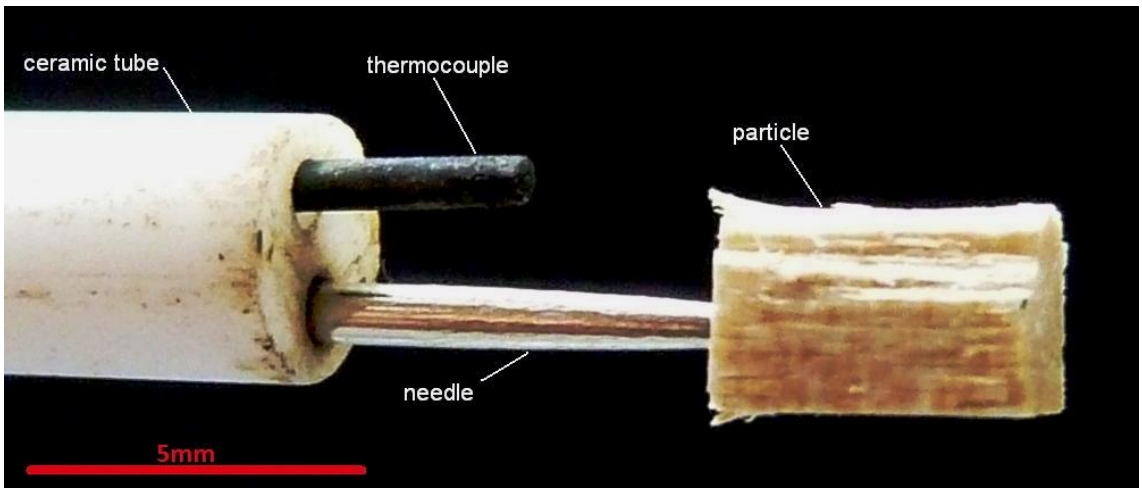

Figure 3-5 - Close up of particle support (view from above)

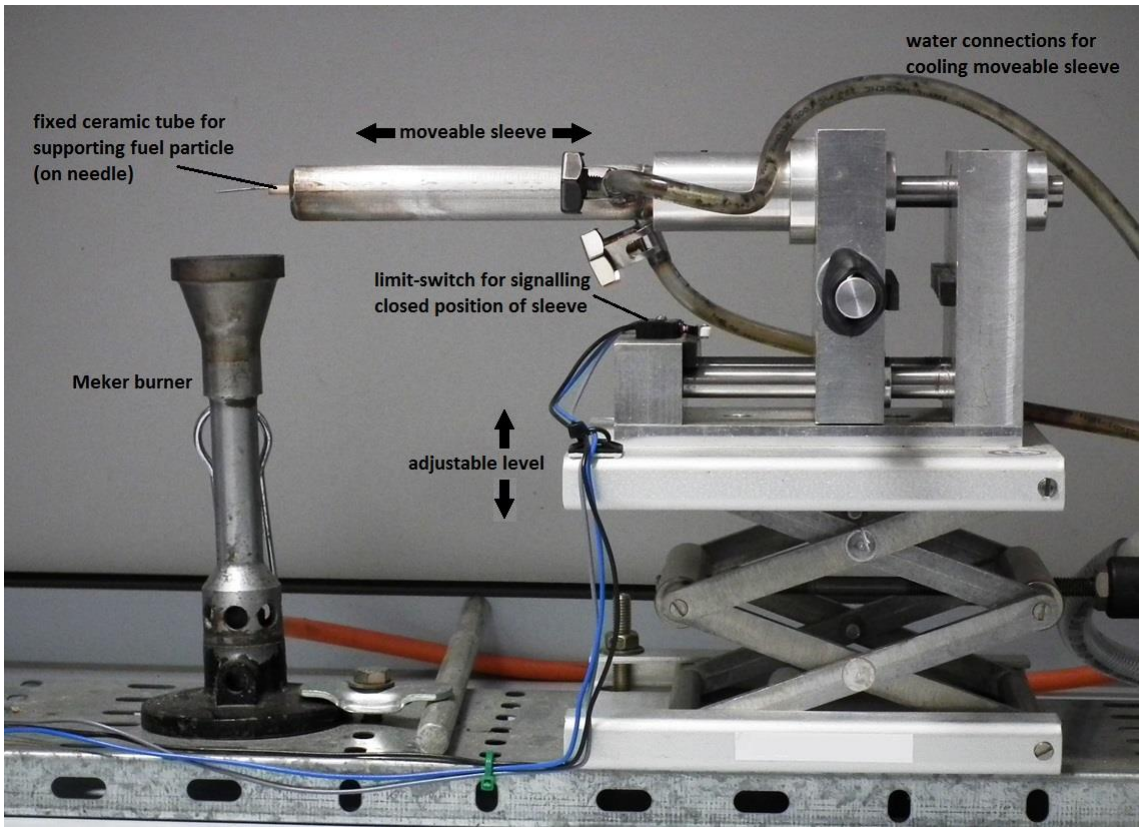

Figure 3-6 – Single particle combustion apparatus showing burner, adjustable support and water-cooled moveable sleeve

3.2.4 Gas burner

It is important that the natural gas (methane) flame environment is consistent for each test. To provide a uniform flame temperature in the horizontal plane, a large diameter (40mm) uniform flame was produced using a Méker burner. To ensure consistency, the test rig was adjusted to maintain the particle at a fixed level above the top-centre of the burner - well within the stable part of the flame. The velocity of the flame was measured to a first approximation by capturing high speed video of burning dust particles dropped into the flame. A velocity of 3 ms^{-1} was estimated for the stream in the centre of the flame. This, along with the thermal and fluid characteristics of the gas may be used to calculate a Reynolds number and Nusselt number required for calculating heat transfer to the particle. The thermal environment (surrounding gas temperature and temperature of enclosing surfaces) and the oxygen concentration are important factors in the combustion behaviour of the single particles. In the experiment, these have been measured and are taken to be not significantly variable from one test to the next.

3.2.4.1 Oxygen concentration

The oxygen concentration in the Méker burner flame is key in the combustion reaction kinetics. It is therefore important that this was also consistent for each test. Furthermore, knowledge of this is required in the context of modelling or verifying models.

To determine the likely oxygen concentration in each single particle combustion run, measurements were made on the stand-alone Méker burner. The burner was set up with a fixed, quartz, gas-probe (O.D. 2.5mm, I.D. 0.8mm) positioned in the centre of the flame. The burner was mounted on a moveable support which allowed the position of the probe relative to the burner to be adjusted precisely in both horizontal and vertical axes. The natural gas supply pressure was taken to be at supply standard pressure of 21mbar +/- 2mbar. With a natural gas flame established, the gas mixture in various parts of the flame was sampled with the probe and passed, dry, through a Horiba VA-3000 gas analyser. The measured concentration was adjusted to account for water vapour content (estimated at 11% of sampled gas). The oxygen concentration measurements (by volume) are plotted on a colour-contour plot in **Figure 3-7**. In the region between 10 and 40mm above the top of the burner, the oxygen concentration was measured 9.0% ± 0.5.

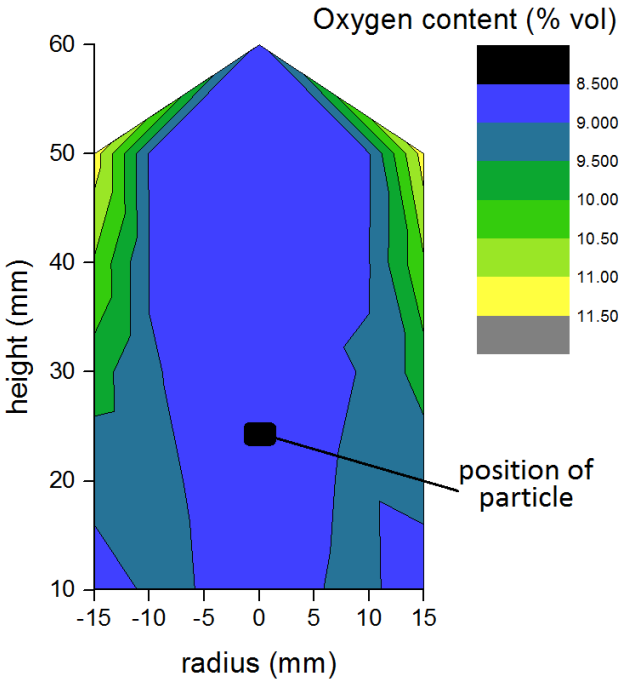

Figure 3-7 – Measured oxygen concentration in Méker burner natural gas flame

3.2.4.2 Flame temperature

The temperature of the Méker burner methane flame was measured using an R-type thermocouple (in the absence of a single particle sample) at 5mm height intervals above the burner grill and also at 5mm radial intervals from the centre. Measurements for each point were logged for 30-60 seconds and the mean taken to smooth out noise and variance in the signal. At such high temperatures with the surrounding conditions at ambient 300K, the radiative heat loss from the thermocouple has to be accounted for as described by Bradley and Matthews (Bradley and Matthews, 1968) using the equation:

$$T_{gas} \approx T_{tc} + \frac{\sigma \varepsilon}{h_{tc}} (T_{tc})^4 \quad \textbf{(3-3)}$$

where:

T_{gas} is the gas temperature

T_{tc} is the thermocouple temperature

σ is the Stefan-Boltzmann constant (5.67 x 10^{-8} W m^{-2} K^{-4})

ε is the emissivity of platinum-rhodium at temperature T_{tc}

h_{tc} is the convective heat transfer coefficient of the thermocouple in the gas flame

The emissivity of platinum was derived from data presented by Bradley and Entwistle (Bradley and Entwistle, 1961) and calculated as an approximated function of the measured temperature as:

$$\varepsilon_{Pt} = 0.1408 \ln(T) - 0.8238 \quad \textbf{(3-4)}$$

To determine the thermal heat transfer coefficient, the Nusselt number and gas thermal conductivity are required. The Nusselt number can be derived using the Ranz-Marshall approximation for the thermocouple bead (Hindasageri et al., 2013) which is given as:

$$Nu = 2 + 0.6 Re^{1/2} Pr^{1/3} \quad \textbf{(3-5)}$$

where:

Pr is the Prandtl number (0.71)

Re is the Reynolds number given by:

$$Re = \frac{U_{gas} \; D_{tc}}{\upsilon_{gas}} \quad \textbf{(3-6)}$$

where:

U_{gas} is the velocity of the gas flow (3.0 ms^{-1})

υ_{gas} is the kinematic viscosity of the gas (0.0001 $m^2 s^{-1}$)

D_{tc} is the diameter of thermocouple (0.45mm)
giving the values:

$$Re = 13.4$$
$$Nu = 3.96$$

The thermal conductivity of the gas was derived from data on air (Shpilrain, 2011) and derived as an approximated function of measured temperature (T) as:

$$\lambda_{gas} = 6.33 \times 10^{-5}\, T + 8.08 \times 10^{-3} \text{ W m}^{-1}\text{ K}^{-1} \qquad \textbf{(3-7)}$$

The thermocouple wires were 0.15mm thickness and the exposed leads were ~8mm from the ceramic sheath. The thermal conduction heat loss was neglected as being less than 1% - which is lower than the noise on the measurement samples.

An additional error arises from the use of an uncoated platinum thermocouple. Platinum can catalyse reactions on the surface of the thermocouple, the energy from which can affect the temperature of the thermocouple. The recorded temperature is therefore likely to be somewhat higher than the average temperature of the flame. An alternative estimate of the flame temperature is therefore necessary. The adiabatic flame temperature may be calculated using CHEMKIN, a proprietary chemical equilibrium modelling software for gas-phase reactions. The flame chemistry was assumed to be methane (CH_4) combusted in excess air. The fuel-air ratio was selected to correspond with the measured O_2 concentration in the flame. For an O_2 concentrations in the range 9.0% $\pm$ 0.3 (see 3.2.4.1), the corresponding flame temperature was calculated to be 1570K $\pm$30K. The calculation parameters and corresponding flame temperatures are as summarised in **Table 1-1**.

Table 3-2 - Flame temperatures estimated from chemical equilibrium calculation

	Reactants			Products				Equilibrium
	CH_4	O_2	N_2	CO_2	H_2O	O_2	N_2	temperature
mol fraction	0.053	0.199	0.748	0.053	0.106	0.093	0.748	**1540K**
mol fraction	0.054	0.199	0.747	0.054	0.109	0.090	0.747	**1574K**
mol fraction	0.057	0.198	0.746	0.057	0.111	0.087	0.746	**1603K**

Initial temperature: 298K
Constant pressure: 1 atm

The Méker burner flame temperature measurements are plotted on a colour-contour plot in **Figure 3-8**. A consistent and stable region of temperature can be identified between 15 and 30mm above the top of the burner and within 5mm of the centre line. The measured temperature in this region is measured as between 1650K and 1700K which is some 100K higher than the estimated value. In later analyses (Chapter 6), a flame temperature of 1600K is assumed. To reconcile the measured and calculated flame temperatures, a large margin of error (± 60K) must be declared. To mitigate for this uncertainty the temperature of the particle surface was also measured (see 3.2.7) and used for model validation (chapter 6).

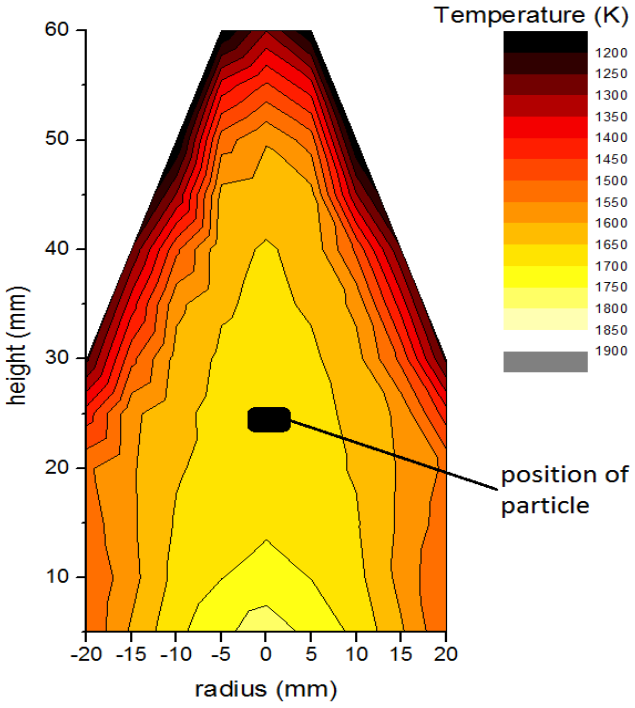

Figure 3-8 – Measured temperature of Méker burner natural gas flame

3.2.5 Video camera

The experimental method involves capturing the image of the burning particle on digital video and subsequently extracting the timing of the start and end of each of the combustion processes by visual examination. To identify the timing of the events with sufficient accuracy, a high frame speed is required. A FujiFilm Finepix HS10 digital camera with high speed video capability and close up focussing was selected for this purpose. A video speed of 120 fps was generally used – giving a resolution of measurement of 8.3ms.

For consistency of video footage, the camera was placed in the same position on each run: level with and 200mm from the lens to particle position as shown in **Figure 3-9**. The particle height above the burner was set at 20-25mm such that it was maintained in the region of stable temperature and oxygen concentration as described above.

Figure 3-9 - Particle position with respect to Méker burner and camera

Standard digital video editing software packages are available which cater for activities requiring stop frame and single frame advance (i.e. video editing) - suitable for the requirements of analysing images of single particle combustion. Use of such software (Quicktime Player version 7.7.4) allowed frame numbers to be identified and the timing between frames simply determined from the selected frame speed. For the purposes of improving the clarity of images, it was found that the ability to adjust the contrast, brightness and colour filters on the video was useful, especially in the identification of the start and end of a volatile flame and the end of char burn-out.

3.2.6 Event Identification

The following criteria were adopted as the definitive means of demarcating the different stages of combustion as described in section 3.1.2.

(i) Exposure to gas flame

The point at which the particle is initially exposed to the gas flame is simply determined by identifying the first video-frame in which the entire particle is visible.

(ii) start of volatile combustion

After the initial ‘ignition delay’ during which the moisture in the particle is evaporating, the first signs of devolatilisation become visible by the appearance of a pale orange flame above or to the side of the particle. However the appearance of this is subject to variability since some particles have small protruding parts which can devolatilise before the main body and so misleading spurious flames are sometimes visible before the main flame starts. A more consistent and reliable criterion for determining the start of volatile combustion is the appearance of a luminous flame above the particle. To assist in identifying the first frame in which this appears, the contrast control for the video image was set to its maximum. The start time of the first frame of the video in which a continuous flame is clearly visible is defined, for the purposes of this study, as the start of the volatile combustion. The identification of this was simplified by the practice of finding a frame with a strong volatile flame visible and running the video backwards frame by frame until it was no longer visible.

(iii) end of volatile combustion

As the volatile content of the particle is exhausted, the volatile flame reduces and finally disappears. To assist in identifying the first frame in which the flame ceases to be visible, the contrast control for the video image was set to its maximum. The end time of the last frame in which the strong flame is visible is defined, for the purposes of this study, as the end of the volatile combustion (see **Figure 3-10**).

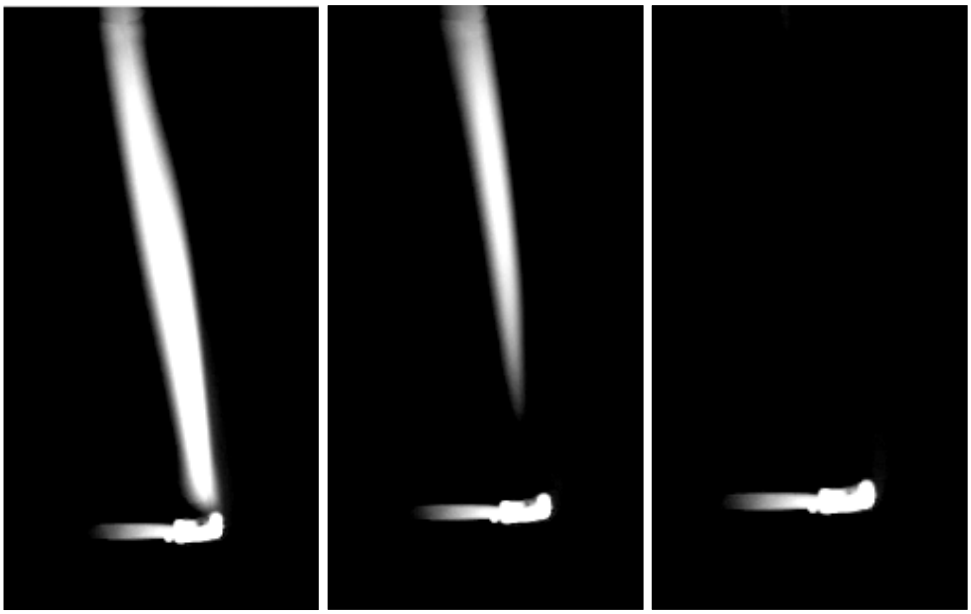

frame 1 frame 2 frame 3

Figure 3-10 – Identifying the end of the volatile flame
In this example, the end of the volatile flame is taken to be the end of frame 2

(iv) start of char burn

In the entrained gas flow, the particles do not burn evenly since the leading edge of the particle in the flame is subject to a higher heat transfer than the trailing edge. One effect of this one-sided heating is that the bottom of the particle commences char combustion before the top part of the particle has completed devolatilisation (see **Figure 3-11**). Demarcating the start of the char combustion stage is therefore difficult to distinguish. For the purposes of the experiment, a consistent and well-defined criterion for identifying the start of char combustion is required and, for convenience, it is taken to be coincident with the end of the volatile flame burn. It is recognised that parts of the particle are combusting as char before the volatile flame has ceased so this measure is not exactly coincident with the actual char combustion process in its entirety. Since this overlapping has been disregarded in the measurements, there is a discrepancy between the measured and actual char burn duration. However, the observed measure is directly related to the overall process and, importantly, it is a clear and consistent point of reference.

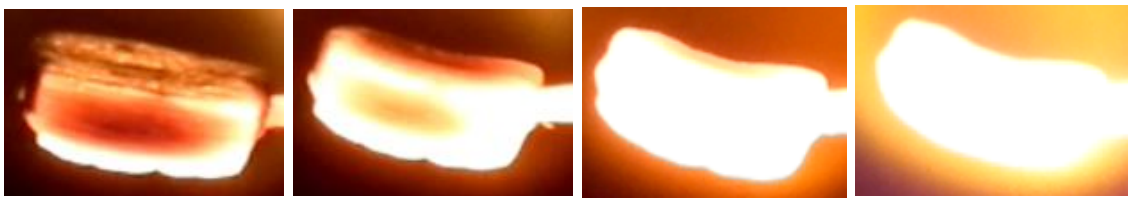

Figure 3-11 – Char combustion video images

In this example, the char combustion can be seen starting in the lower part of the particle in the first frame. Subsequent frames show the bright glow of the char reaction eventually engulfing the entire particle.

(v) end of char burn

The char burn is visually characterised by a luminous gas stream above the particle. This has the appearance of a weak flame although it is not produced by combusting volatiles but from the heated CO and CO_2 gases emanating from the char oxidation. As the char combustion proceeds, the particle steadily shrinks. At the approach to char burn-out, there is a brief crescendo in brightness of the 'flame' which is followed by a more rapid shrinkage and a diminishing in brightness until only a particle of amorphous ash remains. The intensity of the luminous emission brightness can be used as a marker to demarcate the end of char combustion. Adjusting the contrast and the brightness of the image assists in the identification of the point at which the emission stops. For the purposes of this study, the end of char burn is defined as the last frame in which a discernible bright emission or 'flame' is apparent above the particle after the final rapid particle shrinkage (see **Figure 3-12**). It can be seen from the figure that the transition between frame 2 and frame 3 is less distinct than in the case of the volatile flame identification. This introduces a significant level of variability into the measurement since it is not always possible to identify a specific frame in which this occurs but rather a range of frames. The error introduced from the indistinct nature of the visual identification is estimated at +/- 5% of the total measured combustion duration.

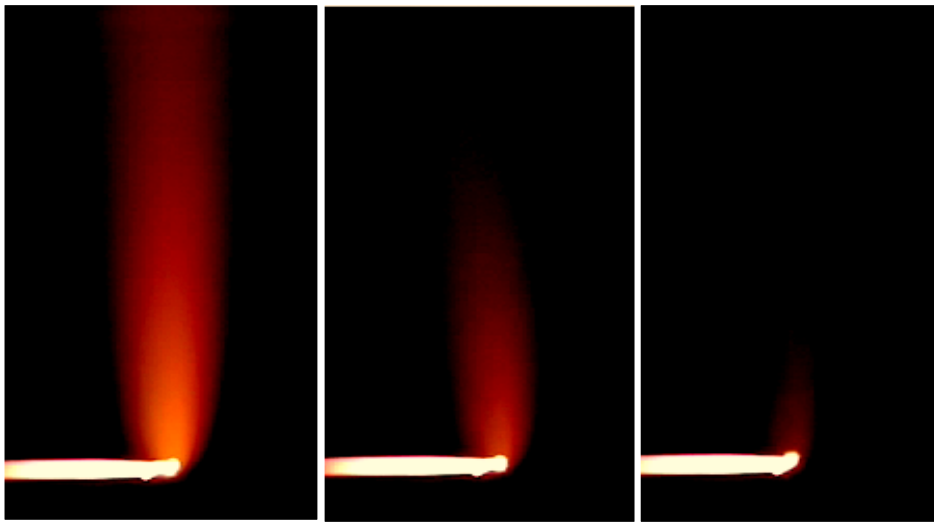

frame 1 frame 2 frame 3

Figure 3-12 – Identifying the end of char burn
In this example, the end of the char burn is taken to be the end of frame 2

3.2.7 Thermographic imaging

Measurement of the particle temperature directly during combustion is problematic for small particles. While it is possible to use a thermocouple inserted into a hole inside the particle as in the experiments by Lu and Baxter (Lu and Baxter, 2011), this is impractical for particles with dimensions less than 5mm and requires modification of the particle itself. Measurement of the surface temperature of the combusting particle in the gas flame is possible by use of a thermal imaging. In this study, an infra-red thermographic camera was used for this purpose. The camera used was a FLIR A600 series which employs a focal-plane-array thermal detector with a measurement range up to 2273K. The sensitivity of the device is specified as 0.05K with an accuracy tolerance of 2% of reading (i.e. ±30K at 1500K).

An example of the thermal images obtained of a particle of pine at different stages of combustion in the methane flame is shown in **Figure 3-13**. This shows, from left to right: (i) initial exposure to the flame with the lower edge heated but rest of particle still cool; (ii) during devolatilisation with the particle heated, but top surface cooler, due to cooling effect of volatile release; (iii) after devolatilisation with the whole particle at high temperature; (iv) advanced char combustion stage.

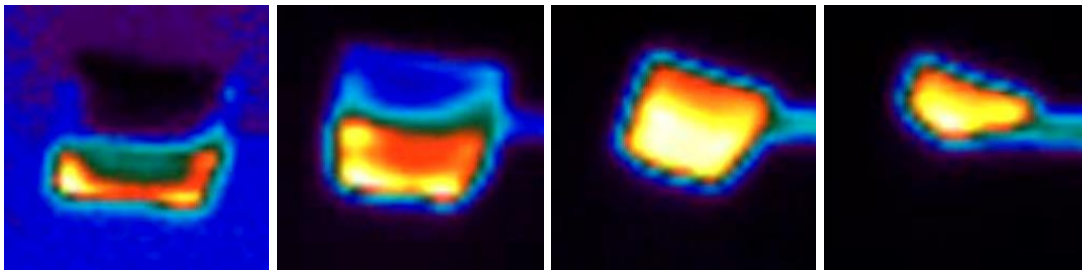

(i) (ii) (iii) (iv)

Figure 3-13 – Thermal imaging of a particle of pine undergoing combustion

The images are derived from the intensity of the infra-red radiation detected by the thermal detector in the camera. The temperature of the particle's surface can be derived from the data although it is necessary to account for the emissivity of the surface. The emissivity of wood has been reported as varying between 0.83 and 0.89 at 333K (López et al., 2013). An emissivity of 0.85 for char has been used in surface temperature measurements of particles in fluidised bed combustors by Salinero et al. (Salinero et al., 2016). These reported values suggest that an emissivity of 0.85 is a reasonable assumption to take for the entire range of the combustion process being observed and this was the value adopted for the derivation of temperatures from the thermal imaging. **Figure 3-14** shows an example of the surface temperature time-history profile of a combusting pine particle. The points on the profile relating to images in **Figure 3-13** (i)-(iv) are indicated.

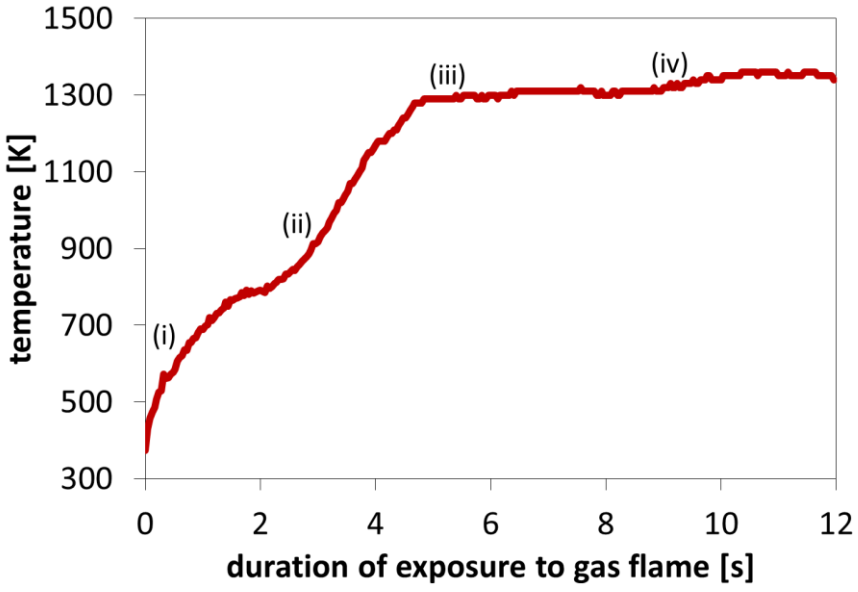

Figure 3-14 – Surface temperature profile derived from thermal imaging

3.2.8 Data processing and statistical analysis

For each individual particle experiment, the particle dimensions, particle mass, moisture content, ignition delay, volatile flame duration and char-burn duration were recorded. In the initial presentation of the results, the timed measurements are plotted against the mass of a dry particle. This was derived from the measured mass and adjusted for the as-received moisture content. The dry mass has been adopted to allow more meaningful comparison between different materials. After the initial drying and onset of ignition, the important mass of material in the particle is the dry mass so it is reasonable to use this in the context.

To evaluate and compare the timed duration of each combustion stage and the total burn out time with respect to the particle mass, the data were characterized by a regression function. This is helpful for comparing the behaviour of different materials and a useful basis for validating models. Visual inspection of the data, shows strong correlations which should allow fitting of the data to a regression function. There is also notable noise and spread in the data both from variability in the samples and measurement error. It is important, therefore, that determination of a “best-fit” regression function is accompanied by error quantification. Statistical analysis of the data was performed using *IBM SPSS Statistics version 21* software. Each set of measurements for each sample were assessed for fitting to both a linear regression and a power function regression. It is noted that the results of others’ single particle experiments have previously approximated to linear functions (Flower and Gibbins, 2009). In all cases in this experiment, the power-function regression provided a higher coefficient of determination (R^2). While the power function regressions are naturally fixed at the origin, the linear regressions tended to have a positive offset at zero mass – which is clearly unrealistic. The power function regression was therefore selected as the most appropriate model for the data. The validity of this premise was checked by evaluating the errors for each data point (i.e. the difference between the selected regression function and the measured datum) and checking the errors for normality (i.e. normal distribution around a mean). In all cases, the data were shown to be statistically normal by either or both the Kolmogorov-Smirnov and Shapiro-Wilk normality

tests. The spread in the error was also determined and the 95% confidence range for this error evaluated.

3.3 Results

3.3.1 Drying and ignition

The time-interval between the withdrawal of the protective sleeve and the on-set of volatile combustion is taken to be the 'ignition delay'. The delay is governed by the time required for the moisture to evaporate and the particle to heat up such that at least part of the particle is at a temperature for devolatilisation to commence. In many cases, the ignition delay was measured in the order of 10-20 frames which imply an error of +/- 10% in the timing. However, the imprecision of this particular measurement appears to be overshadowed by other factors which introduce variability in behaviour from particle to particle. For example, the tendency of smaller parts and protuberances of the particles to ignite before the main bulk thus giving rise to a visible volatile flame earlier for some relatively large particles than smaller ones.

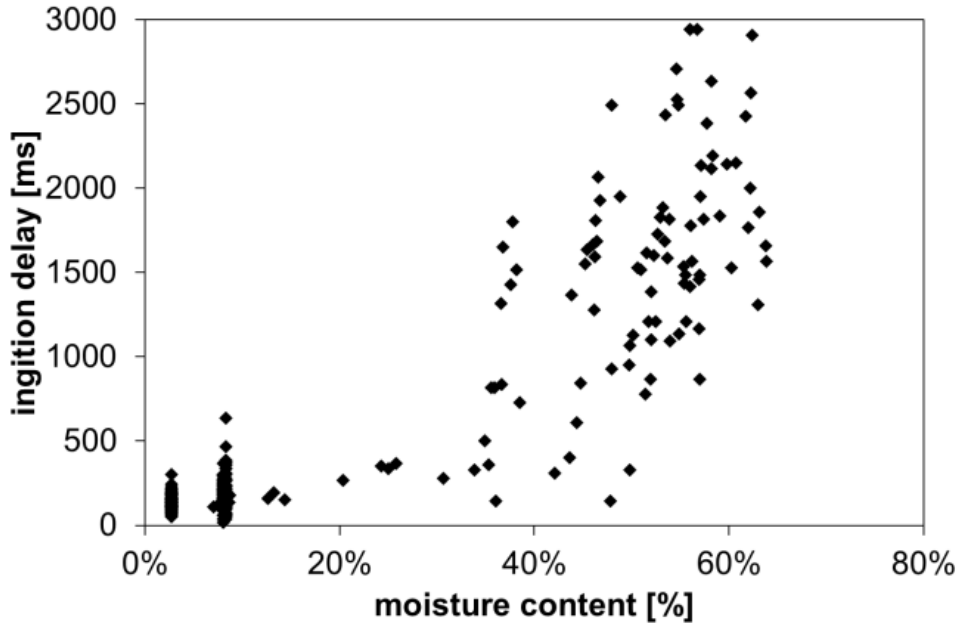

Figure 3-15 –Ignition delay versus moisture content for all samples

The form of the function for relating ignition delay (s) τ_{ign} , to particle dry mass (mg) m_d , that provides the best fit to the measured data is found to be:

$$\tau_{ign} = a_{ign} {m_d}^{b_{ign}} \quad \textbf{(3-8)}$$

where a_{ign} and b_{ign} are empirically derived coefficients

The plot for the ignition delay versus moisture content for all materials (up to 20mg dry mass) is presented in **Figure 3-15**. This shows an expected general correlation for ignition delay to be longer for higher moisture content. Moisture content, *M*, should then also be included as a variable in equation **(3-8)**. While both a_{ign} and b_{ign} could be derived as functions of M, a simplified approximation may be derived from considering a_{ign} to be proportional to M with b_{ign} as a constant. Since the data are heavily influenced by noise and measurement error, derivation of a more complex relationship would be difficult to justify here.

Based on the experimental data for the three materials for which differing moisture content was examined (pine eucalyptus and willow), the empirical functions derived from the data are presented in **Table 3-3**.

Table 3-3 – Regression functions for ignition delay (s) as a function of mass (mg) and moisture (wt%)

$\tau_{ign} = a_{ign} {m_p}^{b_{ign}}$	Pine	Eucalyptus	Willow B
a_{ign}	2.2*M*	1.4*M*	1.5*M*
b_{ign}	0.32	0.34	0.37

The measured ignition delay data for both “as received” and “added moisture” samples are plotted **Figure 3-16** (a) – (c). The best fit regression functions are superimposed on the plot to illustrate the general fit to the data. The coefficients of the regression functions for each of the three materials are as presented in Table 3-3 with the values of moisture content, M, for the “as received” samples and “added moisture” samples respectively as follows: (a) Pine: 8.3% and 57%; (b) Eucalyptus: 8.1% and 42%; (c) Willow B: 3.1 and 53%

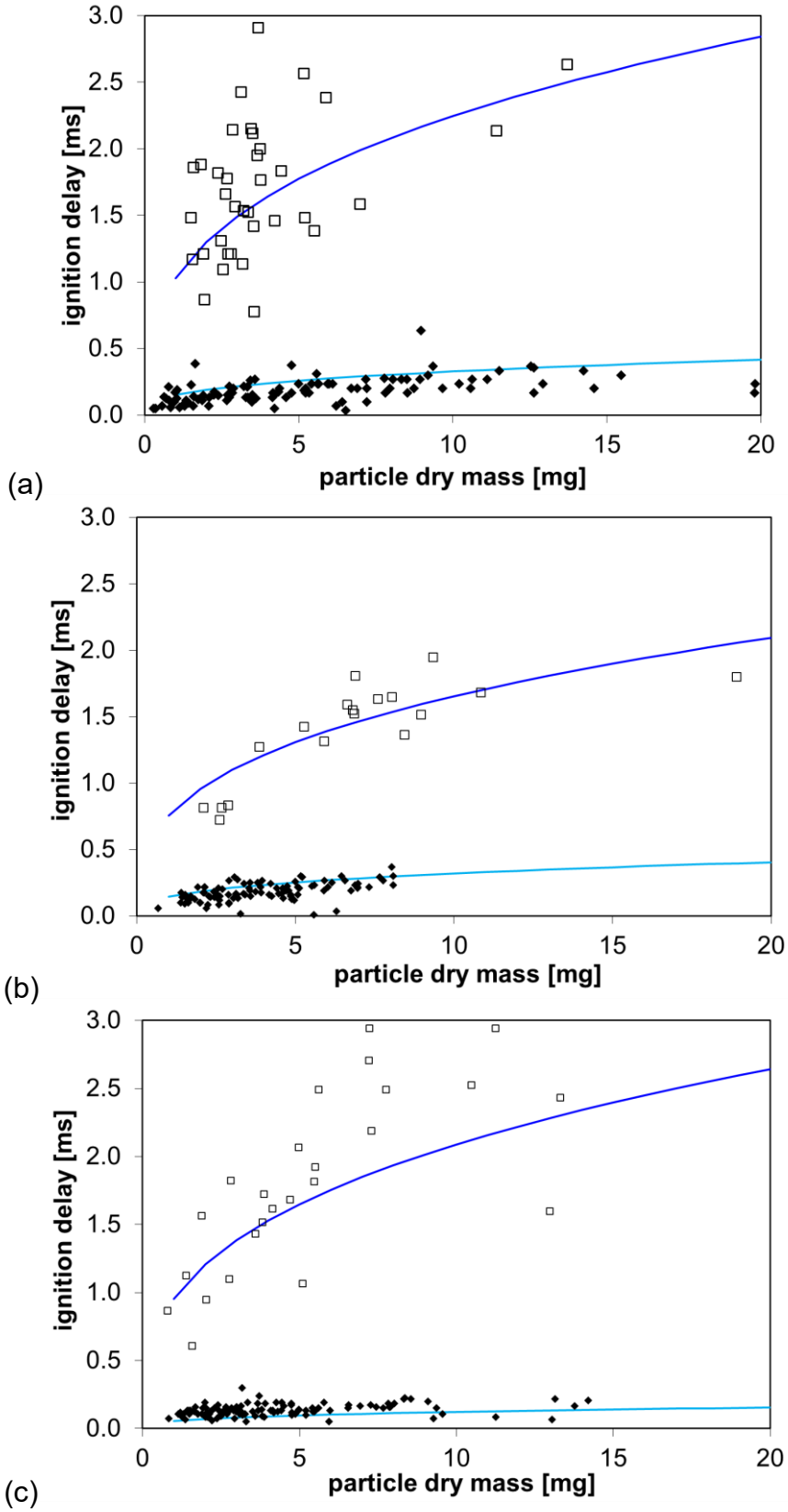

Figure 3-16 – Ignition delay versus dry particle mass for samples as received and with added moisture: (a) pine; (b) eucalyptus; (c) willow B

Legend: ◆ as received □ added moisture

3.3.2 Devolatilisation and volatile combustion

The identification of the start and end of the volatile flame is distinct and the margin of error for these measurements was no more than one or two frames (<1%) of the total duration of around 100 frames. The volatile flame duration for both dry and wet particles is shown plotted against particle dry mass for each of the fuels as presented in **Figure 3-17**.

It is noted that the devolatilisation is slower for those particles that had previously been immersed in water. Since particles with added moisture were subjected to excess water in the wetting process it is possible that this dissolved and extracted a significant proportion of potassium salts from the solid. The extended devolatilisation time observed is evidence of the diminished catalytic effect from reduced alkali metal content in the devolatilisation reaction kinetics. This has been described previously in Jones et al. (Jones et al., 2007) and Saddawi et al. (Saddawi et al., 2012).

The form of the best-fit function to the measured data for the volatile flame duration τ_{vol} is:

$$\tau_{vol} = a_{vol} {m_d}^{b_{vol}} \quad \textbf{(3-9)}$$

where a_{vol} and b_{vol} are empirically derived coefficients

The coefficients for the functions derived from the data are presented in **Table 3-4**.

Table 3-4 – Regression functions for volatile flame duration as a function of mass

$\tau_{vol} = a_{vol} {m_p}^{b_{vol}}$	Pine		Eucalyptus		Willow B	
	a.r.	moisture	a.r.	moisture	a.r.	moisture
a_{vol}	1.33	1.78	1.27	1.58	1.19	1.70
b_{vol}	0.59	0.70	0.62	0.71	0.60	0.68

The measured ignition delay data for both “as received” and “added moisture” samples are plotted **Figure 3-17**(a) – (c). The best fit regression functions are superimposed on the plot to illustrate the general fit to the data.

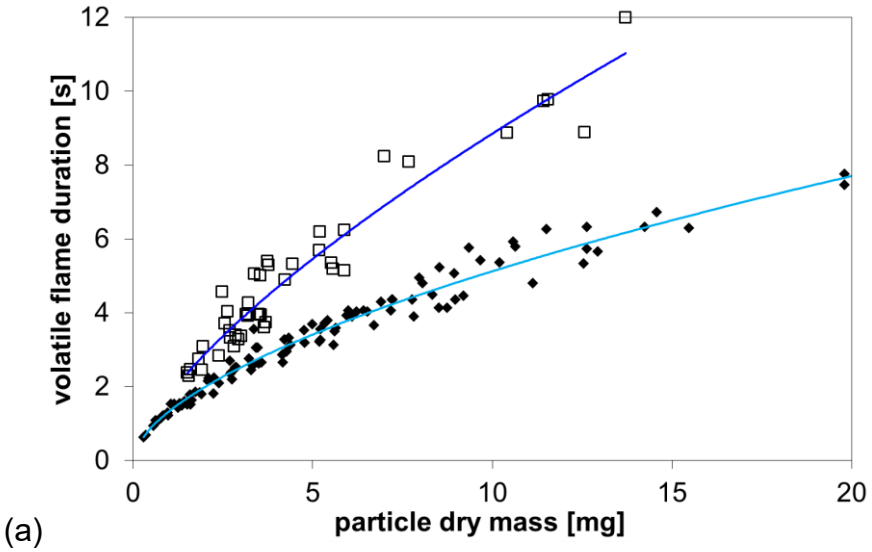

(a)

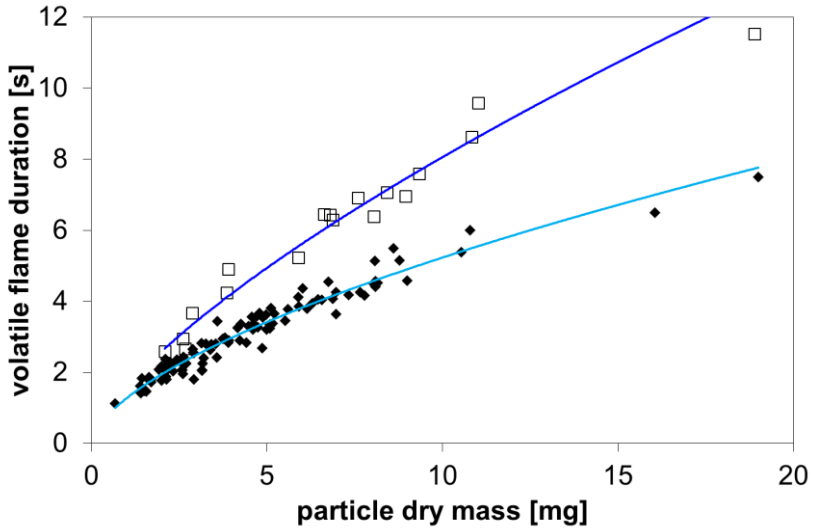

(b)

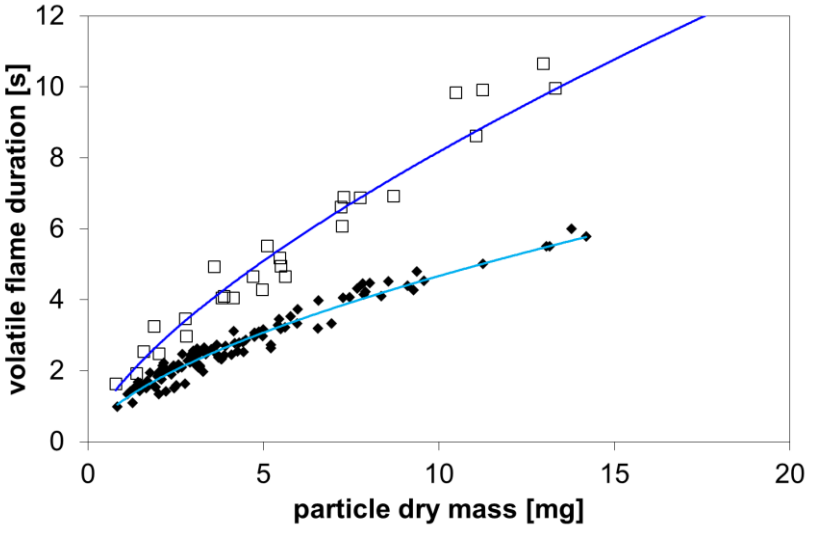

(c)

Figure 3-17 – Volatile flame duration versus dry particle mass for samples as received and with added moisture: (a) pine; (b) eucalyptus; (c) willow B

Legend: ◆ as received □ added moisture

3.3.3 Char combustion

The end of char combustion was measured in accordance with the criteria set out in the experimental methodology. Since the identification of the end of char combustion is less abrupt and not as distinct as the volatile flame identification, the data are subject to more measurement error. For smaller particles (<5mg), the burn-out could usually be identified within a range of around 30 frames (0.25 seconds). For the larger particles (>10mg), the range could be as much as 200 frames (1.7 seconds). By comparing these intervals to the average measured times for the respective particle sizes, the measurement error is therefore estimated at around +/- 5%.

The char burn duration plotted against particle dry mass for each of the fuels is presented in **Figure 3-18**. The data are less consistent than that for the volatile flame duration and this is attributed mainly to the difficulty in identifying a clear end to the char combustion. The plot of the char combustion duration times for the particles with added moisture shows a small difference compared to the as-received samples. There appears to be some variation showing longer burn times in the eucalyptus and willow but with few data points and with much noise on the timing measurement, a significant difference is difficult to infer. Similar marginal differences between raw and water-washed particles have been reported by Jones et al. (Jones et al., 2007).

The form of the best-fit function to the measured data for the char burn duration τ_{chr} is:

$$\tau_{chr} = a_{chr} {m_d}^{b_{chr}} \qquad \textbf{(3-10)}$$

Where a_{chr} and b_{chr} are empirically derived coefficients

The coefficients for the derived functions are presented in **Table 3-5**.

Table 3-5 – Regression functions for char combustion duration as a function of mass

$\tau_{chr} = a_{chr} {m_p}^{b_{chr}}$	Pine		Eucalyptus		Willow B	
	a.r.	moisture	a.r.	moisture	a.r.	moisture
a_{chr}	4.6	3.7	4.7	7.4	2.9	3.3
b_{chr}	0.70	0.84	0.75	0.59	0.78	0.86

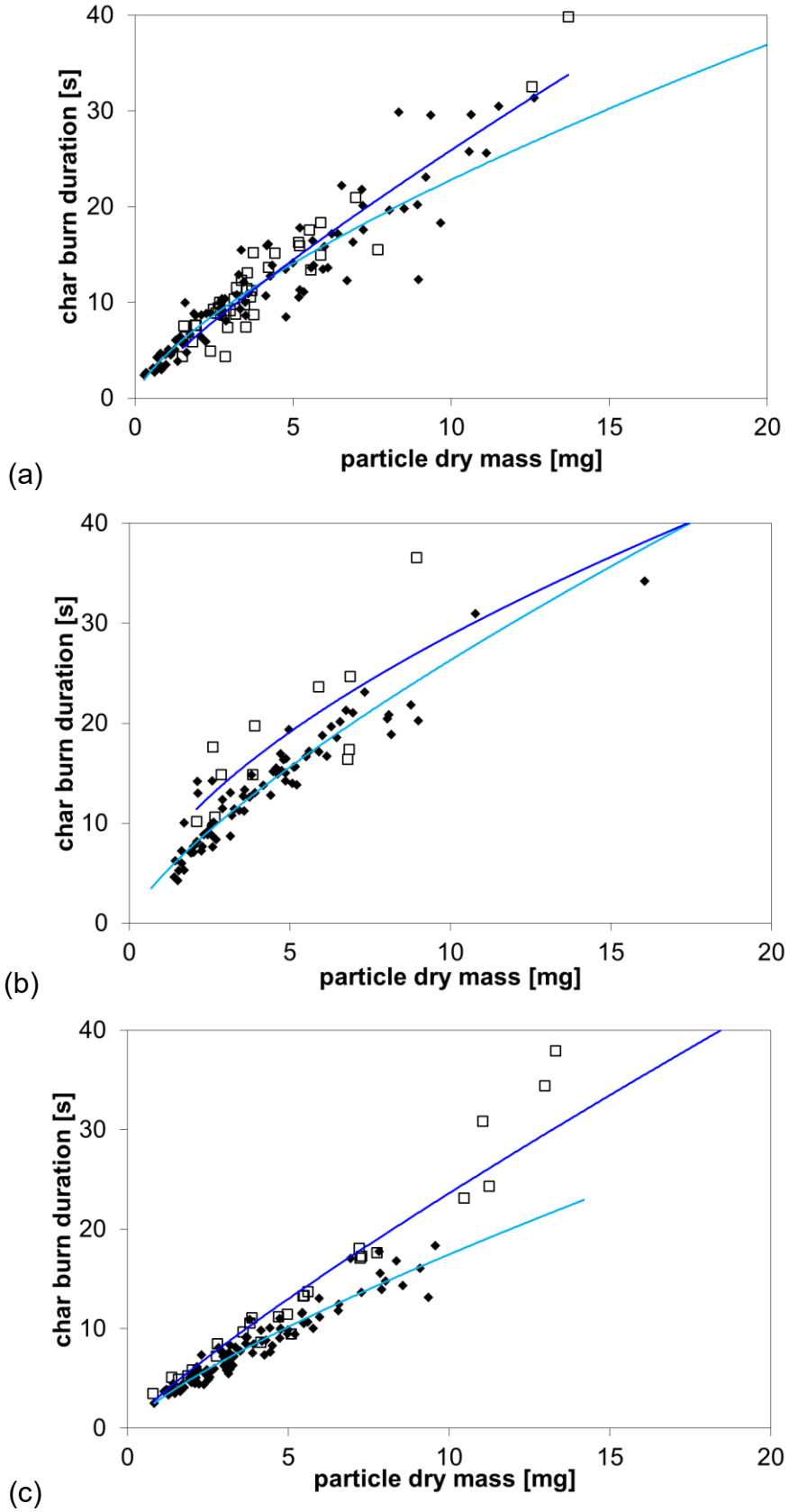

Figure 3-18 – Char burn duration versus dry particle mass for samples as received and with added moisture: (a) pine; (b) eucalyptus; (c) willow B

Legend: ◆ as received □ added moisture

3.3.4 Evaluation of burn-out time

Following the examination of the separate stages of combustion in the preceding sections, an overall picture of the combustion duration can be constructed. While the preceding data are useful for validating aspects of the modelling of single particle combustion, the combustion duration from start to finish is of direct practical value. With regard to the expected residence time in a furnace, this measure should allow the optimal particle size (or size range) to be determined with respect to an expected residence time in a furnace. The results for 13 materials are presented in **Figure 3-19** to **Figure 3-31** which show the total combustion time (■). The ignition time (●) and volatile flame duration (▲) are also plotted - showing these as a proportion of the total combustion time. The coefficients of the regression functions for the three stages of combustion and for the total burn-out time are tabulated next to the plots of the data in each case. The tables also show the coefficient of determination (R^2) for each regression. The error bands (in seconds) are evaluated from the normal distribution of the measured data with respect to the regression function.

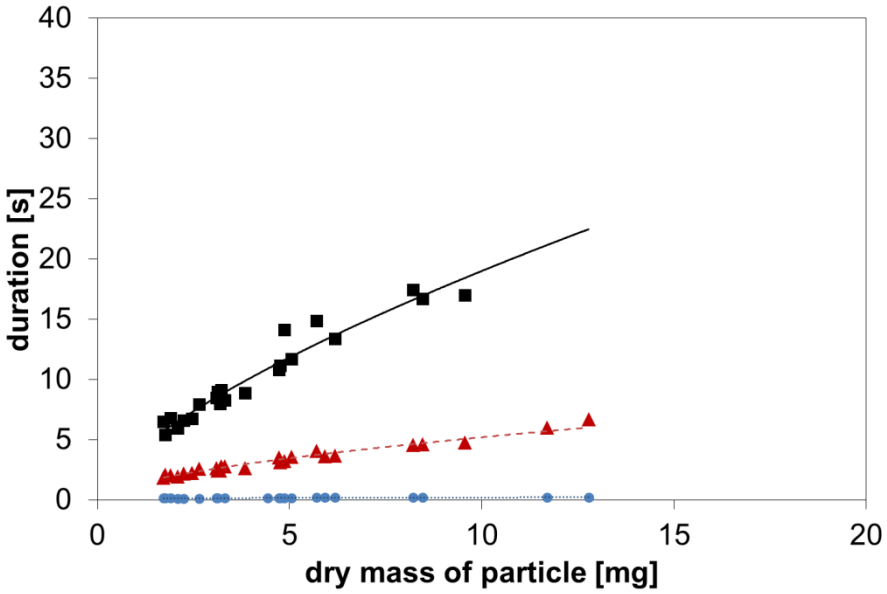

willow A	*n*	*a*	*b*	R^2	*-error[s]*	*+error[s]*
Ignition delay ●	25	0.106	0.269	0.555	0.010	0.007
Devolatilisation ▲	27	1.250	0.595	0.960	0.119	0.925
Char combustion ■	22	2.560	0.726	0.937	0.207	0.373
Burn out	22	3.953	0.672	0.958	0.348	0.297

Figure 3-19 – Measured data and regression functions for burn-out of single particles of willow A

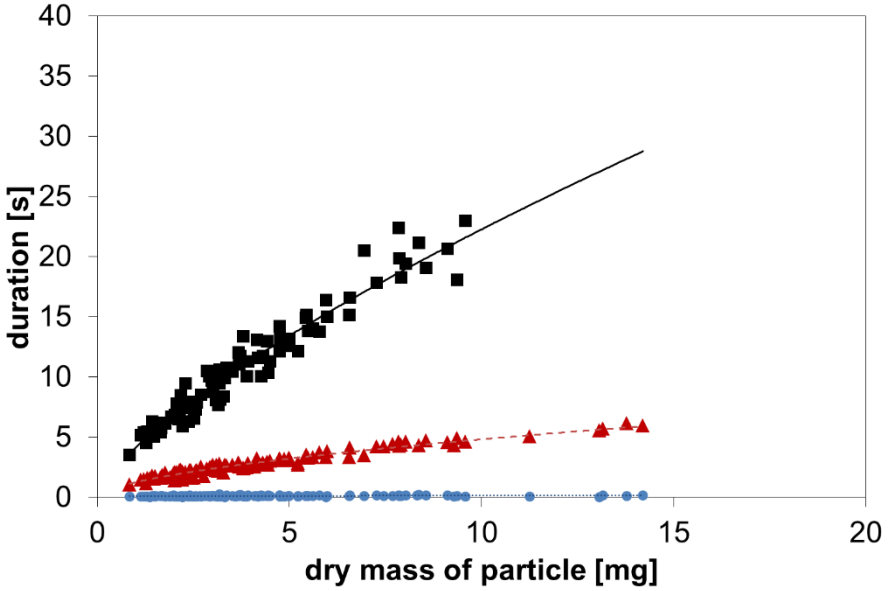

Willow B	*n*	*a*	*b*	R^2	*-error[s]*	*+error[s]*
Ignition delay ●	107	0.094	0.275	0.201	0.011	0.001
Devolatilisation ▲	105	1.187	0.597	0.948	0.048	0.032
Char combustion ■	89	2.918	0.773	0.931	0.237	0.122
Burn out	89	4.182	0.723	0.943	0.243	1.149

Figure 3-20 – Measured data and regression functions for burn-out of single particles of willow B

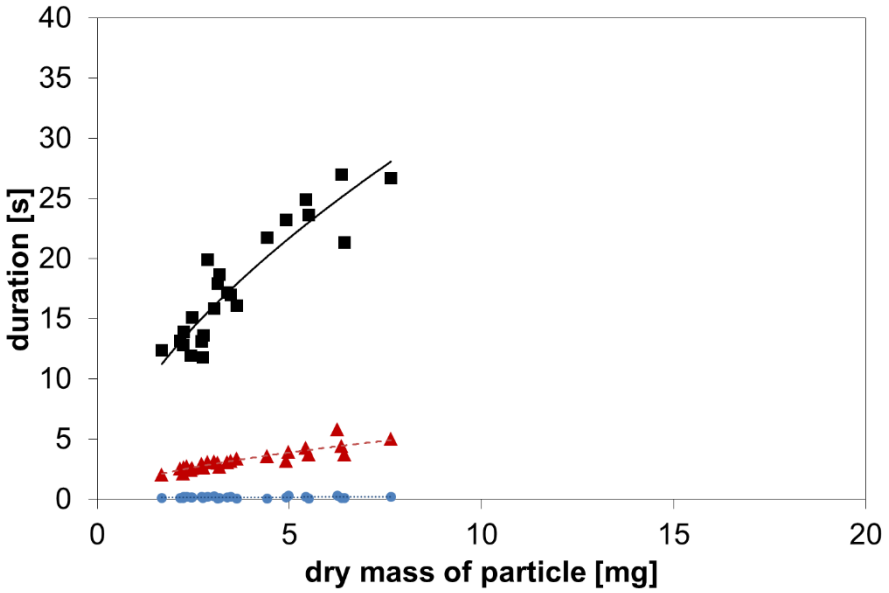

Wood pellet A	*n*	*a*	*b*	R^2	*-error[s]*	*+error[s]*
Ignition delay ●	26	0.155	0.135	0.020	0.043	0.017
Devolatilisation ▲	25	1.460	0.576	0.866	0.105	0.087
Char combustion ■	23	6.570	0.621	0.771	0.953	0.709
Burn out	23	8.228	0.604	0.821	0.940	0.753

Figure 3-21 – Measured data and regression functions for burn-out of single particles of wood pellet A

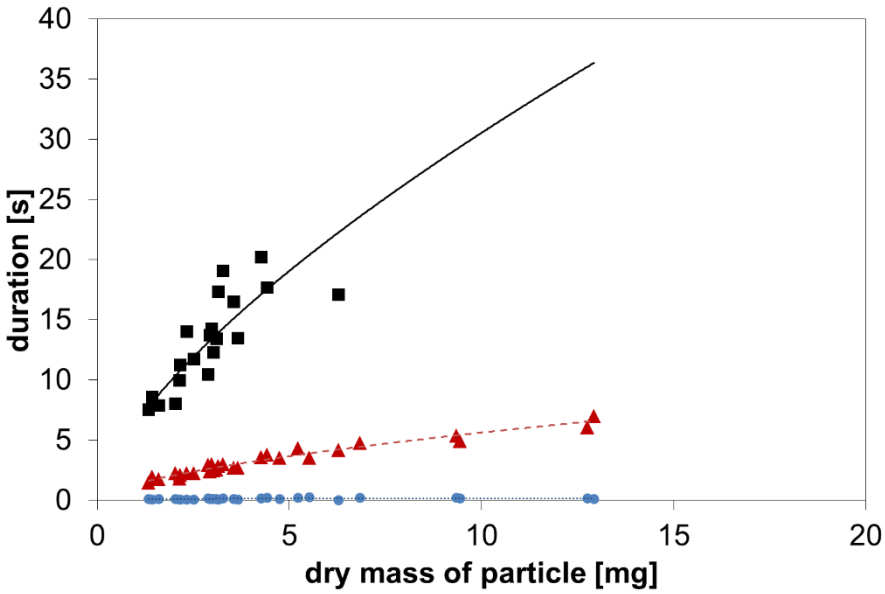

Wood pellet B	*n*	*a*	*b*	R^2	*-error[s]*	*+error[s]*
Ignition delay ●	27	0.113	0.253	0.281	0.023	0.012
Devolatilisation ▲	28	1.256	0.638	0.950	0.114	0.100
Char combustion ■	20	5.048	0.688	0.651	1.233	0.884
Burn out	20	6.398	0.679	0.742	1.213	0.943

Figure 3-22 – Measured data and regression functions for burn-out of single particles of wood pellet B

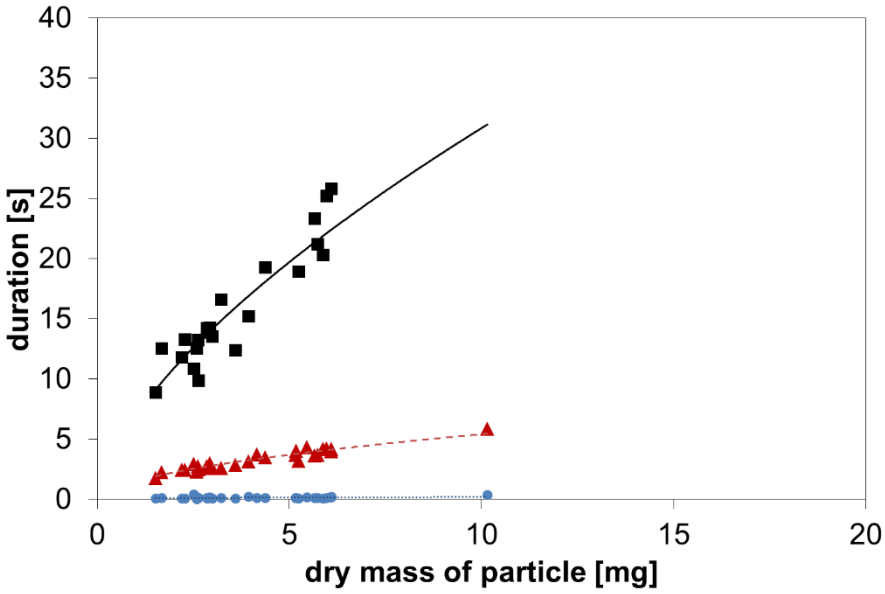

Wood pellet C	*n*	*a*	*b*	R^2	*-error[s]*	*+error[s]*
Ignition delay ●	26	0.091	0.301	0.160	0.019	0.011
Devolatilisation ▲	28	1.444	0.559	0.922	0.096	0.081
Char combustion ■	22	5.400	0.679	0.770	0.969	0.659
Burn out	22	6.981	0.646	0.822	0.960	0.700

Figure 3-23 – Measured data and regression functions for burn-out of single particles of wood pellet C

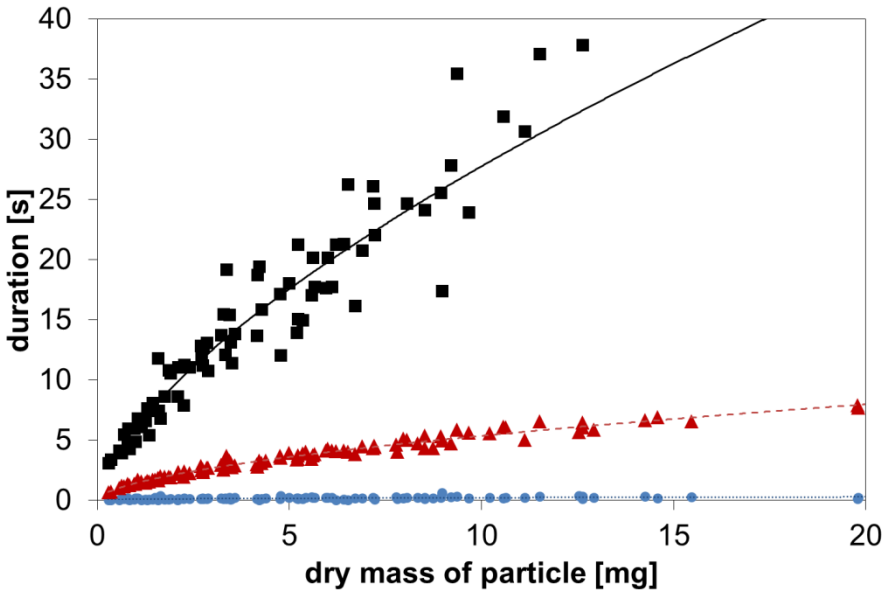

pine	*n*	*a*	*b*	R^2	*-error[s]*	*+error[s]*
Ignition delay ●	96	0.106	0.313	0.483	0.022	0.002
Devolatilisation ▲	99	1.327	0.586	0.981	0.072	0.050
Char combustion ■	78	4.610	0.688	0.918	0.717	0.258
Burn out	77	6.081	0.659	0.942	0.652	0.312

Figure 3-24 – Measured data and regression functions for burn-out of single particles of pine

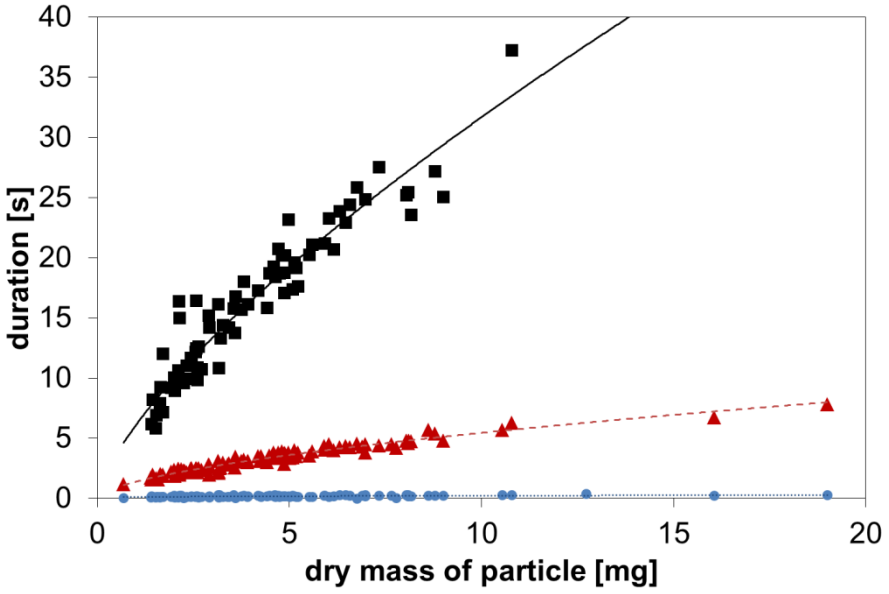

eucalyptus	*n*	*a*	*b*	R^2	*-error[s]*	*+error[s]*
Ignition delay ●	94	0.107	0.373	0.431	0.014	0.004
Devolatilisation ▲	100	1.268	0.615	0.941	0.065	0.040
Char combustion ■	73	4.656	0.752	0.872	0.416	0.351
Burn out	73	6.068	0.718	0.896	0.525	0.383

Figure 3-25 – Measured data and regression functions for burn-out of single particles of eucalyptus

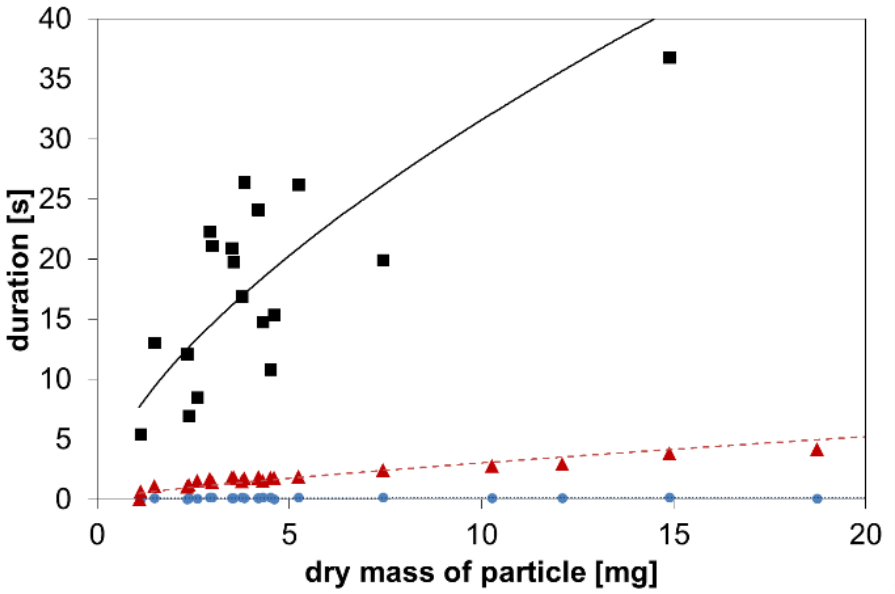

Wheat straw A	*n*	*a*	*b*	R^2	*-error[s]*	*+error[s]*
Ignition delay ●	27	0.091	0.226	0.196	0.028	0.009
Devolatilisation ▲	26	0.681	0.617	0.968	0.079	0.060
Char combustion ■	19	6.469	0.643	0.469	3.420	1.791
Burn out	19	7.286	0.637	0.514	3.375	1.908

Figure 3-26 – Measured data and regression functions for burn-out of single particles of wheat straw A

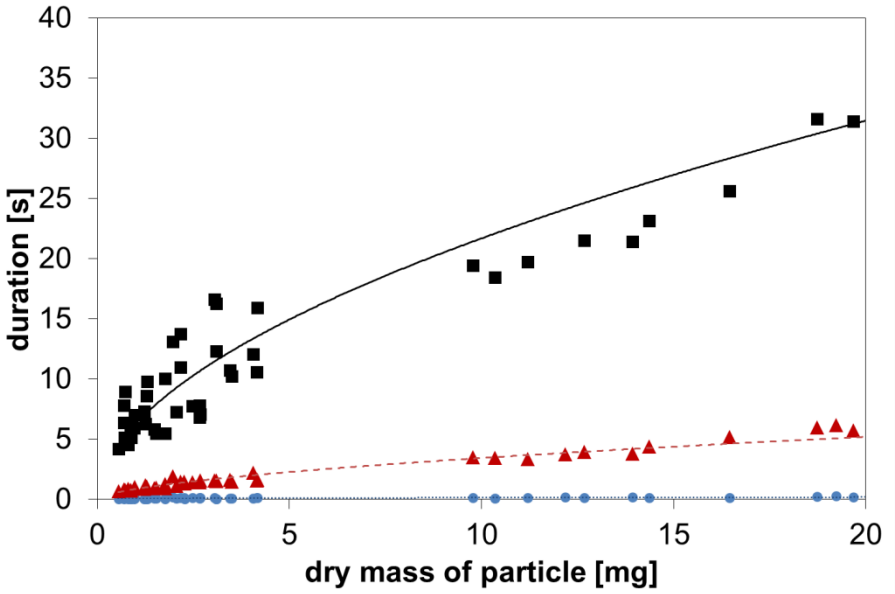

Wheat straw B	*n*	*a*	*b*	R^2	*-error[s]*	*+error[s]*
Ignition delay ●	54	0.070	0.343	0.536	0.016	0.004
Devolatilisation ▲	43	0.819	0.565	0.938	0.088	0.043
Char combustion ■	40	5.627	0.439	0.675	1.020	0.422
Burn out	40	6.536	0.456	0.741	1.014	0.460

Figure 3-27 – Measured data and regression functions for burn-out of single particles of wheat straw B

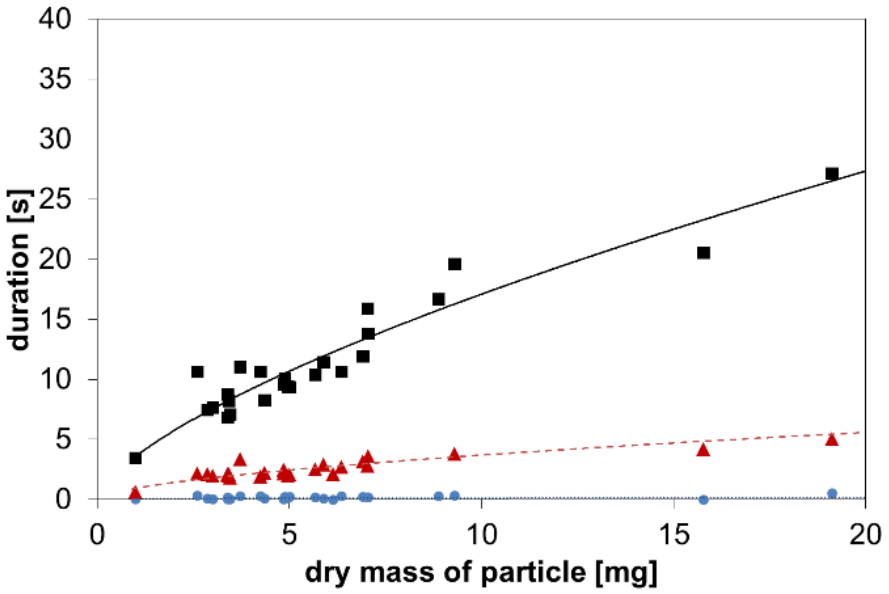

Rape straw	*n*	*a*	*b*	R^2	*-error[s]*	*+error[s]*
Ignition delay ●	16	0.166	0.213	0.154	0.053	0.033
Devolatilisation ▲	28	0.894	0.596	0.825	0.188	0.139
Char combustion ■	26	2.613	0.714	0.873	0.925	0.527
Burn out	25	3.631	0.671	0.897	0.942	0.605

Figure 3-28 – Measured data and regression functions for burn-out of single particles of rape straw

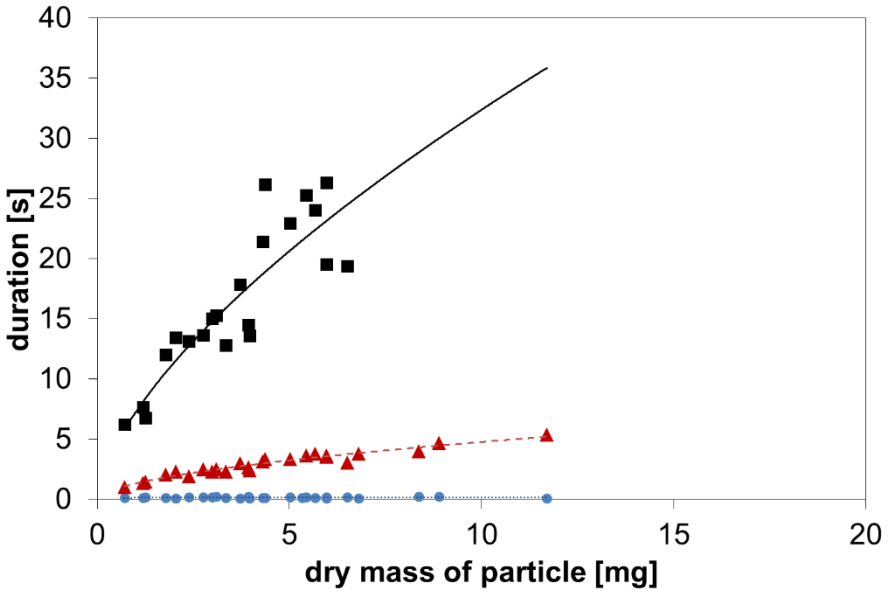

Miscanthus A	*n*	*a*	*b*	R^2	*-error[s]*	*+error[s]*
Ignition delay ●	25	0.136	0.180	0.196	0.022	0.014
Devolatilisation ▲	25	1.191	0.589	0.940	0.125	0.100
Char combustion ■	21	5.928	0.668	0.832	1.491	1.033
Burn out	21	7.262	0.649	0.854	1.565	1.131

Figure 3-29 – Measured data and regression functions for burn-out of single particles of miscanthus A

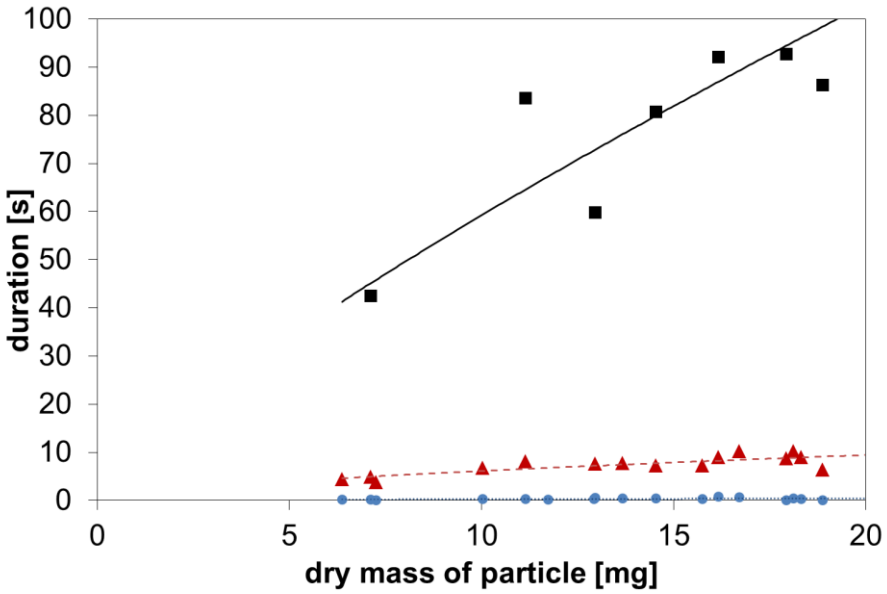

S-E wood pellet	*n*	*a*	*b*	R^2	*-error[s]*	*+error[s]*
Ignition delay ●	22	0.064	0.636	0.404	0.119	0.044
Devolatilisation ▲	20	1.379	0.625	0.936	0.516	0.417
Char combustion ■	9	7.939	0.824	0.916	7.456	6.374
Burn out	9	9.403	0.799	0.919	8.183	6.764

Figure 3-30 – Measured data and regression functions for burn-out of single particles of steam exploded wood pellet

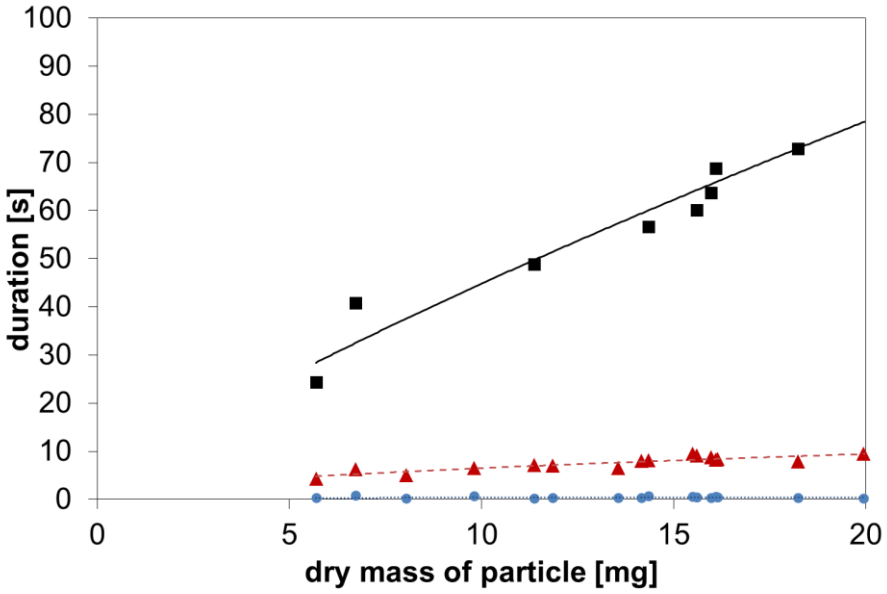

Olive residue	*n*	*a*	*b*	R^2	*-error[s]*	*+error[s]*
Ignition delay ●	32	0.150	0.373	0.271	0.082	0.035
Devolatilisation ▲	33	1.681	0.557	0.954	0.236	0.175
Char combustion ■	15	5.392	0.850	0.945	8.845	7.467
Burn out	15	6.948	0.810	0.951	8.775	7.467

Figure 3-31 – Measured data and regression functions for burn-out of single particles of olive residue

3.4 Analysis

3.4.1 Comparison of burn-out behaviour

The empirical expressions derived from the data to predict ignition delay, volatile flame duration and char burn duration are of practical use. In the design of burners and furnaces and the associated fuel milling requirements, it is important to have design criteria for the required maximum particle size. Even with a maximum particle size determined, the size distribution will vary for different fuels and different mills. The burn-out times applied to different size fractions will then be useful to determine what proportion of the fuel is likely to fully burn out in different parts of the furnace. It is unlikely that the burn-out times inside a furnace will be exactly replicated by the lab-scale experiment. Nevertheless, the experimental data can be expected to indicate the relative behaviour of different fuels. In this respect, it is useful to compare the results and derive a means of quantifying the differences.

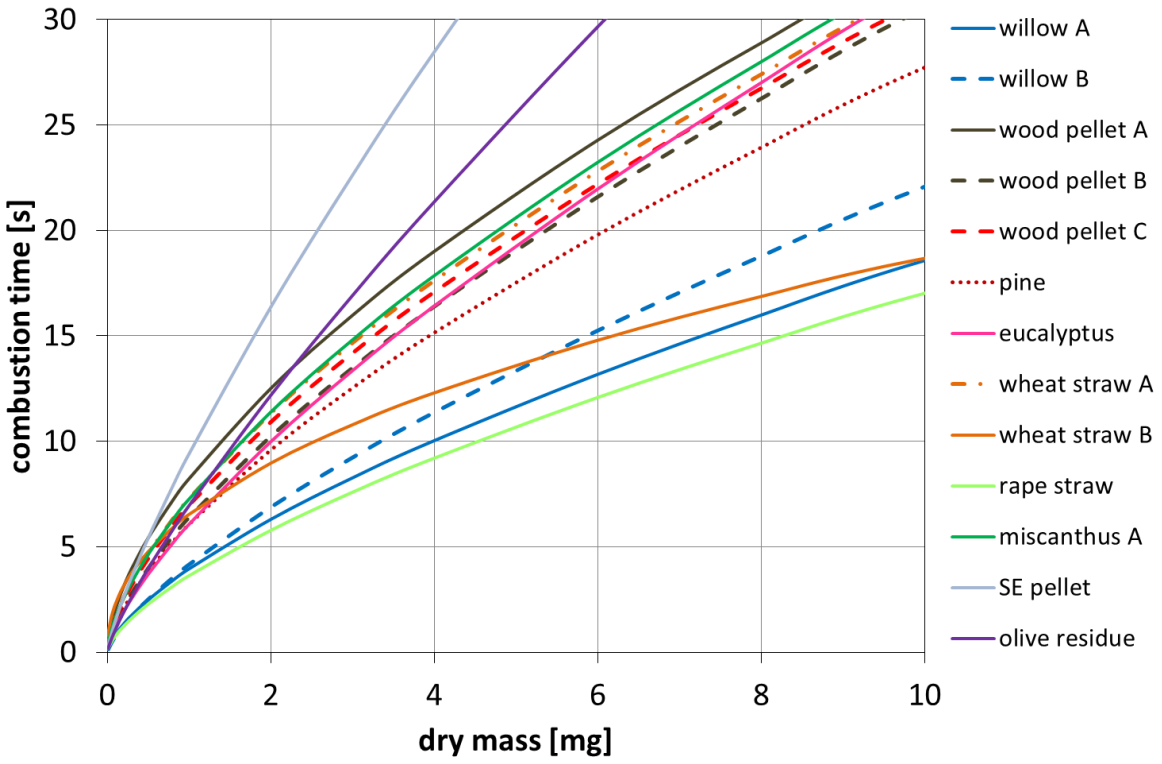

Figure 3-32 – Total burn out times with respect to particle dry mass for selected biomass fuels

Figure 3-32 presents the predicted burn-out times for each of the 13 fuels on the same plot. This illustrates how much burn-out behaviour varies with fuel type.The comparison presented in **Figure 3-32** is with respect to the dry particle mass rather than the particle size. While particle dimensions were measured in the experiment, the variation in aspect ratio, shape and density makes a direct comparison difficult. To overcome this, the analysis can be performed with reference to a 'standard' particle shape of fixed dimensions. The burn-out behaviour related to particle dry mass can then be translated to particle size by assuming a fixed density based on the measured average density. To do this, it is necessary to adopt a particle 'standard' shape that is a reasonable approximation of what is likely to occur in practical applications.

Milled particles may be considered as quasi-spherical shapes (equant) shapes. The equivalent spherical diameter in this case is:

$$D = \sqrt[3]{\frac{6.m_d}{\pi.\rho}} \qquad \textbf{(3-11)}$$

However, particles of most raw woody and herbaceous biomass passing through a mill tend to break into quasi-cylindrical (prolate) shapes. To represent a typical milled particle for these materials, a standard cylindrical shape with length equal to twice the cylinder's radius (aspect ratio = 2) is more representative (Biagini et al., 2008). In this case, the length of the equivalent cylinder is:

$$L = \sqrt[3]{\frac{16.m_d}{\pi.\rho}} \qquad \textbf{(3-12)}$$

Accordingly, in the following analysis, the woody and herbaceous materials are treated as quasi-cylindrical particles of aspect ratio of 2. In these cases, the particle's length for a given mass is given by equation (3-12). However, the olive residue and the steam exploded wood pellet both fracture into more quasi spherical particles with aspect ratio of 1 and so in these cases, equation (3-11) is applied.

Using these equivalent dimensions as an indication of the required sieve size for milled fuel, it is possible to plot, for each fuel, the relationship between particle size and burn-out time. **Figure 3-33** shows the predicted burn-out times as a function of the principal length of a particle. For comparison of indicative

burn-out times for each fuel, the principal dimension of that (modelled) particle which takes a fixed time to burn-out can be used as an index. This gives a simple indication of the relative sieve size required on the fuel mill to give the optimal particle dimensions. Since the residence time in a furnace is in the order of a few seconds, index burn out times of 2-seconds and 10-seconds are selected. These have been extracted from the model and are presented in **Table 3-6**.

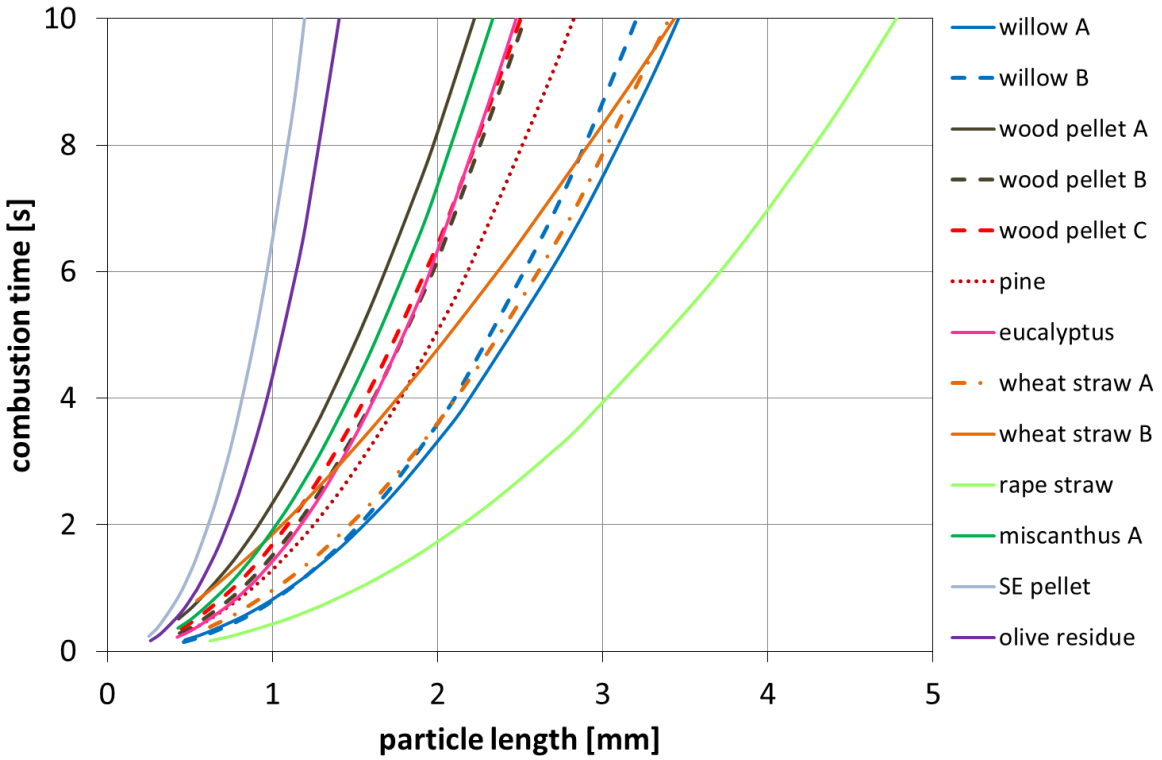

Figure 3-33 – Modelled combustion burn-out times with reference to particle size for selected solid biomass fuels.

For most of the woody biomass materials in the selection, the 2-second burn index size is around 1mm. Wheat straw and willow have faster burn-out times and therefore higher 2-second burn indices up to 1.5mm. The rape straw sample is the fastest burning of the selection with a 2-second index of 2mm. A comparison of the 10-second burn out indices show sizes of 2-2.7mm for most woody biomass, values above 3mm for willow and wheat straw and above 4mm for rape straw.

Table 3-6 – Biomass fuel particle size indices for 2 and 10-second burn-out times

Material	*2-second burn-out size index [mm]*	*10-second burn-out size index [mm]*
Willow A	1.55	3.45
Willow B	1.52	3.20
Wood pellet A	0.92	2.21
Wood pellet B	1.13	2.51
Wood pellet C	1.10	2.50
Pine	1.25	2.83
Eucalyptus	1.18	2.47
Wheat straw A	1.46	3.40
Wheat straw B	1.05	3.43
Rape straw	2.15	4.79
Miscanthus A	1.02	2.33
S-E wood pellet	0.60	1.41
Olive residue	0.73	1.20

3.4.2 Effects of particle density

The density of each particle was derived from the dry particle mass and estimated volume. The statistical spread of the measurements were evaluated using *IBM SPSS Statistics version 21*. **Table 3-7** presents the results of the analysis with the mean density value together with the 95%-confidence-level range. In all cases, the data were shown to be statistically normal by either or both the Kolmogorov-Smirnov and Shapiro-Wilk normality tests.

Table 3-7 – Density (dry basis) of single particles

Material	*Density* [kg/m^3]			
	number of samples	*lower bound*	*mean*	*upper bound*
Willow A	28	455	**490**	526
Willow B	171	508	**519**	530
Wood pellet A	28	609	**634**	659
Wood pellet B	28	570	**609**	647
Wood pellet C	28	527	**563**	598
Pine	169	472	**481**	495
Eucalyptus	133	659	**673**	687
Wheat straw A	28	180	**201**	222
Wheat straw B	56	295	**320**	345
Rape straw	31	195	**211**	228
Miscanthus A	28	598	**650**	701
S-E wood pellet	7	1144	**1200**	1257
Olive residue	7	1175	**1230**	1290

For the different materials, a comparison of burn-out times (for particles of the same mass) with respect to the average density shows that there is a correlation as illustrated in **Figure 3-34**. The relationship is such that higher density materials have longer burn-out times. This is in line with what is expected: firstly, for particles of a certain mass, higher density materials will be smaller and have a smaller surface area for heat transfer; secondly, the diffusion of air/oxygen to the char particle will be higher for less dense materials leading to faster char oxidation.

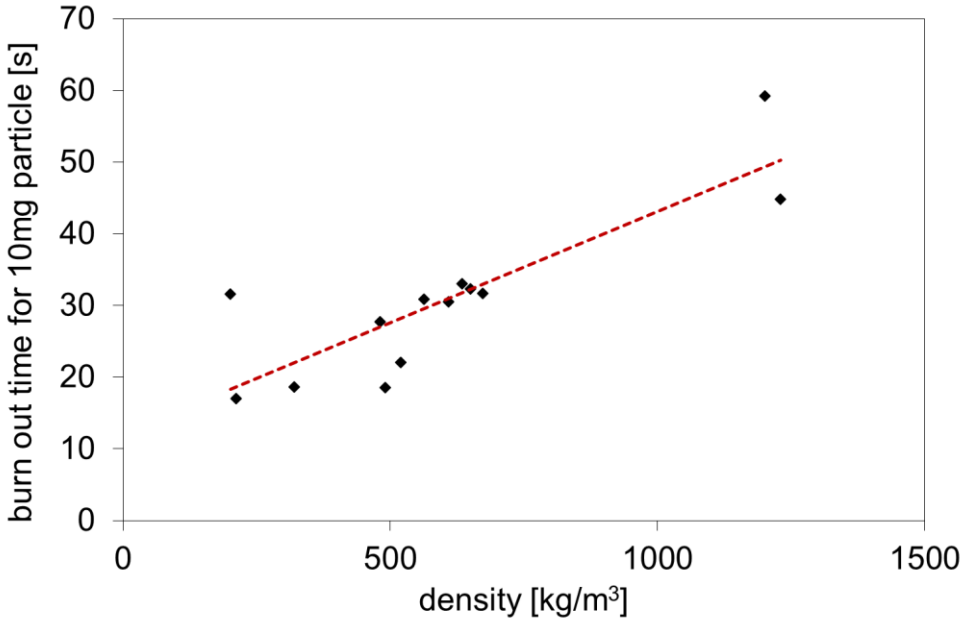

Figure 3-34 – Relationship between material density and predicted average burn-out time for a 10mg particle

A similar analysis can be performed on a single material where sufficient data are available. The data for a single material can also be analysed with respect to density by dividing the data for each material into “higher density” (ρ>mean+0.5σ), “middle density” (mean-0.5σ<ρ<mean+0.5σ) and “lower density” (ρ<mean-0.5σ) fractions. (where σ is the standard deviation of the data set).

In the case of eucalyptus, the full range variation in dry density for 133 particles was from 490 to 880 kg/m^3 with a mean of 673 kg/m^3. The data were able to be sorted so that the lower, middle and upper fractions of the density range could be plotted independently. The analysis with respect to the volatile flame duration is shown in **Figure 3-35** (a). Using the best fit regression line with the form of equation (14) for each fraction shows a discernible effect whereby the volatile burn duration is longer for higher density particles with equal mass.

A similar analysis for the char burn duration is shown in **Figure 3-35** (b). The trend is similar to that of the volatile flame data: the higher density particles have longer char burn duration.

These analyses show that there is a tendency for less dense particles to devolatilise faster and for their char combustion to be quicker. This reinforces

the observations made with respect to **Figure 3-34**. This has implications for high level modelling of pulverized fuel combustion in which it should be necessary to account for the spread of particle densities since this has a distinct effect.

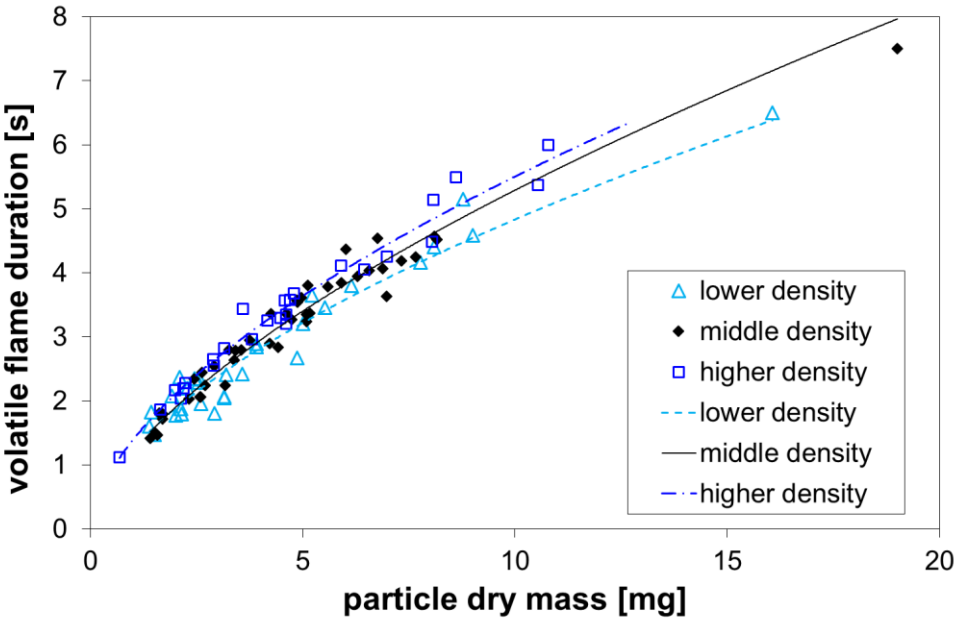

(a)

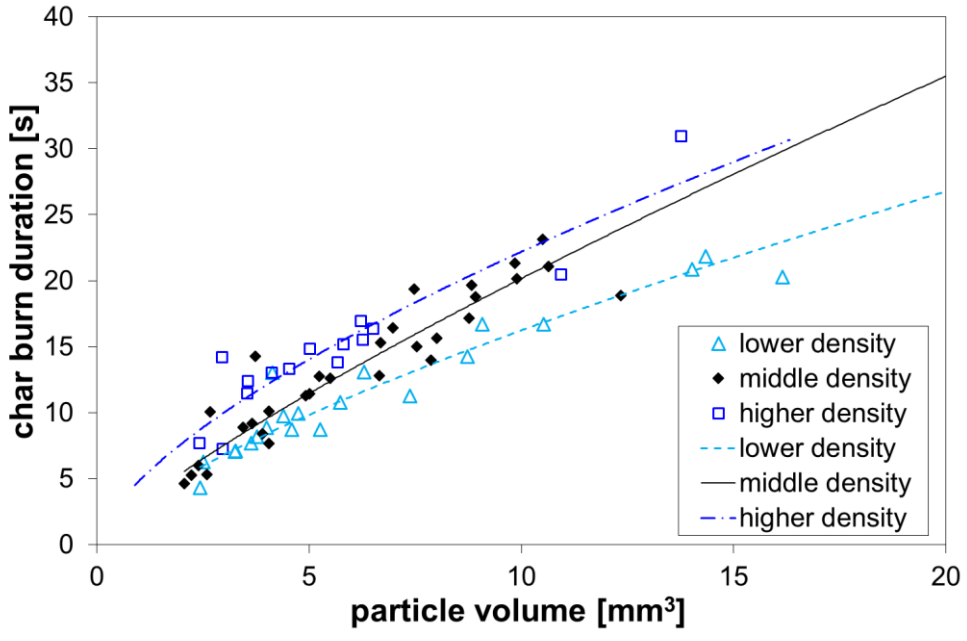

(b)

Figure 3-35 – Experimental data for eucalyptus separated into 3 density fractions for: (a) volatile flame duration versus particle dry mass; (b) char burn duration versus particle dry mass

3.4.3 Effects of Shape

Since the dimensions of each individual particle were recorded, the sample size allows some examination of the effects of shape on the volatile flame duration. The shape of a particle can be examined in a number of ways. Four shape types for convex particles can be classified using Zingg classification (Zingg, 1935). The shape types are based on the various aspect ratios of the 3-axes of the particle which are classified as: equant (ball), prolate (rod), oblate (disc) and bladed (strip). **Figure 3-36** shows a plot of the data which discriminates the four shape types. The differences are minor but trend lines show that bladed particles have a shorter characteristic duration of the volatile flame than equant.

The disparity of the dimensions of a shape, characterised by the “aspect ratio”, can also be examined. The aspect ratio of each particle can be taken to be the ratio of the largest orthogonal dimension to the shortest orthogonal dimension. While all equant shapes have an aspect ratio of less than 2, prolate, oblate and bladed particles can all have large aspect ratios. **Figure 3-37** shows a plot of the willow data which discriminates four aspect ratio ranges (<2, 2-3, 3-4 and >4). In this analysis, there is a more discernible trend in the volatile flame duration characteristic time with respect to aspect ratio such that increased aspect ratio tends towards a quicker volatile burning time. The effect is expected since the heat transfer per unit of mass is greater, and consequently the devolatilisation time shorter, for higher aspect ratio particles - as confirmed in the findings of experiments by Momeni et al. (Momeni et al., 2012) and in modelling investigations as reported by Gubba et al.(Gubba et al., 2011).

While the effect of the orientation (with respect to the gas flame) of higher aspect ratio particles was also examined, the observed differences were marginal and not significant against other measurement noise (not shown here).

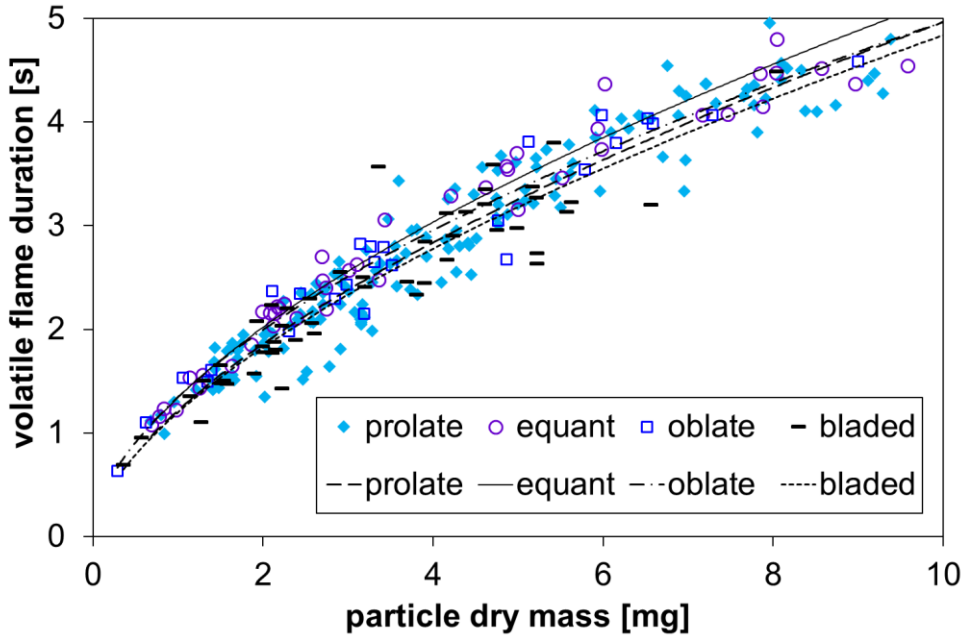

Figure 3-36 – Volatile flame duration versus particle dry mass for 4 shape types

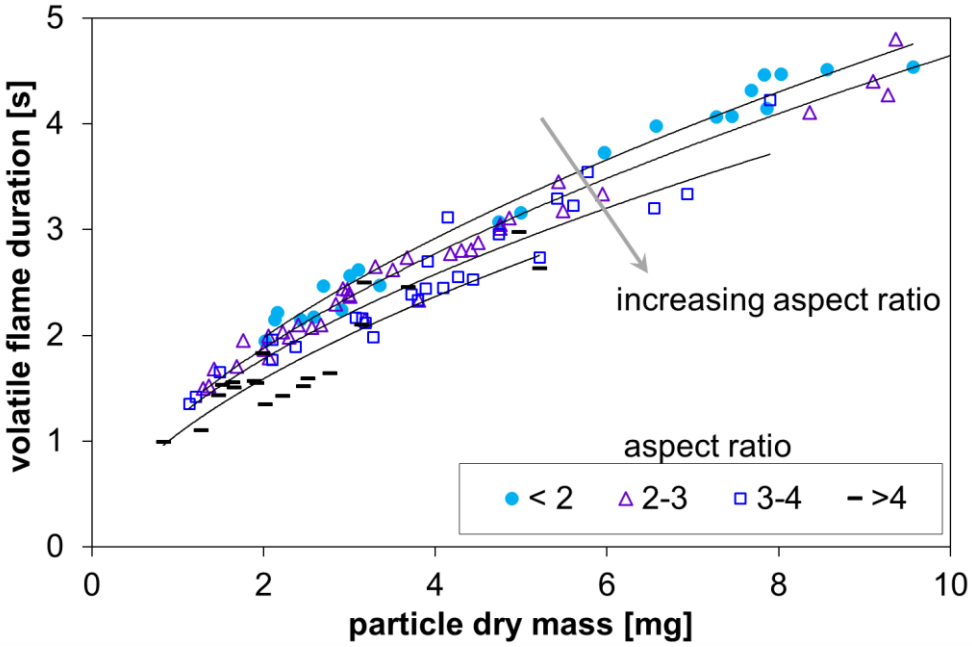

Figure 3-37 – Volatile flame duration versus particle dry mass for 4 aspect ratio ranges (willow B samples)

3.5 Conclusions

In this chapter, an experimental method for examining the duration of the different stages of combustion of single particles has been presented. This was applied to three woody biomass fuels in the first instance to produce a large data set for analysis. The volume of data allowed the evaluation of empirical expressions for the relationship between particle mass and ignition delay, volatile flame duration and char burn duration. This approach provides a means of characterising a fuel with regards to the expected ignition delay, volatile combustion duration and char burn-out times. A further set of fuel samples was characterized in this manner and the results for all 13 biomass fuel samples presented.

Further detailed analysis has provided insight into the effects of the particle density and shape on the duration of the different stages of combustion.

The means of characterizing the duration of devolatilisation and burn-out can be used to inform the modelling of combustion of pulverised biomass as well as being a means of validating existing models. Indeed, data from the experiments in this chapter are used for this purpose in Chapter 6.

By applying the measured characteristics to a standard shaped particle, an empirical “burn-out index” for the various solid biomass fuels has been derived which indicates the relative maximum size of particle required to achieve a chosen burn-out time. Refining this technique could provide a useful tool to predict burn-out behaviour for varying particle size. This would be informative to operators with regards to adjusting milling requirements to achieve optimal particle size distributions for the furnaces.

Evidence that faster particle burn-out times are related to lower density and higher aspect ratios has also been presented.

Chapter 4
Potassium release during combustion of single particles of biomass

4.1 Introduction

In this chapter, the relationships between potassium content and the patterns of its release into the gas-phase during combustion of biomass fuels are investigated. An experimental method for examining the patterns of gas-phase potassium release from a particle of biomass as it combusts is described. Thirteen fuels are examined using the method. The chapter includes a literature review, methodology, results and analysis.

4.1.1 Potassium in biomass materials

Potassium is an essential nutrient for woody plants and has important roles in: transport mechanisms for water, nutrients and energy throughout the plant; photosynthesis; enzyme activation; protein synthesis; starch synthesis and stomata function (Potash&Phosphate_Institute, 1998). It also plays a role in the physiological mechanisms for wood formation. As such, the effects of artificial fertilization with potassium on tree growth can be significant to the extent that, in certain circumstances, application can almost double growth rates in species such as Eucalyptus and Pine (Fromm, 2010). While plants therefore necessarily contain significant quantities of potassium, for the most part, it is not part of the chemical structure but is generally mobile in solution. Even though it is found in all parts of the plant, the distribution is not uniform. For instance, seeds and fruits tend to have very high concentrations of nutrients to facilitate germination so levels of potassium in materials such as olive residue tend to be high compared to wood.

The content of potassium by weight in a dry sample of untreated biomass can therefore vary considerably from species to species and also from plant to plant of the same species depending on state of growth and various environmental factors including levels of artificial fertilisation. Even wood from the same tree

can have varying levels of potassium content as illustrated by **Figure 4-1** which shows the variation in K and Ca in a radial cross-section of a tree stem.

An indicative survey of potassium content in biomass materials similar to those used in this study using the Phyllis2 online database (Phyllis2, 2013) is presented in **Figure 4-2**. It can be seen from this study that woody biomass has potassium present in quantities in the region of 1 to 3 g/kg or 0.1 to 0.3% weight (dry basis). Herbaceous energy crops and straws tend to have higher quantities above 5g/kg. There is a wider variation in the non-woody materials especially in the case of straw which is likely affected by different cultivation conditions and treatments. Olive residue has a very high potassium content (up to 3% weight) for reasons mentioned above. Levels of potassium content in this small selection of materials range from 480 to 34200 mg/kg – almost 2 orders of magnitude spread.

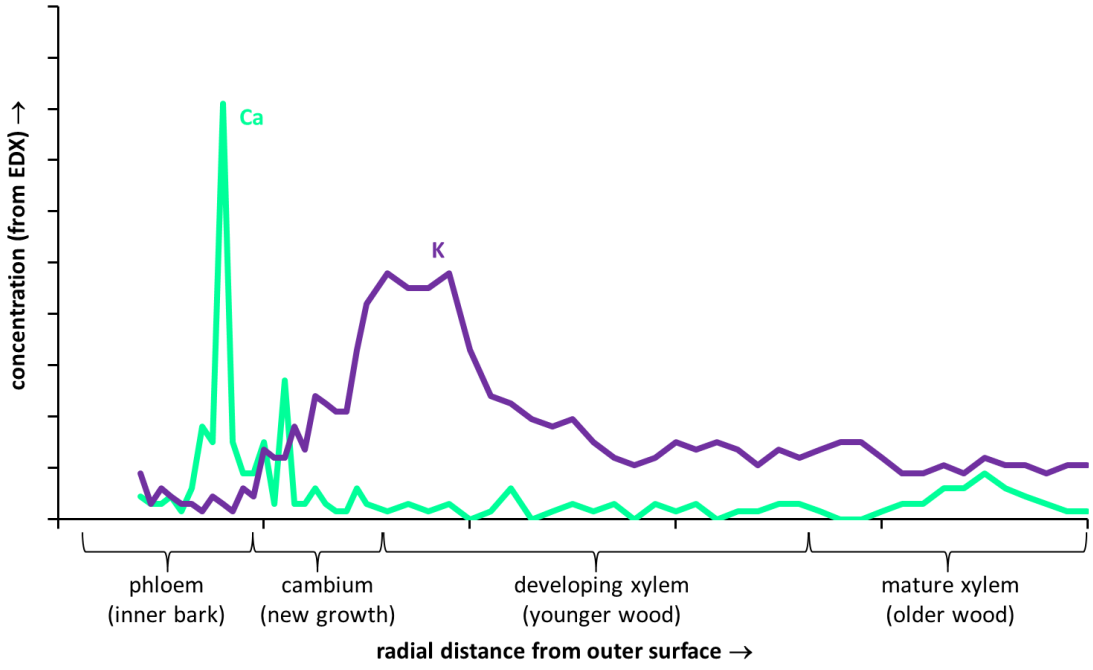

Figure 4-1 – Relative distribution of potassium and calcium in actively growing poplar wood.
Source: (Fromm, 2010)

In raw biomass materials, potassium can be present in inorganic compounds (e.g. KCl, KOH, KNO_3, K_2SO_4) and some organic compounds (e.g. $R\text{-}COO^-K^+$). The salts and organic-bound potassium can be leached from the material since

it is almost all in a water soluble form. Consequently, the majority of the potassium content can be removed from woody biomass fuels by water washing (Werkelin et al., 2010) (Saddawi et al., 2011).

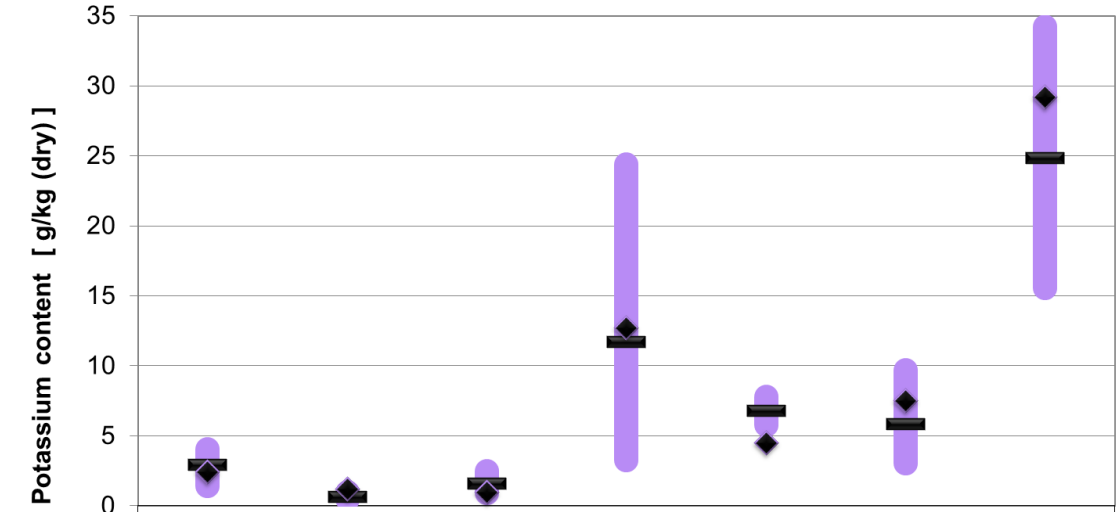

	willow	pine	eucalyptus	wheat straw	rape straw	miscanthus	olive residue
maximum	4.1	1.0	2.5	24.4	7.8	9.7	34.2
minimum	1.4	0.5	0.9	3.3	5.8	3.0	15.6
mean	2.9	0.7	1.6	11.7	6.8	5.8	24.8
measured	2.4	1.2	1.0	12.7	4.5	7.5	29.2

Figure 4-2 – Reported potassium content in various solid biomass fuels (source data: (Phyllis2, 2013)) compared with measured values for samples analysed in this study.

4.1.2 The influence of potassium on combustion reactions

Potassium and other alkali metals have been shown to have a significant catalytic effect on devolatilisation reactions and also on subsequent char oxidation (Jones et al., 2007). Nowakowski et al. (Nowakowski et al., 2007) showed that increased potassium content in willow fuel lowers the apparent first-order activation energy in pyrolysis reactions. Mechanisms for the catalytic effects of alkali metals on biomass have been proposed and applied to modelling of the reaction rates of willow undergoing pyrolysis by Saddawi et al. (Saddawi et al., 2012). Catalytic mechanisms have also been investigated by Di Blasi et al. (Di Blasi et al., 2011) and Liu et al. (Liu et al., 2008) have shown that

the effects also depend on the species of alkali salt (KCl, K_2SO_4 and KCO_3) in the biomass.

The catalytic effect of potassium on the combustion of biomass material is significant. Modelling and investigation of the thermal conversion or combustion of biomass should take into account these effects since two ostensibly identical types of wood with differing potassium content will have differing combustion behaviour. Treatment of biomass (i.e. washing) (Deng et al., 2013) may be beneficial from the perspective of improving ash deposition behaviour but it can introduce other difficulties such as extending the burn out time of certain fuels.

4.1.3 The fate of potassium in combustion

As a particle of fuel combusts, the potassium within it is either released into the gas phase or retained in the condensed-phase ash particle. Potassium released into the gas phase at temperatures above 1000K is generally as KCl(g), KOH(g) or K(g) since these species remain stable in the gas phase at such temperatures (Sorvajärvi et al., 2014). The proportions of these species are dependent on the availability of chlorine and moisture in the material (Westberg et al., 2003). The vaporized potassium species subsequently condense either directly on furnace surfaces where they can cause direct corrosion reactions, or they are recombined with other components into the solid ash which can deposit on heat exchange surfaces and cause fouling. The phase transformations and chemical reactions which take place in the combustion environment are functions of the temperatures of the gases and solids and the presence of other compounds present in the ash. Analysis of some of these aspects of gas-phase potassium partitioning in biomass combustion have been presented in recent years (Blomberg, 2011, Knudsen et al., 2004, Kim et al., 2012, Li et al., 2014, Frandsen et al., 2007, van Lith et al., 2006, van Lith et al., 2008).

Measurement of potassium release from biomass at different combustion temperatures (Knudsen et al., 2004, Kim et al., 2012) has shown relatively low levels of release to the gas phase below 1000K. The vapour pressure of KCl and KOH rises rapidly above 1000K with KOH reaching standard pressure boiling point at 1600K and KCl at 1693K (Rodrigues and Silva Fernandes, 2007, Gurvich et al., 1996). A study based on previously published data (Niu et al.,

2013, van Lith et al., 2008, Knudsen et al., 2004, Misra et al., 1993) on potassium measured in ash at differing combustion temperatures is presented in **Figure 4-3**.

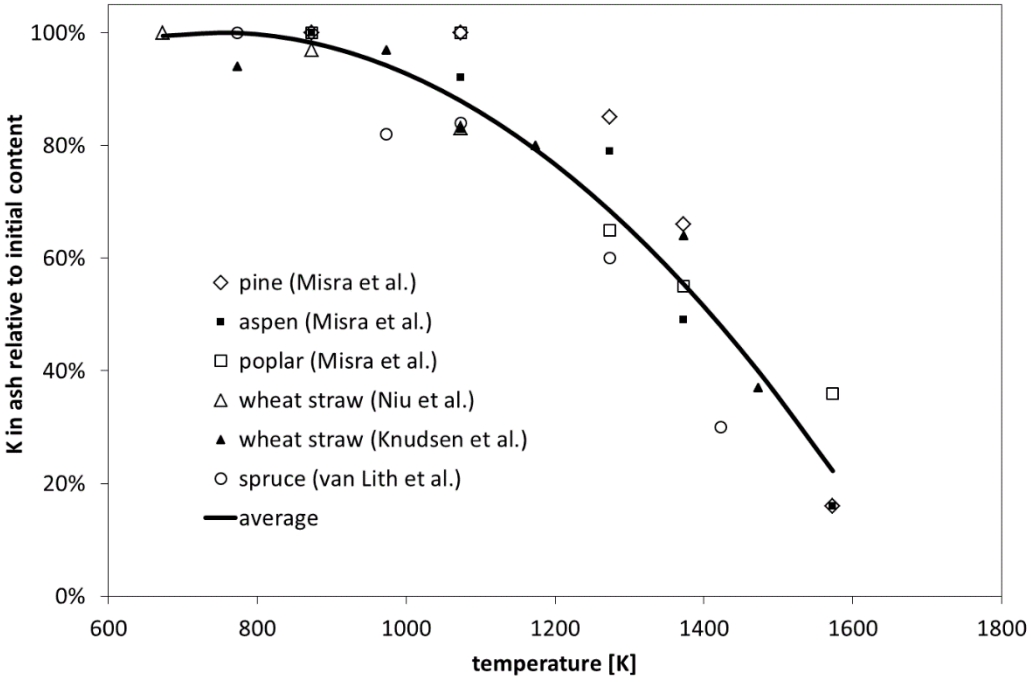

Figure 4-3 - Compilation of published data (Niu et al., 2013, van Lith et al., 2008, Knudsen et al., 2004, Misra et al., 1993) showing relationship between combustion temperature and potassium retained in ash residue

This illustrates that below temperatures of around 1000K, there is very little significant loss of potassium in the ash compared to the initial fuel content. With increasing temperatures, the proportion of potassium left in the ash can be reduced to less than 20% at around 1600K. The inference is that full combustion of particles of these biomass fuels at elevated temperatures (>1400K) is expected to result in the majority of the potassium entering the gas phase and little partitioning to the solid-phase ash. However, the fraction of potassium retained in the char and ash respectively depends on the degree of burn-out and heating of the ash particle which in turn depends on the combustion characteristics of the material and the residence time in the furnace.

Potassium not released to gas phase and remaining in the fuel particle can be retained as, for example, carbonate in the char while some potassium is also retained as metal atoms intercalated between graphitic carbon layers (van Lith

et al., 2008). As char combustion progresses, more potassium is released to gas phase as carbonates decompose and as graphitic carbon oxidizes unlocking intercalated atoms. As complete combustion is reached, potassium retained in the solid phase eventually has the opportunity to react with other solid phase inorganic components producing various forms of ash. The presence of other elements such as silicon, aluminium, calcium, iron and titanium in the fuel also affects the fate of the potassium and leads to the formation of minerals such as $K_2Fe_2O_4$, K_2TiO_3, $KAlSiO_4$ and K_2CaSiO_4 (Li et al., 2014, van Lith et al., 2008). The presence of these elements can therefore influence the retention of potassium in the ash.

Upon deposition, further transformations in the ash can occur with different thermal and oxidizing environments to form feldspars ($KAlSi_3O_8$), feldspathoids ($KAlSi_2O_6$) and micas ($KAl_2(AlSi_3O_{10})(OH)_2$) and many other mineral forms (Vassilev et al., 2013). In high temperature environments, potassium from the transformation and decomposition of ash minerals can continue to be released to gas phase.

In a furnace, the vaporized potassium species subsequently condense either directly on surfaces in cooler regions where they can cause direct corrosion reactions, or they are recombined with other components into the solid ash which can deposit on heat exchange surfaces and cause fouling. The phase transformations and chemical reactions which take place in the combustion environment are functions of the temperatures of the gases and solids and the presence of other compounds present (Westberg et al., 2003). The system is dynamic chemically, thermally and fluid mechanically so measurement of the system is challenging and modelling even more so. Despite this, detailed analysis of certain aspects of potassium partitioning in biomass combustion have been presented in recent years (Blomberg, 2011, Knudsen et al., 2004, Kim et al., 2012, Li et al., 2014, Frandsen et al., 2007, van Lith et al., 2006, van Lith et al., 2008).

The experimental work by Westberg et al. (Westberg et al., 2003) showed that in the presence of water vapor, KOH is released and is stable in the gas-phase. Where sufficient chlorine is present, potassium is also released as KCl. Once in the gas phase, these potassium species interact with the other components in

the gas including other chlorides and sulfates (Müller et al., 2006). Blomberg (Blomberg, 2011) showed that the ratio between potassium and chlorine, and their absolute concentrations affects the relative proportions of KCl versus KOH in the gas phase. The presence of sulphur in the fuel leads to SO_2 in the gas phase and the formation of K_2SO_4 which produces condensed phase aerosols. The process of gas phase sulphation of KCl in biomass combustion has been shown in experimental investigations and modelling by Li et al. (Li et al., 2013), Hindiyarti et al. (Hindiyarti et al., 2008) and by Iisa et al. (Iisa et al., 1999). At high temperatures, potassium pyrosulphate ($K_2S_2O_7$) can also form. The resulting condensed phase sulfates lead to direct deposition on furnace surfaces or agglomeration with other solid phase ash components.

Gas phase potassium will also react with phosphates, if present, to form K_3PO_4 and, with calcium, $K_2CaP_2O_7$ and $KCaPO_4$. These have relatively high melting points and so phosphates can influence how much potassium is retained in the condensed phase ash. This has been demonstrated by Li at al. (Li et al., 2015) in experiments adding ammonium phosphate to the fuel to reduce potassium release.

As combustion gases move to lower temperature parts of the furnace, KCl and KOH will also condense directly on surfaces and on ash particles (Knudsen et al., 2004, Bryers, 1996).

A simplified diagram of the routes of potassium to ash formation and deposition and the phase partitioning of potassium during the combustion process is shown in **Figure 4-4**.

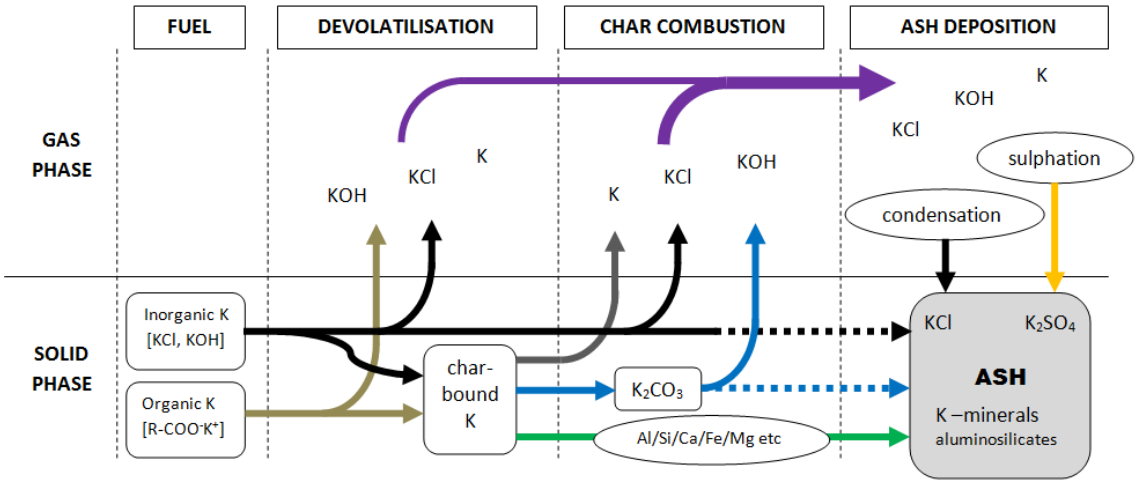

Figure 4-4 – Potassium phase and species transformations during combustion through to ash deposition

4.1.4 Methods of measuring potassium release

Measurement and quantification of the partitioning of potassium between solid and gas phases during combustion requires a means of detecting gas-phase K and a means of determining the quantity of K remaining in the solid phase.

Gas-phase detection of potassium in combustion processes is possible by various forms of spectroscopy, details of which are covered in the review by Monkhouse concerning spectroscopic detection of metal species in industrial processes (Monkhouse, 2011). Some of these methods have been employed in laboratory investigations on potassium release in biomass combustion. Molecular beam mass spectrometry (MBMS) has been used by Dayton et al. (Dayton et al., 1995)to determine mass fractions of the principal potassium species present in the flame during switchgrass combustion. This showed KCl and KOH as significant species in the gas phase with K_3PO_4 , K_2SO_4 and KCl being significant condensed phase species. Collinear photo-fragmentation atomic absorption spectroscopy (CPFAAS) uses a laser to dissociate alkali chloride molecules into dissociated atoms and a second, collinear, laser to detect the concentration of the alkali metal. This method has also been shown by Sorvajarvi et al. (Sorvajärvi et al., 2014) to be effective for detecting and discriminating potassium species (K, KOH and KCl) in flue gases. Laser induced breakdown spectroscopy (LIBS) is a method used by Hsu et al. (Hsu et al., 2011) and more recently by Zhang et al. (Zhang et al., 2015) and Fatehi et al. (Fatehi et al., 2015) to investigate the temporal release of potassium from

combusting wood. The former of these studies showed a means of quantifying the concentration of potassium in the combustion gases by calibrating with a seeded flame. The results from Zhang et al and Fatehi et al. both include a quantification of the potassium release rate and measurement of particle temperature.

Sophisticated and costly laboratory apparatus is required for the techniques as described above. However, studies on the patterns of potassium release during biomass combustion are also possible using simpler emission spectroscopy techniques. An aspect of the work presented here is to demonstrate that use of such techniques for the detection of potassium release in combustion can be effective. The method presented also allows expeditious data capture and therefore multiple experiments on a large range of fuels are practical in a short time frame.

4.2 Experimental method

4.2.1 Biomass fuel samples

The fuels used in this study and their characteristics are those as presented in Chapter 2. While the bulk fuels were supplied in various forms, it was possible to extract single particles with similar mass: 1.1mg $\pm$ 0.1mg (dry basis). For consistency, particles were trimmed to be approximately cuboid with aspect ratios of between 2 and 3. This corresponds to particles with dimensions approximately 1x1x2mm for woody materials and 1x1x3 for the herbaceous materials. Olive residue and black pellet (steam-exploded wood pellet) were fractured into quasi-spherical particles of about 1mm diameter.

4.2.2 Reference samples

A set of samples of willow impregnated with known quantities of potassium was also included in the study. This allows comparison of the other materials against a reference. The differing potassium content in the reference material can also be used to examine the relationship between potassium concentration, release rate and total potassium release. The materials were demineralized by washing in dilute acid and subsequently impregnated with known quantities of potassium. Impregnation was by addition of potassium acetate solution to

batches of particles and subsequent drying. Potassium was added to obtain samples with 0.1 , 0.25, 0.5, 0.75, 1.5% by weight. Details of the sample preparation technique as used in other investigations are described by Saddawi et al.(Saddawi et al., 2012). For consistency with the other samples, particles of 1.1 mg ±0.1 were prepared in the same manner to that described in section 4.2.1.

4.2.3 Measurement of potassium in solid phase

The potassium content was determined for duplicate samples of each biomass material using nitric acid digestion and quantitative determination by AAS in accordance with standard EN 15290:2011. The water-soluble fraction of potassium was also determined in accordance with standard EN 15105:2011. The results are presented in **Figure 4-5**. The values measured are in the same ranges for each material as in **Figure 4-2**. Nevertheless, the analysis serves to re-enforce that the variability of biomass makes predictability of potassium content uncertain even for similar feedstocks. It is notable that for all materials, the fraction of potassium extracted as soluble in water is more that 90% and in some cases up to 100%. This is consistent with the findings reported in a recent review by Gudka et al.(Gudka et al., 2015)

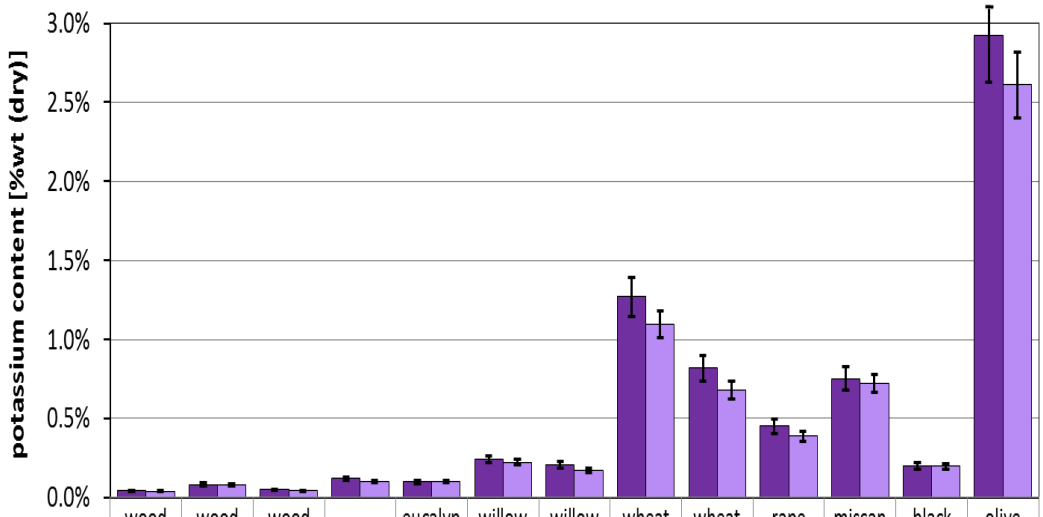

	wood pellet A	wood pellet B	wood pellet C	pine	eucalyptus	willow A	willow B	wheat straw A	wheat straw B	rape straw	miscanthus A	black pellet	olive residue
total potassium	0.04%	0.08%	0.05%	0.12%	0.10%	0.24%	0.21%	1.27%	0.82%	0.45%	0.75%	0.20%	2.92%
water soluble	0.04%	0.08%	0.04%	0.10%	0.10%	0.22%	0.17%	1.10%	0.68%	0.39%	0.72%	0.20%	2.61%

Figure 4-5 – Potassium content of selected solid biomass fuels [total potassium extracted by acid digestion and potassium extracted by water]

4.2.4 Detection of potassium in gas-phase

The combustion behavior of biomass fuels can be examined by studying the combustion of individual single particles exposed to a methane flame. This is done using the same experimental method as described in Chapter 3 in which the demarcation between different stages of combustion (ignition delay, volatile flame combustion and char combustion) was established by use of high speed video recording. In this investigation, the method is complemented by a photo-detector for indicating the relative potassium content in the flame above the combusting particle.

The intensity of the spectral emission of potassium is determined by the proportion of atoms in the excited state which is a function of temperature. In this experiment, the flame temperature above the combusting particle is assumed to be at a steady temperature for the duration of the observation. The intensity of spectral emission is therefore taken to be proportional to the concentration of volatilized potassium in the flame. Flame temperatures of 1600K-1800K are sufficient to excite the gas phase potassium for obtaining a strong spectral emission. The experimental technique is practically limited by this and by the achievable gas flame temperature making it suitable for investigations in the 1600-1800K range. In observing the spectral emissions external to the flame, self-absorption internally in the flame should be considered. This is the phenomenon of one potassium atom absorbing the emission from another atom within the flame. At high concentrations of potassium and in flames with a deep cross-section, self-absorption introduces a nonlinearity to the relationship between concentration and observed emission intensity (Gaydon and Wolfhard, 1970). In these single particle combustion experiments, the concentration of potassium in the flame is low and the observed surface of the flame is large with respect to the cross-section. Any non-linearity is therefore assumed to be small, if not negligible and no adjustment to account for self-absorption has been applied.

A monochromator or an optical band-pass filter can be used to select a signature wavelength from the emitted radiation, the intensity of which can be observed with a photo-detection device. Potassium has a strong spectral emission (doublet) line close to 766nm. In this experiment, a ‘traditional-coated’

(Edmund Optics Techspec®) band-pass interference filter with center wavelength of 766nm and a bandwidth of 10nm was selected. It is important to be aware that, in addition to the potassium emission, there will be a continuous black-body radiation spectrum emitted from any solid phase component of the flame (i.e. soot). It is therefore necessary to measure the intensity of radiation from the flame at a wavelength window close to, but avoiding, 766nm. For this purpose, a second photo-detection device was operated in parallel using a similar type of bandpass interference filter with centre wavelength of 750nm and a bandwidth of 10nm.

The measurement technique does not discriminate potassium species so it is not possible to determine the relative quantities of gas phase KCl and KOH. Both species are volatile in the temperature range of the flame (1600-1800K). Differences in release rates between the two species are not expected to be distinguishable. The measurement and analysis then refers to gas-phase potassium release without qualification of the speciation.

Similar experiments (Jones et al., 2007) have used photomultiplier electron tubes for photo-detection. For this experiment, a solid state photo-detector was purpose designed. The photo-detector device used is a photo-diode (Vishay BPW34) with a linear response to photo-intensity and a relative sensitivity of over 0.8 (of maximum) at 766nm wavelength. A precision op-amp connected to convert the current through the photodiode to a 0-5 volt output signal was designed and built with support from Convertor Technology Ltd. The electronics were mounted in a light sealed enclosure with an aperture for an optical filter and a lens to focus the incoming light onto the photodiode. The output voltage signal was recorded at 1kHz using National Instruments USB-6000 interface and LabView data acquisition software. The photodetector device measurement precision is estimated to be <1%. **Figure 4-6** shows a schematic representation of the principle components of the apparatus. The electronic circuit for the photodetector is presented in **Figure 4-7** and the completed assembly (without lid) is shown in **Figure 4-8**.

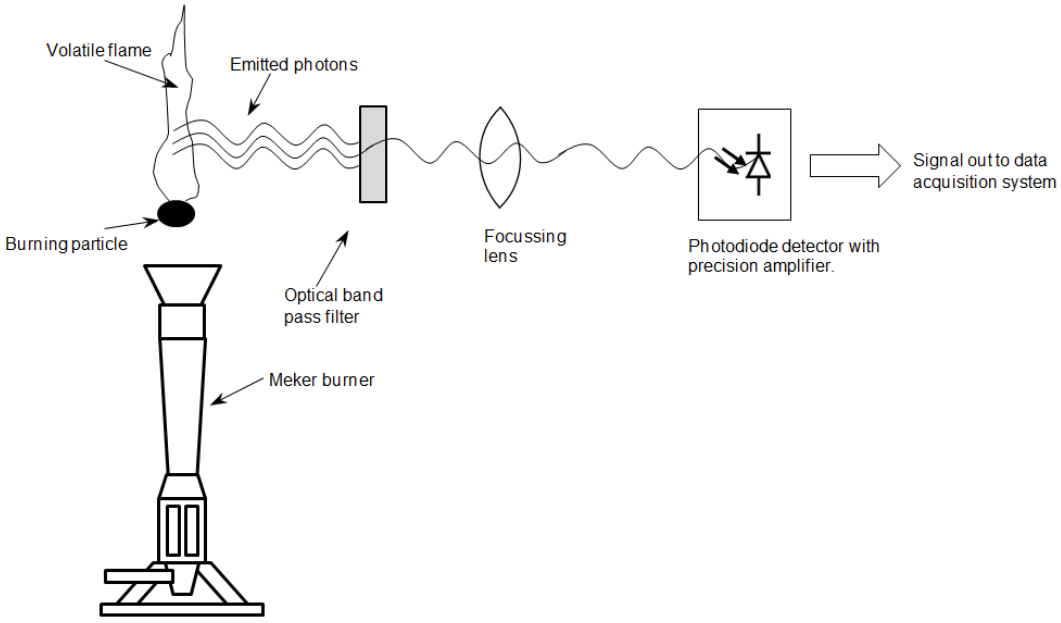

Figure 4-6 – Schematic representation of the photo detector apparatus

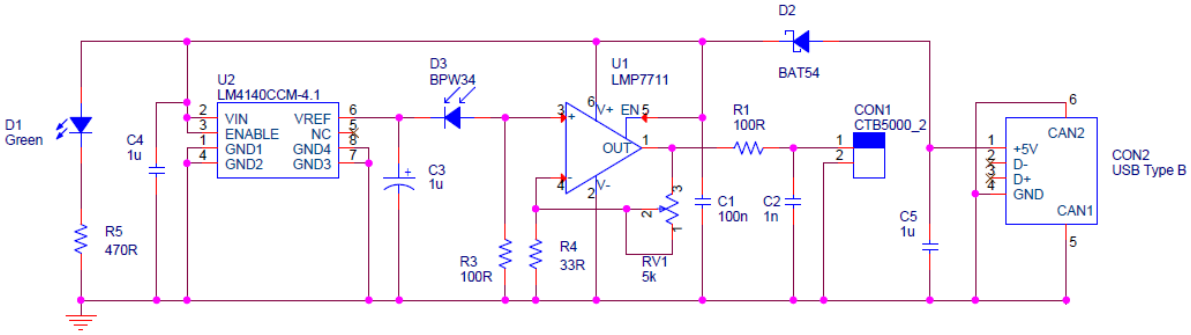

Figure 4-7 – Circuit diagram for photodiode amplifier circuit

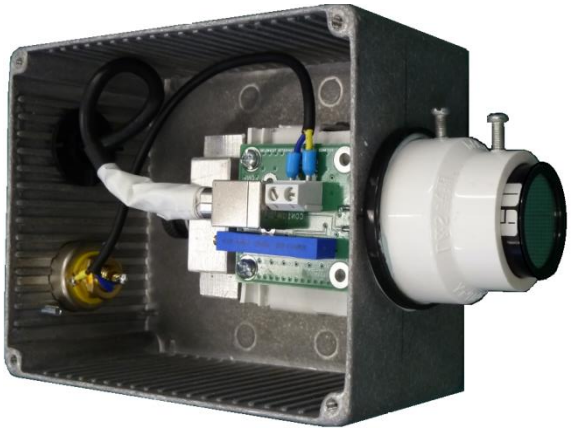

Figure 4-8 – Photo-detector apparatus

4.2.5 Form of recorded data

The two photodetector signals were written to data (text) files in real time using the LabView data acquisition application. **Figure 4-9** shows a screen shot of the application during acquisition of data from a single burning particle. The data obtained from the photo-detectors was subsequently processed to subtract the 750nm signal from the 766nm signal and to remove noise from flame flicker (by smoothing the signal over 10 data points). An example of the output and derived signal is presented in **Figure 4-10**. The various stages of combustion are identified in the profile based on the visual examination of the combusting particle as described in Chapter 3. The labelling describes the dominant process at each stage. The end of char combustion is a useful reference point but it should be noted that the demarcation does not imply any sudden transition from char to ash but simply the point at which char combustion has effectively completed.

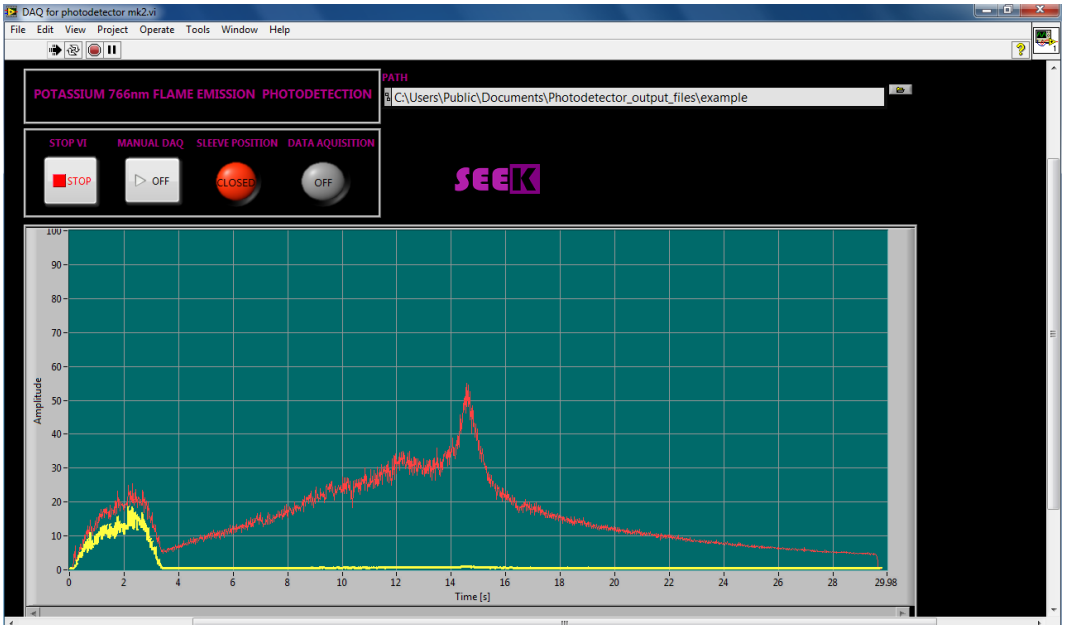

Figure 4-9 – Screen shot of front panel of LabVIEW data acquisition application

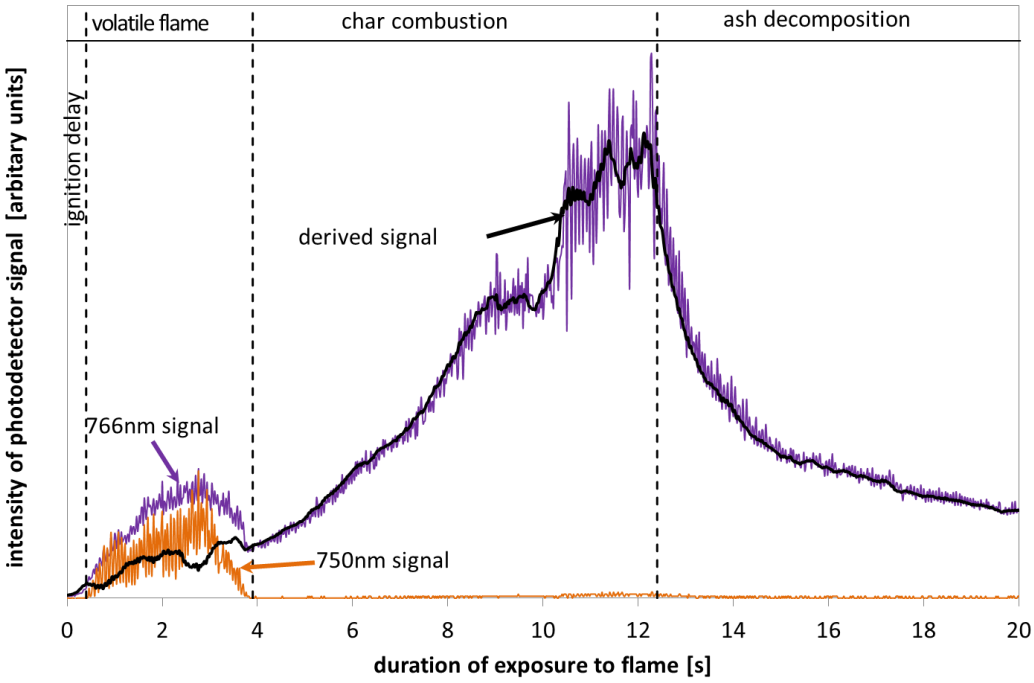

Figure 4-10 – Recorded output of photo-detectors from the combustion of a 10mg willow particle indicating dominant processes at different stages

There is a short ignition delay from the initial withdrawal of the water-cooled sleeve to the signal(s) initial rise. Following this, the volatile flame produces a distinct signature from both the 766nm and 750nm detectors. At the end of the volatile flame, the 750nm signal falls to zero (since thereafter there is no black-body radiation from soot). The derived signal in this period shows a low level of potassium release compared with the subsequent period. Nevertheless, there is an increased release rate noticeable above the underlying trend which may be attributed to entrainment of potassium in the volatilized gases. This is more accentuated in some fuels while virtually absent in others. The char combustion stage is characterized by an approximately steady increase in the release rate which appears to peak just before the char burn-out is complete. Thereafter, the remaining material being heated in the methane flame is mostly ash. The potassium release profile at this stage is, in most cases, an exponential decay as any remaining potassium available for volatilization is released. The shape of this part of the profile is influenced by the proportion of ash content.

Since there is noise in the recorded signals and variations from one particle to the next, in order to produce a more representative “typical” profile for each

material the data from multiple experiments should be taken and a mean average derived. In all cases, data from between 3 and 6 samples were obtained. This approach is used for the materials presented in the following sections. The mean difference between the measured data and the averaged signal varied for different materials ranging up to ± 8% owing to variability in the samples – only the averaged signal is shown on **Figure 4-11** through to **Figure 4-14**.

4.3 Results

4.3.1 Profiles of potassium release from reference samples

A series of experiments were performed using the reference materials with five different levels of potassium content (0.1, 0.25, 0.5, 0.75 and 1.5% by dry weight). Although not fully quantitative, the data from the reference can provide a baseline for comparison with the fuels being examined. To determine a typical release profile for each concentration level, the data from at least 3 particles were obtained and a mean of the measured signal was derived. The results of this are presented in **Figure 4-11**. The data were analysed to determine the magnitude of total observed potassium release (area under each profile curve), peak release rate (maximum point on each profile curve) and duration of the combustion (burn-out time). The correlation between potassium content and the potassium released to the gas phase is clear enough from a superficial examination. This is examined in more detail in the following discussion and the correlation is used to normalize the photo-detector signal to an estimated release rate. The peak release rate and potassium content also have an apparent positive correlation and it is noted that the burn-out time is extended for samples with a lower potassium content. Similar relationships should be expected for the fuel samples and these aspects are examined later in the analysis.

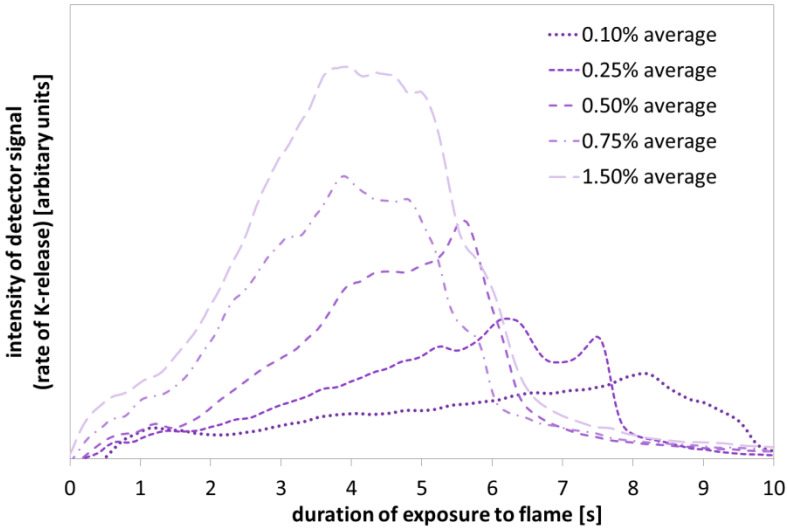

Figure 4-11 – Comparative potassium release profiles (average of at least 3 samples) for 1.1mg willow particles impregnated with potassium at 0.1, 0.25, 0.5, 0.75 and 1.5%

4.3.2 Profiles of potassium release from biomass fuel samples

4.3.2.1 Woody biomass materials

The woody biomass materials (wood pellets, pine, eucalyptus and willow) all have a potassium content measured to be less than 0.4% by weight. The potassium release profiles for all the woody materials are shown in **Figure 4-12**a-c in which some notable similarities and differences are observable. In most cases, the volatile combustion stage is discernible by a minor peak or shoulder in the potassium release rate. The general shapes of the release patterns are similar. For similar materials (especially for the wood pellets) there is a strong resemblance in the release curves with a steady increase in release rate during char combustion up to a peak which is coincident with the ending of char burn-out. The materials with lowest potassium content and lower ash content show a more rapid decrease in release rate after char burn-out (just after the peak of the curve). This implies that the potassium content is “exhausted” during the char combustion process.

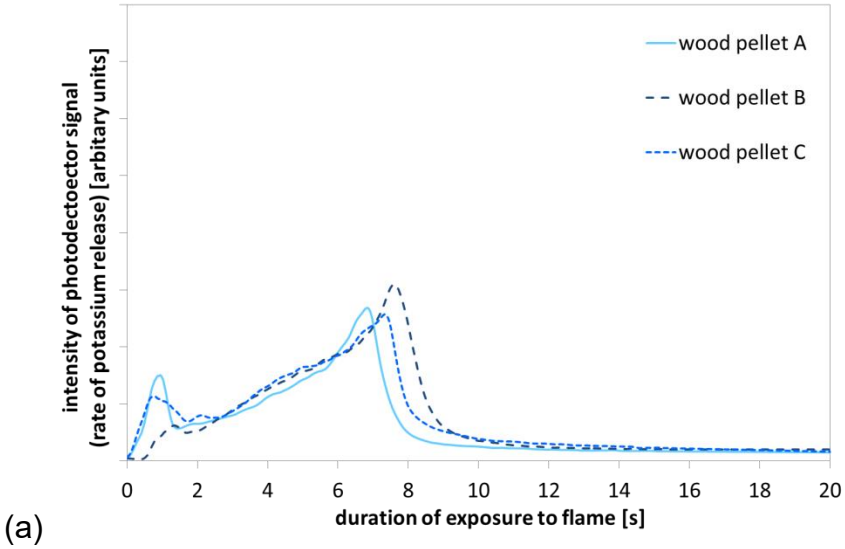

(a)

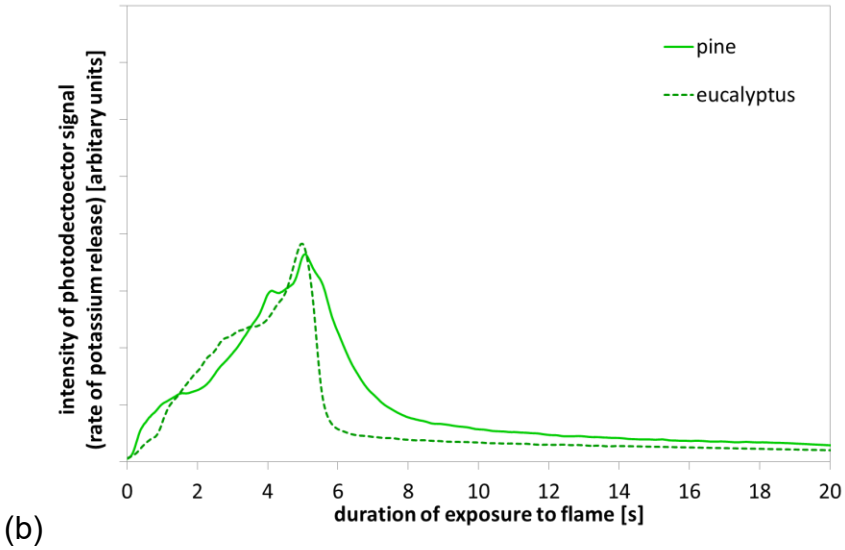

(b)

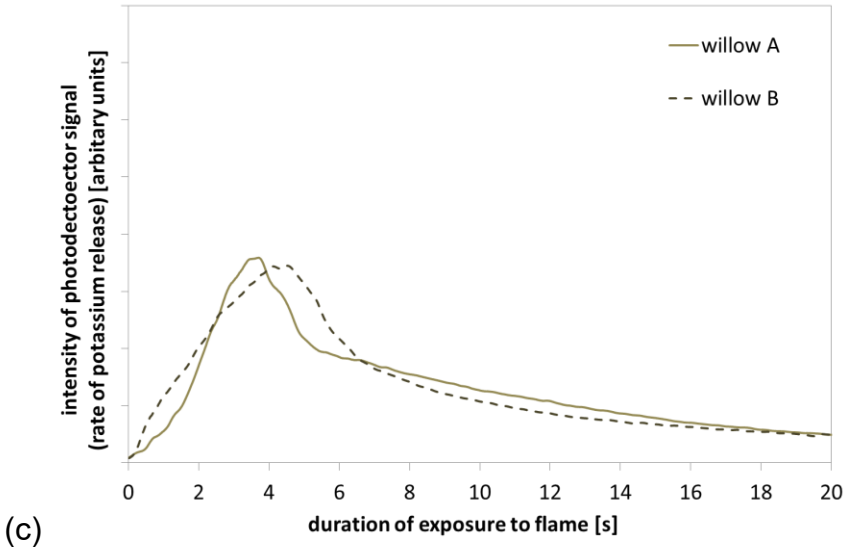

(c)

Figure 4-12 – Potassium release profiles for 1.1mg single particles of various woody materials: (a) wood pellets; (b) pine and eucalyptus; (c) willow.

(same scale on y-axes)

4.3.2.2 Herbaceous biomass materials

The herbaceous biomass materials (wheat straw, rape straw and miscanthus) all have potassium contents measured to be more than 0.4% but less than 1.5% by weight. The potassium release profiles for all the herbaceous materials are shown together in **Figure 4-13**a-b. The plot is on the same scale as Figure 4-12 and it is immediately clear that the quantity of potassium released from these materials is greater than for any of the woody materials. From the moment of first exposure to the flame, the rate of potassium release increases much more rapidly than for the woody materials. The rate is so steep that the volatile combustion stage which is discernible in the woody biomass is not easily distinguishable. It is notable that all these materials have a more extended release of potassium after char burn-out than woody materials. This implies a significantly larger quantity of potassium remaining in the ash after the char combustion stage. This may be through the formation of a different mineral form which is itself vapourised or transformed in the ash decomposition stage. Two distinct combustion profiles were observed for wheat straw A and miscanthus A: denoted by suffix A(1) and A(2). There did not appear to be an intermediate mode of potassium release for the particles observed. The profiles with lower release rates - wheat straw A(2) and miscanthus A(2) - reach a certain release rate and then level off to become coincident with the release rate of the ash from those particles with higher release rates. There may be a number of reasons for this. It is possible that there is uneven distribution of potassium and possibly different K-species in the straw even though all particles were prepared from a similar part of the stem of the respective plants. Another possibility is the presence of other inorganic species (e.g. SiO_2) in the samples which form minerals that tend to retain potassium in the ash.

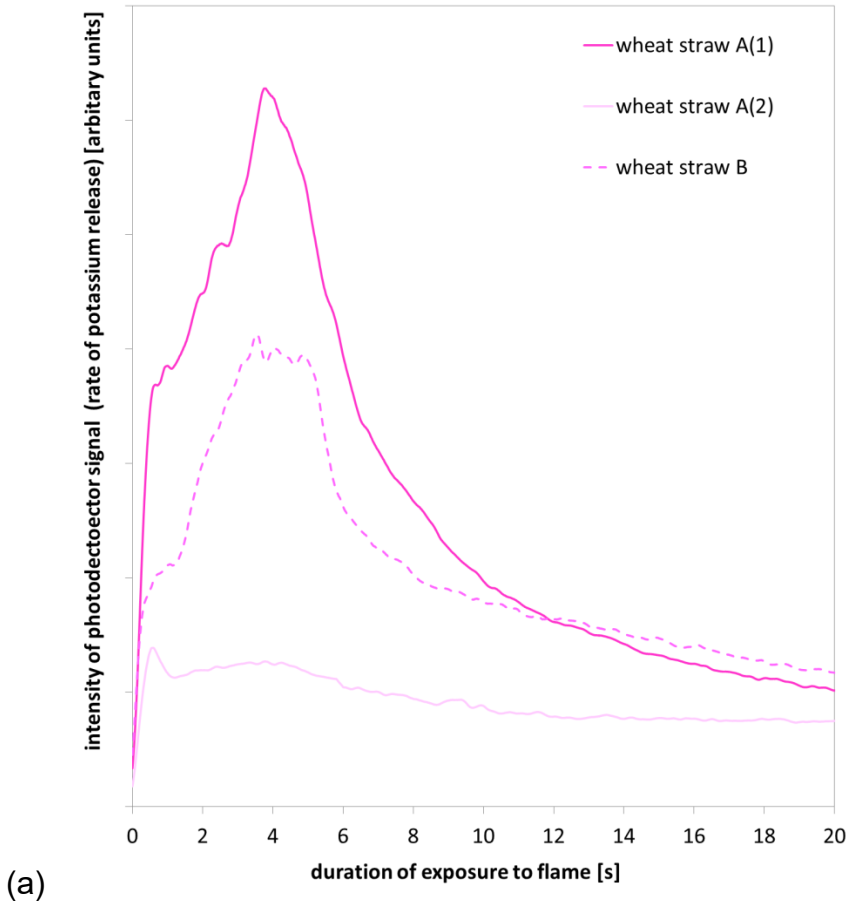

(a)

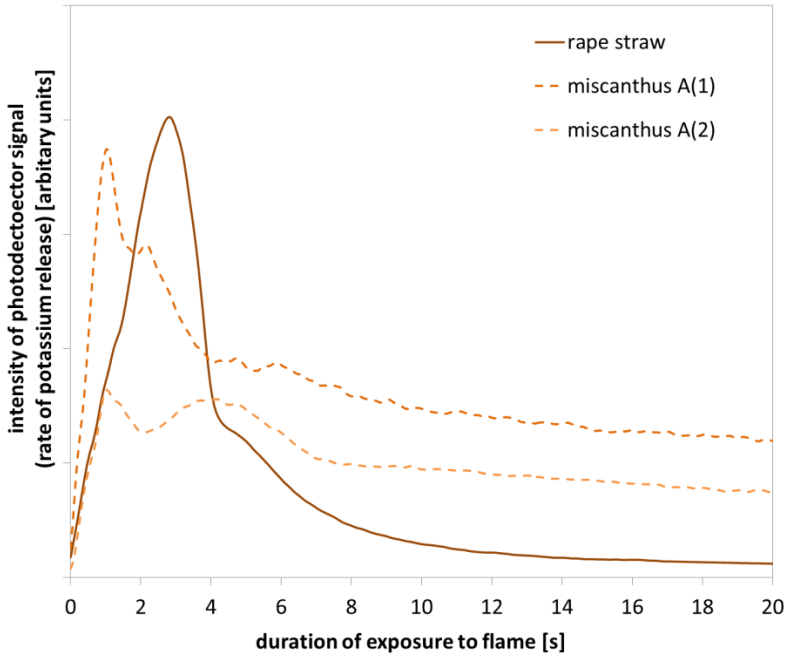

(b)

Figure 4-13 – Potassium release profiles for 1.1mg single particles of various herbaceous materials: (a) wheat straw; (b) rape straw and miscanthus (same scale on y-axes)

4.3.2.3 Olive residue and black pellet

The remaining materials, olive residue and “black pellet” are distinguished by having a much higher density than the other materials examined. The potassium release profiles are presented in **Figure 4-14.** Note that the horizontal-axis of this figure is to a different scale to **Figure 4-12** and **Figure 4-13** to allow the extended combustion time for the materials to be fitted. The vertical-axis is to the same scale. The general shapes of the profiles are consistent with the patterns observed for the other materials in that there is a distinct peak of release during the volatile combustion stage, the subsequent release rate shows an increase to a peak at burn-out and is followed by a long decaying tail of release from the ash. Both materials took much longer for devolatilisation and full burn-out compared to the other materials. This is related to the density, heat transfer properties and kinetics of the materials as discussed in Chapter 3.

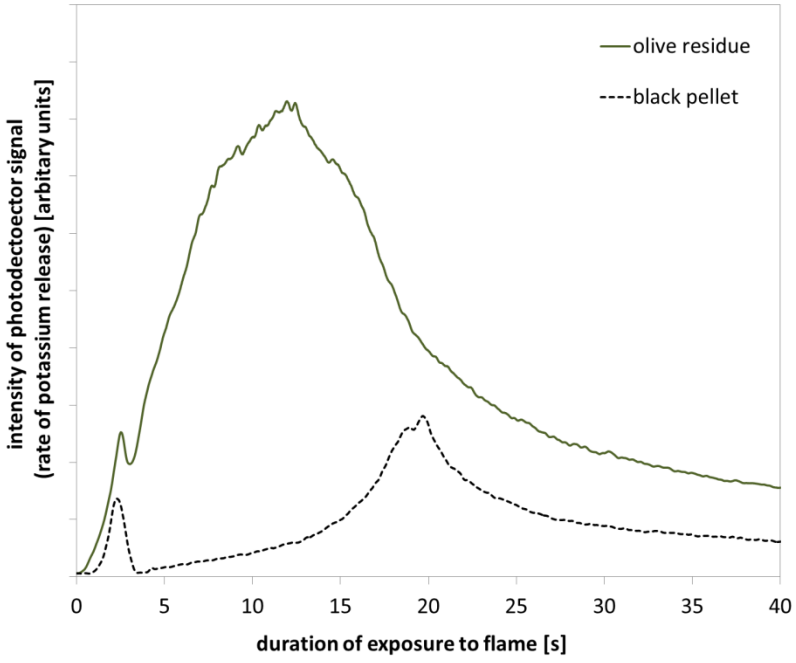

Figure 4-14 – Potassium release profiles for 1.1mg single particles of olive residue and black pellet

4.4 Analysis and discussion

The release profiles all appear to comply with a general form with the peak of potassium release occurring near or at the point at which there is effective char burn-out (indicated on the figures by the vertical lines) followed by a rapid decay in release rate. These patterns are consistent with the observations made by recent similar studies including Fatehi et al. (Fatehi et al., 2015) and Zhang et al. (Zhang et al., 2015) both of which studied combustion of larger (>20mg) particles of a single wood type in gas-flame burners. In both these studies softwoods were used, the published profiles resembling that of pine in this study (**Figure 4-12** (b)).

The previous discussions of the form and features of the recorded potassium release profiles note a number of apparent correlations. These are worthy of further analysis to determine the quality of the relationships. An important feature to verify in this experiment is the relationship between the total quantity of potassium contained in the sample and the cumulative total of that which is detected. While the photo detection measurement does not provide an absolute measure of potassium release, there should be strong correlation between the area enclosed by the recorded profile (determined by simple integration of the data) and the total potassium content. This is shown to be the case in **Figure 4-15** where the potassium content of the sample is plotted against the inferred potassium released to gas phase – including the release during ash decomposition. The linear regression function (forced to the origin) fitted to the data does indeed show a strong correlation (with a regression function R^2 value of 0.93). The experiments were run until the observed potassium release was negligible so it may be inferred that the full transformation of all potassium in the sample to gas phase is detected. Assuming this to be the case, the potassium release values in **Figure 4-15** have been normalized using the willow reference material with 0.75%wt potassium content as the datum (on the basis that this sample is mid-range). From this relationship, the intensity of the photo-detector signal can be translated to a potassium release rate (which is used in **Figure 4-16**(a) below). It should be noted that for the following analyses, the data for olive residue has been omitted in some cases for the purposes of clarity (since

the potassium content is an order of magnitude higher than the woody materials and so outside the scale of the plots).

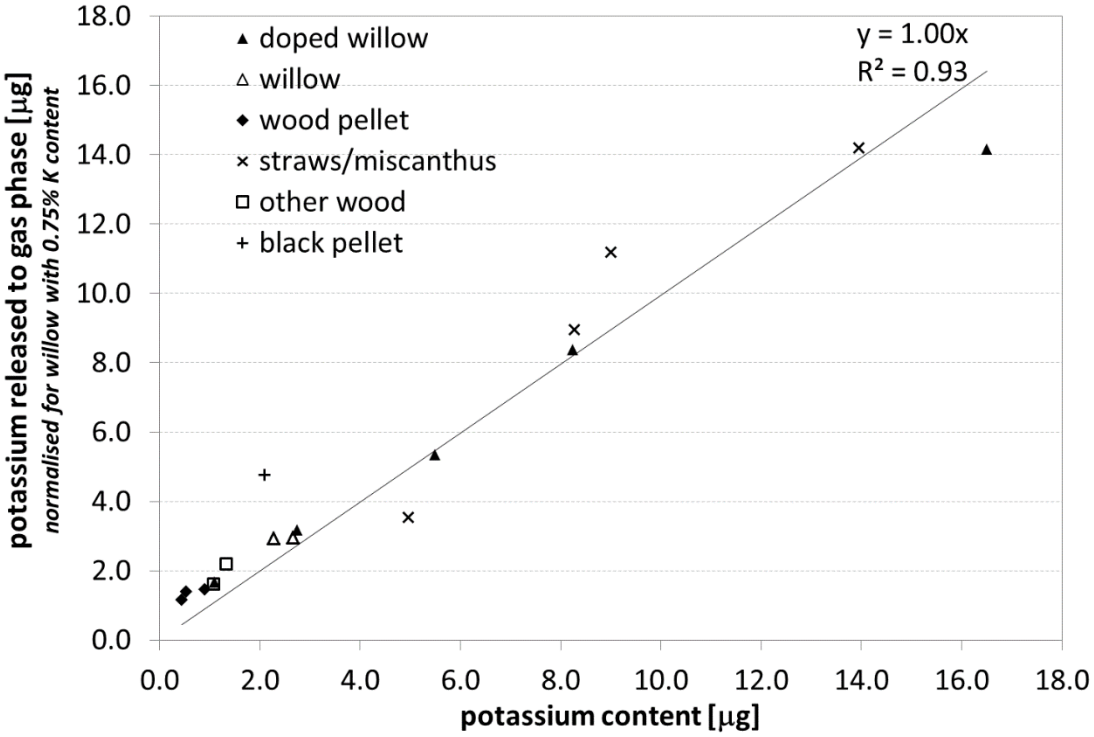

Figure 4-15 – Correlation between total measured release of potassium to gas phase and initial potassium content in the 1.1mg particle [data normalized for values of K content and K release for the 0.75%wt (mid-range) doped willow].

It has been observed from **Figure 4-11** that, in the case of the reference materials, the peak potassium release rate is correlated to the potassium content of the sample. **Figure 4-16**(a) shows the peak value of the release rate for each material plotted against the initial potassium content of the particle. There is a clear trend identifiable (with a regression function R^2 value of 0.84) which indicates that the peak release rate is a function of the concentration of potassium in the particle. This would be consistent with the potassium release being governed by a diffusion mechanism and proportional to the concentration gradient of potassium at the surface of the particle (this is explored further in Chapter 6). **Figure 4-16**(b) shows the duration of the volatile and char combustion stages (total burn-out time) for each material plotted against initial potassium content of the particle. While the herbaceous materials do not fit into a clear trend, there is a good correlation between burn-out time and potassium content for the woody materials. This is consistent with the observed catalytic effect of potassium on the thermal decomposition and char reactivity as

described in Jones et al. (Jones et al., 2007) and Saddawi et al.(Saddawi et al., 2012) [Note: the data for olive residue have been omitted for the purposes of clarity - since its potassium content is an order of magnitude higher than the woody materials and so outside the scale of the plots.]

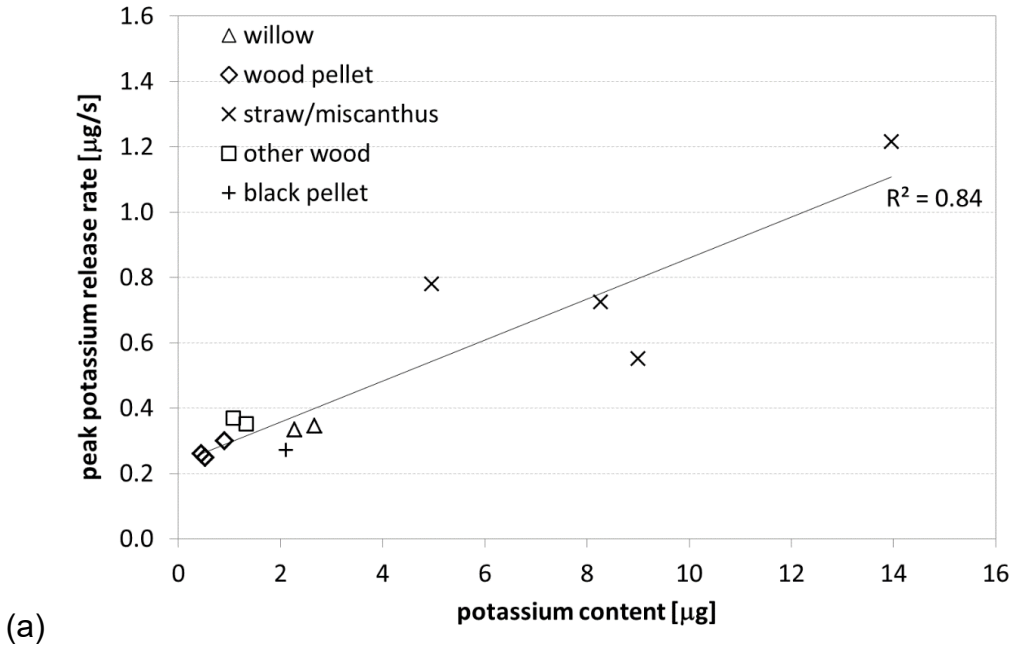

(a)

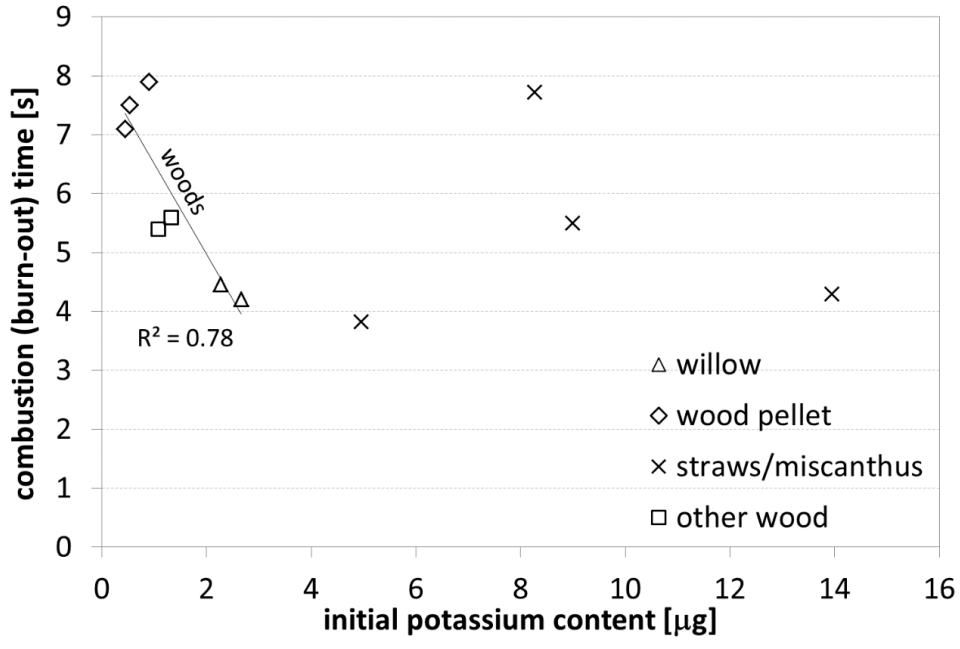

(b)

Figure 4-16 – Relationships between initial potassium content in the 1.1mg particle and: (a) peak measured release rate of potassium to gas phase; (b) the duration of the volatile and char combustion stages (or burn-out time).

Having established a means of relating the potassium content of the samples to the total detected potassium release, it is also possible to employ a similar method to estimate the relative quantity of potassium released at each stage of combustion. The devolatilisation and char combustion stages are clear in many of the recorded profiles. Where the demarcation is not clear, the devolatilisation duration can be established using characteristics obtained from the previous single particle experiments in Chapter 3. By integration of the respective areas of each stage as identified in the profiles, an estimate of the relative proportion of potassium released during devolatilisation and char combustion can be determined. The inferred fraction of potassium retained in the solid ash particle at the end of char burn-out is derived from the area under that part of the profile following the char combustion stage (subject to an evaluation error of ±5%). In the experiment this fraction of potassium is released by continued heating of the ash particle in the high temperature flame.

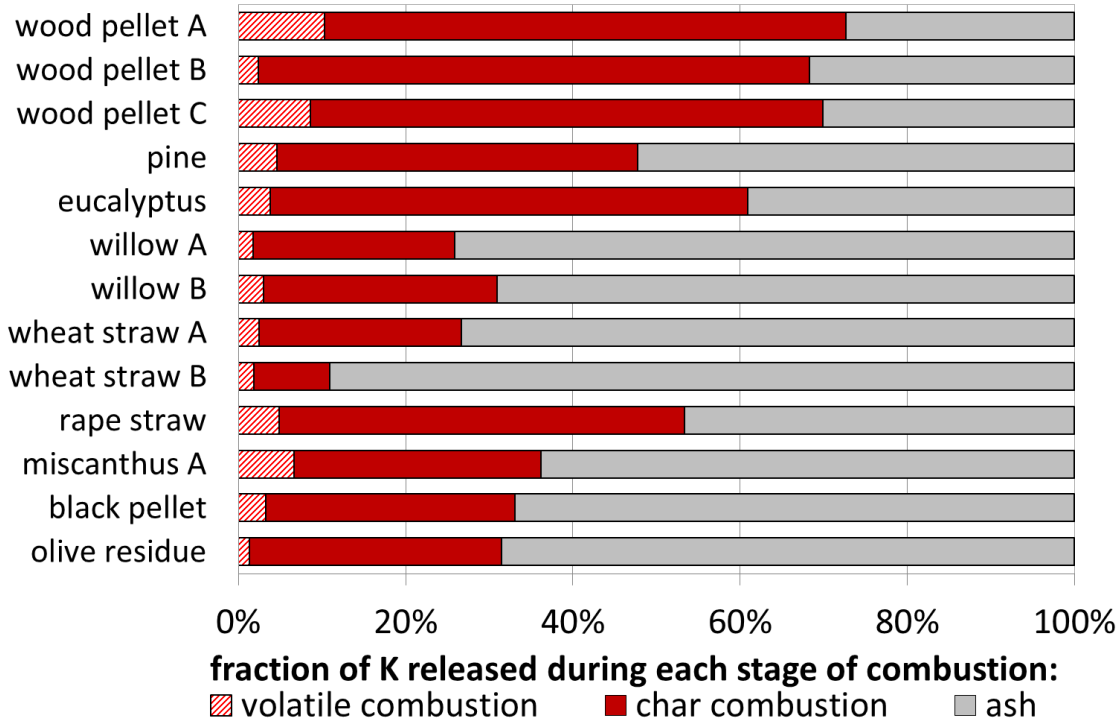

Figure 4-17 – Partitioning of potassium between combustion stages and ash

The results of such an analysis are presented in **Figure 4-17**. It is noted that the proportions of potassium release in each stage for pine in this figure are similar to those presented in other analyses performed in the study by Fatehi et al. In

the context of the situation inside a furnace, as opposed to the conditions of the experiment, the continuing exposure of the ash particle to high temperatures is dependent on the residence time, the temperature gradient in the furnace and whether it is entrained in the gas flow as fly-ash or drops out as bottom ash.

An examination of this derived data leads to other relationships of interest. The fraction of potassium released during combustion plotted against the initial potassium content of the particle is presented in **Figure 4-18**.

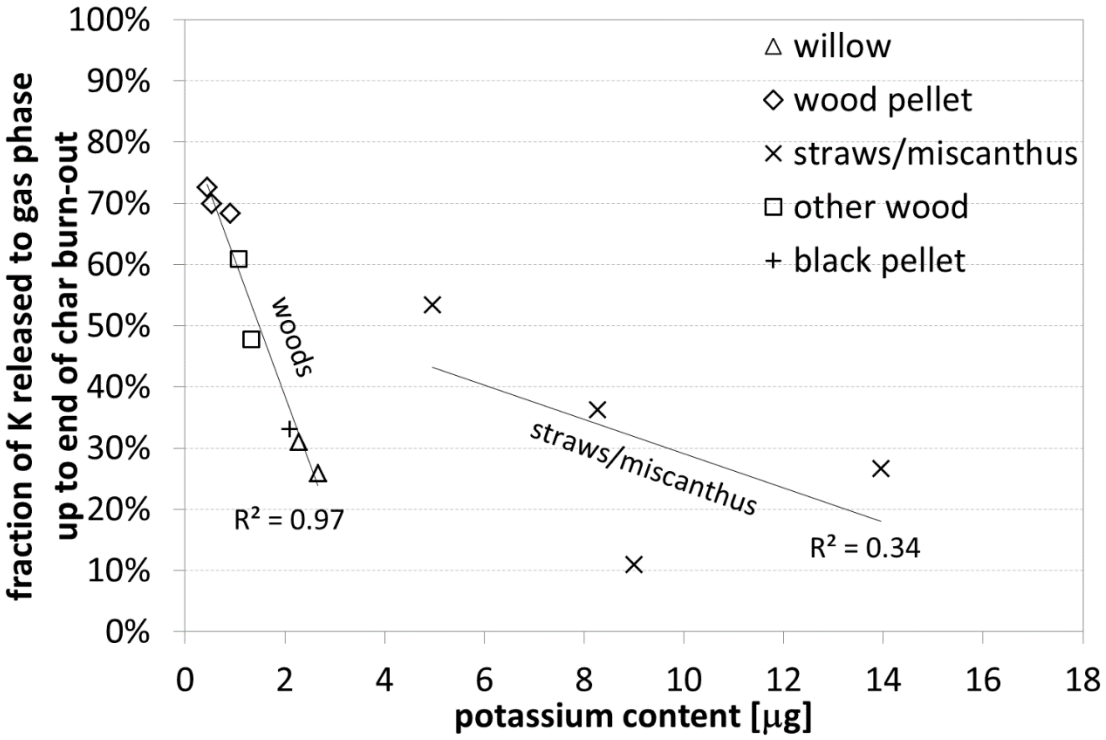

Figure 4-18 – Relationships between the proportions of potassium released to gas phase up to end of char burn-out and the initial potassium content of the 1.1mg particle

While the overall data show a weak correlation, there is a strong correlation shown for the woody materials. This shows a similar pattern to **Figure 4-16**(b) and it is apparent that the fraction of potassium released during combustion is directly related to the burn-out time. An analysis of these parameters for the selected woody materials alone does indeed show a good correlation (with a regression function R^2 value of 0.83). The implication is that a higher potassium content leads to faster burn-out (by a catalytic effect) which in turn reduces the time during which potassium can be volatilized and diffuse away from the particle. Taken alongside the observations made on the data in **Figure 4-16**(b),

it seems that the behaviour of the herbaceous materials is distinct from that of the woody materials. This distinction between the two types of material is probably related to other ash components which affect the retention of potassium in the particle. To investigate this aspect further will require a more detailed analysis of the ash composition of each fuel.

4.5 Conclusion

Solid biomass fuels contain significant amounts of potassium. In large scale power generation plant using pulverized fuel, this is of concern since high levels of potassium in the ash or the flue gases can lead to deposition and corrosion problems on heat exchange surfaces. Investigating patterns of potassium release to the gas phase is therefore important in the understanding of the potential ash deposition behavior of biomass. Typical ranges of potassium content for various types of biomass fuel have been presented along with those measured for a selection of fuels used in this study.

An emission spectroscopy method has been developed using an optical filter and custom-built photodiode detector. This has been shown to be an effective and expeditious means of observing the patterns of potassium release from a range of biomass fuels undergoing combustion at flame temperatures in the range 1600-1800K. The resulting potassium release profiles allow the fractions of potassium retained in ash and char relative to that released to gas phase to be estimated.

The potassium temporal release patterns for 13 different solid biomass fuel samples have been presented. These illustrate the variability and similarities in potassium phase partitioning in conditions similar to industrial pulverized fuel furnaces. The resulting data have allowed the identification of certain trends, the more noteworthy observations being as follows:

- There are similar shaped patterns of release for similar materials but differences between material types.
- Long exposure to high temperature eventually results in the release of virtually all the potassium to the gas phase from the ash particle.

- The release of potassium during the devolatilisation stage of combustion is small compared with the subsequent release during char combustion for all materials examined.
- The peak rate of release of potassium during char combustion is correlated to the potassium content in the particle.
- The proportion of potassium released during combustion to that retained in the ash is correlated to the initial potassium content, although this relationship differs between wood and herbaceous materials.

These relationships will be referred to in Chapter 6 in which it is attempted to model the mechanisms for gas-phase potassium release during combustion and reproduce the patterns observed.

Chapter 5
Thermal conductivity of solid biomass fuels

5.1 Introduction

This chapter examines the variation in thermal conductivity of different types of biomass fuel. An experiment for measuring the effective thermal conductivity of various biomass materials is described. Measurements are presented for fourteen different biomass fuel materials. The chapter includes a literature review, methodology, results and analysis.

5.1.1 Applications for biomass thermal conductivity data

Knowledge of thermal properties and heat transfer in biomass materials is important for modelling biomass thermal conversion processes including combustion, torrefaction, gasification and liquefaction. In particular, the thermal conductivity of a material is a significant parameter in determining internal heat transfer of fuel particles. It is also relevant in the context of bulk biomass storage where modelling self-heating and predicting self-ignition behaviour of large volumes of material is a safety concern.

Models of the combustion of individual particles of biomass fuel have been developed at a fundamental level (Yang et al., 2008, Saastamoinen et al., 2010) and these have been used as sub-models for higher-level modelling of furnaces using computational fluid dynamics (Ma et al., 2007, Backreedy et al., 2005). While the power of the modelling tools has increased, the usefulness of the models has been limited by the lack of detailed and accurate data on the properties and behaviour of biomass fuels. Knowledge of fuel properties is understandably challenging because of the vast variability in materials classed as biomass. In power generation applications, these may include various softwoods, hardwoods, herbaceous energy crops, agricultural residues and other wastes or industrial by-products.

To effectively model the heat transfer to and within a biomass particle undergoing pyrolysis or combustion it is necessary to know the thermal conductivity of the material. The significance of the heat transfer properties of

small biomass particles in evaluating the chemical kinetics of pyrolysis and char combustion has been described by Hayhurst (Hayhurst, 2013). Differences in thermal conductivity affect the internal temperature gradients and heating rates in the particle which, in turn, affect the apparent reaction kinetics. This is also relevant on the larger scale especially in the phenomenon of self-heating of combustible materials such as the bulk storage of biomass fuel where the risk of self-ignition arising from this is a distinct safety concern (Jones et al., 2015). Self-ignition temperatures for biomass materials are dependent on thermal conductivity since this affects the balance between internal heat generation from chemical kinetics and heat dissipation to the external surface (Thomas and Bowes, 1961). The risk of self-ignition may be predicted through modelling (Everard et al., 2014) provided reliable data on thermal conductivity and internal heat generation are available.

5.1.2 Models of biomass thermal conductivity

When considering or discussing the thermal properties of biomass materials, it is important to note that such materials are far from being uniform and most – woods for example – are highly anisotropic. Furthermore, the thermal conductivity of lignocellulosic materials is a combination of the thermal conductivities of the solid fibrous cell structure, the moisture (i.e. water) and gases (i.e. air) contained in the interstices between the fibres. These factors have been recognised and have led to the development of structural models of wood as a means of predicting thermal conductivity (Thunman and Leckner, 2002). In the modelling proposed by Thunman and Leckner, each of the three constituents, solid, liquid and gas are applied as components connected in series or parallel or a combination - analogous to an electrical circuit - depending on the anisotropy. The relationship between moisture content and thermal conductivity has been observed to be approximately linear by Yu et al. (Yu et al., 2011) . Applying this to the dry solid and the moisture components, the thermal conductivity of a sample of biomass can be modelled as a linear function with respect to moisture content :

$$\lambda_{eff} = (1 - M)\lambda_{dry} + M\lambda_{w} \qquad \textbf{(5-1)}$$

where:
λ_{eff} is effective thermal conductivity

λ_{dry} is thermal conductivity of dry solid
λ_w is the thermal conductivity of water at 300K: taken as 0.61 W.m^{-1}K^{-1} (Raznjevic, 1976)
M is the proportion of moisture by mass (mass of moisture/total mass)

Also, for the dry solid and gaseous components:

$$\lambda_{dry} = (1 - \gamma)\lambda_f + \gamma\lambda_g \quad \textbf{(5-2)}$$

where:
λ_f is thermal conductivity of the solid biomass fibre
λ_g is thermal conductivity of the interstitial gas
γ is the proportion of gas in the particle by volume

Since the relative density of (for example) air (1.23 kg/m^3) to cellulose (1500 kg/m^3) allows the gaseous mass to be neglected for low values of γ, the density, ρ is a function of γ such that:

$$\rho \propto (1 - \gamma) \quad \textbf{(5-3)}$$

Since γ is not a parameter that is known or easily measured, the thermal conductivity of a dry sample can then be expressed in the form:

$$\lambda_{dry} = F\rho + c \quad \textbf{(5-4)}$$

where:
F is a constant which may be determined empirically
c is a constant estimated as the thermal conductivity of dry air at 300K taken as 0.026 Wm-1K-1 (Shpilrain, 2011)

5.1.3 Thermal conductivity measurement methods

To determine the thermal conductivity of solid materials, measurement of heat flow through the material and the temperature differential across the material is necessary. Details of various techniques for thermal conductivity measurements of bulk materials are presented by Tritt and Weston in (Tritt and Weston, 2004). Techniques can either use measurements of steady state systems or measure the temperature time-history of a dynamical system. Steady state methods generally involve using a heat source at a fixed temperature and heat sinks on either side of the sample. The heat flow in these techniques can be determined by either direct measurement of the input power to the heat source or by measurement of temperature differential across a reference material either in

series or parallel to the sample. Such systems should be insulated to minimise heat losses and heat losses must be evaluated.

Using a similar arrangement as the steady state method but with a fixed heat sink (i.e. no input power), the dynamical thermal behaviour of materials can be measured. The ‘Fitch’ method is an example of this type of system. Other dynamical heat flow techniques include the “laser-flash” diffusivity method and pulse-power methods. In these techniques, a known quantity of heat is applied in a short pulse and the temporal change in temperature in and across the sample is measured. This allows the thermal diffusivity (ratio of thermal conductivity to density x specific heat capacity) to be derived. The ‘Maldonado’ method uses dynamical measurement of a reference material in contact with the sample to indirectly determine thermal conductivity.

Temperature measurements are generally made using proprietary thermocouples although dynamical measurements such as with ‘laser-flash’ methods can use of thermographic imaging to capture fast temperature changes. Depending on the geometry of the application, heat-flux sensors can be employed to determine the flow of heat through the materials. Heat flux sensors consist of multiple thermocouple junctions in a thin, flat planar arrangement giving a voltage output proportional to the heat flow through the plane.

5.1.4 Published data on the thermal conductivity of biomass

Published data on thermal conductivity of wood materials are mainly in the context of their use in construction and is generally to inform calculations of building insulation. Well established data from published literature are included in the *CRC handbook of physics and chemistry* (Haynes and Lide, 2013) and Austin and Eastman (Austin and Eastman, 1900). Selected examples of published data are summarized in **Table 5-1**. Thermal properties of the bulk mass of biomass materials specifically in the context of wood pellet storage and using transient heat flow measurement methods have been published by Guo et al. and Sjöström and Blomqvist (Guo et al., 2013, Sjöström and Blomqvist, 2014).

Measurements of thermal properties of softwood particles specifically in the context of combustion applications have also been published. Values for the

thermal conductivity and specific heat capacity for samples of softwood, softwood bark and softwood char are reported by Gupta et al. (Gupta et al., 2003). Similar experiments specifically on pine wood and char samples were also undertaken by Hanklin et al.(Hankalin et al., 2009) while properties of larger specimens (300x300x100mm) of various hardwoods and softwoods were reported by Yu et al. (Yu et al., 2011) using heat flux sensors and with reference to the effects of moisture and temperature.

While the above published data on some types of wood exist, there are little data on herbaceous materials or other non-woody biomass fuels. The main reason for this is the difficulty in obtaining a suitably sized uniform sample of material to perform a measurement on. The techniques used for measuring bulk material properties are not practical on a small particle. Both Gupta et al. (Gupta et al., 2003) and Hankalin et al. (Hankalin et al., 2009) have used 'Fitch'-type apparatus. In these examples the samples of wood were regular discs in the order of a few millimetres thickness. A similar approach can be used for investigating the thermal properties of other biomass materials but it is clearly not practical to use such a technique on, for instance, raw unprocessed wheat straw. Since biomass is non-homogeneous and most is distinctly anisotropic, it is difficult to obtain samples which are both large enough for measurement and representative of the material in small particle form.

In an attempt to overcome this issue, an experimental method has been developed in which samples of any solid biomass material can be assessed on a comparative basis. The method requires that the samples are prepared in a consistent way to produce a homogenized disc of material with dimensions and density within a similar range. The test discs are a simple physical form convenient for measuring thermal conductivity. It is important to note that this is not the form in which the fuels are normally utilized. Nevertheless, it is contended that the relative thermal conductivity measurements obtained from the discs are a valid and useful representation of the respective materials. The data may be used to determine the thermal conductivity of various forms of the fuel by applying it to a model of the macrostructure of the material. Modelling of wood by considering the different structural characteristics of different components (solid matter, moisture and interstitial gas) such as that proposed

by Thunman et al. (Thunman and Leckner, 2002) is one approach to achieve this.

Table 5-1 - Published thermal conductivity data for biomass materials

Material	*Density* $kg\ m^{-3}$	*Thermal conductivity* $W\ m^{-1}K^{-1}$	*Source ref.*
Group 1 - perpendicular to fibre orientation:			
Sequoia	380	0.082	(Austin and Eastman, 1900)
Pine	406	0.086	(Austin and Eastman, 1900)
white wood	506	0.102	(Austin and Eastman, 1900)
Cherry	534	0.108	(Austin and Eastman, 1900)
Gum	559	0.109	(Austin and Eastman, 1900)
Walnut	609	0.115	(Austin and Eastman, 1900)
white oak	615	0.113	(Austin and Eastman, 1900)
brown ash	649	0.129	(Austin and Eastman, 1900)
red birch	711	0.126	(Austin and Eastman, 1900)
sewage sludge	760	0.130	(Hayhurst, 2013)
Balsa	113	0.034	(Kotlarewski et al., 2014)
Balsa	137	0.037	(Kotlarewski et al., 2014)
softwood	360	0.099	(Gupta et al., 2003)
pinewood	450	0.110	(Haynes and Lide, 2013)
fir	540	0.140	(Haynes and Lide, 2013)
spruce	400	0.128	(Raznjevic, 1976)
maple	710	0.158	(Raznjevic, 1976)
Group 2 - parallel to fibre orientation:			
pinewood ||	450	0.260	(Haynes and Lide, 2013)
fir ||	540	0.350	(Haynes and Lide, 2013)
spruce ||	400	0.279	(Raznjevic, 1976)
maple ||	710	0.419	(Raznjevic, 1976)

The objective of the experiment described in the following sections is to provide thermal conductivity data for accounting for differences between types of biomass fuel in the modelling of thermal conversion and combustion.

5.2 Description of the experiment

5.2.1 Sample preparation

The materials selected for the investigation were mainly taken from those used in other investigations as listed in Chapter 2. In addition, two samples of torrefied pine were obtained. The full list of the samples examined in this study is presented in **Table 3-7** along with the measured moisture in the milled sample and the mean single particle (dry basis) density. Samples were received in various forms including pellets, chips and bales. All samples were milled using a liquid-nitrogen cooled impact mill until the entire sample was passed through a 90μm sieve. Since moisture from the original bulk sample is reduced in this process, moisture measurements of the milled samples were obtained using a TA Instruments TA5000 thermo-gravimetric analyser subsequently. It is noted that moisture content in the samples ranges from 2 to 6%. A correction, described later, to the measurements based on these values is used to compensate for the variation. The single particle density was derived using measurements from single particle combustion studies (as described in Chapter 3). The single particle density presented in **Table 3-7** is on a dry basis (i.e. the density of the particle with no moisture).

Two test pieces weighing 200mg (±10%) and 400mg (±10%) respectively were formed from the milled samples for each material. The test pieces were formed using a 13mm diameter cylindrical steel die in a hydraulic press to a pressure between 360 and 380 MPa. The resulting pellets were weighed on a digital microbalance to a precision of ±1mg. The thickness of the pellets was measured using a micro-meter to a precision of ±0.01mm.

Additional test samples of unprocessed pine wood were prepared with similar dimensions to the pellets and with fibre orientation either parallel or perpendicular to the heat flow. This was to provide a comparison with the measured thermal conductivity of the pellets and with the published values of other woods (from **Table 5-1**).

Table 5-2 – Materials selected for thermal conductivity measurement

Material	*Sample moisture content* [%wt]	*Single particle dry density (mean)* [kg/m^3]
Willow A	5.9	490
Willow B	4.1	519
Wood pellet A	2.7	634
Wood pellet B	4.1	609
Wood pellet C	5.1	563
Wheat straw A	5.5	201
Wheat straw B	5.2	320
Rape straw	6.1	211
Miscanthus A	4.6	650
Miscanthus B	3.7	650
Olive residue	4.8	1230
Torrefied Pine A	2.4	401
Torrefied Pine B	1.9	383
S-E wood pellet	4.2	1200

5.2.2 Measurement apparatus

The experiment was aimed at small test pieces with relatively low thermal conductivities. To satisfy these criteria, a bespoke test apparatus was designed and built specifically for the purpose. The design was based on the 'split-bar' method which has been used for measuring thermal conductivity of polymers (Anderson, 1966). The arrangement of the apparatus is such that the test piece is sandwiched between two reference components of known thermal conductivity. A heat source controlled to be at a fixed temperature is applied to the extremity of one reference piece and a constant temperature heat sink applied to the opposite end of its counterpart. The axial temperature gradient across the two reference pieces is measured and the heat flow in each determined. The heat flow through the test piece is taken to be the average of that in the two reference pieces. Given the dimensions of the test piece and the measured temperature differential across it, its thermal conductivity is thereby derived.

The system described was implemented using CZ121M engineering brass (Aalco) as the reference material having a thermal conductivity of 123 $Wm^{-1}K^{-1}$. The diameter of the brass rods was made to be coincident with the test pieces at 13mm. The length of the brass rods was determined mainly by practical considerations of physical support and the required contact area with the heat source and heat sink. The temperature gradient was measured in the sections of each brass rod adjacent to the test piece between 65 and 5mm away from the contact interface using 0.5mm diameter mineral insulated J-type thermocouples. These were inserted into holes drilled radially to the centre of each brass rod.

The power requirement for the constant temperature heat source was estimated for a 'worst case' with a sample thermal conductivity higher than the expected value for biomass (0.5 $Wm^{-1}K^{-1}$) and test piece of minimum thickness (1mm). Accounting for heat losses along the length of the brass rods, the steady state power requirement was calculated at 3 Watts. This was provided by a surface-mounted 'sub-miniature proportionally-controlled' heater with a nominal rating of 5W (ThermOptics). The heater was mounted on a 50mm diameter x 50mm brass cylinder to act as a heat reservoir. This was in turn mounted on the respective 'hot' brass rod. The opposite 'cold' brass rod was extended such that it could be immersed in an ice-bath (i.e. constant temperature) heat sink formed using a vacuum-insulated steel flask. Polyethylene insulation was applied to the brass rods to reduce heat loss. A removable 50mm-thick layer of polystyrene insulation was applied around the sample holder section. The whole apparatus was mounted vertically. A schematic and a photograph of the assembly are illustrated in **Figure 5-1**.

The test piece was mounted between the two brass rods and held in place by the moderate pressure from the weight of the upper rod. A thermally conductive paste (proprietary product as used for mounting electronic components with λ=0.19 $Wm^{-1}K^{-1}$) was applied to the contact interfaces. Initial measurements omitted this and significant variations in repeat measurements were noted owing to imperfect surface contact (i.e. air-gaps). A *Picolog* TC-08 thermocouple data acquisition interface and data logging software were used for recording the temperatures.

With the heater and the heat sink applied, the apparatus was left until the temperatures indicated on the measurement thermocouples had stabilized. The thermocouple measurements were then logged at a rate of one sample per second for a period of at least 30 minutes. The logged data were checked for stability (i.e. gradient of less than 0.001 K s^{-1}) and the mean averages recorded for calculation. At least two measurements were performed on each material.

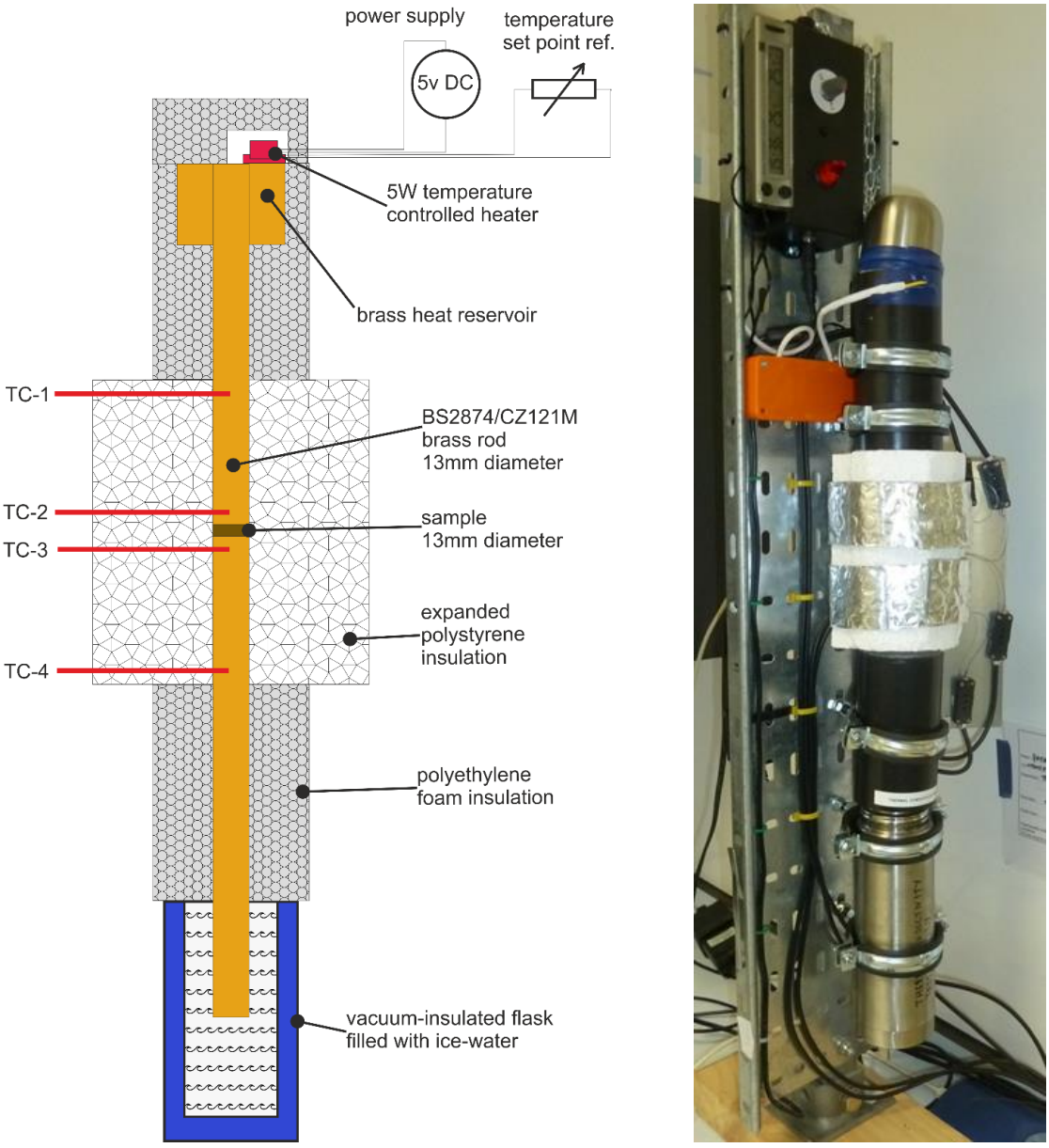

Figure 5-1 – (L) Diagram of test apparatus in cross-section; (R) Photograph of the apparatus

5.2.3 Calculations

The axial heat flow in the upper rod is calculated from the ideal heat flow and a correction for the radial heat loss. The calculation is approximated in the expression:

$$Q_1 = \frac{\lambda_{Brass} \cdot \mathcal{A}_{CS} \cdot (T_1 - T_2)}{L_{TC}} - \left\{\left(\frac{(T_1 - T_2)}{2} - T_{amb}\right) \cdot \left(\frac{\mathcal{A}_{ins} \cdot \lambda_{ins}}{L_{ins}}\right)\right\} \quad \textbf{(5-5)}$$

where:

T_1 and T_2 are the temperatures measured by thermocouples TC1 and TC2 respectively

T_{amb} is the ambient temperature (~23°C)

λ_{Brass} is the thermal conductivity of brass (123 $W.m^{-1}K^{-1}$)

$\mathcal{A}_{CS}$ is the cross sectional area of brass rod (133mm^2)

L_{TC} is the axial distance between thermocouples TC1 and TC2 (60mm)

$\mathcal{A}_{ins}$ is the effective surface area of insulation layer (5.5x$10^{-3}m^2$)

L_{ins} is the thickness of insulation layer (40mm)

λ_{ins} is the thermal conductivity of insulation (0.065 $W.m^{-1}K^{-1}$)

The axial heat flow in the lower rod, Q_2 is calculated with a similar expression substituting T_1 and $T_2$with T_3 and T_4 respectively.

The axial heat flow through the sample is approximated as the average of the heat flows in the upper and lower brass rods:

$$Q_S = \frac{Q_1 + Q_2}{2} \quad \textbf{(5-6)}$$

The temperature differential across the sample ΔT_S is derived from the difference of T_2 and T_3 with a correction for the 5mm of brass rod between the thermocouples and interface surface as:

$$\Delta T_S = \left(T_2 - \frac{Q_1 \times 0.005}{\mathcal{A}_{CS} \times \lambda_{Brass}}\right) - \left(T_3 + \frac{Q_2 \times 0.005}{\mathcal{A}_{CS} \times \lambda_{Brass}}\right) \quad \textbf{(5-7)}$$

The thermal conductivity of a sample λ_S with axial length L_S is then calculated from:

$$\lambda_S = \frac{L_S . Q_S}{\mathcal{A}_{CS} . \Delta T_S} \quad \textbf{(5-8)}$$

5.3 Results

5.3.1 Validation of measurements

The thermal conductivity and the density of wood are strongly correlated as shown by Austin and Eastman (Austin and Eastman, 1900). This correlation is the basis of modelling the thermal properties of woody materials as described in section 5.1.2. The relationship is also consistent for bulk quantities of wood pellet as shown in the study by Sjöström and Blomqvist (Sjöström and Blomqvist, 2014).

Examination of the relationship between material density and thermal conductivity is therefore useful for deriving or validating models of biomass in various applications including single-particle combustion, self-heating in bulk storage and the combustion of layers of dust. A plot of density against thermal conductivity is also a useful means of visualizing the similarities and differences between the materials measured in this study.

Before presenting the data for the homogenized biomass pellets, validation of the measurement method should be demonstrated by comparing the measured properties of materials against known published values for similar materials. For this purpose, a set of test pieces were made from polytetrafluoroethylene (PTFE) and their thermal conductivity measured in the same manner as for the biomass samples. The resulting measurements showed an average thermal conductivity within 3% of the published value for PTFE (Price and Jarratt, 2002) and with a standard deviation of less than 3%. In addition, test samples made of bulk pieces of pinewood were formed both with perpendicular and parallel fibre orientation (cross-grain and parallel-grain). The resulting measurements showed strong agreement with the published data for wood with similar density. Figure 5-2 shows a plot of the measured thermal conductivity versus the material density for the PTFE and pinewood reference samples together with the respective published data (Price and Jarratt, 2002) for comparison.

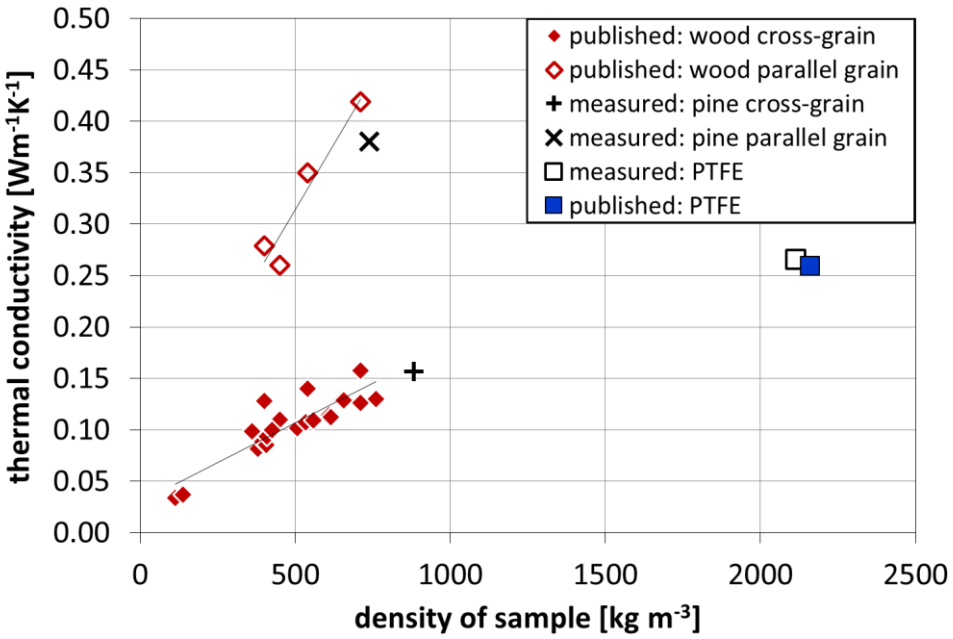

Figure 5-2 - Measured thermal conductivity of cross-grain and parallel grain pine samples compared to published values for woods [ref. Table 5-1]. Measured thermal conductivity of PTFE samples compared to published value.

5.3.2 Experimental results

Having shown the measurement method to be consistent with published data, the measured values for the homogenized biomass pellets, which fall between the values of the reference materials, can be reported with a high level of confidence. Each material was measured using at least two test samples and at two different heater settings (70°C and 60°C). The calculated standard deviation of the data obtained for each material was, on average only 3.5%. This value is close to that evaluated for the reference measurements for the PTFE test pieces.

The measured thermal conductivity of the materials tested is presented in **Table 5-3**. These data, plotted against sample density, is presented in **Figure 5-3**. This also includes the published data from selected biomass materials as listed in **Table 5-1** for comparison. **Figure 5-4** shows the data for the homogenized biomass in more detail along with indications of the type of biomass for each data point.

Table 5-3 – Measured thermal conductivity for homogenized-densified biomass

Material	*Density* ±2% [kg m^{-3}]	*Thermal conductivity* ±5% [W $m^{-1} K^{-1}$]
willow a	1180	0.16
willow b	1140	0.18
wood pellets a	1180	0.18
wood pellets b	1130	0.21
wood pellets c	1140	0.19
wheat straw a	1150	0.16
wheat straw b	1170	0.16
rape straw	1190	0.19
miscanthus a	1140	0.16
miscanthus b	1170	0.15
olive residue	1140	0.21
torrefied materials:		
torrefied pine a	1200	0.29
torrefied pine b	1180	0.29
black pellet	1260	0.24

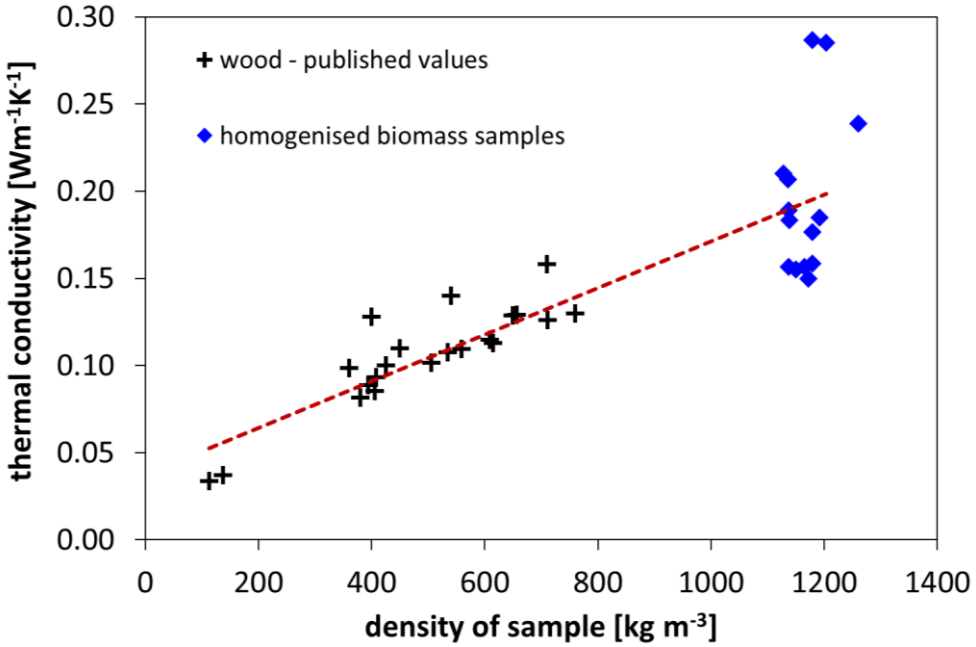

Figure 5-3 - Measured thermal conductivity of homogenized-densified biomass plotted against density compared with published values of wood

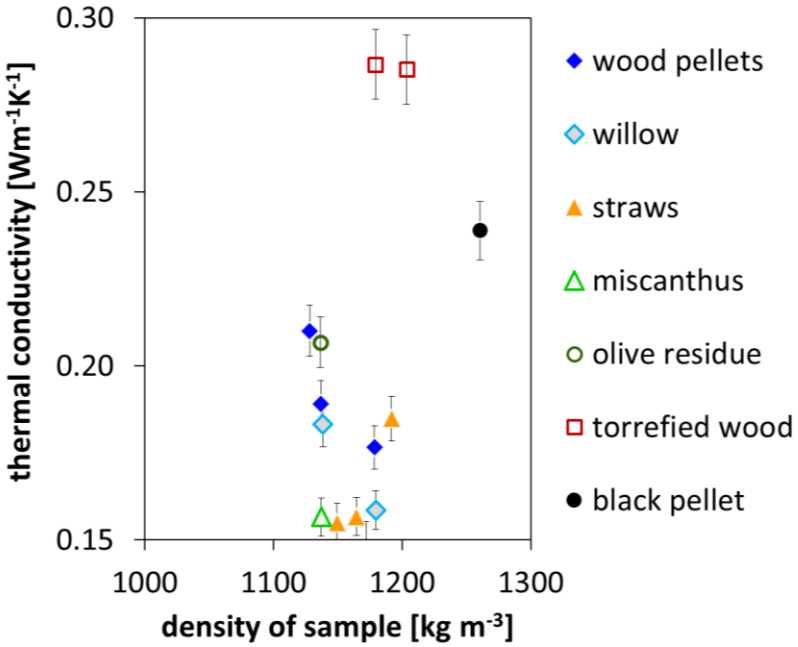

Figure 5-4 - Measured thermal conductivity of homogenized-densified biomass plotted against density with indication of type of biomass

5.4 Analysis and discussion

Key differences between the various biomass material types can be identified from the data presented in **Figure 5-3** and **Figure 5-4**. It is clear from this plot that the torrefied materials (torrefied pine and black pellet) have a significantly higher thermal conductivity than natural wood materials. There is less of a difference between the woody and herbaceous materials although, on average, the latter show slightly lower thermal conductivities than the former. Olive residue has a slightly higher conductivity than the woody and herbaceous materials but not as high as the torrefied materials.

Examination of the results of the experiment show that the expected relationship between density and thermal conductivity for wood conforms to a linear function. The plot of the results together with the published data for wood in **Figure 5-3** shows that the results fall broadly along the expected linear regression (dashed line).

Considering only the published data on wood, a linear regression function for the thermal conductivity (λ_{wood}) to density (ρ) relation can be derived, similar to equation (5.4) as:

$$\lambda_{wood} = 1.5\text{x}10^{-4}\,\rho + 0.030 \qquad \textbf{(5-9)}$$

For comparison with the measured values, this function may be applied to the wood pellet data. Thus assuming a density of 1148 kg.m^{-3} for a wood pellet gives a thermal conductivity value of 0.20 Wm^{-1}K^{-1}. This is close to the average measured value for the wood pellets at 0.19 Wm^{-1}K^{-1}. Although the moisture content of the published data is not clear, the two sets of data nevertheless appear to be in good agreement.

To account for the moisture content in the test samples, a correction to the calculated value of λ_S can be estimated by assuming the moisture content contributes uniformly to the measured value and the contribution is directly proportional to the moisture content by weight. Rearranging equation **(5-1)**, the dry basis thermal conductivity λ_{dry} is given by:

$$\lambda_{dry} = \frac{\lambda_S - M\lambda_w}{1 - M} \qquad \textbf{(5-10)}$$

The measured density of the samples can also be adjusted proportionately for moisture to give the estimates dry density of the sample as:

$$\rho_{dry} = \rho_{wet}(1 - M) \qquad \textbf{(5-11)}$$

Using these parameters, (λ_{dry} and ρ_{dry}) the coefficient F for equation **(5-4)** can be determined for each material.

Table 5-4 – Dry basis density and thermal conductivity of measured samples and derived coefficient F

Material	*Density of dry material* $\pm 2\%$ [kg m^{-3}]	*Thermal conductivity of dry material* $\pm 5\%$ [W m^{-1} K^{-1}]	*Coefficient* F [W m kg^{-1} K^{-1}]
willow a	1110	0.13	9.37E-05
willow b	1090	0.17	1.27E-04
wood pellets a	1150	0.17	1.21E-04
wood pellets b	1080	0.19	1.54E-04
wood pellets c	1080	0.17	1.30E-04
wheat straw a	1090	0.13	9.43E-05
wheat straw b	1100	0.13	9.57E-05
rape straw	1120	0.16	1.17E-04
miscanthus a	1090	0.14	1.00E-04
miscanthus b	1130	0.14	9.40E-05
olive residue	1080	0.19	1.48E-04
torrefied materials:			
torrefied pine a	1180	0.28	2.14E-04
torrefied pine b	1160	0.28	2.20E-04
black pellet	1210	0.22	1.63E-04

The derived coefficients, from **Table 5-4**, can be used with equation **(5-4)** to calculate the thermal conductivity of a dry particle with the density of the original material rather than the test sample. Inserting the moisture content of each sample into equation **(5-1)**, the thermal conductivity of the particle with moisture can then also be derived. Using the values for the materials as presented in **Table 3-7**, **Figure 5-5** shows a plot of the thermal conductivity of each of the

tested samples recalculated according to the density and moisture content of the original materials.

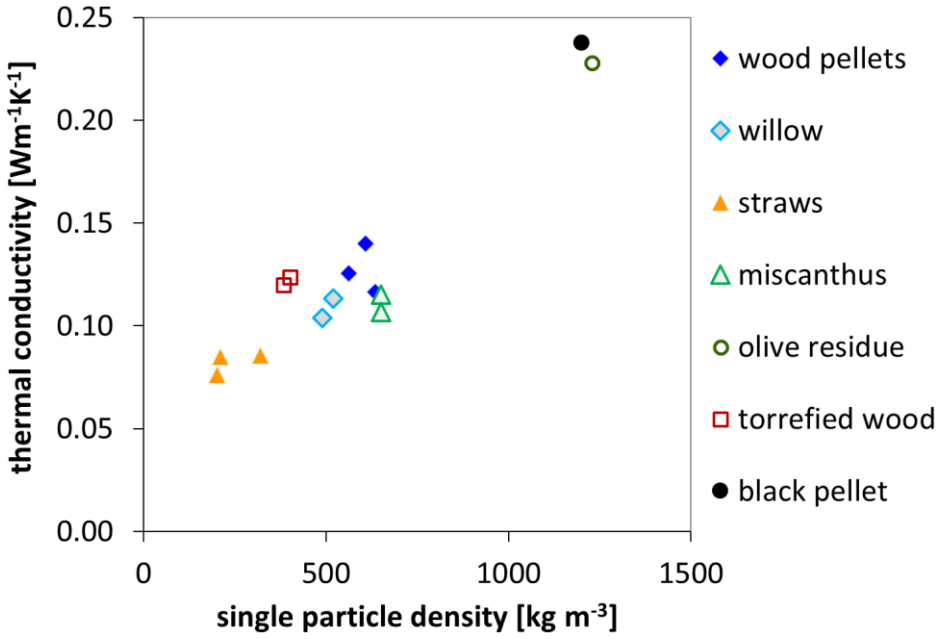

Figure 5-5 - Thermal conductivity of single particles of biomass derived from measurements on densified pellets and density of original particles (all on dry basis)

The following observations are made concerning the thermal conductivity of these materials in their original form. Both olive residue and black pellet, having high “as-received” densities (similar to that of the test samples) show the highest values. Wood pellets miscanthus and willow are grouped at similar values with the wood pellet average slightly higher than the other materials while straws have somewhat lower values owing to lower density particles.

Notably, torrefied wood shows a high value in the compressed pellet form but an uncompressed torrefied wood particle has a value similar to that of an uncompressed, un-torrefied wood particle – the increase in conductivity of the solid matter is compensated by reduction in density of the structure.

The derived values presented in Figure 5-5 apply to the effective thermal conductivity of quasi-homogenous particles – that is materials in which the fibre orientation is randomly dispersed. In large particles of un-milled wood the conductivity parallel to fibre orientation may be around 2-3 times higher than the perpendicular direction (as apparent in **Figure 5-2**). While the measurement

method does not allow verification of this for herbaceous materials, for the purposes of modelling for large particles, a multiplier may be assumed to account for the anisotropy of straw and miscanthus in the same way as for woods. This does not apply to olive residue and black pellet since their structure is more isotropic.

5.5 Conclusion

A method for determining the relative thermal conductivities of various biomass fuels has been presented. The method has been shown to be effective by comparison with existing published data. The experiment has provided data on the thermal properties of small particles of both woody biomass, herbaceous and other non-woody biomass and also torrefied biomass. While there is a considerable amount of published data on thermal properties of wood, there is little, if any comparable data available for the other materials investigated.

Analysis of the data has confirmed that woody biomass fuels conform to a general linear relationship between material density and thermal conductivity.

The compressed solid matter in torrefied wood was shown to have a significantly higher thermal conductivity than un-torrefied wood. Olive residue pellets and black pellet are shown to have higher thermal conductivities than wood while herbaceous materials tend to have lower values than wood.

The data presented in this study informs the choice of value of thermal conductivity to be used in calculating heat transfer in combustion models for different materials. The models for accounting for moisture content and particle dry density also allow estimation of thermal conductivity across different stages of combustion. The model presented in Chapter 6 adopts these models and the measured values of thermal conductivity of certain materials are used also.

Chapter 6
Modelling combustion of single particles of biomass

6.1 Introduction

6.1.1 Single particle combustion modelling

Modelling the combustion processes in large scale furnaces is one of the essential tools for the design of plant including burners and boilers, for the optimization of operational parameters such as milled particle size and for the analysis of ash fouling and deposition behaviour. The use of computational fluid dynamical (CfD) software with on-going improvements in computational power has led to considerably detailed modelling of pulverized fuel combustion in large scale boilers (Ma et al., 2007, Gubba et al., 2012, Backreedy et al., 2005, Yin et al., 2004). However, the effectiveness of CfD models depends on the validity and reliability of the sub-models used to calculate the heat flows and mass flows. In models specific to pulverized biomass, the key sub-model is that for the combustion of a single particle. This sub-model requires data on heat transfer properties, chemical kinetics, mass transfer and details of physical behaviours derived either phenomenologically or from a fundamental theoretical basis.

Woody and herbaceous biomass materials are anisotropic, non-homogeneous and there is a natural variation in physical and chemical characteristics even within samples from the same source (Chapter 2). It is therefore important to recognize that any model must be of an idealized version of the actual material. In the case of modelling heat transfer, the particle shape is often idealized to be quasi-spherical, even though in most cases biomass particles tend to be more quasi-cylindrical. This allows mathematical models to be simplified to one-dimensional systems such as described by Porteiro et al. (Porteiro et al., 2006) and Haseli et al.(Haseli et al., 2011a). Two-dimensional models are able to account for the effects of shape such as that described by Yang et al.(Yang et al., 2008) and can also account for anisotropy in material properties (e.g. thermal conductivity).

Since the thermal conductivity of biomass is low in relation to particle sizes and heating rates in the relevant applications, accounting for internal heat transfer is an important consideration. In particular, temperature differences within the particle will result in different respective reaction rates such that the apparent kinetics are influenced by particle size (Hayhurst, 2013). The effects of the size and shape of particles on internal temperature gradients have been investigated by Lu et al.(Lu et al., 2010) and illustrated with experimental data on relatively large particles (~11mm diameter). Internal thermal gradients may be approximated using idealized analytical equations. However, to account practically for the intrinsic thermal effects of combustion reactions, numerical methods are necessary. One approach is to consider the particle as being comprised of a series of concentric, discrete layers or “shells” such that heat flow and mass transfer from the surface to the centre and vice versa can be accounted for. Such an approach has been adopted by Thunman et al.(Thunman et al., 2002) and Porteiro et. al (Porteiro et al., 2006).

6.1.2 Potassium release

Experimental studies of the release of potassium from biomass combustion have shown that the evolution of potassium to the gas-phase is highly dependent on the particle’s temperature and higher proportions of potassium are released in the latter stages of the char combustion (Jones et al., 2007, Fatehi et al., 2015, Zhang et al., 2015, Sorvajärvi et al., 2014). This pattern is confirmed by the experiments described in Chapter 4. Models for predicting potassium release have been proposed in association with the experimental works previously referenced (Jones et al., 2007, Fatehi et al., 2015, Zhang et al., 2015, Sorvajärvi et al., 2014). Modelling of the phase transformation of potassium species to the gas phase is founded on the temperature dependent vapour pressure of the potassium species (KOH and KCl) and diffusion mechanisms from the particle. Prediction of potassium release is therefore closely linked to predicting the temperature of the combusting particle and the concentration of potassium during the progressing stages of combustion. In this study, the combustion of a single particle has been modelled so that the temperature inside the particle is used to predict potassium release to gas phase. The results of the model are compared to experimental data including

the measured particle surface temperature and the observed potassium released in the gas flame.

6.1.3 Development of a model for single particle combustion

While the single particle combustion model is considered as a sub-model in the context of CfD analyses of large combustion plant, the model is more realistically described as a collection of interconnected sub-sub-models. Many of the individual elements of the model describing heat transfer, mass transfer and chemical kinetics can be developed independently. When these elements are combined in the main model, the inter-dependence should be defined at the outset and, where possible, provision made for the progressive expansion and improvement of the model. To allow validation of each feature, the model has been developed in stages and the performance of each of these features 'tested' at each stage. This approach also allows the effects of refinements to the model to be examined as they are introduced. The following sections describe the basis of each element of the model.

The model was implemented through a FORTRAN code. The code used to produce the results presented in later sections is contained in appendix B.

6.2 Structure of the model

6.2.1 The concentric-layered particle model

An important aspect of the investigation of the combustion of single particles of solid biomass is the study of the effects that particle size has on combustion behaviour. The particle can be considered as a uniform, symmetrical entity in which all thermal and chemical processes proceed together identically. In this case, changes in particle size have a simple scaling effect. To account for the more complex effects of internal heat transfer, diffusion and the consequent differing reaction rates that these influence, it is necessary to breakdown the model of the particle into multiple parts. This not only allows differing conditions to be applied to each sub-part but also allows interactions between the parts such as heat and mass transfer to be modelled. One approach is to consider the particle as comprising of a series of concentric, discrete layers or "shells" such that heat flow and mass transfer from the surface to the centre and vice

versa can be accounted for. Such an approach has been adopted by Thunman et al (Thunman et al., 2002) and Porteiro et al (Porteiro et al., 2006). The concept of the concentric layered spherical particle model is illustrated in Figure 6-1. The particle is divided into n layers each of equal radial thickness (Δr). Each layer may be treated separately with a mass, volume, temperature, moisture content, volatile content and oxygen concentration specific to that layer. Heat and mass transfer between internal layers can be calculated as the balance of quantities at the interface. The boundary at the central layer of the particle has no further internal interface and so internal heat and mass transfer are set to zero. The particle's exterior is the boundary of the outermost layer where the external heat flux is applied and ambient concentrations for diffusion calculations are fixed (i.e. oxygen and potassium species concentrations).

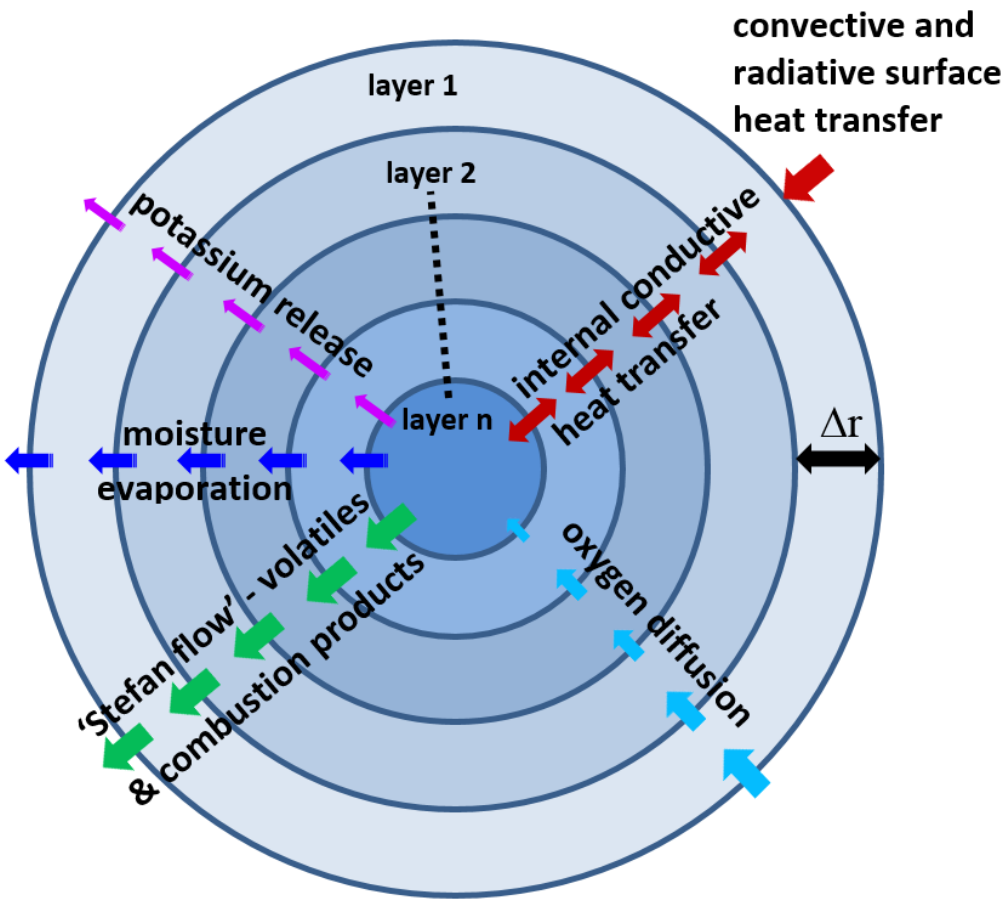

Figure 6-1 - The concentric layered spherical particle

6.2.2 Particle shape

A notable feature of milled lignocellulosic biomass particles is that they are distinctly non-spherical. The adoption of a spherical model then needs to be justified. The approximation to a spherical geometry allows the calculations of mass and heat transfer to be one-dimensional which simplifies the model considerably. The discrepancy between this and a realistic particle shape is mainly in the heat transfer to the surface and internally.

The surface heat transfer can be dealt with by adopting a 'shape factor' whereby the surface area used to determine the surface heat flux is based on the real particle geometry. All other dimensions used in the spherical model are determined from equating the volume, V_P of the 'real' particle with the volume of the sphere. Given V_P ,the diameter and surface area of the sphere are:

$$D = \sqrt[3]{\frac{6V_P}{\pi}} \qquad \textbf{(6-1)}$$

$$S_s = \pi D^2 \qquad \textbf{(6-2)}$$

For example, a particle with dimensions 3x1x1mm has a volume of 3mm^3 and a surface area, a_p , of 14mm^2. The equivalent spherical diameter in this case is 1.79mm. The surface area of the equivalent sphere is 10.1mm^2 . The 'shape factor' is the ratio of the real particle surface area to the area of the spherical model such that:

$$shape\ factor = \frac{S_p}{S_s} \qquad \textbf{(6-3)}$$

The adjustment to account for the difference between the idealised heat transfer for a sphere and an irregular shaped particle is not easily quantifiable but the increased surface area can be taken into account by applying the shape factor to the surface heat transfer coefficient.

Non-symmetrical internal heat transfer is more problematic to account for in a one-dimensional model. The anisotropy of woody particles leads to a tendency for milled particles to be quasi-cylindrical with aspect ratios of 2 or more. However, the same anisotropy results in the thermal conductivity along the long-axis of the particle to be 2-3 times higher than in the radial direction. Consequently, for particles with aspect ratios of 2-3, the thermal conduction

paths to the particle centre both radially and axially are approximately equivalent. This is a coarse approximation but allows a uniform thermal conductivity value to be adopted for each layer of the spherical model.

6.2.3 Density and volume

Having set the initial spherical model particle dimensions as in equations **(6-1)** and **(6-2)**. The volume of each layer in the model is then calculated as a spherical annulus with radial thickness Δr. Initially the particle has uniform, homogeneous properties throughout all layers. The mass of each layer is then simply a product of the layer volume and initial density.

$$m_p = \sum_{i=1}^{N} m_i = \sum_{i=1}^{N} \rho\, V_i \qquad \textbf{(6-4)}$$

Where:
i is the layer number
m_i is the mass of layer i
V_i is the volume of layer i
ρ is the initial density of particle

The mass of each layer is the sum of four components as follows:

$$m_i = m_{w,i} + m_{vol,i} + m_{char,i} + m_{ash,i} \qquad \textbf{(6-5)}$$

Where:
$m_{w,i}$ is the moisture in layer i
$m_{vol,i}$ volatile matter in layer i
$m_{char,i}$ is the fixed carbon (char) in layer i
$m_{ash,i}$ is the mass of ash in layer i

While the density of the particle in its initial state is the same for all layers, the density of the material will change as first moisture and then volatile matter are removed. The change in material density is modelled on the basis that loss of moisture and volatile matter results in mass loss but no change in volume. The mass loss resulting from char oxidation is accompanied by a proportional reduction in volume such that the char material maintains a constant density. The volume of the layer is then re-calculated during combustion as:

$$V_i = \frac{m_{char,i}}{\rho_{char}} + \frac{m_{ash,i}}{\rho_{ash}} \qquad \textbf{(6-6)}$$

Where:

ρ_{char} is the effective density of the char material
ρ_{ash} is the effective density of the ash material (taken as 1000kg/m^3 from (Hasler and Nussbaumer, 1998))

The radial thickness of each layer is therefore also recalculated as the volume of the layer changes. As the process proceeds, the particle shrinks and the overall diameter and surface area are also recalculated accordingly.

6.3 Heat transfer

6.3.1 Heat transfer to particle surface

The heating of a solid particle in a hot gas environment is a result of both convective and radiative heat transfer. In the context of the single particle combustion experiments, the dominant process is convective heat transfer since the particle is in isolation and the enclosing surfaces are at ambient temperature. In a pulverised fuel boiler, the radiative heat transfer from surrounding combusting particles is more dominant (Yin, 2016). It is important to recognise this difference and account properly for both heat transfer mechanisms in each case. The differences in the resulting heating rates in each situation will lead to differences in the predicted combustion processes. However, validation of the model in one situation (the experiment) will lend confidence in the predictive capability in the other (the p.f. boiler).

Convective Heat Transfer

The convective heat transfer from the gas to the particle is determined by the surface heat transfer coefficient which is a function of the *Nusselt* number, the particle dimensions and the external fluid thermal conductivity. For a spherical particle, the heat transfer coefficient is taken as (Incropera and DeWitt, 1986):

$$h_{conv} = \frac{Nu\ \lambda_{gas}}{D} \qquad \textbf{(6-7)}$$

Where:
h_{conv} is the convective heat transfer coefficient
Nu is the Nusselt number
D is the diameter of the spherical particle
$\lambda_{gas}$is the thermal conductivity of the gas (external fluid)

The Nusselt number is a dimensionless ratio of the convective heat transfer in the fluid to the conductive heat transfer in the solid. For a gas flowing over a sphere, the Nusselt number can be obtained from the expression derived by Ranz and Marshall for a spherical drop of liquid (Ranz and Marshall, 1952):

$$Nu = 2 + (0.6 \sqrt{Re}\, \sqrt[3]{Pr}) \qquad \textbf{(6-8)}$$

Where:
Re is the Reynolds number
Pr is the Prantl number for the gas

The Reynolds number, Re for gas passing over a sphere is:

$$Re = \frac{U_{gas}\ D}{\upsilon_{gas}} \qquad \textbf{(6-9)}$$

Where:
U_{gas} is the velocity of the gas flow
υ_{gas} is the kinematic viscosity of the gas

The heat flux to the particle surface is the product of the heat transfer coefficient, surface area and temperature difference between solid and gas and is described by the equation:

$$Q_{conv} = S_S\, h_{conv}\, (T_{gas} - T_S).\, dt \qquad \textbf{(6-10)}$$

Where:
Q_{conv} is the quantity of convective heat at the surface
S_S is the surface area of the particle
T_S is the surface temperature of the particle
T_{gas} is the temperature of the surrounding gas

Radiative Heat Transfer

Heat transfer to the particle surface through radiation is governed by the Stefan-Boltzmann law whereby the energy flux is a function of the fourth power of the absolute temperature of the surface. The heat transfer at the surface is also proportional to its emissivity. The rate of change of temperature of the particle is determined by this heat flux over the heat capacity of the solid and is described by the equation:

$$Q_{rad} = S_p\, \varepsilon\, \sigma\, (T_R^4 - T_S^4).\, dt \qquad \textbf{(6-11)}$$

Where:

Q_{rad} is the quantity of radiative heat at the surface
T_R is the temperature of the enclosing radiative surface
ε is the particle surface emissivity
σ is the Sefan-Boltzman constant (5.67x10^{-8} W m^{-2} K^{-4})

In the case of the experiment, the enclosing radiative surface is the ambient surrounding so temperature T_R is taken as ~300K. Consequently, as the particle heats up through convective heating, the radiative heat flux will be negative meaning that there is a cooling effect from radiation away from the particle.

6.3.2 Internal heat transfer

For a spherical solid with an initial uniform internal temperature, the application of a heat flux to the surface will raise the surface temperature. The heat will be conducted internally and ultimately, the entire particle will be raised to the same temperature as the surface.

In the concentric-layered model, the temperature rise from the net heat flux into a layer is calculated from:

$$\frac{dT_i}{dt} = \frac{Q_i}{C_i} \qquad \textbf{(6-12)}$$

Where:
dT_i is the incremental change in temperature in layer i
Q_i is the net heat flux into the layer
C_i is the heat capacity of layer i

The heat capacity of a layer is derived as a superposition of the heat capacities of the various mass components as follows:

$$C_i = \frac{1}{m_p}\{(m_{w,i}\ C_w) + (m_{vol,i}\ C_{vol}) + (m_{char,i}\ C_{char}) + (m_{ash,i}\ C_{ash})\} \qquad \textbf{(6-13)}$$

Where:
C_w is the specific heat capacity of water (4181 J kg^{-1} K^{-1})
C_{vol} is the specific heat capacity of volatile part (~1600 J kg^{-1} K^{-1})
C_{char} is the specific heat capacity of char (1000 J kg^{-1} K^{-1}) (Dupont et al., 2014)
C_{ash} is the specific heat capacity of ash (800 J kg^{-1} K^{-1})(Eisermann et al., 1980)

The net heat flux for each layer is the sum of heat flux from the outer and inner surfaces. The heat flux at the inner surface (towards the centre of the particle) of the each layer from conductive heat flow is calculated from:

$$Q_{cond,i} = \frac{S_{i+1}\ \lambda_i\ (T_i - T_{i+1})}{\Delta r_i}.dt \qquad \textbf{(6-14)}$$

The relationship between thermal conductivity and moisture as discussed in Chapter 5 is adopted as the basis of the model for the thermal conductivity of each layer. This is derived as a superposition of the thermal conductivities of the various mass components as follows:

$$\lambda_i = \frac{1}{m_p}\{(m_{w,i}\,\lambda_w) + (m_{vol,i}\,\lambda_{vol}) + (m_{char,i}\,\lambda_{char}) + (m_{ash,i}\ \lambda_{ash})\} \qquad \textbf{(6-15)}$$

Where:

λ_w is the thermal conductivity of water (0.6 W m^{-1} K^{-1})

λ_{vol} is the thermal conductivity of volatile fraction (0.14 W m^{-1} K^{-1})

λ_{char} is the thermal conductivity of char (0.1 W m^{-1} K^{-1}) (Gupta et al., 2003)

λ_{ash} is the thermal conductivity of ash (1.0 W m^{-1} K^{-1}) (Rezaei et al., 2000)

For the external layer (layer 1), the heat flux to the outer surface is given by equations **(6-10)**, **(6-11)** and **(6-14)**.The net heat flux into the layer is then:

$$Q_{net,1} = Q_{conv} + Q_{rad} - Q_{cond,1} \qquad \textbf{(6-16)}$$

The net heat flux into each internal layer is then the sum of the heat fluxes on both inner and outer surfaces given by:

$$Q_{net,i} = Q_{cond,i} - Q_{cond,i+1} \qquad \textbf{(6-17)}$$

The net heat flux into the centre-most layer, is:

$$Q_{net,n} = Q_{cond,N} \qquad \textbf{(6-18)}$$

6.4 Mass transfer

6.4.1 Moisture evaporation

An approximation for modelling the drying rate for small particles is given by Peters (Peters, 2003) as being a function of the difference between the particle temperature and the temperature at which the initial moisture content is at equilibrium. The rate of moisture loss is also proportional to the quantity of moisture in the particle. The moisture evaporation rate can be modelled by:

$$\frac{dm_w}{dt} = \zeta\left(T_p - T_{eq}\right)m_w \qquad \text{for } T_p \geq T_{eq}$$

$$\frac{dm_w}{dt} = 0 \qquad \text{for } T_p < T_{eq} \qquad \textbf{(6-19)}$$

Where:
m_w is the mass of moisture in the particle
T_p is the temperature of the particle at time t
T_{eq} is the temperature with initial moisture at equilibrium (~310K)
ζ is a coefficient derived from the density, specific heat capacity and enthalpy of vaporisation of the water (Peters, 2003)

This model has been described in Chapter 2 in the context of thermogravimetric analysis of various biomass samples. The factor, ζ, is related to the enthalpy of evaporation of water, the heat capacity of the water and the apparent density of moisture in the particle. For a specific heat capacity of 4181 J kg^{-1} K^{-1} , enthalpy of vaporisation of 2.26x10^6 J kg^{-1} and an effective density of 1000 kg m^{-3} x proportion of moisture content, is estimated as 1.85 x M_W. For a particle with 5% moisture content, $\zeta = 0.0925$.

The energy balance associated with moisture evaporation should be accounted for in the calculation of particle temperature. As water vapour leaves the particle surface, the enthalpy of vaporisation results in a cooling effect. The effective heat flux resulting from evaporation from the surface layer is:

$$Q_{evap} = dm_w \,.H_{evap} \qquad \textbf{(6-20)}$$

Where:
Q_{evap} is the quantity of heat loss by vaporisation at the surface
H_{evap} is the enthalpy of vaporisation of water (2.26x10^6 J kg^{-1})

6.4.2 Devolatilisation

The rate of devolatilisation may be modelled in a simplified form as a first-order, single step Arrhenius reaction (see section 2.3.9) as:

$$\frac{dm_{vol}}{dt} = -m_{vol}\, A_{vol}\, exp\left(-\frac{E_{vol}}{RT_p}\right) \qquad \textbf{(6-21)}$$

Where:
m_{vol} is volatile mass content of the particle at time t
A_{vol} and E_{vol} are the reactivity pre-exponential coefficient and activation energy for devolatilisation respectively.

In the first instance, the reaction rate coefficients derived from thermogravimetic analysis (Chapter 2) can be used in the model.

6.4.3 Devolatilisation energy balance

The energy balances associated with the conversion of the volatile mass from solid phase to gas phase should be taken into account. There are two aspects to the energy balance of the devolatilisation process. Firstly, the decomposition of the complex carbohydrates into smaller hydrocarbon molecules is endothermic. Secondly, the transition from condensed phase to gas phase of volatile matter at the surface of the particle also leads to a cooling effect.

The effective cooling resulting from the enthalpy of the devolatilisation reaction is directly related to the rate of devolatilisation and the enthalpy of the decomposition reaction:

$$Q_{vol} = dm_{vol}.H_{vol} \qquad \textbf{(6-22)}$$

Where:
Q_{vol} is the quantity of heat loss by devolatilisation
H_{vol} is the enthalpy of devolatilisation

The value for the enthalpy of devolatilisation is taken as ~0.2 MJ/kg from estimated heat of pyrolysis in published literature (Kung and Kalelkar, 1973).

At the surface of the particle, the effective cooling resulting from the phase transition of products escaping the surface to the gas phase:

$$Q_{volv} = dm_{vol}\,.H_{volv} \qquad \textbf{(6-23)}$$

Where:
Q_{volv} is the heat loss from vaporisation of volatile matter

H_{volv} is the effective enthalpy of vaporisation of the products escaping the surface

The value for the enthalpy of vaporisation of organic products at the particle surface is estimated at ~0.5 MJ/kg - based on the enthalpy of vaporisation of simple hydrocarbons - CH_4, C_2H_6, C_3H_8 (Haynes and Lide, 2013).

6.4.4 Char oxidation

While other models for char oxidation might be used, as a starting point for the single particle combustion model in this study, a single-step first-order model is adopted. This validity of adopting this simplification has been discussed in section 2.3.10. The rate of char oxidation is then modelled as a single step Arrhenius reaction as:

$$\frac{dm_{char}}{dt} = -m_{char} \left[\frac{O_2}{0.21}\right]^{\eta} A_{char}\, exp\left(-\frac{E_{char}}{RT_p}\right) \qquad \textbf{(6-24)}$$

Where:
m_{char} is the mass of char (fixed carbon) in the particle at time t
A_{char} and E_{char} are the reactivity pre-exponential coefficient and activation energy for char oxidation respectively.
$[O_2]$ is the volumetric concentration of oxygen relative to air
η is the order of the reaction with respect to oxygen

Again, in the first instance, the reaction rate coefficients derived from thermo-gravimetric analysis (Chapter 2) can be used in the model. However, the reaction kinetic parameters measured are for the case where the oxygen concentration is that of air. To be representative of the combustion regime applicable to the char particle, the relative partial pressure of oxygen at the carbon surface in the particle should be accounted for (Glassman and Yetter, 2008). Assuming the partial pressure to be directly proportional to the volumetric oxygen concentration, the term $[O_2]$ is included as the volumetric concentration. This is specified relative to atmospheric oxygen concentration (21%) and is dimensionless. In the single particle combustion experiment using a methane flame, the concentration of oxygen is taken to be around 9.0% ±0.3 at the surface (see Figure 3-7).

The apparent order of the reaction, η , for carbon oxidation is reported at lower temperatures (<900K) to be in the range 0.68±0.08 (Suuberg et al., 1989). At

higher temperatures (>1200K), the apparent reaction order is reported as varying between 0.5 or 1.0 (Murphy and Shaddix, 2006, Hurt and Calo, 2001) and a value of 0.79 or 1.0 being reported for coal chars at 1223K (Karlström et al., 2011). For modelling purposes, it is possible to select a fixed value or vary the value as a function of temperature. Since the exact nature of the relationship between reaction order and temperature is unknown for the biomass materials in this study a fixed value of 0.75 is selected since this is close to satisfying most reported values.

6.4.5 Oxygen diffusion

In the char oxidation model, the oxygen concentration influences the reaction rate as given in equation **(6-24)**. A means of representing the oxygen concentration in the interior of the particle is therefore required. The extent of diffusion of oxygen into a char particle defines the so-called ‘zones of combustion’ as defined in various texts on combustion (Glassman and Yetter, 2008, Marsh, 1989). The model should aim to emulate these combustion ‘zones’ as the combustion process progresses.

Zone I: Initially, the oxygen concentration is assumed to be uniform throughout the particle. The oxygen concentration is then set to the ambient condition. In the case of the methane flame in the single particle experiment, the volumetric concentration is taken as ~10%. In zone I, this concentration level is uniform throughout the particle.

Zone II: As combustion progresses and the particle heats up, the reaction rate increases accordingly. This results in the oxygen in the interior of the particle being consumed at a faster rate than the oxygen can diffuse from the exterior. The concentration of oxygen in a given layer of the model will therefore be the net sum of the oxygen consumption in that layer and the oxygen diffusion to and from the layers either side. In zone II, there is a gradient of oxygen concentration from the surface to the interior of the particle.

Zone III: At the highest rate of reaction on the outer layers, the net oxygen concentration will be so low that the diffusion into the next interior layer will be minimal and layers lying beneath will be depleted of oxygen such that the reaction rate is retarded. In zone III, the interior layers will have almost zero

oxygen concentration. The oxygen in the outer layer will be governed by that of the gas-phase reaction zone surrounding the surface.

In the external zone at the particle surface, there is oxygen consumption in the homogeneous gas-phase reaction:

$$2CO(g) + O_2(g) \Rightarrow 2CO_2(g) \qquad \textbf{(6-25) (a)}$$

The rate of consumption of O_2 is then half the rate of production of CO which, at most, is equal to the rate of char oxidation given by equation **(6-24)**. To estimate the rate of consumption of O_2 in the external zone in the context of the experiments, it is useful to consider the case for a 1mm cube of biomass with mass of 0.5mg. The maximum rate (i.e.'worst case') of the char oxidation reaction in this case can be estimated using the following parameters:

T_{char} = 1400 K $\qquad \left[\frac{O_2}{0.2}\right]$ = 0.5

A_{char} = 1x10^5 s^{-1} $\qquad E_{char}$ = 92 kJ.mol^{-1}

This gives a rate of carbon reaction of 6.6x10^{-9} kg.s^{-1} which implies a maximum production rate for CO of 15.4x10^{-9} kg.s^{-1}. The maximum O_2 consumption in the gas phase would then be in the order of 8.8x10^{-9} kg.s^{-1}.

In the experiment the particle is inside a flame with a flow of gas over the surface. The gas velocity was estimated at 3 m.s^{-1} and the gas density at 1600K is 0.22 kg.m^{-3}. Over the projected surface area of the particle (1x10^{-6} m^2), this gives a mass flow rate of 6.6x10^{-7} kg.s^{-1}, almost 2 orders of magnitude higher than the highest estimated oxygen consumption rate. The oxygen concentration at the surface is therefore considered to be constant and equal to that of the gas flame.

For the purposes of evaluating the reaction rate in the outermost layer of the solid particle the initial oxygen concentration in that layer is equated to the oxygen concentration in the surrounding flame. The depletion of oxygen in the layer is then calculated based on the rate of its consumption in the combustion process. This can be determined from the rate of char mass conversion **(6-24)**. The principal heterogeneous reactions involved are:

$$C(s) + O_2(g) \Rightarrow CO_2(g) \qquad \textbf{(6-26) (a)}$$

$$2C(s) + O_2(g) \Rightarrow 2CO(g) \qquad \textbf{(6-26) (b)}$$

These reactions run in parallel but the relative proportions of products are dependent on the oxygen partial pressure and the temperature. An expression for the ratio of CO_2/CO produced internally in char as a function of these parameters has been derived by Tognotti et al. (Tognotti et al., 1991) as is given by:

$$\frac{\mathrm{CO_2}}{\mathrm{CO}} = 0.02\, P_{O_2}^{0.21}\, exp\left(\frac{3070}{T}\right) \qquad \textbf{(6-27)}$$

At temperatures between 1200K and 1400K and with a partial pressure of 0.1, this ratio is in the range 0.11 to 0.16. On this basis, the mass balance gives approximately 1.5kg of oxygen consumption for each 1.0kg of carbon consumption. The consumption of oxygen in each layer is then determined by the expression:

$$\frac{dm_{O_2}}{dt} = 1.5\frac{dm_{char}}{dt} \qquad \textbf{(6-28)}$$

Since the oxygen concentration in the layer is specified in terms of volume, a density of gas in the layer is required. The density of air reduces with temperature according to the following relationship:

$$\rho_{air} = \frac{353.18}{T} \qquad \textbf{(6-29)}$$

The mass of oxygen in the particle layer is:

$$m_{O_2,i} = [\mathrm{O_2}]\,\rho_{air} V_i \qquad \textbf{(6-30)}$$

The mass concentration of oxygen in the particle layer is:

$$\Phi_{O_2,i} = \frac{m_{O_2.i}}{V_i} \qquad \textbf{(6-31)}$$

The diffusion of oxygen between internal layers is calculated from:

$$\frac{dm_{O_2,i}}{dt} = \Gamma_{O_2}\frac{S_{i+1}}{\Delta r_i}\{\Phi_{O_2,i} - \Phi_{O_2,i+1}\} \qquad \textbf{(6-32)}$$

Where:

Γ_{O_2} is the diffusion coefficient for oxygen inside the particle

During combustion, the oxygen inside the particle will be within an atmosphere predominantly consisting of the combustion products CO and CO_2. If this were a static atmosphere, a diffusivity coefficient can be derived from the mean average of published data (Haynes and Lide, 2013) for O_2-CO and O_2-CO_2 systems as a function of temperature as:

$$\Gamma_{O_2,CO-CO_2} \approx 8.5 \times 10^{-10}\ T^{1.76} \qquad \text{m}^2\,\text{s}^{-1} \qquad \textbf{(6-33)}$$

In the temperature range 1200K - 1400K, this gives values of $2.2\text{x}10^{-4}$ to $2.9\text{x}10^{-4}$ $\text{m}^2\,\text{s}^{-1}$. This represents the case for the free gases but it does not account for the influence of the solid char in which the porosity and tortuosity of the structure decrease the effective diffusion. Diffusivity in char combustion has been modelled (Sotirchos and Burganos, 1986) and predict the effective diffusivity in char with porosity of 0.25 to be between 1.1 to $2.5\text{x}10^{-5}$ $\text{m}^2\,\text{s}^{-1}$ at 1400K. These values are around 0.1 times the diffusivity of the free gases given by equation **(6-33)**. The diffusivity coefficient in the model is then modified to:

$$\Gamma_{O_2,char} \approx 8.5 \times 10^{-11}\ T^{1.76} \qquad \text{m}^2\,\text{s}^{-1} \qquad \textbf{(6-34)}$$

For simplicity, this value is derived from the temperature of the char layer only and changes in the char porosity are not accounted for. For much of the char oxidation process, this is not an unreasonable approximation for the char being modelled with a constant density, shrinking particle.

6.4.6 Char reaction energy balance

Associated with the char oxidation, the energy balance of the reaction must be accounted for in the calculation of the particle's temperature. The char oxidation reaction is exothermic and the resulting effective heat flux is given by:

$$Q_{char} = dm_{char}\,.\,H_{char} \qquad \textbf{(6-35)}$$

Where:
Q_{char} is the heat generated from char oxidation
H_{char} is the enthalpy of the char reaction

H_{char} is derived from the enthalpies of formation of CO (110 kJ.mol^{-1}) and CO_2 (393 kJ.mol^{-1}). The ratio for the CO_2/CO production derived from equation **(6-27)** is taken to be around 0.15. The mean average heat of the reactions in this case is approximately 12.7 MJ.kg^{-1} of carbon.

6.5 Potassium release

6.5.1 Vaporization of potassium species

The modelling of potassium release is based on the direct vaporization of KOH and KCl from the biomass particle. These two species of potassium are stable in the gas phase in the relevant temperature range. The rate of vaporization is governed by the vapour pressures of the respective potassium species P_{KOH} and P_{KCl}. Fatehi et al.(Fatehi et al., 2015) have shown that overall potassium release rate observed in similar experiments can be modelled as a first order Arrhenius expression. This is consistent with the kinetics of the phase transition from a condensed phase to a gas phase described by the Clausius–Clapeyron relationship which is of a similar form to the Arrhenius relation. The vapour pressure can be modelled as a function of temperature using the expression:

$$P_K = B_K \, exp\left(\frac{-H_K}{R\,T_p}\right) \qquad \textbf{(6-36)}$$

Where:
P_K is the vapour pressure of the potassium species (KCl, KOH etc.)
B_K is the pre-exponential coefficient for the potassium species
H_K is the enthalpy of vaporisation for the potassium species

The kinetic parameters for KCl and KOH taken from the literature (Rodrigues and Silva Fernandes, 2007, Rudnyi et al., 1994, Gurvich et al., 1996) are:

B_{KOH} = 6.44x10^6 N.m^{-2} $\quad$ H_{KOH}=147 kJ mol^{-1}

B_{KCl} = 1.16x10^8 N.m^{-2} $\quad$ H_{KCl}=164 kJ mol^{-1}

The rate of release of potassium has been observed (Chapter 4) to be approximately proportional to the concentration of solid phase potassium species in the particle. The quantity of each K species in the gas phase in each layer of the particle is then assumed to be also dependent on the quantity of solid phase material. The mass of the gas phase potassium species can then be estimated by combining a proportional solid phase mass term and a vaporisation term from equation **(6-36)** giving:

$$m_{K(g),i} = \alpha \, m_{K(s),i} \, exp\left(\frac{-H_K}{R\,T_i}\right) \qquad \textbf{(6-37)}$$

Where:

$m_{K(g)}$ is the mass of gas phase potassium species in the volume
$m_{K(s)}$ is the mass of solid phase potassium species in the volume
α is a coefficient relating solid phase mass to gas phase mass

(In the model, a value of $\alpha = 0.065$ has been used as a best fit to the empirical data.) The mass concentration of gas-phase KOH and KCl is then be derived from the gas-phase mass and volume of each layer of the model as:

$$\Phi_{K(g),i} = \frac{m_{K(g),i}}{V_i} \qquad \textbf{(6-38)}$$

Where:
$\Phi_{K(g)}$ is the mass concentration of gas phase of potassium in layer

Having estimated the mass concentration of the potassium species in the layer of the particle, a means by which mass transfer to other layers and ultimately to the surface of the particle is required. This can be either by entrainment or by diffusion and which of these is the dominant mechanism is influenced by the dominant stage of the combustion process.

6.5.2 Devolatilisation stage

The mechanisms for the release of potassium in to the gas phase during the initial devolatilisation stage of combustion are: (i) direct vaporization of inorganic potassium (KCl and KOH); (ii) potassium arising from the combustion of organic volatiles released by pyrolysis. The latter of these is more significant in lower temperature pyrolysis processes as described by Yu and Zhang (Yu and Zhang, 2001) while, at higher temperatures there is higher vaporization of the inorganic species and the former dominates. The evaporation rate is a function of the concentration of gas-phase potassium and the rate at which the vapour is removed by either diffusion or convective mass transfer. In the devolatilisation stage, a strong convective mass transfer mechanism is provided by the Stefan flux resulting from the generation of gas-phase organic volatiles inside and at the surface of the particle. This flux will entrain the evaporated potassium species as well as any potassium bound to the organic species themselves. The release of potassium in the devolatilisation stage will then be related to both the rate of devolatilisation and the total potassium mass concentration:

$$\frac{dm_{K(E)}}{dt} = \beta\, \Phi_{K(s)}\, \frac{dm_{vol}}{dt} \qquad \textbf{(6-39)}$$

Where:
β is a coefficient relating to the rate of release by entrainment
$dm_{K(E)}$ is the mass of potassium released by entrainment

The coefficient β in this expression relates the volume of the gas phase potassium species that is entrained in the mass of volatile matter released from the particle. For the model, the value of $\beta = 1.0 \times 10^{-3}$ has been selected to fit the measured data.

6.5.3 Char combustion stage

In the char combustion stage, the mass transfer mechanism for the release of potassium is mainly governed by diffusion in the gas phase. The rate of release by diffusion can be modelled with Fick's law (Cussler, 2009). For a spherical system, the flux through the surface of the particle is proportional to the radial concentration gradient at the surface, the diffusivity coefficient and the surface area. The concentration gradient at the surface of each layer is modelled as simply the difference between the calculated gas-phase mass concentration of KOH and KCl and radial distance between successive layers. The external concentration outside the particle is taken to be zero so the release rate from the particle surface is then directly proportional to the concentration in the outer layer.

$$\frac{dm_{K(D)}}{dt} = \Gamma_K \frac{S_i}{\Delta r_i}\left\{ \Phi_{K(g),i} - \Phi_{K(g),i-1}\right\} \qquad \textbf{(6-40)}$$

Where:
Γ_K is diffusion coefficient for the gas phase potassium species

The diffusion coefficient Γ_K, is assumed to be related to a similar temperature dependency as the oxygen diffusivity given in equation **(6-34)**. Using an approximation of diffusivity derived from the relative molecular masses of gas components (Fuller et al., 1966) such that:

$$\Gamma \propto \sqrt{\frac{1}{\mathcal{M}_1} + \frac{1}{\mathcal{M}_2}} \qquad \textbf{(6-41)}$$

Where:
$\mathcal{M}_1$ and $\mathcal{M}_2$ are the molecular masses of the respective gases

Assuming that the gas phase potassium species are diffusing in, predominantly, CO, the diffusivity of the potassium species can be approximated from a factor derived from **(6-41)** and the diffusivity derived for O_2 in **(6-34)**. For KOH-CO **(6-41)** gives a factor of 0.88. In the model, the diffusivity is then taken as:

$$\Gamma_{KOH,char} = G \times \Gamma_{O_2,char} \qquad \text{m}^2\,\text{s}^{-1} \qquad \textbf{(6-42)}$$

where: $G = 8.8$

This approximation is used, in the initial case, for the potassium release model. The diffusion variable, G, can be adjusted in the model to investigate the influence of the internal diffusion mechanism on the release patterns.

6.5.4 Ash decomposition stage

For materials with relatively low potassium content, high temperature combustion may release virtually all the potassium to the gas phase by the end of the char combustion stage. For other materials with higher potassium content, a significant amount of potassium is retained in the ash particle. It is possible that much of the potassium retained in the particle at this stage will combine with other ash components such as silicon, aluminium and calcium. However, It has been noted from experimental observations in Chapter 4 that if the ash particle continues to be exposed to the high temperature flame, potassium continues to be released to the gas phase. If the potassium is in the form of different species to KOH and KCL, the release rate will be subject to a different set of kinetic parameters.

6.6 Model validation, analysis and discussion

6.6.1 Mass transfer and burn-out

The coefficients of the reaction kinetics derived from thermogravimetric analysis (Chapter 2) can be used in the model and the resulting devolatilisation times and burn-out times compared against the measured data from the single particle combustion experiments (Chapter 3). The resulting analysis for the pine sample is presented in **Table 6-1**. A comparison of the devolatilisation times and burn-out times for each model and the measured data is shown in **Figure 6-2**. In the model, the devolatilisation time is referred to as the point at

which the mass of volatile content decreases below 5μg. Similarly, the char burn-out is taken as the point at which the char mass reduces to below 5μg. These are arbitrary limits but represent 0.5% of a 1mg particle which is within the bounds of the measurement limits of the experiment.

Table 6-1 - Comparison of modelled and measured combustion characteristics (measured values from tables 2-11, 2-12 and figure 3.23)

	reaction kinetic coefficients				combustion duration coefficients			
	$\ln[A_{vol}]$	E_{vol}	$\ln[A_{char}]$	E_{char}	a_{vol}	b_{vol}	$a_{burnout}$	$b_{burnout}$
	s^{-1}	$kJ.mol^{-1}$	s^{-1}	$kJ.mol^{-1}$	duration, $t = a.m^b$			
Pine								
measured	7.0	61	11.6	92	1.33	0.59	6.1	0.66
model a	7.0	61	11.6	92	2.35	0.54	5.3	0.67
model b	9.0	61	10.6	92	1.34	0.58	6.2	0.62

Using the measured reaction kinetics parameters directly in the model (model a) produces discrepancies between the predicted devolatilisation and burn-out times and those observed in the experiment. An adjustment to the pre-exponential factors in both cases results in a model (model b) which is very close to the experimental results. It is difficult to identify where the discrepancy arises in model a since the reaction rates are sensitive to the temperature and the modelled temperature is dependent on many variables. The char reaction is also dependent on the assumed oxygen diffusion rates and resulting concentrations. Model b is adopted in the overall model since this replicates the measured data more closely.

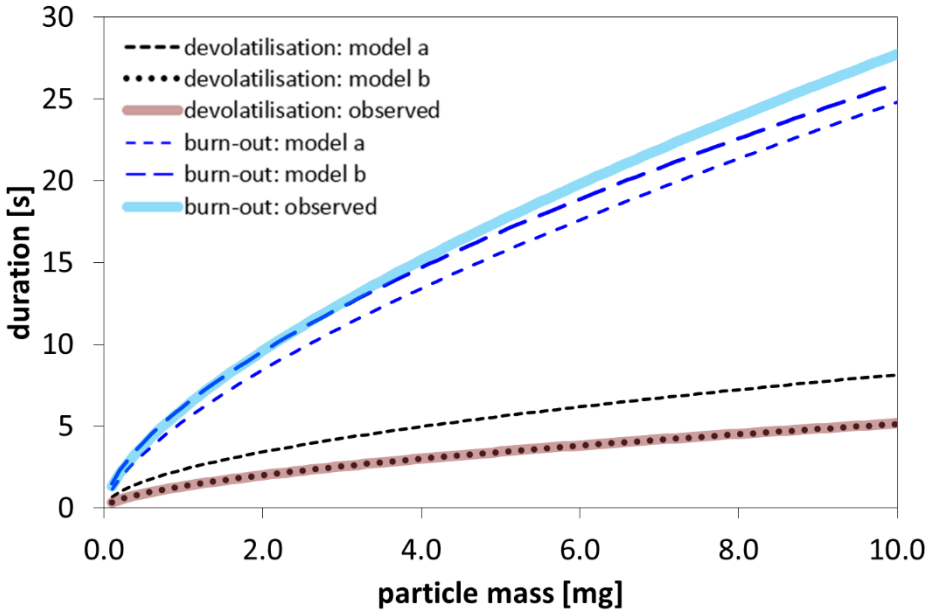

Figure 6-2 – Comparison of modelled devolatilisation time and burn-out time compared with observed behaviour for pine

Having established values for the reaction kinetics coefficients which are both realistic and produce satisfactory results for the characteristic times of devolatilisation and burn-out, other processes can be examined. The mass-loss time history of the individual components of the particle (moisture, volatile matter, char and ash) from the output of the model is shown in **Figure 6-3**. This illustrates well that the modelled processes behave as expected. The first part of the mass loss is mainly a result of the moisture evaporation. As the temperature of the particle exceeds 500K, devolatilisation starts and accelerates to rapid mass loss such that all volatiles are removed before 20% of the burn-out time has elapsed. At the end of devolatilisation, the particle temperature levels out at around 1350K and the char combustion proceeds. The rate of char combustion is fairly steady but there is a slight retardation in the rate towards the end of the burn-out as the combustion of the inner layers continues to be impeded by diffusion through the outer ash layers. The data from the same model output are shown in **Figure 6-4** but in this case, plotted against the proportion of total mass conversion. This shows a different perspective with regards the relationship between the particle temperature and the rate at which the solid particle is consumed. The effect of the heat of char oxidation on the surface temperature is clearer in this plot.

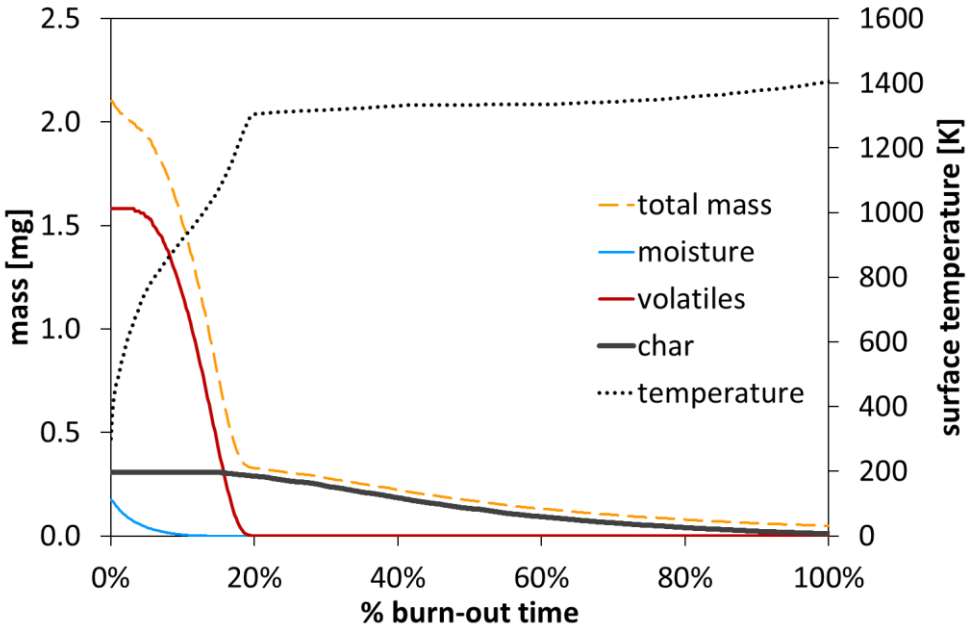

Figure 6-3 – Modelled time-history of the mass loss during combustion of a 2.1mg pine particle

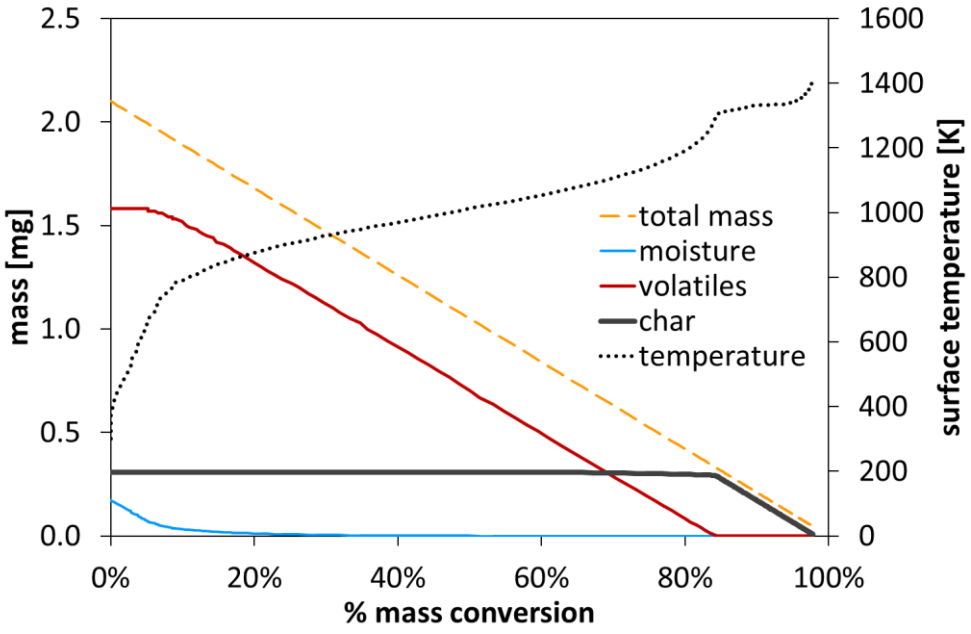

Figure 6-4 – Modelled mass loss as a proportion of total mass conversion during combustion of a 2.1mg pine particle

6.6.2 Particle surface temperature

A means of validating the surface heat transfer in the model is to compare the surface temperature of the modelled particle with that determined from thermographic imaging in the single particle combustion experiment (Chapter 3). Three example plots of the measured surface temperatures of pine particles

of varying sizes are shown in **Figure 6-5**. The surface temperature calculated by the model plotted using the parameters in **Table 6-2** are shown on the same plots for comparison.

Table 6-2 - Particle parameters for surface temperature comparison

physical parameters		
density (dry)	500	$kg.m^{-3}$
moisture content	8.0	%wt
ash content	2.0	%wt (dry)
volatile content	82.0	%wt (dry)
combustion kinetics		
E_{vol}	61	$kJ.mol^{-1}$
A_{vol}	8000	s^{-1}
E_{char}	92	$kJ.mol^{-1}$
A_{char}	40000	s^{-1}

A notable feature of the temperature profile is the retardation of heating rate between ~600K and 1000K which results from the cooling effects of devolatilisation. The modelled surface temperature profile replicates the measured data well in this respect confirming that the devolatilisation energy balances in the model are realistic. The final particle temperature of the modelled particle is also very close to the measured data which confirms that the modelled convective heat transfer and radiative heat transfer are also realistic.

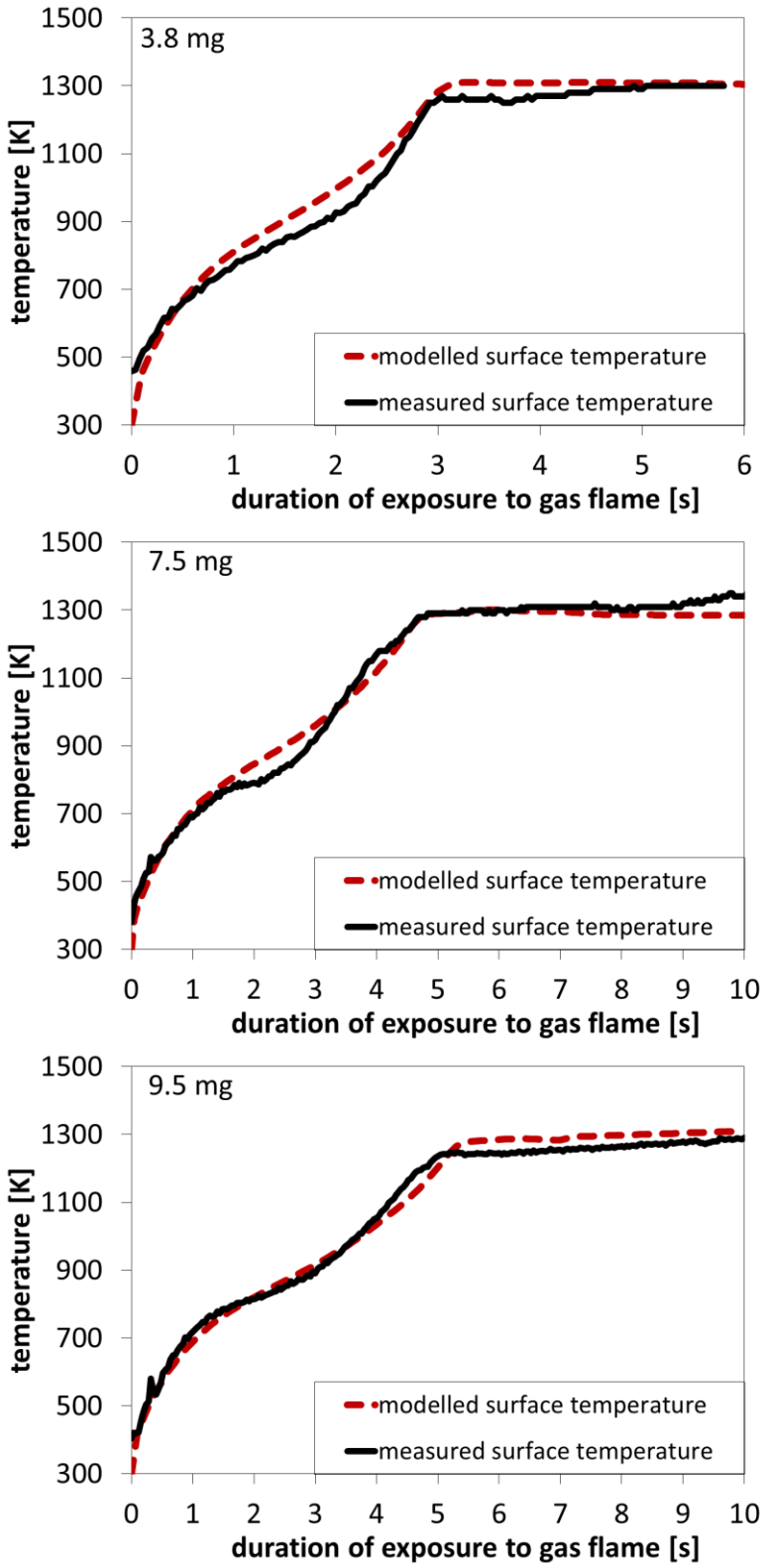

Figure 6-5 - Modelled surface temperature compared with measured data for pine particles exposed to a methane flame

6.6.3 Internal heat transfer

The concentric-layer heat transfer model can be validated by reference to the analytical solution for internal heat transfer. Calculation of the internal temperature distribution in a sphere is not a straight-forward since there is no closed-form algebraic solution. However, an infinite-series solution has been derived (Carslaw and Jaeger, 1947) and is given by:

$$T = T_S + \frac{DT_S}{\pi r}\sum_{j=1}^{\infty}\frac{(-1)^j}{n}\sin\frac{2n\pi r}{D}\,exp\left\{\frac{-2\,j^2\,\pi^3\,\lambda_p\,D\,t}{3\,m_p\,C_p}\right\} \quad \textbf{(6-43)}$$

Where:
T_S = particle surface temperature
T = internal temperature of particle at radius r (=T_0 at t=0)
t = time from initial condition (at uniform particle temperature)
r = radial distance from centre of particle
λ_p = thermal conductivity of particle
C_p= specific heat capacity of particle

The temperature differential ΔT_r between the centre of the particle and the surface is then given by:

$$\Delta T_r = 2T_S\sum_{j=1}^{\infty}(-1)^j\,exp\left\{\frac{-4\,j^2\,\pi^2\,\kappa}{D^2}\,t\right\} \quad \textbf{(6-44)}$$

Where the thermal diffusivity of the material is:

$$\kappa = \frac{\lambda_p}{\rho\,C_p} \quad \textbf{(6-45)}$$

The characteristic time for internal heat transfer is the time at which the temperature differential ΔT_rhas reduced to $1/e$, (0.3679) of the initial value, ΔT_{r0} such that:

$$\frac{\Delta T_r}{\Delta T_{r0}} = \frac{1}{e} \quad \textbf{(6-46)}$$

The first term in the numerical expansion of **(6-44)** then gives:

$$\Delta T_r = 2\,\Delta T_{r0}\,exp\left\{\frac{-4\,\pi^2\,\kappa}{D^2}\,t\right\} \quad \textbf{(6-47)}$$

Rearranging to satisfy **(6-46)** gives:

$$t_{n=1} = \left(\frac{-D^2}{4\,\pi^2\,\kappa}\right)\ln\left(\frac{1}{2e}\right) \qquad \textbf{(6-48)}$$

The characteristic time for the internal heat transfer can expressed in terms of the thermal diffusivity and particle diameter as:

$$\tau \approx 0.043\frac{D^2}{\kappa} \qquad \textbf{(6-49)}$$

The solution to the expression **(6-44)** (from a finite expansion) is shown in Figure 6-6 along with the solution from the concentric-layered model. The plot is normalised for particle diameter and thermal diffusivity. The two solutions are very closely matched including the characteristic time for the heat transfer which is indicated on the plot.

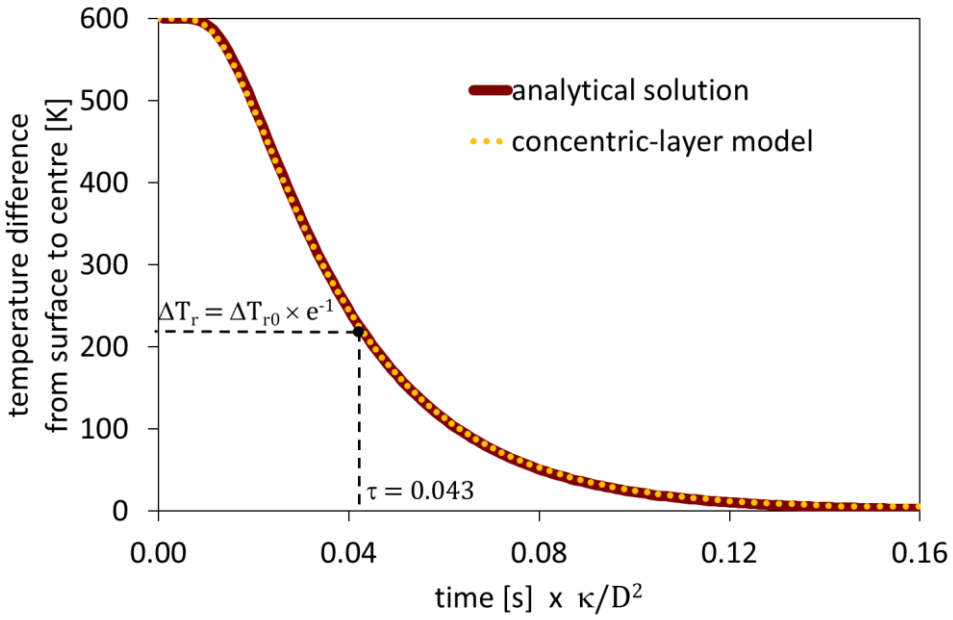

Figure 6-6 - Temperature difference between the surface and the centre of a particle as a result of heat flux to the surface

In the case of a particle placed in a hot gas flame, the initial temperature difference between surface and centre is zero. As the particle surface heats up, the temperature differential will increase and heat conduction to the centre of the particle will follow. There is another difference to the ideal case which is that there is a cooling effect from the endothermic devolatilisation as illustrated in **Figure 6-5**. The temperature of each concentric layer in the model can show how there is a different temporal-temperature profile for each layer and how

quickly the particle heats up compared to the ideal case. **Figure 6-7** shows the temperature profiles for each of 6 concentric layers (~0.1mm radial thickness) in a 1mg pine particle (~1.24mm equivalent diameter).

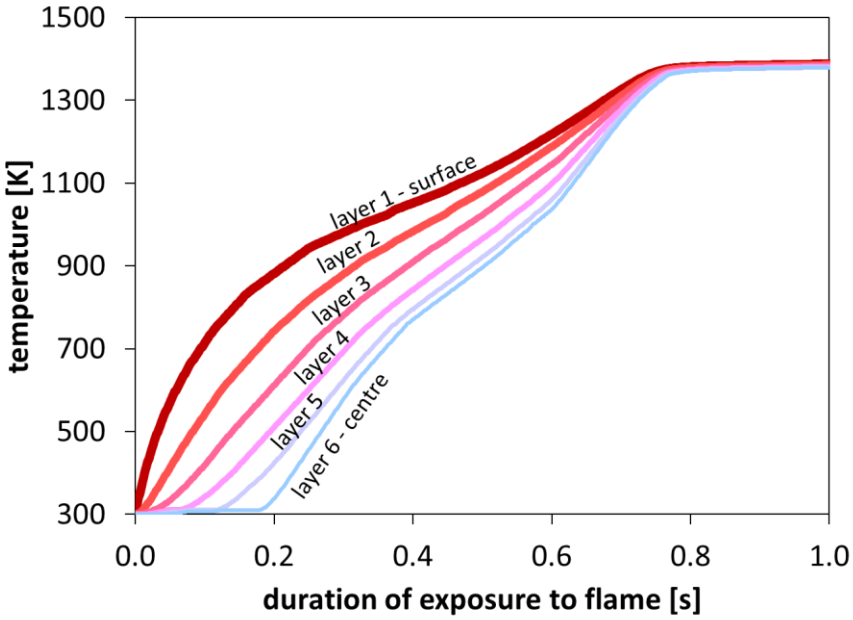

Figure 6-7 - Temporal temperature profiles in concentric layers of modelled 1mg pine particle

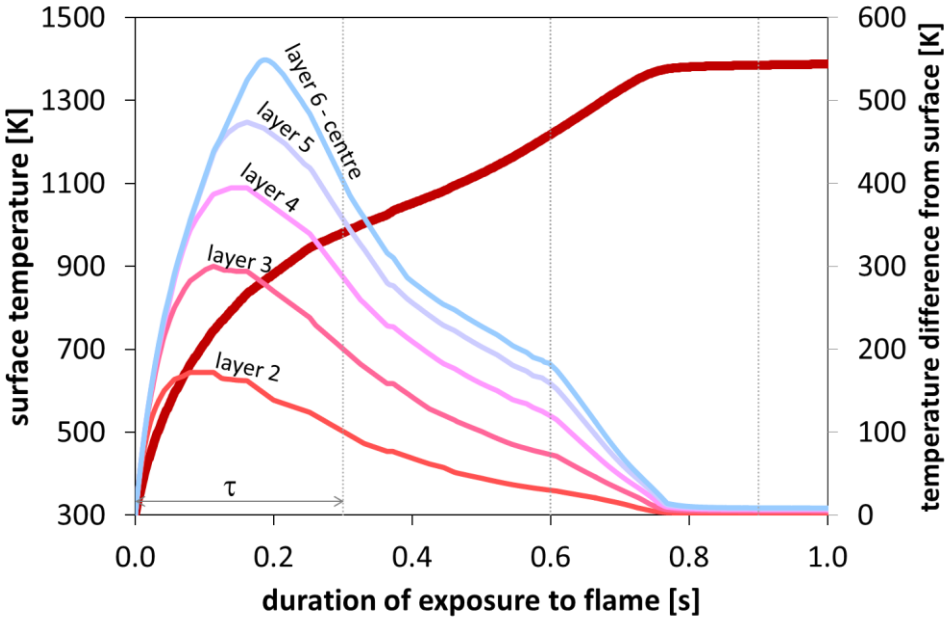

Figure 6-8 - Temperature difference between surface and concentric layers of modelled 1mg pine particle

The heating rates in each layer are distinctly different and this will affect the rate of devolatilisation in each layer. **Figure 6-8** shows the temperature differential between the surface of the particle and each concentric layer. The effect of devolatilisation can be seen in these profiles and this extends the time for the particle to reach a uniform temperature. The characteristic time for internal heat transfer calculated from the ideal case given by equation **(6-49)** is around 0.3 seconds – as indicated on the figure. The particle effectively reaches a uniform temperature around 2.5 times the ideal characteristic time.

6.6.4 Oxygen diffusion and combustion zones

The oxygen concentration in the interior of the particle determines the combustion 'zone' that characterises the process as discussed in section 6.4.5. As an example to illustrate this, a particle with the parameters given in Table 6-2 and an equivalent diameter of 2mm is modelled. **Figure 6-9** shows the surface temperature profile and particle mass as time histories (top). The profile of the oxygen concentration at certain points in the combustion process are also shown. From the initial condition (bottom left, t=0) whereby there is uniform ambient oxygen concentration throughout the particle up to around half way through the devolatilisation stage (bottom left, t=10%) the combustion regime is in zone I passing into zone II. By the end of devolatilisation (bottom left, t=20%) the oxygen concentration in most of the particle interior is at zero which corresponds to zone III regime. This continues for the first part of the char combustion stage (bottom right, t=50%). By the latter stages of the char combustion, the particle has shrunk to around 10% of the original volume and there is very little carbon in the outer layers to oxidise so more oxygen can diffuse into the centre and the combustion is in zone II. At the effective end of the char combustion stage, oxygen is diffusing to the centre of the particle.

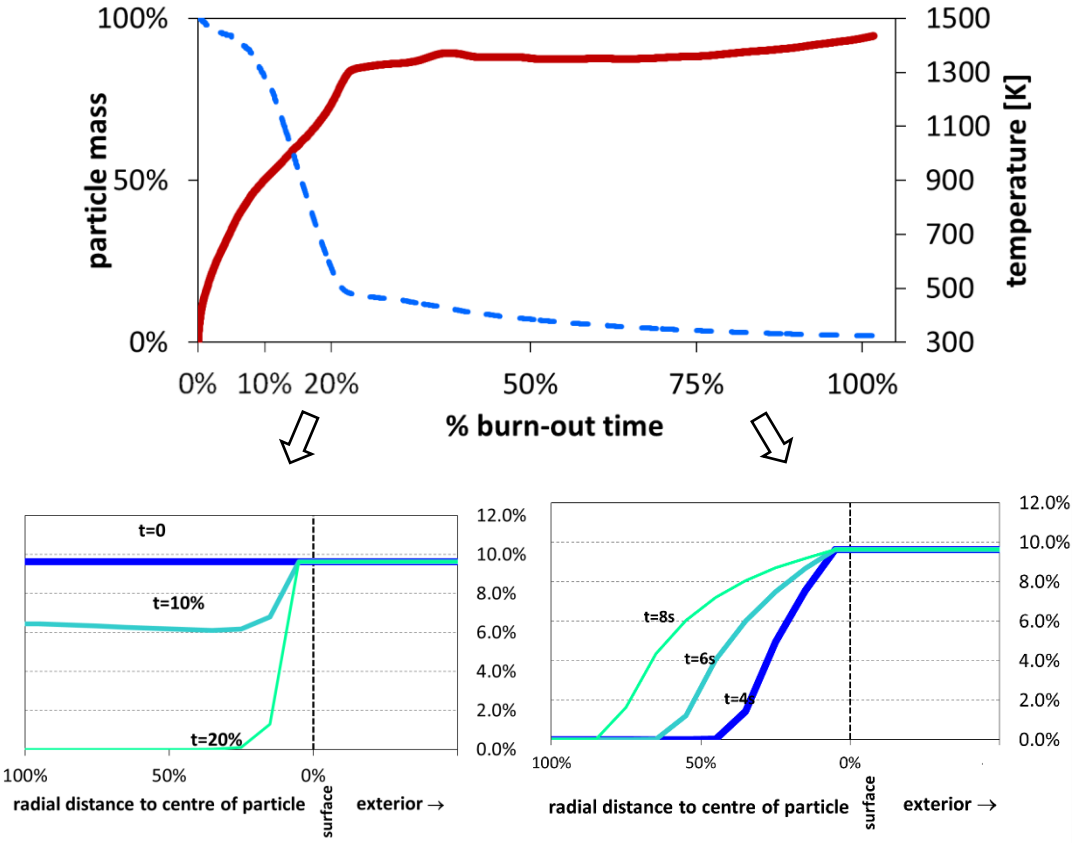

Figure 6-9 - Oxygen concentration in interior of a modelled particle with diameter=2mm

6.6.5 Potassium release

While the modelling of the combustion process of a single particle of biomass is an end in itself and aids the understanding of the observations in Chapter 3, most of the processes and phenomena discussed so far have been discussed and modelled extensively by others to various extents. Gas phase potassium release during combustion of biomass has been observed by Fatehi et al. (Fatehi et al., 2015) and Zhang et al. (Zhang et al., 2015) and both have published some results based on modelling. In this work, one of the key objectives has been to model and replicate as close as possible the observed patterns of gas phase potassium release as presented in Chapter 4. This required a suitable model of the single particle combustion to be developed and tested first. Having established that this performs reasonably close to the combustion of single particles as observed in the experiments, it is possible to examine the proposed model of potassium release and examine how close this performs to the experimental observations too.

A means of validating certain aspects of the model is to simulate the potassium release for the test samples of wood doped with potassium acetate as described in Chapter 4. The model was run with the same parameters as presented in **Table 6-2** with potassium concentrations (by mass) of 0.1%, 0.25%, 0.5% and 0.75% respectively – corresponding to the concentrations in the doped samples of wood in the experiment. The parameters for potassium release in this case were based on those of KOH species (see section 6.5.1) since it is assumed that this is the principal product of the decomposition of CH_3COOK.

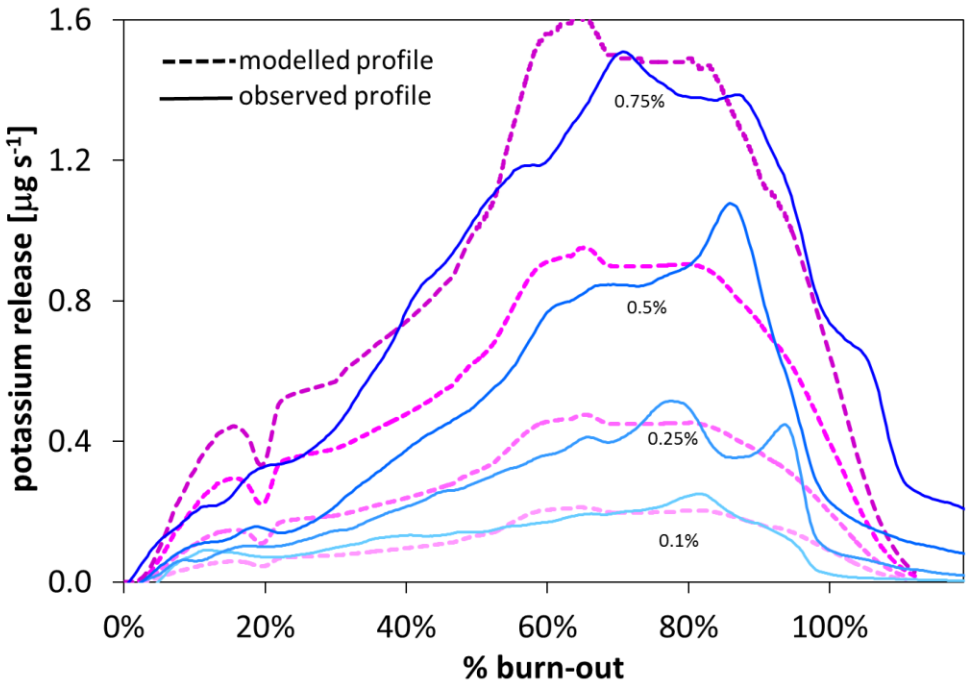

Figure 6-10 - Comparison of modelled potassium release profiles and those observed from particles of wood doped with potassium acetate

Figure 6-10 shows the results of the model (dashed lines) compared against the measured profiles. In this figure, the data are plotted against the proportion of the burn-out time for each particle, rather than the absolute time for combustion. The rationale for this is that the model has fixed reaction kinetics whereas the doped particles burned out at differing rates owing to catalysis by the potassium itself. This is then principally a qualitative comparison. The total areas under each modelled profile and the respective observed profile are approximately equal since these represent the total potassium content which is equal in both cases.

While there is some variation in the detail of the curve shapes, certain features are consistent with those observed in the experiment: (i) The peak rate of potassium release occurs just before the end of char burn-out; (ii) the peak rate of potassium release is approximately proportional to the initial mass concentration in the particle; (iii) The rate of release profile is skewed such that there is a steady (or slightly accelerating) increase before the peak and a more rapid decrease after the peak.

This analysis provides some evidence that the assumptions on the mechanisms of gas-phase KOH release (vaporization and diffusion) in the char combustion stage are substantially correct since the broad shape of the profiles are similar. There is not sufficient evidence in this case to confirm the validity of the proposed mechanism of entrainment in the devolatilisation stage, although neither are there sufficient grounds to dismiss it.

The assumptions made in the description of the single particle combustion model have been shown in section 6.6 to have produced results which replicate the experimental observations presented in Chapters 3 and 4. The modelled results are also consistent with established understanding of the combustion of single particles of biomass. Nevertheless, caution should be taken not to accept the output from any model without being aware of the limitations and possibility of misleading or erroneous predictions. With that caveat stated, the model can be used as a tool to investigate which parameters have significant influence on the observed patterns in gas-phase potassium release. In conclusion to this chapter, some of these parameters are examined with a qualitative assessment of the effects of adjusting them.

6.6.5.1 Gas-phase potassium diffusion coefficient

The chosen diffusion coefficient for the gas-phase KOH in the model was based on an estimate from equation **(6-41)** based on the calculated oxygen diffusion coefficient and the relative molecular masses of the respective gases. The initial value of the proportional factor G was estimated at 0.88. There may be considerable variation in this parameter owing to differing gas mixture inside the particle and differing porosity and tortuosity of the solid. The effects of changing this parameter can be seen in **Figure 6-11**.

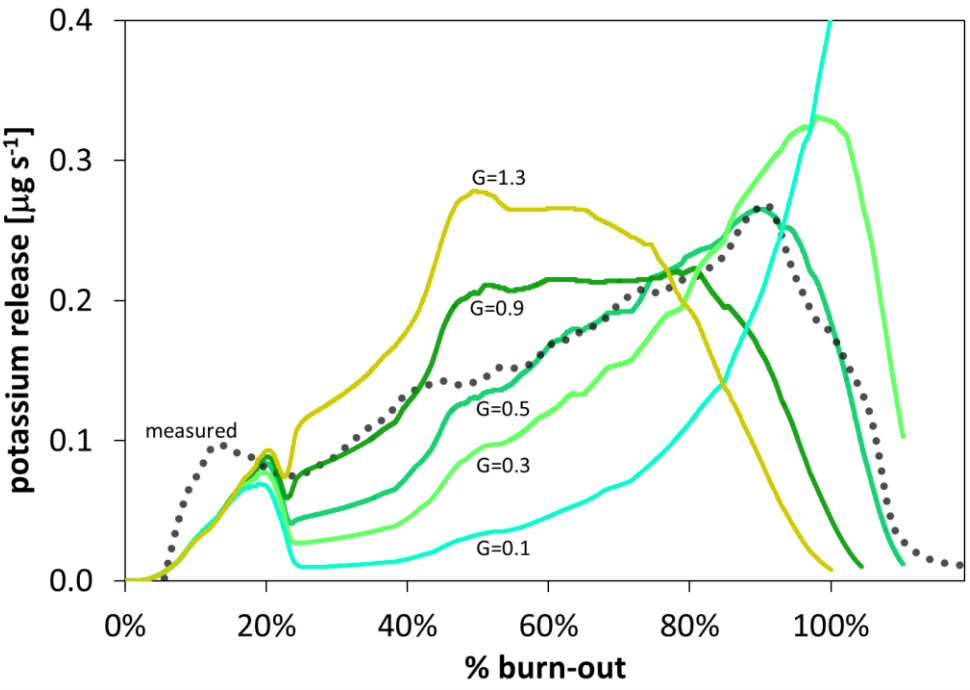

Figure 6-11 - Gas phase KOH release profiles modelled with varying diffusion coefficients

The difference in the shape of the profiles from altering the factor G from 0.1 to 1.3 is considerable. At higher diffusivity, the release of gas from the particle is rapid, at first and then the release rate appears to saturate until diminishing as the potassium content is depleted. As the diffusivity is reduced, the gas release is much impeded and the release rate increases more slowly. Where there are lower levels of release in earlier stages of combustion, the peak rate towards the end of combustion is correspondingly higher and a more distinct peak is observed. The peak is also closer to the point of burn-out. At very low diffusivity ($G = 0.1$) , the peak is very high and narrow such that about 80%of the potassium is released in the last 20% of the burn-out time.

Figure 6-12 shows modelled profiles compared against the profiles for wood pellets and willow presented in Chapter 4. The shape of the potassium release profiles for the wood pellets is modelled more effectively with a lower diffusion coefficient (G=0.3). The potassium release profiles for the willow particles are closer to the shape modelled with a higher diffusion coefficient (G=0.9). This qualitative analysis suggests that the diffusivity of the potassium species in the char is a key parameter in determining the characteristic of the potassium release.

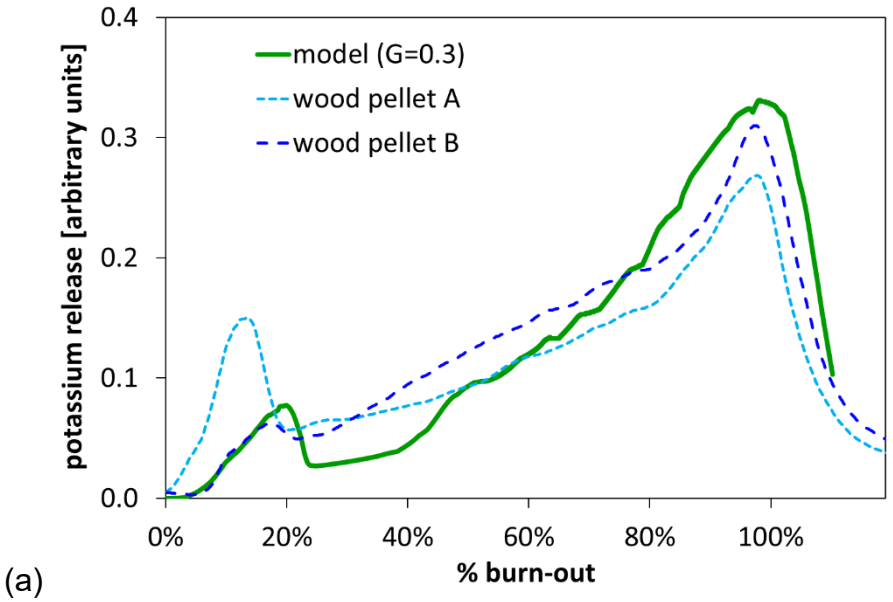

(a)

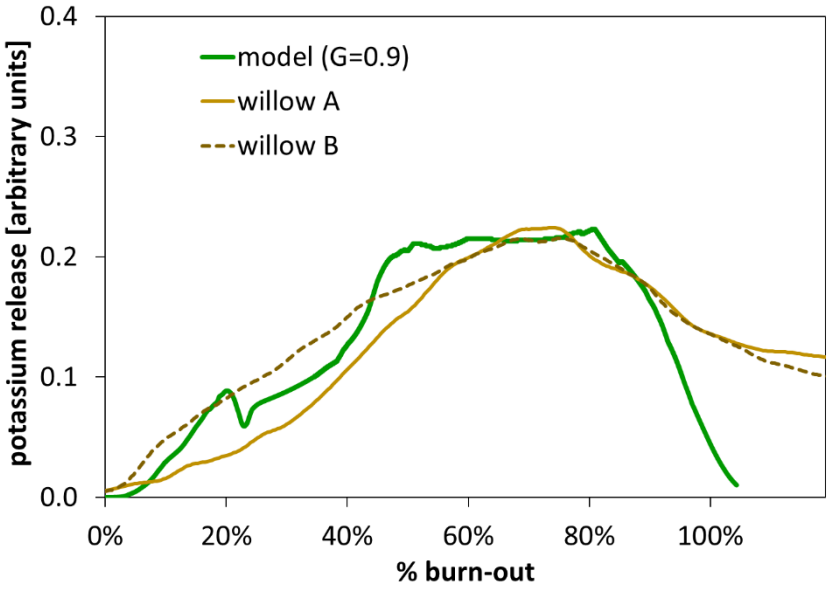

(b)

Figure 6-12 – Measured potassium release profiles for: (a) wood pellet; (b) willow compared with models with diffusion coefficients adjusted

6.6.5.2 Effects of particle size

To examine the influence of particle size on the modelled potassium release pattern, three particle masses 0.55, 1.1 and 2.2 mg (wet mass) were selected and the release profile modelled for an initial potassium content of 0.1%. The 1.1mg mass corresponds to the mass of the doped reference particles to facilitate direct comparison.

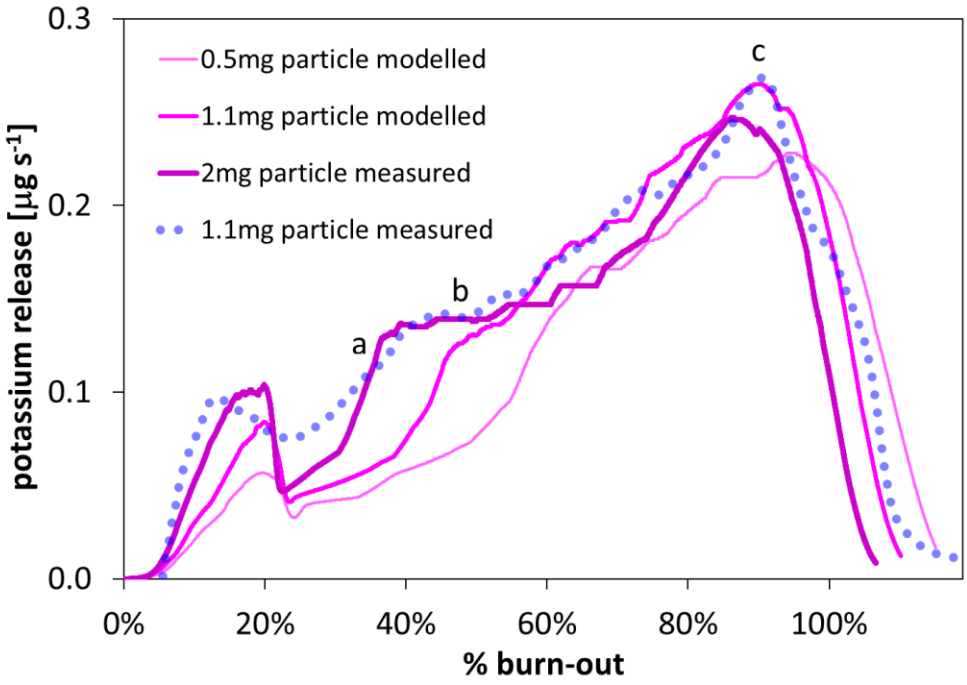

Figure 6-13 Comparison of potassium release profiles for 3 different sized particles (normalised to burn-out time)

Figure 6-13 shows the resulting release profiles normalised in the time-axis to the duration of burn-out. There is a broad similarity between the profiles for the differing sizes of particle with the notable difference being the shape of the curve immediately after devolatilisation (from 20% to 40% burn out time). As particle size increases, there is a more rapid release early in the char combustion stage (a) followed by a 'shoulder' (b) and a peak (c) roughly at the same point relative to the burn-out time. The increased release rate (a) during char combustion appears to be linked to the increasing particle temperature at this point. The shoulder (b) appears to be linked to a retardation in the heating effect of the char oxidation. This could be an artefact of the model but the profile measured form the experiments shows a similar feature so this suggests that the effect is real.

6.7 Conclusion

The capability of predicting the release of potassium to the gas phase during the combustion of biomass in large scale furnaces is very useful for understanding the potential ash fouling and corrosion potential of various fuels. Since the thermal, kinetic and physical changes that occur during combustion

all influence the rate of potassium release, it is important that modelling takes into account as many of these aspects as practical. It has been shown that use of single-step kinetic models for devolatilisation and char oxidation together are sufficient to model, with good effect, the mass loss as a function of particle temperature. Heat transfer and mass transfer internal to the particle are effectively modelled using a spherical approximation with discrete concentric layers. Using data from laboratory scale experiments as presented in Chapter 3, the modelling of devolatilisation and burn-out have been validated. The predicted surface temperature time-profile has also been validated using measurements derived from thermal imaging of the combusting particle.

Having established the model adequately simulates the combustion process that the single particles of biomass are subject to in the experimental method, it is used as the basis of modelling the release of gas-phase potassium.

The mechanisms for gas-phase potassium release were based on an assumed vaporization of KCL and KOH inside the particle and subsequent diffusion out of the surface. With the initial assumptions, the model produces temporal release patterns for potassium which display a generic form close to those observed using the flame spectroscopy technique described in Chapter 4.

By adjusting variables in the model, the effects of initial potassium concentration, particle temperature, gas-phase diffusion and particle size have been examined and these have been related to the patterns of potassium release observed in experiment. This confirms that the assumed mechanisms for gas-phase potassium release are valid. The code developed for the model is capable for further refinement and development and can be a useful tool for future investigation of solid biomass combustion.

Chapter 7
Conclusions

7.1 Summary of findings

The investigations presented in this thesis included characterisation and analysis of fourteen solid biomass fuels, typical of those used in large scale power plant. Using these fuels, three experimental studies aimed at specific aspects of biomass combustion were undertaken. These were complemented with development of a theoretical model, and the related computer code, for the combustion of single particles of biomass.

The first of the experimental studies (Chapter 3) led to a demonstration that a power-function can be can be consistently applied to describe the relationship between particle size and burn-out duration. This gives a characteristic function of each fuel which can be used to estimate the maximum particle size required for optimal burn-out. These characteristic functions, with coefficients derived from the data, also provide a means of validating and calibrating combustion models both with regards to devolatilisation and full char burn-out.

The experiment was extended to use a thermal imaging camera for observing surface temperature and the use of a photo-detector to observe potassium in the methane flame. The gas-phase potassium observations provided insights into the varied way in which potassium is released in the gas-phase throughout the different stages of the combustion process. Data obtained from this provided a basis for the modelling of gas-phase potassium release during combustion.

A further experimental study to examine the variability in thermal conductivity of biomass fuels showed the variation in thermal conductivity between the different biomass fuel types. This produced useful data for modelling the combustion of small particles of biomass.

Following from this, a model was developed incorporating a wide range of sub-models for heat transfer, mass transfer, chemical kinetics and particle structure. The full model was compared against empirical data to validate: the relationship

between particle size and burn-out duration; the surface temperature of the particle throughout the combustion process; the relationships between potassium content and patterns of gas-phase potassium release. It has been demonstrated that the model can replicate to a reasonable degree, the results of the experimental observations.

Drawing together the results of several experimental studies and analyses, the culmination of the research presented in this thesis is represented by the functioning model of a combusting particle of biomass fuel. The development of the model started as a reductive approach to the interpretation of experimental observations. With the resulting comprehensive model, the observations drawn from the experimental work are supported by theoretical analysis.

The modelling helped establish how the relationship between particle size and burn-out is affected by both reaction kinetics and heat transfer. The form of the characteristic power-function identified in experiments (Chapter 3) arises from the rate at which the particle heats up. The heat transfer to the particle is influenced by the thermal conductivity of the materials. From the results of thermal conductivity measurements (Chapter 5), this has been shown to vary between different fuel types. While the form of the relationship is given by the power function, the characteristic curve is scaled by the relative reaction rates of the fuels. These have also been shown to be variable from the thermogravimetric analyses (Chapter 2). The combined variability in these properties produces the wide range of characteristic burn-out times.

The observations of the patterns of potassium release from combusting single particles provided both qualitative and quantitative information. While some of the characteristics of the quantitative data appear intuitively sensible (e.g. the peak rate of potassium release is correlated to the overall potassium concentration in the fuel), the full picture is difficult to interpret without the assistance of the model. After having established that the modelled mechanism for potassium release agreed with the quantitative data, it was possible to use the model to investigate the influence of varying diffusion rates and particle size. This analysis was able to provide some insight into the differences in the observed release profile shapes. The similarities between the modelled profiles

and observed profiles are evidence (though not proof) to support the validity of the assumed mechanisms of potassium release in the model.

7.2 Relevance to industrial applications

Solid biomass has an important role as a fuel that can displace coal in large scale power generation. On a domestic scale, the UK is already benefitting from electricity generation from biomass combustion in large scale power stations. Between 2012 and 2015, Drax power station in North Yorkshire has proved the required technologies to be practical and commercially viable (Mason, 2015). In 2016 a second UK large scale power station at Lynemouth commenced full conversion to biomass fuel (The_Daily_Telegraph, 2016). Nevertheless, there remain a number of issues which have the potential to cause operational problems or at least diminish operational efficiency in these applications. Several of these issues have been specifically addressed in this thesis and contribute towards the following:

- Better understanding of the relationship between particle size and burn-out allowing improvement of burn-out efficiency through milling controls and plant design. In particular, a measured ‘burn-out’ index has been proposed which provides a means of comparing maximum particle size limits for optimum burn-out efficiency.

- Better understanding of the mechanism of gas-phase potassium release from biomass during combustion. Development of modelling of potassium release mechanisms enabling investigation of the behaviour of different fuels and fuel mixtures for potential improvement of ash fouling and corrosion problems.

- Data on the thermal conductivity for different biomass materials allowing better informed modelling of combustion and thermal conversion of fuel and enabling improved assessment of the risks associated with self-heating in biomass storage.

7.3 Future research

7.3.1 Modelling

Having established a functional and validated model as part of this study, there is potential for further investigation examining various details of thermal conversion and combustion. In particular, there is scope for expanding the modelling of potassium release and developing this to account for the evolution of potassium from solid-phase minerals in the ash. This should aim to replicate the ‘ash decomposition stage’ of the observed profiles which is currently not incorporated in the model. This area of investigation is connected to understanding the interaction between potassium in the fuel and the other accompanying inorganic content. The influence of other elements in the fuel on potassium release is of interest since the inherent ash content and use of certain minerals as additives may affect the partitioning of potassium between gas-phase species and solid-phase minerals. An understanding of how to control this partitioning by means of additive minerals could then lead to development of ash behaviour control. This would then allow a means of moderating the effects of ash fouling and slagging in pulverised fuel boilers.

The model is capable of being adapted to simulate other combustion conditions. Future studies may be performed to interpret observations from other single particle experiments using radiative heat transfer rather than the convective heat transfer in the flame experiments.

There is scope for studies which use a combination of the single particle combustion model with other models. One such study would be to use the modelled relationship between burn-out time and particle size together with a particle size distribution obtained from a model of the milling/grindability behaviour. This would be useful for determining optimum milling operations for specific fuels.

7.3.2 Experimental work

The instrument developed for the detection of potassium spectral emission in flames is a useful tool for future experimental studies. Using the experimental method with single particles of fuel mixed with ash-fouling mitigant additives

would allow the effects of the additive on potassium release/retention to be investigated.

The experimental method developed as a means of measuring the thermal conductivity also provides potential for future experimental work on a wider selection of materials.

7.4 Research dissemination

The research presented in this thesis has directly produced four journal publications and numerous conference presentations. It has also been the basis of reports delivered to the Future Conventional Power research consortium in fulfilment of University of Leeds remit within that project.

The fundamental characterisation data (Chapter 2) provides a useful resource for other researchers, providing extensive detail on the composition and thermal behaviour of a variety of fuels for future reference. The results have been summarised in individual data-sheets for each fuel and are included in Appendix A.

The single particle combustion experiment described in Chapter 3 formed the basis of a journal article:

> Mason, P.E., et al., *Single particle flame-combustion studies on solid biomass fuels.* Fuel, 2015. **151**(0): p. 21-30.

The experiments for detecting the gas-phase potassium release during single particle combustion which are described in Chapter 4 formed the basis of a journal article:

> Mason, P.E., et al., *Observations on the release of gas-phase potassium during the combustion of single particles of biomass*. Fuel, 2016. 182: p. 110-117

This work was also presented at the 22nd International Symposium on Combustion Processes, Poland, September 2015.

The experiments on thermal conductivity of solid biomass materials which is described in Chapter 5 formed the basis of a journal article:

Mason, P.E., et al., *Comparative Study of the Thermal Conductivity of Solid Biomass Fuels.* Energy & Fuels, 2016. **30**(3): p. 2158-216

The modelling of single particle-combustion and gas-phase potassium release as described in Chapter 6 formed the basis of a journal article:

Mason, P.E., et al., *Gas phase potassium release from a single particle of biomass during high temperature combustion.* Proceedings of the Combustion Institute, 2016

This work was also presented at the 36th International Symposium on Combustion, Seoul, August 2016.

References

AALCO. *Data Sheet - CZ121/CW614N Brass* [Online]. Aalco. Available: http://www.aalco.co.uk/datasheets [Accessed July 2014].

ADAMS, P., BOWS, A., GILBERT, P., HAMMOND, J., HOWARD, D., LEE, R., MCNAMARA, N., THORNLEY, P., WHITTAKER, C. & WHITAKER, J. 2013. Understanding Greehouse Gas Balances of Bioenergy Systems. *In:* THORNLEY, P. (ed.). Manchester: SuperGen BioEnergy Hub.

ANDERSON, D. R. 1966. Thermal Conductivity of Polymers. *Chemical Reviews,* 66**,** 677-690.

AUSTIN, L. W. & EASTMAN, C. W. 1900. On the relation between heat conductivity and density in some of the common woods. *Wisconsin Academy of Sciences, Arts, and Letters*.

BACKREEDY, R. I., FLETCHER, L. M., JONES, J. M., MA, L., POURKASHANIAN, M. & WILLIAMS, A. 2005. Co-firing pulverised coal and biomass: a modeling approach. *Proceedings of the Combustion Institute,* 30**,** 2955-2964.

BERNA, F., GOLDBERG, P., HORWITZ, L. K., BRINK, J., HOLT, S., BAMFORD, M. & CHAZAN, M. 2012. Microstratigraphic evidence of in situ fire in the Acheulean strata of Wonderwerk Cave, Northern Cape province, South Africa. *Proceedings of the National Academy of Sciences,* 109**,** E1215–E1220.

BIAGINI, E., NARDUCCI, P. & TOGNOTTI, L. 2008. Size and structural characterization of lignin-cellulosic fuels after the rapid devolatilization. *Fuel,* 87**,** 177-186.

BIERMANN, C. J. 1996. *Handbook of Pulping and Papermaking*, Elsevier Science.

BIOASH 2007. Ash and aerosol related problems in biomass combustion and co-firing. *In:* OBERNBERGER, I. (ed.).

BIOMASS_ENERY_CENTRE. 2014. *UK biomass power stations* [Online]. UK: Biomass Energy Centre / Forestry Commission. Available: http://www.biomassenergycentre.org.uk [Accessed May 2014].

BLOMBERG, T. 2011. A thermodynamic study of the gaseous potassium chemistry in the convection sections of biomass fired boilers. *Materials and Corrosion,* 62**,** 635-641.

BORZECKA-WALKER, M., FABER, A., PUDELKO, R., KOZYRA, J., SYP, A. & BOREK, R. 2011. Life cycle assessment (LCA) of crops for energy production. *Journal of Food, Agriculture & Environment,* 9**,** 698-700.

BP 2015. BP Statistical Review of World Energy BP.

BRACMORT, K. 2013. Is Biopower Carbon Neutral. USA: Congressional Reseach Service.

BRADLEY, D. & ENTWISTLE, A. G. 1961. Determination of the emissivity, for total radiation, of small diameter platinum-10% rhodium wires in the temperature range 600-1450°C. *British Journal of Applied Physics,* 12**,** 708.

BRADLEY, D. & MATTHEWS, K. J. 1968. Measurement of High Gas Temperatures with Fine Wire Thermocouples. *Journal of Mechanical Engineering Science,* 10**,** 299-305.

BRIDGEMAN, T. G., JONES, J. M., SHIELD, I. & WILLIAMS, P. T. 2008. Torrefaction of reed canary grass, wheat straw and willow to enhance solid fuel qualities and combustion properties. *Fuel,* 87**,** 844-856.

BRIDGEMAN, T. G., JONES, J. M., WILLIAMS, A. & WALDRON, D. J. 2010. An investigation of the grindability of two torrefied energy crops. *Fuel,* 89**,** 3911-3918.

BRYERS, R. W. 1996. Fireside slagging, fouling, and high-temperature corrosion of heat-transfer surface due to impurities in steam-raising fuels. *Progress in Energy and Combustion Science,* 22**,** 29-120.

CARSLAW, H. S. & JAEGER, J. C. 1947. *Conduction of Heat in Solids*, Oxford University Press.

CHERUBINI, F., BIRD, N. D., COWIE, A., JUNGMEIER, G., SCHLAMADINGER, B. & WOESS-GALLASCH, S. 2009. Energy- and greenhouse gas-based LCA of biofuel and bioenergy systems: Key issues, ranges and recommendations. *Resources Conservation and Recycling,* 53**,** 434-447.

CUSSLER, E. L. 2009. *Diffusion: Mass Transfer in Fluid Systems,* New York, Cambridge University Press.

DARVELL, L. I., MA, L., JONES, J. M., POURKASHANIAN, M. & WILLIAMS, A. 2014. Some Aspects of Modeling NOx Formation Arising from the Combustion of 100% Wood in a Pulverized Fuel Furnace. *Combustion Science and Technology,* 186**,** 672-683.

DAYTON, D. C., FRENCH, R. J. & MILNE, T. A. 1995. Direct Observation of Alkali Vapor Release during Biomass Combustion and Gasification. 1. Application of Molecular Beam/Mass Spectrometry to Switchgrass Combustion. *Energy & Fuels,* 9**,** 855-865.

DECC 2012. UK Bioenergy Strategy. *In:* CHANGE, D. O. E. C. (ed.). UK: Department for Energy and Climate Change.

DECC 2013. Electricty Market Reform Delivery Plan. *In:* DECC (ed.). UK: Department for Energy and Climate Change.

DECC 2015. Digest of United Kingdom Energy Statistics. *In:* CHANGE, D. O. E. A. C. (ed.). UK: Department for Energy and Climate Change.

DEFRA 2012. Wood waste: A short review of recent research. London: Department of Environment, Food and Rural Affairs.

DEFRA 2015. Area of Crops Grown For Bioenergy in England and the UK: 2008 - 2014. *In:* DEPARTMENT FOR ENVIRONMENT, F. A. R. A. (ed.). UK: Department for Environment, Food and Rural Affairs.

DENG, L., ZHANG, T. & CHE, D. 2013. Effect of water washing on fuel properties, pyrolysis and combustion characteristics, and ash fusibility of biomass. *Fuel Processing Technology,* 106**,** 712-720.

DEVRIES, B. J. M., VANVUUREN, D. P. & HOOGWIJK, M. M. 2007. Renewable energy sources: Their global potential for the first-half of the 21st century at a global level: An integrated approach *Energy Policy,* 35**,** 2590 - 2610.

DI BLASI, C. 2009. Combustion and gasification rates of lignocellulosic chars. *Progress in Energy and Combustion Science,* 35**,** 121-140.

DI BLASI, C., GALGANO, A. & BRANCA, C. 2011. Analysis of the Physical and Chemical Mechanisms of Potassium Catalysis in the Decomposition Reactions of Wood. *Industrial & Engineering Chemistry Research,* 50**,** 3864-3873.

DTI 2006. The Energy Challenge - Energy Review Report 2006. *In:* INDUSTRY, D. O. T. A. (ed.). UK: Department for Trade and Industry.

DUPONT, C., CHIRIAC, R., GAUTHIER, G. & TOCHE, F. 2014. Heat capacity measurements of various biomass types and pyrolysis residues. *Fuel,* 115**,** 644-651.

EIA 2014. Monthly Energy Review. *In:* ENERGY, U. D. O. (ed.). USA.

EIA 2015. International Energy Statistics. US Energy Information Administration.

EISERMANN, W., JOHNSON, P. & CONGER, W. L. 1980. Estimating thermodynamic properties of coal, char, tar and ash. *Fuel Processing Technology,* 3**,** 39-53.

ENERGY_INSTITUTE 2016. *Safe handling and storage of biomass in thermal power stations,* London.

EPSRC 2012. EP/K02115X/1 - Future Conventional Power Research Consortium. *In:* EPSRC (ed.).

ESTEBAN, L. S. & CARRASCO, J. E. 2006. Evaluation of different strategies for pulverization of forest biomasses. *Powder Technology,* 166**,** 139-151.

EU 2001. Directive 2001/80/EC - on the limitation of emissions of certain pollutants into the air from large combustion plants. The European Parliament and the Council of the European Union: ec.europa.eu.

EU 2009. Directive 2009/28/EC - on the promotion of the use of energy from renewable sources. The European Parliament and the Council of the European Union: ec.europa.eu.

EUBIA 2009. Logistic management of wood pellets: Data collection on transportation, storage and delivery management. *In:* STÉPHANE SÉNÉCHAL, G. G. (ed.) *pellets@las.* EUBIA.

EUBIA 2015. Experiences in Europe and List of Biomass Co-firing Plants. European Biomass Industry Association.

EUROSTAT 2015. Crop statistics. EU: Eurostat.

EVERARD, C. D., SCHMIDT, M., MCDONNELL, K. P. & FINNAN, J. 2014. Heating processes during storage of Miscanthus chip piles and numerical simulations to predict self-ignition. *Journal of Loss Prevention in the Process Industries,* 30**,** 188-196.

FAOSTAT 2015. Global Forest Products Facts and Figures. Food and Agriculture Organization of the United Nations.

FATEHI, H., HE, Y., WANG, Z., LI, Z. S., BAI, X. S., ALDÉN, M. & CEN, K. F. 2015. LIBS measurements and numerical studies of potassium release during biomass gasification. *Proceedings of the Combustion Institute,* 35**,** 2389-2396.

FISHER, E. M., DUPONT, C., DARVELL, L. I., COMMANDRE, J. M., SADDAWI, A., JONES, J. M., GRATEAU, M., NOCQUET, T. & SALVADOR, S. 2012. Combustion and gasification characteristics of chars from raw and torrefied biomass. *Bioresource Technology,* 119**,** 157-165.

FLOWER, M. & GIBBINS, J. 2009. A radiant heating wire mesh single-particle biomass combustion apparatus. *Fuel,* 88**,** 2418-2427.

FORESTRY_COMMISSION 2011. The UK Forestry Standard. Edinburgh: Forestry_Commission.

FORESTRY_COMMISSION 2016. Forestry Statistics. UK: Forestry Commission.

FRANDSEN, F. J., VAN LITH, S. C., KORBEE, R., YRJAS, P., BACKMAN, R., OBERNBERGER, I., BRUNNER, T. & JÖLLER, M. 2007. Quantification of the release of inorganic elements from biofuels. *Fuel Processing Technology,* 88**,** 1118-1128.

FRIEDL, A., PADOUVAS, E., ROTTER, H. & VARMUZA, K. 2005. Prediction of heating values of biomass fuel from elemental composition. *Analytica Chimica Acta,* 544**,** 191-198.

FROMM, J. 2010. Wood formation of trees in relation to potassium and calcium nutrition. *Tree Physiology,* 30**,** 1140-1147.

FULLER, E. N., SCHETTLER, P. D. & GIDDINGS, J. C. 1966. NEW METHOD FOR PREDICTION OF BINARY GAS-PHASE DIFFUSION COEFFICIENTS. *Industrial & Engineering Chemistry,* 58**,** 18-27.

GANG, L. & YONG, Y. 2006. Temperature profiling of pulverized coal flames using multicolor pyrometric and digital imaging techniques. *Instrumentation and Measurement, IEEE Transactions on,* 55**,** 1303-1308.

GAUR, S. & REED, T. B. 1995. An atlas of thermal data for biomass and other fuels. National Renewable Energy Laboratory.

GAYDON, A. G. & WOLFHARD, H. G. 1970. *Flames,* London, Chapman and Hall.

GERA, D., MATHUR, M. P., FREEMAN, M. C. & ROBINSON, A. 2002. Effect of large aspect ratio of biomass particles on carbon burnout in a utility boiler. *Energy & Fuels,* 16**,** 1523-1532.

GLASSMAN, I. & YETTER, R. A. 2008. *Combustion,* London, Academic Press.

GOERING, H. K. & SOEST, P. J. V. 1970. Forage fiber analysis (apparatus, reagent, procedures and some applications). *Agricultural Handbook.* Washington DC.

GREMYACHKIN, V. M. 2006. Kinetics of heterogeneous reactions of carbon and oxygen during combustion of porous carbon particles in oxygen. *Combustion Explosion and Shock Waves,* 42**,** 254-263.

GRONLI, M. G., VARHEGYI, G. & DI BLASI, C. 2002. Thermogravimetric analysis and devolatilization kinetics of wood. *Industrial & Engineering Chemistry Research,* 41**,** 4201-4208.

GUBBA, S. R., INGHAM, D. B., LARSEN, K. J., MA, L., POURKASHANIAN, M., TAN, H. Z., WILLIAMS, A. & ZHOU, H. 2012. Numerical modelling of the co-firing of pulverised coal and straw in a 300 MWe tangentially fired boiler. *Fuel Processing Technology,* 104**,** 181-188.

GUBBA, S. R., MA, L., POURKASHANIAN, M. & WILLIAMS, A. 2011. Influence of particle shape and internal thermal gradients of biomass particles on pulverised coal/biomass co-fired flames. *Fuel Processing Technology,* 92**,** 2185-2195.

GUDKA, B., JONES, J. M., LEA-LANGTON, A. R., WILLIAMS, A. & SADDAWI, A. 2015. A review of the mitigation of deposition and emission problems during biomass combustion through washing pre-treatment. *Journal of the Energy Institute*.

GUO, W., LIM, C. J., BI, X., SOKHANSANJ, S. & MELIN, S. 2013. Determination of effective thermal conductivity and specific heat capacity of wood pellets. *Fuel,* 103**,** 347-355.

GUPTA, M., YANG, J. & ROY, C. 2003. Specific heat and thermal conductivity of softwood bark and softwood char particles. *Fuel,* 82**,** 919-927.

GURVICH, L. V., BERGMAN, G. A., GOROKHOV, L. N., IORISH, V. S., LEONIDOV, V. Y. & YUNGMAN, V. S. 1996. Thermodynamic Properties of Alkali Metal Hydroxides. Part 1. Lithium and Sodium Hydroxides. *Journal of Physical and Chemical Reference Data,* 25**,** 1211-1276.

HABERL, H., ERB, K.-H., KRAUSMANN, F., RUNNING, S., SEARCHINGER, T. D. & SMITH, W. K. 2013. Bioenergy: how much can we expect for 2050? *Environmental Research Letters,* 8**,** 031004.

HABERL, H., SPRINZ, D., BONAZOUNTAS, M., COCCO, P., DESAUBIES, Y., HENZE, M., HERTEL, O., JOHNSON, R. K., KASTRUP, U., LACONTE, P., LANGE, E., NOVAK, P., PAAVOLA, J., REENBERG, A., VAN DEN HOVE, S., VERMEIRE, T., WADHAMS, P. & SEARCHINGER, T. 2012. Correcting a fundamental error in greenhouse gas accounting related to bioenergy. *Energy Policy,* 45**,** 18-23.

HALL, C. W. 1987. The evolution and utilization of mathematical models for drying. *Mathematical Modelling,* 8**,** 1-6.

HANKALIN, V., AHONEN, T. & RAIKO, R. On Thermal Properties of a Pyrolysing Wood Particle. Finnish-Swedish Flame Days 2009, 2009 Naantali, Finland. International Flame Research Foundation.

HASELI, Y., VAN OIJEN, J. A. & DE GOEY, L. P. H. 2011a. A detailed one-dimensional model of combustion of a woody biomass particle. *Bioresource Technology,* 102**,** 9772-9782.

HASELI, Y., VAN OIJEN, J. A. & DE GOEY, L. P. H. 2011b. Modeling biomass particle pyrolysis with temperature-dependent heat of reactions. *Journal of Analytical and Applied Pyrolysis,* 90**,** 140-154.

HASLER, P. & NUSSBAUMER, T. 1998. Particle size distribution of the fly ash from biomass combustion. *Biomass for Energy and Industry, 10th European Conference and Technology Exhibition.* Würzburg.

HAYHURST, A. N. 2013. The kinetics of the pyrolysis or devolatilisation of sewage sludge and other solid fuels. *Combustion and Flame,* 160**,** 138-144.

HAYNES, W. M. & LIDE, D. R. 2013. *CRC handbook of chemistry and physics : a ready-reference book of chemical and physical data,* Boca Raton, Fla., CRC Press.

HINDASAGERI, V., VEDULA, R. P. & PRABHU, S. V. 2013. Thermocouple error correction for measuring the flame temperature with determination of emissivity and heat transfer coefficient. *Rev Sci Instrum,* 84**,** 024902.

HINDIYARTI, L., FRANDSEN, F., LIVBJERG, H., GLARBORG, P. & MARSHALL, P. 2008. An exploratory study of alkali sulfate aerosol formation during biomass combustion. *Fuel,* 87**,** 1591-1600.

HON, D. N.-S. & SHIRAISHI, N. (eds.) 2001. *Wood and cellulosic chemistry*: Marcel Dekker.

HOSSEINABADI, H. Z., DOOSTHOSEINI, K. & LAYEGHI, M. 2012. Drying Kinetics of Poplar (Populus Deltoides) Wood Particles by a Convective Thin Layer Dryer. *Drvna Industrija,* 63.

HSU, L. J., ALWAHABI, Z. T., NATHAN, G. J., LI, Y., LI, Z. S. & ALDEN, M. 2011. Sodium and potassium released from burning particles of brown coal and pine wood in a laminar premixed methane flame using quantitative laser-induced breakdown spectroscopy. *Appl Spectrosc,* 65**,** 684-91.

HURT, R. H. & CALO, J. M. 2001. Semi-global intrinsic kinetics for char combustion modeling†. *Combustion and Flame,* 125**,** 1138-1149.

IEA 2009. Bioenergy review of status and prospects. International Energy Agency.

IISA, K., LU, Y. & SALMENOJA, K. 1999. Sulfation of Potassium Chloride at Combustion Conditions. *Energy & Fuels,* 13**,** 1184-1190.

INCROPERA, F. P. & DEWITT, D. P. 1986. *Fundamentals of heat and mass transfer*, Wiley.

IPCC 2012. *Special Report on Renewable Energy Sources and Climate Change Mitigation,* New York, NY, USA, Cambridge University Press.

IPCC 2014. Climate Change 2014: Mitigation of Climate Change - Contribution of Working Group III to the Fifth Assessment Report of the Intergovernmental Panel on Climate Change. UK: Intergovernmental Panel on Climate Change.

IPCC 2015. Climate Change 2014 Synthesis Report - Contribution of Working Groups I, II and III to the Fifth Assessment Report of the Intergovernmental Panel on Climate Change. *In:* PACHAURI, R. K. & MEYER, L. A. (eds.). Geneva: The Intergovernmental Panel On Climate Change.

IWPB 2012a. Industrial Pellets Specifications. *Wood Pellets Specifications.* Initiative Wood Pellets Buyers.

IWPB 2012b. Proposal for Sustainability Principles for Woody Biomass Sourcing and Trading. Draft ed.: Initiative Wood Pellets Buyers.

J COPELAND, D. T. 2008. National and Regional Supply/Demand Balance for Agricultural Straw in Great Britain. York: National Non-Food Crops Centre.

JANSE, A. M. C., DE JONGE, H. G., PRINS, W. & VAN SWAAIJ, W. P. M. 1998. Combustion Kinetics of Char Obtained by Flash Pyrolysis of Pine Wood. *Industrial & Engineering Chemistry Research,* 37**,** 3909-3918.

JOHNSON, E. 2009. Goodbye to carbon neutral: Getting biomass footprints right. *Environmental Impact Assessment Review,* 29**,** 165-168.

JONES, J. M., DARVELL, L. I., BRIDGEMAN, T. G., POURKASHANIAN, M. & WILLIAMS, A. 2007. An investigation of the thermal and catalytic behaviour of potassium in biomass combustion. *Proceedings of the Combustion Institute,* 31**,** 1955-1963.

JONES, J. M., SADDAWI, A., DOOLEY, B., MITCHELL, E. J. S., WERNER, J., WALDRON, D. J., WEATHERSTONE, S. & WILLIAMS, A. 2015. Low temperature ignition of biomass. *Fuel Processing Technology,* 134**,** 372-377.

KARLSTRÖM, O., BRINK, A., HUPA, M. & TOGNOTTI, L. 2011. Multivariable optimization of reaction order and kinetic parameters for high temperature oxidation of 10 bituminous coal chars. *Combustion and Flame,* 158**,** 2056-2063.

KEOLEIAN, G. A. & VOLK, T. A. 2005. Renewable Energy from Willow Biomass Crops: Life Cycle Energy, Environmental and Economic Performance. *Critical Reviews in Plant Sciences,* 24**,** 385-406.

KHAWAM, A. & FLANAGAN, D. R. 2006. Solid-State Kinetic Models: Basics and Mathematical Fundamentals. *The Journal of Physical Chemistry B,* 110**,** 17315-17328.

KIM, S. S., KANG, Y. S., LEE, H. D., KIM, J. K. & HONG, S. C. 2012. Release of potassium and sodium species during combustion of various rank

coals, biomass, sludge and peats. *Journal of Industrial and Engineering Chemistry,* 18**,** 2199-2203.

KNUDSEN, J. N., JENSEN, P. A., DAM-JOHANSEN, K., KNUDSEN, J. N., JENSEN, P. A. & DAM-JOHANSEN, K. 2004. Transformation and Release to the Gas Phase of Cl, K, and S during Combustion of Annual Biomass. *Energy & Fuels,* 18**,** 1385-1399.

KOTLAREWSKI, N. J., OZARSKA, B. & GUSAMO, B. K. 2014. *Thermal Conductivity of Papua New Guinea Balsa Wood Measured using the Needle Probe Procedure*.

KUKK, L., ROOSTALU, H., SUUSTER, E., ROSSNER, H., SHANSKIY, M. & ASTOVER, A. 2011. Reed canary grass biomass yield and energy use efficiency in Northern European pedoclimatic conditions. *Biomass and Bioenergy,* 35**,** 4407-4416.

KUNG, H.-C. & KALELKAR, A. S. 1973. On the heat of reaction in wood pyrolysis. *Combustion and Flame,* 20**,** 91-103.

LAM, P. S. 2011. *Steam explosion of biomass to produce durable wood pellets.* PhD PhD, The University of British Columbia.

LAMERS, P., JUNGINGER, M., HAMELINCK, C. & FAAIJ, A. 2012. Developments in international solid biofuel trade-An analysis of volumes, policies, and market factors. *Renewable & Sustainable Energy Reviews,* 16**,** 3176-3199.

LEWANDOWSKI, I., CLIFTON-BROWN, J. C., SCURLOCK, J. M. O. & HUISMAN, W. 2000. Miscanthus: European experience with a novel energy crop. *Biomass & Bioenergy,* 19**,** 209-227.

LI, B., SUN, Z., LI, Z., ALDÉN, M., JAKOBSEN, J. G., HANSEN, S. & GLARBORG, P. 2013. Post-flame gas-phase sulfation of potassium chloride. *Combustion and Flame,* 160**,** 959-969.

LI, H., HAN, K., WANG, Q. & LU, C. 2015. Influence of Ammonium Phosphates on Gaseous Potassium Release and Ash-Forming Characteristics during Combustion of Biomass. *Energy & Fuels,* 29**,** 2555-2563.

LI, R., KAI, X., YANG, T., SUN, Y., HE, Y. & SHEN, S. 2014. Release and transformation of alkali metals during co-combustion of coal and sulfur-rich wheat straw. *Energy Conversion and Management,* 83**,** 197-202.

LIU, Q., WANG, S., LUO, Z. & CEN, K. 2008. Catalysis Mechanism Study of Potassium Salts on Cellulose Pyrolysis by Using TGA-FTIR Analysis. *JOURNAL OF CHEMICAL ENGINEERING OF JAPAN,* 41**,** 1133-1142.

LÓPEZ, G., BASTERRA, L. A., ACUÑA, L. & CASADO, M. 2013. Determination of the Emissivity of Wood for Inspection by Infrared Thermography. *Journal of Nondestructive Evaluation,* 32**,** 172-176.

LU, H. & BAXTER, L. L. 2011. Biomass Combustion Characteristics and Implications for Renewable Energy. *In:* GRAMMELIS, P. (ed.) *Solid Biofuels for Energy: a Lower Greenhouse Gas Alternative.* Springer.

LU, H., IP, E., SCOTT, J., FOSTER, P., VICKERS, M. & BAXTER, L. L. 2010. Effects of particle shape and size on devolatilization of biomass particle. *Fuel,* 89**,** 1156-1168.

LYNCH, A. J. & ROWLAND, C. A. 2005. *The history of grinding*, Society for Mining, Metallurgy and Exploration.

MA, L., JONES, J. M., POURKASHANIAN, M. & WILLIAMS, A. 2007. Modelling the combustion of pulverized biomass in an industrial combustion test furnace. *Fuel,* 86**,** 1959-1965.

MARSH, H. 1989. *Introduction to carbon science,* Sevenoaks, UK, Butterworth.

MASON, P. E. 2015. Renewable Power in Yorkshire. theiet.org: IET.
MATSUOKA, S., KENNEDY, A. J., SANTOS, E. G. D. D., TOMAZELA, A., #XE9, L. & RUBIO, L. C. S. 2014. Energy Cane: Its Concept, Development, Characteristics, and Prospects. *Advances in Botany,* 2014**,** 13.
MATTHEWS, R., MORTIMER, N., MACKIE, E., HATTO, C., EVANS, A., MWABONJE, O., RANDLE, T., ROLLS, W., SAYCE, M. & TUBBY, I. 2012. Carbon impacts of using biomass in bioenergy and other sectors: forests. *In:* MATTHEWS, R. (ed.). Forest Research and North Energy Associates.
MCLAUGHLIN, S. B. & ADAMS KSZOS, L. 2005. Development of switchgrass (Panicum virgatum) as a bioenergy feedstock in the United States. *Biomass and Bioenergy,* 28**,** 515-535.
MILES, T. R., MILES JR, T. R., BAXTER, L. L., BRYERS, R. W., JENKINS, B. M. & ODEN, L. L. 1996. Boiler deposits from firing biomass fuels. *Biomass and Bioenergy,* 10**,** 125-138.
MILLER, B. G. 2005. *Coal Energy Systems*, Elsevier.
MISRA, M. K., RAGLAND, K. W. & BAKER, A. J. 1993. Wood ash composition as a function of furnace temperature. *Biomass & Bioenergy,* 4**,** 103-116.
MOMENI, M., YIN, C., KÆR, S. K., HANSEN, T. B., JENSEN, P. A. & GLARBORG, P. 2012. Experimental Study on Effects of Particle Shape and Operating Conditions on Combustion Characteristics of Single Biomass Particles. *Energy & Fuels,* 27**,** 507-514.
MOMENI, M., YIN, C., KNUDSEN KÆR, S. & HVID, S. L. 2013. Comprehensive Study of Ignition and Combustion of Single Wooden Particles. *Energy & Fuels,* 27**,** 1061-1072.
MONKHOUSE, P. 2011. On-line spectroscopic and spectrometric methods for the determination of metal species in industrial processes. *Progress in Energy and Combustion Science,* 37**,** 125-171.
MÜLLER, M., WOLF, K.-J., SMEDA, A. & HILPERT, K. 2006. Release of K, Cl, and S Species during Co-combustion of Coal and Straw. *Energy & Fuels,* 20**,** 1444-1449.
MURPHY, J. J. & SHADDIX, C. R. 2006. Combustion kinetics of coal chars in oxygen-enriched environments. *Combustion and Flame,* 144**,** 710-729.
NIU, Y. Q., DU, W. Z., TAN, H. Z., XU, W. G., LIU, Y. Y., XIONG, Y. Y. & HUI, S. 2013. Further study on biomass ash characteristics at elevated ashing temperatures: The evolution of K, Cl, S and the ash fusion characteristics. *Bioresource Technology,* 129**,** 642-645.
NOWAKOWSKI, D. J., JONES, J. M., BRYDSON, R. M. D. & ROSS, A. B. 2007. Potassium catalysis in the pyrolysis behaviour of short rotation willow coppice. *Fuel,* 86**,** 2389-2402.
NUSSBAUMER, T. 2003. Combustion and Co-combustion of Biomass: Fundamentals, Technologies, and Primary Measures for Emission Reduction†. *Energy & Fuels,* 17**,** 1510-1521.
ORFAO, J. J. M., ANTUNES, F. J. A. & FIGUEIREDO, J. L. 1999. Pyrolysis kinetics of lignocellulosic materials - three independent reactions model. *Fuel,* 78**,** 349-358.
PARIKKA, M. 2004. Global biomass fuel resources. *Biomass & Bioenergy,* 27**,** 613-620.
PETERS, B. 2003. *Thermal conversion of solid fuels*, WIT Press.

PHYLLIS2 2013. Phyllis2 - Database for biomass and waste. Energy Research Centre of the Netherlands ECN.

PORTEIRO, J., MÍGUEZ, J. L., GRANADA, E. & MORAN, J. C. 2006. Mathematical modelling of the combustion of a single wood particle. *Fuel Processing Technology,* 87**,** 169-175.

POTASH&PHOSPHATE_INSTITUTE 1998. Potassium for Agriculture. *In:* ARMSTRONG, D. L. (ed.) *Better Crops with Plant Food.* USA: International Plant Nutrition Institute.

PRICE, D. M. & JARRATT, M. 2002. Thermal conductivity of PTFE and PTFE composites. *Thermochimica Acta,* 392–393**,** 231-236.

PRIESTLEY, J. 1777. *Experiments and Observations On Different Kinds of Air,* London, J. Johnson.

RANZ, W. E. & MARSHALL, W. R. 1952. EVAPORATION FROM DROPS .1. *Chemical Engineering Progress,* 48**,** 141-146.

RAVEENDRAN, K., GANESH, A. & KHILAR, K. C. 1996. Pyrolysis characteristics of biomass and biomass components. *Fuel,* 75**,** 987-998.

RAZNJEVIC, K. 1976. *Handbook of Thermodynamic Tables and Charts,* New York, McGraw-Hill.

REZAEI, H. R., GUPTA, R. P., BRYANT, G. W., HART, J. T., LIU, G. S., BAILEY, C. W., WALL, T. F., MIYAMAE, S., MAKINO, K. & ENDO, Y. 2000. Thermal conductivity of coal ash and slags and models used. *Fuel,* 79**,** 1697-1710.

RIAZA, J., KHATAMI, R., LEVENDIS, Y. A., ÁLVAREZ, L., GIL, M. V., PEVIDA, C., RUBIERA, F. & PIS, J. J. 2014. Combustion of single biomass particles in air and in oxy-fuel conditions. *Biomass and Bioenergy,* 64**,** 162-174.

RÖDER, M., WHITTAKER, C. & THORNLEY, P. 2015. How certain are greenhouse gas reductions from bioenergy? Life cycle assessment and uncertainty analysis of wood pellet-to-electricity supply chains from forest residues. *Biomass and Bioenergy,* 79**,** 50-63.

RODRIGUES, P. C. R. & SILVA FERNANDES, F. M. S. 2007. Phase diagrams of alkali halides using two interaction models: A molecular dynamics and free energy study. *The Journal of Chemical Physics,* 126**,** 024503.

RSPB, GREENPEACE & FRIENDS_OF_THE_EARTH 2013. Dirtier Than Coal? Why Governement plans to subsidise burning trees are bad news for the planet. *In:* RSPB, GREENPEACE & FRIENDS_OF_THE_EARTH (eds.).

RUDNYI, E. B., BONNELL, D. W. & HASTIE, D. W. 1994. Vaporization thermodynamics of KCl - Combined processing of total vapor pressure and evaporation rates. *Moscow University Chemistry Bulletin,* 35**,** 291-308.

SAASTAMOINEN, J., AHO, M., MOILANEN, A., SØRENSEN, L. H., CLAUSEN, S. & BERG, M. 2010. Burnout of pulverized biomass particles in large scale boiler – Single particle model approach. *Biomass and Bioenergy,* 34**,** 728-736.

SADDAWI, A., JONES, J. M. & WILLIAMS, A. 2012. Influence of alkali metals on the kinetics of the thermal decomposition of biomass. *Fuel Processing Technology,* 104**,** 189-197.

SADDAWI, A., JONES, J. M., WILLIAMS, A. & LE COEUR, C. 2011. Commodity Fuels from Biomass through Pretreatment and Torrefaction:

Effects of Mineral Content on Torrefied Fuel Characteristics and Quality. *Energy & Fuels,* 26**,** 6466-6474.
SADDAWI, A., JONES, J. M., WILLIAMS, A. & WOJTOWICZ, M. A. 2010. Kinetics of the Thermal Decomposition of Biomass. *Energy & Fuels,* 24**,** 1274-1282.
SALINERO, J., GÓMEZ-BAREA, A., TRIPIANA, M. & LECKNER, B. 2016. Measurement of char surface temperature in a fluidized bed combustor using pyrometry with digital camera. *Chemical Engineering Journal,* 288**,** 441-450.
SALZMANN, R. & NUSSBAUMER, T. 2001. Fuel Staging for NOx Reduction in Biomass Combustion: Experiments and Modeling. *Energy & Fuels,* 15**,** 575-582.
SCHOFIELD, K. 2012. The chemical nature of combustion deposition and corrosion: The case of alkali chlorides. *Combustion and Flame,* 159**,** 1987-1996.
SCOTT, S. A., DENNIS, J. S., DAVIDSON, J. F. & HAYHURST, A. N. 2006. An algorithm for determining the kinetics of devolatilisation of complex solid fuels from thermogravimetric experiments. *Chemical Engineering Science,* 61**,** 2339-2348.
SHPILRAIN, E. E. 2011. Air (Properties of). *In:* HEWITT, G. F. (ed.) *Thermopedia.* Online: Semantic Globe Thermal Sciences.
SJÖSTRÖM, J. & BLOMQVIST, P. 2014. Direct measurements of thermal properties of wood pellets: Elevated temperatures, fine fractions and moisture content. *Fuel,* 134**,** 460-466.
SLADE, R., SAUNDERS, R., GROSS, R. & BAUEN, A. 2011. Energy from biomass: the size of the global resource. *In:* SLADE, R. (ed.). UKERC.
SMEETS, E. M. W., FAAIJ, A. P. C., LEWANDOWSKI, I. M. & TURKENBURG, W. C. 2007. A bottom-up assessment and review of global bio-energy potentials to 2050. *Progress in Energy and Combustion Science,* 33**,** 56-106.
SORVAJÄRVI, T., DEMARTINI, N., ROSSI, J. & TOIVONEN, J. 2014. In Situ Measurement Technique for Simultaneous Detection of K, KCl, and KOH Vapors Released During Combustion of Solid Biomass Fuel in a Single Particle Reactor. *Applied Spectroscopy,* 68**,** 179-184.
SOTIRCHOS, S. V. & BURGANOS, V. N. 1986. Intraparticle diffusion and char combustion. *Chemical Engineering Science,* 41**,** 1599-1609.
SPINELLI, R., CAVALLO, E., FACELLO, A., MAGAGNOTTI, N., NATI, C. & PALETTO, G. Performance and energy efficiency of alternative comminution principles: Chipping versus grinding. *Scandinavian Journal of Forest Research,* 27**,** 393-400.
STANDARD, A. S. T. M. 2013. ASTM D1106-96 - Standard Test Method for Acid-Insoluble Lignin in Wood. West Conshohocken, PA: ASTM International.
STANDARD, B. S. I. 2012. PAS 111:2012 Specification for the requirements and test methods for processing waste wood BSI.
STANDARD, C. E. N. 2006a. CEN/TS 15370-1:2006 - Solid biofuels. Method for the determination of ash melting behaviour. Characteristic temperatures method. BSI.
STANDARD, C. E. N. 2009a. BS EN 14774-3:2009 Solid biofuels - Determination of moisture content. Oven dry method. Moisture in general analysis sample. BSI.

STANDARD, C. E. N. 2009b. BS EN 14775:2009 Solid biofuels - Determination of ash content. BSI.
STANDARD, C. E. N. 2009c. BS EN 14918:2009 Solid Biofuels - Determination of calorific value. BSI.
STANDARD, C. E. N. 2009d. BS EN 15148:2009 Solid biofuels - Determination of the content of volatile matter. BSI.
STANDARD, C. E. N. 2010. BS EN 14961-1:2010 Solid biofuels Fuel specifications and classes - General requirements. BSI.
STANDARD, C. E. N. 2011a. BS EN 14780:2011 Solid biofuels - Sample preparation. BSI.
STANDARD, C. E. N. 2011b. BS EN 15104:2011 Solid biofuels - Determination of total content of carbon, hydrogen and nitrogen - Instrumental methods. BSI.
STANDARD, C. E. N. 2011c. BS EN 15290:2011 Solid biofuels - Determination of major elements. BSI.
STANDARD, I. S. O. 2006b. ISO 16472 - Animal feeding stuffs - Determination of amylase-treated neutral detergent fibre content (aNDF).
STANDARD, I. S. O. 2008. ISO 13906 - Animal feeding stuffs - Determination of acid detergent fibre (ADF) and acid detergent lignin (ADL) contents.
STEPHENSON, A. L. & MACKAY, D. J. C. 2014. Life Cycle Impacts of Biomass Electricity in 2020. Department of Energy and Climate Change.
SUUBERG, E. M., WÓJTOWICZ, M. & CALO, J. M. 1989. Reaction order for low temperature oxidation of carbons. *Symposium (International) on Combustion,* 22**,** 79-87.
SUZUKI, S., SHINTANI, H., PARK, S.-Y., SAITO, K., LAEMSAK, N., OKUMA, M. & IIYAMA, K. 1998. Preparation of Binderless Boards from Steam Exploded Pulps of Oil Palm *Holzforschung - International Journal of the Biology, Chemistry, Physics and Technology of Wood.*
TEMMERMAN, M., JENSEN, P. D. & HEBERT, J. 2013. Von Rittinger theory adapted to wood chip and pellet milling, in a laboratory scale hammermill. *Biomass & Bioenergy,* 56**,** 70-81.
THE_DAILY_TELEGRAPH. 2016. RWE sells Lynemouth power plant to EPH ahead of biomass conversion. *The Daily Telegraph*, 7 January 2016.
THE_GUARDIAN. 2014. Drax drops 13% as government changes subsidy terms / Drax surges 5% after winning court ruling against government / Drax admits defeat on state subsidy as court of appeal rules for government *The Guardian*, 23 April / 14 July / 7 August 2014.
THERMOPTICS. *Data Sheet - DN505-05 subminiature proportionally controlled heater* [Online]. ThermOptics.com. Available: http://thermoptics.com [Accessed July 2014.
THOMAS, P. H. & BOWES, P. C. 1961. Some aspects of the self-heating and ignition of solid cellulosic materials. *British Journal of Applied Physics,* 12**,** 222.
THORNLEY, P., TOMEI, J. & UPHAM, P. 2008. Supergen Biomass and Bioenergy Consortium**:** Resource Assessment - Feedstock Properties.
THUNMAN, H., DAVIDSSON, K. & LECKNER, B. 2004. Separation of drying and devolatilization during conversion of solid fuels. *Combustion and Flame,* 137**,** 242-250.
THUNMAN, H. & LECKNER, B. 2002. Thermal conductivity of wood - models for different stages of combustion. *Biomass and Bioenergy,* 23**,** 47-54.

THUNMAN, H., LECKNER, B., NIKLASSON, F. & JOHNSSON, F. 2002. Combustion of wood particles—a particle model for eulerian calculations. *Combustion and Flame,* 129**,** 30-46.

TOGNOTTI, L., LONGWELL, J. P. & SAROFIM, A. F. 1991. The products of the high temperature oxidation of a single char particle in an electrodynamic balance. *Twenty-Third International Symposium on Combustion,* 23**,** 1207-1213.

TRITT, M. T. & WESTON, D. 2004. Measurement techniques and considerations for determining thermal conductivity of bulk materials. *In:* TRITT, M. T. (ed.) *Thermal Conductivity - Theory, Properties and Applications.* Springer.

UK_FOREST_RESEARCH 2015. Biomass Energy Centre.

UK_GOVERNMENT 2007. The Large Combustion Plants (National Emission Reduction Plan) Regulations 2007. UK.

UK_GOVERNMENT 2008. Climate Change Act 2008 (c.27). UK.

USEWOODFUELSCOTLAND. 2014. *Pelletising* [Online]. Forestry Commission Scotland. Available: http://www.usewoodfuel.co.uk/ [Accessed March 2014].

VAN KREVELEN, D. W. 1950. Graphical-statistical method for the study of structure and reaction processes of coal. *Fuel,* 29**,** 269-84.

VAN LITH, S. C., ALONSO-RAMÍREZ, V., JENSEN, P. A., FRANDSEN, F. J. & GLARBORG, P. 2006. Release to the Gas Phase of Inorganic Elements during Wood Combustion. Part 1: Development and Evaluation of Quantification Methods. *Energy & Fuels,* 20**,** 964-978.

VAN LITH, S. C., JENSEN, P. A., FRANDSEN, F. J. & GLARBORG, P. 2008. Release to the Gas Phase of Inorganic Elements during Wood Combustion. Part 2: Influence of Fuel Composition. *Energy & Fuels,* 22**,** 1598-1609.

VAN LOO, S. & KOPPEJAN, J. 2008. *The handbook of biomass combustion and co-firing*, Earthscan.

VASSILEV, S. V., BAXTER, D. & VASSILEVA, C. G. 2013. An overview of the behaviour of biomass during combustion: Part I. Phase-mineral transformations of organic and inorganic matter. *Fuel,* 112**,** 391-449.

WEC 2013. World Energy Scenarios: Composing energy futures to 2050

WERKELIN, J., SKRIFVARS, B.-J., ZEVENHOVEN, M., HOLMBOM, B. & HUPA, M. 2010. Chemical forms of ash-forming elements in woody biomass fuels. *Fuel,* 89**,** 481-493.

WESTBERG, H. M., BYSTRÖM, M. & LECKNER, B. 2003. Distribution of Potassium, Chlorine, and Sulfur between Solid and Vapor Phases during Combustion of Wood Chips and Coal. *Energy & Fuels,* 17**,** 18-28.

WILLIAMS, A., POURKASHANIAN, M. & JONES, J. M. 2001. Combustion of pulverised coal and biomass. *Progress in Energy and Combustion Science,* 27**,** 587-610.

XING, P., MASON, P. E., CHILTON, S., LLOYD, S., JONES, J. M., WILLIAMS, A., NIMMO, W. & POURKASHANIAN, M. 2016. A comparative assessment of biomass ash preparation methods using X-ray fluorescence and wet chemical analysis. *Fuel,* 182**,** 161-165.

YANG, H., YAN, R., CHEN, H., LEE, D. H. & ZHENG, C. 2007. Characteristics of hemicellulose, cellulose and lignin pyrolysis. *Fuel,* 86**,** 1781-1788.

YANG, Y. B., SHARIFI, V. N., SWITHENBANK, J., MA, L., DARVELL, L. I., JONES, J. M., POURKASHANIAN, M. & WILLIAMS, A. 2008. Combustion of a single particle of biomass. *Energy & Fuels,* 22**,** 306-316.

YIN, C. 2016. Effects of moisture release and radiation properties in pulverized fuel combustion: A CFD modelling study. *Fuel,* 165**,** 252-259.

YIN, C., ROSENDAHL, L., K. KÆR, S. & J. CONDRA, T. 2004. Use of numerical modeling in design for co-firing biomass in wall-fired burners. *Chemical Engineering Science,* 59**,** 3281-3292.

YU, C. & ZHANG, W. 2001. Modelling Potassium Release in Biomass Pyrolysis. *In:* BRIDGEWATER, A. V. (ed.) *Progress in Thermochemical Biomass Conversion.* Oxford: Blackwell Science.

YU, Z.-T., XU, X., FAN, L.-W., HU, Y.-C. & CEN, K.-F. 2011. Experimental Measurements of Thermal Conductivity of Wood Species in China: Effects of Density, Temperature, and Moisture Content. *Forest Products Journal,* 61**,** 130-135.

ZANCHI, G., PENA, N. & BIRD, N. 2012. Is woody bioenergy carbon neutral? A comparative assessment of emissions from consumption of woody bioenergy and fossil fuel. *Global Change Biology Bioenergy,* 4**,** 761-772.

ZHANG, Z.-H., SONG, Q., ALWAHABI, Z. T., YAO, Q. & NATHAN, G. J. 2015. Temporal release of potassium from pinewood particles during combustion. *Combustion and Flame,* 162**,** 496-505.

ZINGG, T. 1935. *Beitrag zur Schotteranalyse.* PhD, ETH Zurich.

Appendix A

Solid biomass fuel data sheets

Willow A	unit	ar	dry	daf
Proximate Analysis				
Moisture content	wt%	8.3	-	-
Ash content	wt%	5.0	5.4	-
Volatile matter	wt%	71.5	78.0	82.5
Fixed carbon	wt%	15.2	16.6	17.5
Ultimate Analysis				
Carbon	wt%	42.9	46.8	49.5
Hydrogen	wt%	6.0	5.5	5.8
Nitrogen	wt%	0.4	0.5	0.5
Sulphur	wt%	0.1	0.1	0.1
Oxygen	wt%	37.3	41.8	44.1
Biochemical composition				
Cellulose	wt%	13.7	14.6	15.4
Hemicellulose	wt%	49.8	52.9	55.8
Lignin	wt%	24.7	26.3	27.7
Extractives	wt%	1.0	1.0	1.1
Calorific Values				
Net calorific value	MJ/kg		17.7	18.7
Gross calorific value	MJ/kg	17.3	18.9	20.0
Density				
Density of single particle	kg/m^3	490	± 35	
Bulk density of pellets	kg/m^3			

INORGANIC CONTENT				
Major Elements		**WCA**	**EDX**	**XRF**
Na	ppm (dry)		400	
Mg	ppm (dry)		565	
Al	ppm (dry)		1247	
Si	ppm (dry)		5812	
P	ppm (dry)		800	
S	ppm (dry)		2635	
Cl	ppm (dry)	700	282	
K	ppm (dry)	2400	*2400*	
Ca	ppm (dry)		7200	
Ti	ppm (dry)		188	
Mn	ppm (dry)		165	
Fe	ppm (dry)		1779	
Trace Elements		**ICP**		
Zn	ppm (dry)	107		
Pb	ppm (dry)	52		
Ash Composition		**WCA**	**EDX**	**XRF**
Na_2O	wt% (ash)	1.66%		1.59%
MgO	wt% (ash)	2.24%		1.75%
Al_2O_3	wt% (ash)	4.74%		4.22%
SiO_2	wt% (ash)	41.0%		35.1%
P_2O_5	wt% (ash)	2.99%		2.71%
K_2O	wt% (ash)	5.90%		4.45%
CaO	wt% (ash)	20.2%		18.5%
TiO_2	wt% (ash)	0.36%		0.69%
MnO	wt% (ash)	0.15%		0.13%
Fe_2O_3	wt% (ash)	4.26%		3.40%

COMBUSTION				
Single Particle Combustion Data				
$t = a.m^{b}$ (m = dry mass in mg)		**a**	**b**	**units**
Ignition delay		0.11	0.27	s
Volatile flame		1.25	0.60	s
Char combustion		2.56	0.73	s
Total burn-out time		3.95	0.67	s
Combustion Kinetics				
$k = A.exp^{(-E/RT)}$	**ln(A)**	**units**	**E**	**units**
Devolatilisation	11.5	s^{-1}	80	J/kg
Char combustion	11.5	s^{-1}	95	J/kg

PHOTOGRAPHS

AS RECEIVED

MILLED

PULVERIZED

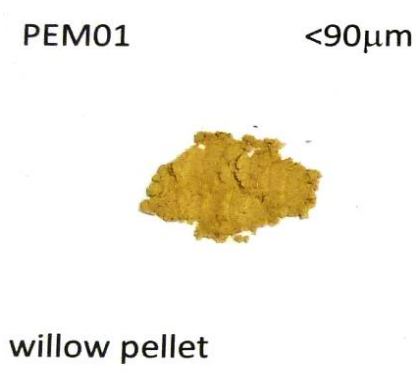

Willow B	unit	ar	dry	daf
Proximate Analysis				
Moisture content	wt%	3.1	-	-
Ash content	wt%	1.8	1.9	-
Volatile matter	wt%	79.5	82.0	83.6
Fixed carbon	wt%	15.6	16.1	16.4
Ultimate Analysis				
Carbon	wt%	48.3	49.9	50.8
Hydrogen	wt%	6.1	5.9	6.0
Nitrogen	wt%	0.4	0.4	0.4
Sulphur	wt%	0.0	0.0	0.0
Oxygen	wt%	40.3	41.9	42.7
Biochemical composition				
Cellulose	wt%	12.5	13.0	13.3
Hemicellulose	wt%	47.9	49.9	50.9
Lignin	wt%	25.7	26.8	27.3
Extractives	wt%	8.0	8.3	8.5
Calorific Values				
Net calorific value	MJ/kg		17.9	18.3
Gross calorific value	MJ/kg	19.1	19.8	20.1
Density				
Density of single particle	kg/m^3	519	± 11	
Bulk density of pellets	kg/m^3			

INORGANIC CONTENT				
Major Elements		**WCA**	**EDX**	**XRF**
Na	ppm (dry)		440	
Mg	ppm (dry)		400	
Al	ppm (dry)		33	
Si	ppm (dry)		833	
P	ppm (dry)		867	
S	ppm (dry)		3700	
Cl	ppm (dry)	1100	167	
K	ppm (dry)	2100	*2100*	
Ca	ppm (dry)		5167	
Ti	ppm (dry)		133	
Mn	ppm (dry)		167	
Fe	ppm (dry)		200	
Trace Elements		**ICP**		
Zn	ppm (dry)	152		
Pb	ppm (dry)	2		
Ash Composition		**WCA**	**EDX**	**XRF**
Na_2O	wt% (ash)	1.21%		1.11%
MgO	wt% (ash)	1.73%		2.40%
Al_2O_3	wt% (ash)	1.52%		0.50%
SiO_2	wt% (ash)	7.90%		6.49%
P_2O_5	wt% (ash)	2.05%		8.39%
K_2O	wt% (ash)	15.7%		11.3%
CaO	wt% (ash)	49.8%		45.0%
TiO_2	wt% (ash)	0.08%		0.49%
MnO	wt% (ash)	0.07%		0.14%
Fe_2O_3	wt% (ash)	0.15%		0.49%

COMBUSTION				
Single Particle Combustion Data				
$t = a.m^{b}$ (m = dry mass in mg)		**a**	**b**	**units**
Ignition delay		0.09	0.28	s
Volatile flame		1.19	0.60	s
Char combustion		2.92	0.77	s
Total burn-out time		4.18	0.72	s
Combustion Kinetics				
$k = A.exp^{(-E/RT)}$	**ln(A)**	**units**	**E**	**units**
Devolatilisation	6.3	s^{-1}	58	J/kg
Char combustion	10.9	s^{-1}	92	J/kg

PHOTOGRAPHS

AS RECEIVED

MILLED

PULVERIZED

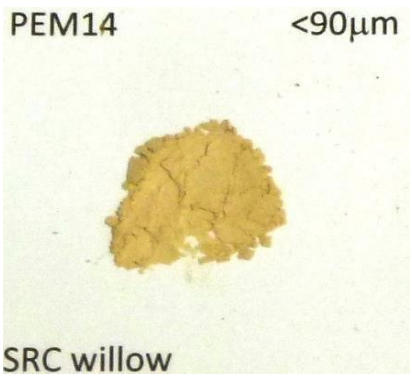

Wood Pellet A	unit	ar	dry	daf
Proximate Analysis				
Moisture content	wt%	26.3	-	-
Ash content	wt%	0.2	0.3	-
Volatile matter	wt%	62.5	84.8	85.0
Fixed carbon	wt%	11.0	15.0	15.0
Ultimate Analysis				
Carbon	wt%	36.2	49.1	49.2
Hydrogen	wt%	7.3	6.0	6.0
Nitrogen	wt%	0.0	0.0	0.0
Sulphur	wt%	0.0	0.1	0.1
Oxygen	wt%	29.9	44.6	44.7
Biochemical composition				
Cellulose	wt%	15.1	15.5	15.5
Hemicellulose	wt%	46.3	47.6	47.7
Lignin	wt%	27.1	27.8	27.9
Extractives	wt%	8.7	8.9	8.9
Calorific Values				
Net calorific value	MJ/kg		18.2	18.2
Gross calorific value	MJ/kg	14.4	19.5	19.5
Density				
Density of single particle	kg/m^3	634	± 25	
Bulk density of pellets	kg/m^3	290		

INORGANIC CONTENT				
Major Elements		**WCA**	**EDX**	**XRF**
Na	ppm (dry)		62	
Mg	ppm (dry)		138	
Al	ppm (dry)		92	
Si	ppm (dry)		338	
P	ppm (dry)		62	
S	ppm (dry)		1046	
Cl	ppm (dry)	400	77	
K	ppm (dry)	400	*400*	
Ca	ppm (dry)		508	
Ti	ppm (dry)		108	
Mn	ppm (dry)		92	
Fe	ppm (dry)		92	
Trace Elements		**ICP**		
Zn	ppm (dry)	43		
Pb	ppm (dry)	3		
Ash Composition		**WCA**	**EDX**	**XRF**
Na_2O	wt% (ash)	2.60%		2.49%
MgO	wt% (ash)	6.41%		5.90%
Al_2O_3	wt% (ash)	2.88%		3.07%
SiO_2	wt% (ash)	21.2%		18.0%
P_2O_5	wt% (ash)	4.50%		3.63%
K_2O	wt% (ash)	15.3%		10.6%
CaO	wt% (ash)	27.3%		25.5%
TiO_2	wt% (ash)	0.24%		0.61%
MnO	wt% (ash)	3.20%		3.41%
Fe_2O_3	wt% (ash)	2.13%		1.91%

COMBUSTION				
Single Particle Combustion Data				
$t = a.m^{b}$ (m = dry mass in mg)		**a**	**b**	**units**
Ignition delay		0.16	0.14	s
Volatile flame		1.46	0.58	s
Char combustion		6.57	0.62	s
Total burn-out time		8.23	0.60	s
Combustion Kinetics				
$k = A.exp^{(-E/RT)}$	**ln(A)**	**units**	**E**	**units**
Devolatilisation	12.4	s^{-1}	86	J/kg
Char combustion	13.4	s^{-1}	108	J/kg

PHOTOGRAPHS

AS RECEIVED

MILLED

PULVERIZED

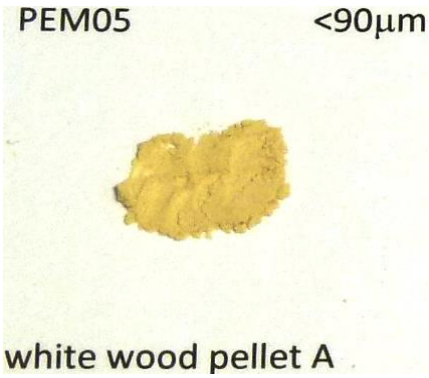

Wood Pellet B	unit	ar	dry	daf
Proximate Analysis				
Moisture content	wt%	6.4	-	-
Ash content	wt%	0.9	1.0	-
Volatile matter	wt%	77.7	83.0	83.9
Fixed carbon	wt%	14.9	16.0	16.1
Ultimate Analysis				
Carbon	wt%	46.9	50.2	50.7
Hydrogen	wt%	6.3	6.0	6.0
Nitrogen	wt%	0.1	0.1	0.1
Sulphur	wt%	0.0	0.0	0.0
Oxygen	wt%	39.3	42.8	43.2
Biochemical composition				
Cellulose	wt%	15.9	16.6	16.7
Hemicellulose	wt%	45.2	47.1	47.6
Lignin	wt%	27.9	29.0	29.3
Extractives	wt%	6.1	6.3	6.4
Calorific Values				
Net calorific value	MJ/kg		18.8	19.0
Gross calorific value	MJ/kg	18.8	20.0	20.2
Density				
Density of single particle	kg/m^3	609	± 39	
Bulk density of pellets	kg/m^3			

INORGANIC CONTENT				
Major Elements		**WCA**	**EDX**	**XRF**
Na	ppm (dry)		140	
Mg	ppm (dry)		260	
Al	ppm (dry)		240	
Si	ppm (dry)		600	
P	ppm (dry)		140	
S	ppm (dry)		1240	
Cl	ppm (dry)	100	120	
K	ppm (dry)	800	*800*	
Ca	ppm (dry)		1220	
Ti	ppm (dry)		120	
Mn	ppm (dry)		160	
Fe	ppm (dry)		160	
Trace Elements		**ICP**		
Zn	ppm (dry)	11		
Pb	ppm (dry)	3		
Ash Composition		**WCA**	**EDX**	**XRF**
Na_2O	wt% (ash)	1.50%		
MgO	wt% (ash)	6.80%		
Al_2O_3	wt% (ash)	4.40%		
SiO_2	wt% (ash)	25.4%		
P_2O_5	wt% (ash)	2.80%		
K_2O	wt% (ash)	14.8%		
CaO	wt% (ash)	20.4%		
TiO_2	wt% (ash)	0.20%		
MnO	wt% (ash)	1.90%		
Fe_2O_3	wt% (ash)	3.10%		

COMBUSTION				
Single Particle Combustion Data				
$t = a.m^{b}$ (m = dry mass in mg)		**a**	**b**	**units**
Ignition delay		0.11	0.25	s
Volatile flame		1.26	0.64	s
Char combustion		5.05	0.69	s
Total burn-out time		6.40	0.68	s
Combustion Kinetics				
$k = A.exp^{(-E/RT)}$	**ln(A)**	**units**	**E**	**units**
Devolatilisation	9.0	s^{-1}	71	J/kg
Char combustion	11.3	s^{-1}	101	J/kg

PHOTOGRAPHS

AS RECEIVED

MILLED

PULVERIZED

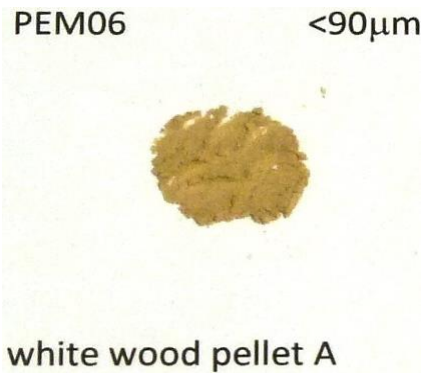

Wood Pellet C

Wood Pellet C	unit	ar	dry	daf
Proximate Analysis				
Moisture content	wt%	7.4	-	-
Ash content	wt%	1.1	1.2	-
Volatile matter	wt%	77.7	83.8	84.8
Fixed carbon	wt%	13.9	15.0	15.2
Ultimate Analysis				
Carbon	wt%	46.5	50.2	50.8
Hydrogen	wt%	6.4	6.0	6.1
Nitrogen	wt%	0.0	0.0	0.0
Sulphur	wt%	0.0	0.0	0.0
Oxygen	wt%	38.6	42.6	43.1
Biochemical composition				
Cellulose	wt%	12.5	13.1	13.3
Hemicellulose	wt%	45.3	47.7	48.3
Lignin	wt%	28.3	29.8	30.2
Extractives	wt%	7.7	8.1	8.2
Calorific Values				
Net calorific value	MJ/kg		19.0	19.3
Gross calorific value	MJ/kg	18.8	20.3	20.6
Density				
Density of single particle	kg/m^3	563	±36	
Bulk density of pellets	kg/m^3			

INORGANIC CONTENT				
Major Elements		**WCA**	**EDX**	**XRF**
Na	ppm (dry)		74	
Mg	ppm (dry)		222	
Al	ppm (dry)		278	
Si	ppm (dry)		1093	
P	ppm (dry)		93	
S	ppm (dry)		1037	
Cl	ppm (dry)	0	74	
K	ppm (dry)	500	*500*	
Ca	ppm (dry)		1241	
Ti	ppm (dry)		130	
Mn	ppm (dry)		130	
Fe	ppm (dry)		204	
Trace Elements		**ICP**		
Zn	ppm (dry)	13		
Pb	ppm (dry)	5		
Ash Composition		**WCA**	**EDX**	**XRF**
Na_2O	wt% (ash)	2.78%		2.31%
MgO	wt% (ash)	4.69%		4.28%
Al_2O_3	wt% (ash)	5.28%		4.48%
SiO_2	wt% (ash)	34.8%		26.4%
P_2O_5	wt% (ash)	1.65%		1.85%
K_2O	wt% (ash)	8.40%		6.42%
CaO	wt% (ash)	22.5%		21.2%
TiO_2	wt% (ash)	0.43%		0.68%
MnO	wt% (ash)	1.78%		2.08%
Fe_2O_3	wt% (ash)	3.56%		2.79%

COMBUSTION				
Single Particle Combustion Data				
$t = a.m^{b}$ (m = dry mass in mg)		**a**	**b**	**units**
Ignition delay		0.09	0.30	s
Volatile flame		1.44	0.56	s
Char combustion		5.40	0.68	s
Total burn-out time		6.98	0.65	s
Combustion Kinetics				
$k = A.exp^{(-E/RT)}$	**ln(A)**	**units**	**E**	**units**
Devolatilisation	7.3	s^{-1}	64	J/kg
Char combustion	13.4	s^{-1}	108	J/kg

PHOTOGRAPHS

AS RECEIVED

MILLED

PULVERIZED

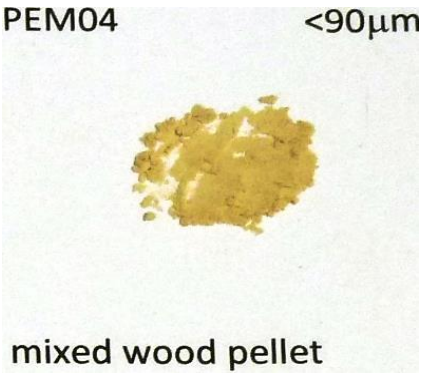

Pine	unit	ar	dry	daf
Proximate Analysis				
Moisture content	wt%	8.3	-	-
Ash content	wt%	1.8	2.0	-
Volatile matter	wt%	74.2	80.9	82.5
Fixed carbon	wt%	15.7	17.1	17.5
Ultimate Analysis				
Carbon	wt%	42.6	46.5	47.4
Hydrogen	wt%	5.7	5.2	5.3
Nitrogen	wt%	1.2	1.3	1.3
Sulphur	wt%	0.0	0.0	0.0
Oxygen	wt%	40.3	45.0	45.9
Biochemical composition				
Cellulose	wt%	10.5	10.9	11.2
Hemicellulose	wt%	53.2	55.7	56.8
Lignin	wt%	28.0	29.3	29.9
Extractives	wt%	2.1	2.2	2.2
Calorific Values				
Net calorific value	MJ/kg		17.4	17.8
Gross calorific value	MJ/kg	17.0	18.6	19.0
Density				
Density of single particle	kg/m^3	481	± 14	
Bulk density of pellets	kg/m^3			

INORGANIC CONTENT				
Major Elements		**WCA**	**EDX**	**XRF**
Na	ppm (dry)		53	
Mg	ppm (dry)		227	
Al	ppm (dry)		87	
Si	ppm (dry)		313	
P	ppm (dry)		578	
S	ppm (dry)		655	
Cl	ppm (dry)	1300	53	
K	ppm (dry)	1200	*1200*	
Ca	ppm (dry)		3171	
Ti	ppm (dry)		34	
Mn	ppm (dry)		48	
Fe	ppm (dry)		135	
Trace Elements		**ICP**		
Zn	ppm (dry)	168		
Pb	ppm (dry)	7		
Ash Composition		**WCA**	**EDX**	**XRF**
Na_2O	wt% (ash)	0.80%		0.54%
MgO	wt% (ash)	3.90%		2.84%
Al_2O_3	wt% (ash)	0.70%		1.01%
SiO_2	wt% (ash)	4.50%		10.8%
P_2O_5	wt% (ash)	10.1%		8.50%
K_2O	wt% (ash)	14.7%		6.71%
CaO	wt% (ash)	36.3%		34.2%
TiO_2	wt% (ash)	0.00%		0.53%
MnO	wt% (ash)	0.10%		0.11%
Fe_2O_3	wt% (ash)	0.70%		1.14%

COMBUSTION				
Single Particle Combustion Data				
$t = a.m^{b}$ (m = dry mass in mg)		**a**	**b**	**units**
Ignition delay		0.11	0.31	s
Volatile flame		1.33	0.59	s
Char combustion		4.61	0.69	s
Total burn-out time		6.08	0.66	s
Combustion Kinetics				
$k = A.exp^{(-E/RT)}$	**ln(A)**	**units**	**E**	**units**
Devolatilisation	7.0	s^{-1}	61	J/kg
Char combustion	11.6	s^{-1}	92	J/kg

PHOTOGRAPHS

AS RECEIVED

MILLED

PULVERIZED

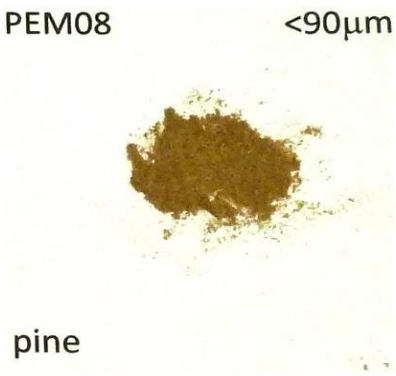

Eucalyptus	unit	ar	dry	daf
Proximate Analysis				
Moisture content	wt%	8.1	-	-
Ash content	wt%	0.8	0.9	-
Volatile matter	wt%	75.9	82.6	83.3
Fixed carbon	wt%	15.2	16.5	16.7
Ultimate Analysis				
Carbon	wt%	44.8	48.7	49.2
Hydrogen	wt%	6.0	5.6	5.6
Nitrogen	wt%	0.1	0.1	0.1
Sulphur	wt%	0.0	0.0	0.0
Oxygen	wt%	40.2	44.7	45.1
Biochemical composition				
Cellulose	wt%	10.0	10.5	10.6
Hemicellulose	wt%	55.4	58.3	58.8
Lignin	wt%	28.4	29.9	30.2
Extractives	wt%	0.4	0.5	0.5
Calorific Values				
Net calorific value	MJ/kg		18.2	18.3
Gross calorific value	MJ/kg	17.8	19.4	19.6
Density				
Density of single particle	kg/m^3	673	± 14	
Bulk density of wood chips	kg/m^3			

INORGANIC CONTENT				
Major Elements		**WCA**	**EDX**	**XRF**
Na	ppm (dry)		932	
Mg	ppm (dry)		273	
Al	ppm (dry)		318	
Si	ppm (dry)		727	
P	ppm (dry)		182	
S	ppm (dry)		2205	
Cl	ppm (dry)	0	636	
K	ppm (dry)	1000	*1000*	
Ca	ppm (dry)		2136	
Ti	ppm (dry)		45	
Mn	ppm (dry)		114	
Fe	ppm (dry)		136	
Trace Elements		**ICP**		
Zn	ppm (dry)	7		
Pb	ppm (dry)	7		
Ash Composition		**WCA**	**EDX**	**XRF**
Na_2O	wt% (ash)			
MgO	wt% (ash)			
Al_2O_3	wt% (ash)			
SiO_2	wt% (ash)			
P_2O_5	wt% (ash)			
K_2O	wt% (ash)			
CaO	wt% (ash)			
TiO_2	wt% (ash)			
MnO	wt% (ash)			
Fe_2O_3	wt% (ash)			

COMBUSTION				
Single Particle Combustion Data				
$t = a.m^{b}$ (m = dry mass in mg)		**a**	**b**	**units**
Ignition delay		0.11	0.37	s
Volatile flame		1.27	0.62	s
Char combustion		4.66	0.75	s
Total burn-out time		6.07	0.72	s
Combustion Kinetics				
$k = A.exp^{(-E/RT)}$	**ln(A)**	**units**	**E**	**units**
Devolatilisation	7.0	s^{-1}	62	J/kg
Char combustion	10.5	s^{-1}	64	J/kg

PHOTOGRAPHS

AS RECEIVED

MILLED

PULVERIZED

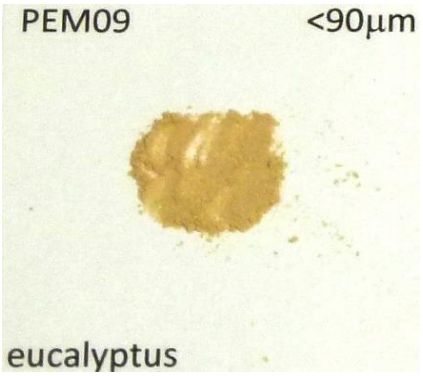

Wheat Straw A

Wheat straw A	unit	ar	dry	daf
Proximate Analysis				
Moisture content	wt%	10.8	-	-
Ash content	wt%	6.7	7.5	-
Volatile matter	wt%	65.5	73.4	79.3
Fixed carbon	wt%	17.1	19.1	20.7
Ultimate Analysis				
Carbon	wt%	40.1	44.9	48.6
Hydrogen	wt%	6.1	5.5	6.0
Nitrogen	wt%	0.5	0.6	0.6
Sulphur	wt%	0.1	0.1	0.1
Oxygen	wt%	35.7	41.4	44.8
Biochemical composition				
Cellulose	wt%	23.2	24.6	26.4
Hemicellulose	wt%	41.4	43.8	47.1
Lignin	wt%	19.2	20.3	21.9
Extractives	wt%	4.0	4.2	4.5
Calorific Values				
Net calorific value	MJ/kg		16.9	18.3
Gross calorific value	MJ/kg	16.2	18.2	19.6
Density				
Density of single particle	kg/m^3	201	± 21	
Bulk density of loose straw	kg/m^3			

INORGANIC CONTENT				
Major Elements		**WCA**	**EDX**	**XRF**
Na	ppm (dry)		273	
Mg	ppm (dry)		795	
Al	ppm (dry)		348	
Si	ppm (dry)		18565	
P	ppm (dry)		646	
S	ppm (dry)		3156	
Cl	ppm (dry)	2600	2908	
K	ppm (dry)	12700	*12700*	
Ca	ppm (dry)		5865	
Ti	ppm (dry)		621	
Mn	ppm (dry)		423	
Fe	ppm (dry)		348	
Trace Elements		**ICP**		
Zn	ppm (dry)	3		
Pb	ppm (dry)	27		
Ash Composition		**WCA**	**EDX**	**XRF**
Na_2O	wt% (ash)			
MgO	wt% (ash)			
Al_2O_3	wt% (ash)			
SiO_2	wt% (ash)			
P_2O_5	wt% (ash)			
K_2O	wt% (ash)			
CaO	wt% (ash)			
TiO_2	wt% (ash)			
MnO	wt% (ash)			
Fe_2O_3	wt% (ash)			

COMBUSTION				
Single Particle Combustion Data				
$t = a.m^{b}$ (m = dry mass in mg)		**a**	**b**	**units**
Ignition delay		0.09	0.23	s
Volatile flame		0.68	0.62	s
Char combustion		6.47	0.64	s
Total burn-out time		7.29	0.64	s
Combustion Kinetics				
$k = A.exp^{(-E/RT)}$	**ln(A)**	**units**	**E**	**units**
Devolatilisation	7.0	s^{-1}	59	J/kg
Char combustion	12.5	s^{-1}	95	J/kg

PHOTOGRAPHS

AS RECEIVED

MILLED

PULVERIZED

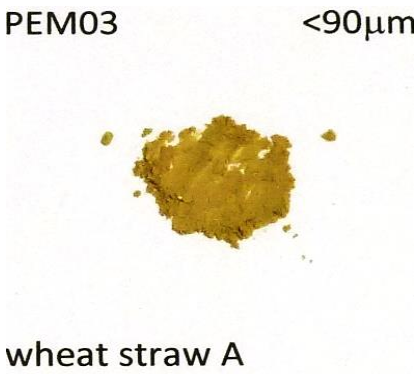

Wheat Straw B

Wheat straw B	unit	ar	dry	daf
Proximate Analysis				
Moisture content	wt%	8.1	-	-
Ash content	wt%	5.8	6.4	-
Volatile matter	wt%	70.4	76.6	81.8
Fixed carbon	wt%	15.6	17.0	18.2
Ultimate Analysis				
Carbon	wt%	42.0	45.8	48.9
Hydrogen	wt%	6.1	5.7	6.1
Nitrogen	wt%	0.5	0.5	0.6
Sulphur	wt%	0.0	0.0	0.0
Oxygen	wt%	37.3	41.6	44.5
Biochemical composition				
Cellulose	wt%	27.4	28.8	30.7
Hemicellulose	wt%	40.1	42.2	45.0
Lignin	wt%	18.6	19.6	20.9
Extractives	wt%	3.0	3.1	3.3
Calorific Values				
Net calorific value	MJ/kg		17.1	18.2
Gross calorific value	MJ/kg	16.6	18.1	19.3
Density				
Density of single particle	kg/m^3	320	± 25	
Bulk density of pellets	kg/m^3	200		

INORGANIC CONTENT				
Major Elements		**WCA**	**EDX**	**XRF**
Na	ppm (dry)		300	
Mg	ppm (dry)		625	
Al	ppm (dry)		150	
Si	ppm (dry)		13325	
P	ppm (dry)		425	
S	ppm (dry)		2100	
Cl	ppm (dry)	6100	450	
K	ppm (dry)	8200	*8200*	
Ca	ppm (dry)		5575	
Ti	ppm (dry)		25	
Mn	ppm (dry)		175	
Fe	ppm (dry)		250	
Trace Elements		**ICP**		
Zn	ppm (dry)	0		
Pb	ppm (dry)	4		
Ash Composition		**WCA**	**EDX**	**XRF**
Na_2O	wt% (ash)	0.47%		0.27%
MgO	wt% (ash)	0.85%		1.02%
Al_2O_3	wt% (ash)	0.57%		0.23%
SiO_2	wt% (ash)	45.1%		46.6%
P_2O_5	wt% (ash)	0.46%		2.21%
K_2O	wt% (ash)	15.9%		11.75%
CaO	wt% (ash)	14.5%		10.15%
TiO_2	wt% (ash)	0.15%		0.47%
MnO	wt% (ash)	0.05%		0.13%
Fe_2O_3	wt% (ash)	0.04%		0.24%

COMBUSTION				
Single Particle Combustion Data				
$t = a.m^{b}$ (m = dry mass in mg)		**a**	**b**	**units**
Ignition delay		0.07	0.34	s
Volatile flame		0.82	0.57	s
Char combustion		5.63	0.44	s
Total burn-out time		6.54	0.46	s
Combustion Kinetics				
$k = A.exp^{(-E/RT)}$	**ln(A)**	**units**	**E**	**units**
Devolatilisation	5.0	s^{-1}	55	J/kg
Char combustion	16.0	s^{-1}	111	J/kg

PHOTOGRAPHS

AS RECEIVED

MILLED

PULVERIZED

Rape Straw

Rape straw	unit	ar	dry	daf
Proximate Analysis				
Moisture content	wt%	14.3	-	-
Ash content	wt%	5.4	6.3	-
Volatile matter	wt%	65.9	76.9	82.1
Fixed carbon	wt%	14.4	16.8	17.9
Ultimate Analysis				
Carbon	wt%	39.1	45.6	48.7
Hydrogen	wt%	6.3	5.5	5.9
Nitrogen	wt%	0.9	1.0	1.1
Sulphur	wt%	0.1	0.2	0.2
Oxygen	wt%	33.9	41.4	44.2
Biochemical composition				
Cellulose	wt%	17.1	18.5	19.6
Hemicellulose	wt%	41.6	45.0	47.8
Lignin	wt%	17.8	19.3	20.5
Extractives	wt%	10.6	11.4	12.1
Calorific Values				
Net calorific value	MJ/kg		17.2	18.4
Gross calorific value	MJ/kg	15.8	18.4	19.6
Density				
Density of single particle	kg/m^3	211	± 17	
Bulk density of loose straw	kg/m^3	230		

INORGANIC CONTENT				
Major Elements		**WCA**	**EDX**	**XRF**
Na	ppm (dry)		475	
Mg	ppm (dry)		761	
Al	ppm (dry)		3993	
Si	ppm (dry)		2567	
P	ppm (dry)		729	
S	ppm (dry)		4025	
Cl	ppm (dry)	3200	1933	
K	ppm (dry)	4500	*4500*	
Ca	ppm (dry)		16194	
Ti	ppm (dry)		63	
Mn	ppm (dry)		222	
Fe	ppm (dry)		539	
Trace Elements		**ICP**		
Zn	ppm (dry)	6		
Pb	ppm (dry)	4		
Ash Composition		**WCA**	**EDX**	**XRF**
Na_2O	wt% (ash)	2.49%		1.88%
MgO	wt% (ash)	2.30%		1.96%
Al_2O_3	wt% (ash)	0.63%		0.54%
SiO_2	wt% (ash)	9.70%		9.79%
P_2O_5	wt% (ash)	3.62%		3.42%
K_2O	wt% (ash)	11.7%		6.62%
CaO	wt% (ash)	53.0%		51.1%
TiO_2	wt% (ash)	0.05%		0.48%
MnO	wt% (ash)	0.04%		0.00%
Fe_2O_3	wt% (ash)	0.44%		0.41%

COMBUSTION				
Single Particle Combustion Data				
$t = a.m^{b}$ (m = dry mass in mg)		**a**	**b**	**units**
Ignition delay		0.17	0.21	s
Volatile flame		0.89	0.60	s
Char combustion		2.61	0.71	s
Total burn-out time		3.63	0.67	s
Combustion Kinetics				
$k = A.exp^{(-E/RT)}$	**ln(A)**	**units**	**E**	**units**
Devolatilisation	9.3	s^{-1}	70	J/kg
Char combustion	12.1	s^{-1}	93	J/kg

PHOTOGRAPHS

AS RECEIVED

MILLED

PULVERIZED

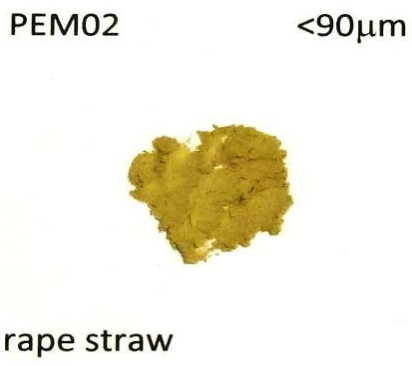

Miscanthus A	unit	ar	dry	daf
Proximate Analysis				
Moisture content	wt%	7.4	-	-
Ash content	wt%	4.6	4.9	-
Volatile matter	wt%	71.8	77.6	81.6
Fixed carbon	wt%	16.2	17.5	18.4
Ultimate Analysis				
Carbon	wt%	42.7	46.1	48.5
Hydrogen	wt%	6.1	5.7	6.0
Nitrogen	wt%	0.5	0.6	0.6
Sulphur	wt%	0.0	0.0	0.0
Oxygen	wt%	38.7	42.7	44.9
Biochemical composition				
Cellulose	wt%	27.1	28.4	29.8
Hemicellulose	wt%	39.5	41.4	43.5
Lignin	wt%	21.0	22.0	23.1
Extractives	wt%	3.2	3.4	3.5
Calorific Values				
Net calorific value	MJ/kg		17.6	18.5
Gross calorific value	MJ/kg	17.4	18.8	19.8
Density				
Density of single particle	kg/m^3	650	± 52	
Bulk density of pellets	kg/m^3			

INORGANIC CONTENT				
Major Elements		**WCA**	**EDX**	**XRF**
Na	ppm (dry)		301	
Mg	ppm (dry)		438	
Al	ppm (dry)		164	
Si	ppm (dry)		9684	
P	ppm (dry)		793	
S	ppm (dry)		1997	
Cl	ppm (dry)	4600	4158	
K	ppm (dry)	7500	*7500*	
Ca	ppm (dry)		3830	
Ti	ppm (dry)		109	
Mn	ppm (dry)		55	
Fe	ppm (dry)		246	
Trace Elements		**ICP**		
Zn	ppm (dry)	21		
Pb	ppm (dry)	2		
Ash Composition		**WCA**	**EDX**	**XRF**
Na_2O	wt% (ash)	0.81%		2.19%
MgO	wt% (ash)	1.53%		1.65%
Al_2O_3	wt% (ash)	1.01%		0.44%
SiO_2	wt% (ash)	43.4%		40.8%
P_2O_5	wt% (ash)	0.98%		3.72%
K_2O	wt% (ash)	18.5%		11.0%
CaO	wt% (ash)	10.7%		8.31%
TiO_2	wt% (ash)	0.08%		0.47%
MnO	wt% (ash)	0.03%		0.07%
Fe_2O_3	wt% (ash)	0.16%		0.40%

COMBUSTION				
Single Particle Combustion Data				
$t = a.m^{b}$ (m = dry mass in mg)		**a**	**b**	**units**
Ignition delay		0.14	0.18	s
Volatile flame		1.19	0.59	s
Char combustion		5.93	0.67	s
Total burn-out time		7.26	0.65	s
Combustion Kinetics				
$k = A.exp^{(-E/RT)}$	**ln(A)**	**units**	**E**	**units**
Devolatilisation	12.0	s^{-1}	76	J/kg
Char combustion	11.3	s^{-1}	91	J/kg

PHOTOGRAPHS

AS RECEIVED

MILLED

PULVERIZED

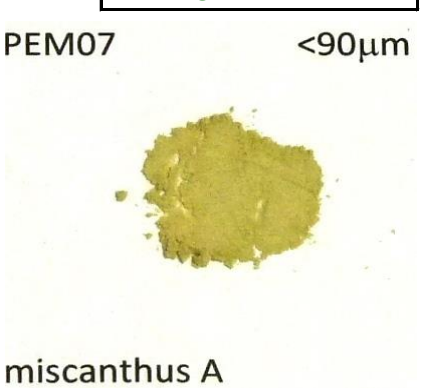

Miscanthus B	unit	ar	dry	daf
Proximate Analysis				
Moisture content	wt%	2.5	-	-
Ash content	wt%	1.8	1.8	-
Volatile matter	wt%	81.3	83.4	85.0
Fixed carbon	wt%	14.4	14.8	15.0
Ultimate Analysis				
Carbon	wt%	47.1	48.3	49.2
Hydrogen	wt%	6.1	5.9	6.0
Nitrogen	wt%	0.2	0.2	0.2
Sulphur	wt%	0.0	0.0	0.0
Oxygen	wt%	42.4	43.8	44.6
Biochemical composition				
Cellulose	wt%	28.1	29.2	29.7
Hemicellulose	wt%	31.0	32.2	32.8
Lignin	wt%	20.1	20.9	21.3
Extractives	wt%	15.4	15.9	16.2
Calorific Values				
Net calorific value	MJ/kg		17.4	17.8
Gross calorific value	MJ/kg	18.6	19.1	19.5
Density				
Density of single particle	kg/m^3	n/a		
Bulk density of pellets	kg/m^3			

INORGANIC CONTENT				
Major Elements		**WCA**	**EDX**	**XRF**
Na	ppm (dry)		362	
Mg	ppm (dry)		339	
Al	ppm (dry)		113	
Si	ppm (dry)		4094	
P	ppm (dry)		679	
S	ppm (dry)		1832	
Cl	ppm (dry)	6700	995	
K	ppm (dry)	1900	*1900*	
Ca	ppm (dry)		1448	
Ti	ppm (dry)		45	
Mn	ppm (dry)		45	
Fe	ppm (dry)		204	
Trace Elements		**ICP**		
Zn	ppm (dry)	32		
Pb	ppm (dry)	1		
Ash Composition		**WCA**	**EDX**	**XRF**
Na_2O	wt% (ash)	0.68%		0.98%
MgO	wt% (ash)	1.89%		2.51%
Al_2O_3	wt% (ash)	0.41%		0.14%
SiO_2	wt% (ash)	63.6%		46.7%
P_2O_5	wt% (ash)	1.18%		4.95%
K_2O	wt% (ash)	11.7%		7.85%
CaO	wt% (ash)	11.4%		8.54%
TiO_2	wt% (ash)	0.15%		0.46%
MnO	wt% (ash)	0.40%		1.77%
Fe_2O_3	wt% (ash)	0.08%		0.29%

COMBUSTION				
Single Particle Combustion Data				
$t = a.m^{b}$ (m = dry mass in mg)		a	b	units
Ignition delay				s
Volatile flame				s
Char combustion				s
Total burn-out time				s
Combustion Kinetics				
$k = A.exp^{(-E/RT)}$	ln(A)	units	E	units
Devolatilisation	8.3	s^{-1}	68	J/kg
Char combustion	12.4	s^{-1}	105	J/kg

PHOTOGRAPHS

AS RECEIVED

MILLED

PULVERIZED

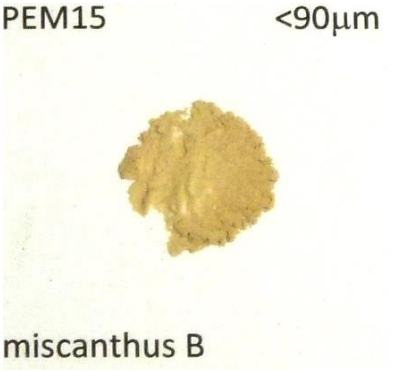

S.E. black pellets	unit	ar	dry	daf
Proximate Analysis				
Moisture content	wt%	7.2	-	-
Ash content	wt%	3.9	4.2	-
Volatile matter	wt%	70.6	76.1	79.4
Fixed carbon	wt%	18.3	19.7	20.6
Ultimate Analysis				
Carbon	wt%	46.9	50.5	52.7
Hydrogen	wt%	6.0	5.6	5.8
Nitrogen	wt%	0.2	0.2	0.2
Sulphur	wt%	0.0	0.0	0.0
Oxygen	wt%	35.9	39.5	41.2
Biochemical composition				
Cellulose	wt%	0.0	0.0	0.0
Hemicellulose	wt%	41.0	42.8	44.6
Lignin	wt%	38.0	39.6	41.3
Extractives	wt%	12.9	13.5	14.0
Calorific Values				
Net calorific value	MJ/kg		18.7	19.6
Gross calorific value	MJ/kg	18.5	20.0	20.8
Density				
Density of single particle	kg/m^3	1200	± 57	
Bulk density of pellets	kg/m^3	745		

INORGANIC CONTENT				
Major Elements		**WCA**	**EDX**	**XRF**
Na	ppm (dry)		429	
Mg	ppm (dry)		452	
Al	ppm (dry)		405	
Si	ppm (dry)		1881	
P	ppm (dry)		190	
S	ppm (dry)		1548	
Cl	ppm (dry)	500	143	
K	ppm (dry)	2000	*2000*	
Ca	ppm (dry)		8881	
Ti	ppm (dry)		143	
Mn	ppm (dry)		286	
Fe	ppm (dry)		1238	
Trace Elements		**ICP**		
Zn	ppm (dry)	214		
Pb	ppm (dry)	2		
Ash Composition		**WCA**	**EDX**	**XRF**
Na_2O	wt% (ash)	0.00%		0.00%
MgO	wt% (ash)	1.68%		1.57%
Al_2O_3	wt% (ash)	2.06%		0.67%
SiO_2	wt% (ash)	10.8%		9.21%
P_2O_5	wt% (ash)	1.53%		1.81%
K_2O	wt% (ash)	7.0%		5.33%
CaO	wt% (ash)	43.0%		42.3%
TiO_2	wt% (ash)	0.00%		0.00%
MnO	wt% (ash)	1.96%		0.78%
Fe_2O_3	wt% (ash)	0.65%		1.21%

COMBUSTION				
Single Particle Combustion Data				
$t = a.m^{b}$ (m = dry mass in mg)		a	b	units
Ignition delay		0.06	0.64	s
Volatile flame		1.38	0.63	s
Char combustion		7.94	0.82	s
Total burn-out time		9.40	0.80	s
Combustion Kinetics				
$k = A.exp^{(-E/RT)}$	ln(A)	units	E	units
Devolatilisation	1.6	s^{-1}	37	J/kg
Char combustion	12.1	s^{-1}	99	J/kg

PHOTOGRAPHS

AS RECEIVED

MILLED

PULVERIZED

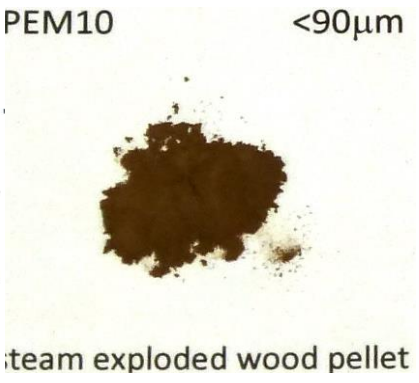

Olive Residue

Olive residue	unit	ar	dry	daf
Proximate Analysis				
Moisture content	wt%	5.9	-	-
Ash content	wt%	7.2	7.6	-
Volatile matter	wt%	69.6	74.0	80.1
Fixed carbon	wt%	17.3	18.4	19.9
Ultimate Analysis				
Carbon	wt%	45.9	48.8	52.8
Hydrogen	wt%	6.3	6.0	6.5
Nitrogen	wt%	1.4	1.5	1.6
Sulphur	wt%	0.0	0.0	0.0
Oxygen	wt%	33.3	36.1	39.1
Biochemical composition				
Cellulose	wt%	9.4	9.8	10.6
Hemicellulose	wt%	19.4	20.4	22.1
Lignin	wt%	27.7	29.1	31.5
Extractives	wt%	31.5	33.1	35.8
Calorific Values				
Net calorific value	MJ/kg		18.8	20.4
Gross calorific value	MJ/kg	18.9	20.1	21.8
Density				
Density of single particle	kg/m^3	1066	± 48	
Bulk density of pellets	kg/m^3	710		

INORGANIC CONTENT				
Major Elements		**WCA**	**EDX**	**XRF**
Na	ppm (dry)		341	
Mg	ppm (dry)		2005	
Al	ppm (dry)		602	
Si	ppm (dry)		2547	
P	ppm (dry)		1745	
S	ppm (dry)		2407	
Cl	ppm (dry)	2800	2266	
K	ppm (dry)	29200	*29200*	
Ca	ppm (dry)		6899	
Ti	ppm (dry)		160	
Mn	ppm (dry)		80	
Fe	ppm (dry)		762	
Trace Elements		**ICP**		
Zn	ppm (dry)	39		
Pb	ppm (dry)	2		
Ash Composition		**WCA**	**EDX**	**XRF**
Na_2O	wt% (ash)	0.89%		2.17%
MgO	wt% (ash)	2.19%		2.41%
Al_2O_3	wt% (ash)	1.86%		0.58%
SiO_2	wt% (ash)	8.5%		5.19%
P_2O_5	wt% (ash)	0.94%		3.52%
K_2O	wt% (ash)	46.5%		33.0%
CaO	wt% (ash)	11.3%		8.36%
TiO_2	wt% (ash)	0.07%		0.48%
MnO	wt% (ash)	0.02%		0.00%
Fe_2O_3	wt% (ash)	0.24%		0.46%

COMBUSTION				
Single Particle Combustion Data				
$t = a.m^{b}$ (m = dry mass in mg)		**a**	**b**	**units**
Ignition delay		0.15	0.37	s
Volatile flame		1.68	0.56	s
Char combustion		5.39	0.85	s
Total burn-out time		6.95	0.81	s
Combustion Kinetics				
$k = A.exp^{(-E/RT)}$	**ln(A)**	**units**	**E**	**units**
Devolatilisation	12.9	s^{-1}	76	J/kg
Char combustion	25.5	s^{-1}	205	J/kg

PHOTOGRAPHS

AS RECEIVED

MILLED

PULVERIZED

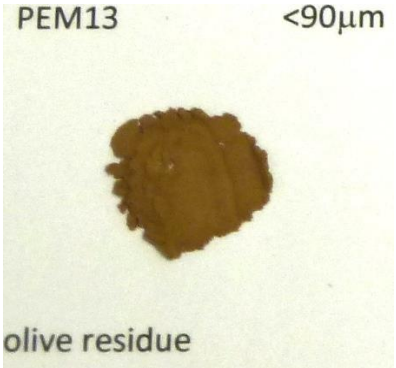

Coal A

Kellingley Coal	unit	ar	dry	daf
Proximate Analysis				
Moisture content	wt%	2.2	-	-
Ash content	wt%	18.0	18.4	-
Volatile matter	wt%	29.6	30.3	37.1
Fixed carbon	wt%	50.2	51.3	62.9
Ultimate Analysis				
Carbon	wt%	62.4	63.8	78.2
Hydrogen	wt%	4.4	4.2	5.1
Nitrogen	wt%	1.8	1.8	2.2
Sulphur	wt%	1.7	1.7	2.1
Oxygen	wt%	9.6	10.1	12.3
Calorific Values				
Net calorific value	MJ/kg		27.1	33.3
Gross calorific value	MJ/kg	27.4	28.0	34.3
Density				
Density of single particle	kg/m^3			
Bulk density	kg/m^3			

INORGANIC CONTENT				
Major Elements		**WCA**	**EDX**	**XRF**
Na	ppm (dry)			
Mg	ppm (dry)			
Al	ppm (dry)			
Si	ppm (dry)			
P	ppm (dry)			
S	ppm (dry)			
Cl	ppm (dry)			
K	ppm (dry)			
Ca	ppm (dry)			
Ti	ppm (dry)			
Mn	ppm (dry)			
Fe	ppm (dry)			
Trace Elements		**ICP**		
Zn	ppm (dry)			
Pb	ppm (dry)			
Ash Composition		**WCA**	**EDX**	**XRF**
Na_2O	wt% (ash)			
MgO	wt% (ash)			
Al_2O_3	wt% (ash)			
SiO_2	wt% (ash)			
P_2O_5	wt% (ash)			
K_2O	wt% (ash)			
CaO	wt% (ash)			
TiO_2	wt% (ash)			
MnO	wt% (ash)			
Fe_2O_3	wt% (ash)			

COMBUSTION				
Single Particle Combustion Data				
$t = a.m^{b}$ (m = dry mass in mg)		a	b	units
Ignition delay				ms
Volatile flame				s
Char combustion				s
Total burn-out time				s
Combustion Kinetics				
$k = A.exp^{(-E/RT)}$	ln(A)	units	E	units
Devolatilisation	5.4	s^{-1}	71	J/kg
Char combustion	20.4	s^{-1}	159	J/kg

PHOTOGRAPHS

AS RECEIVED

PULVERIZED

Coal B

El Cerrejón coal	unit	ar	dry	daf
Proximate Analysis				
Moisture content	wt%	5.5	-	-
Ash content	wt%	1.4	1.5	-
Volatile matter	wt%	37.3	39.5	40.1
Fixed carbon	wt%	55.8	59.0	59.9
Ultimate Analysis				
Carbon	wt%	68.0	71.9	73.0
Hydrogen	wt%	5.5	5.1	5.2
Nitrogen	wt%	2.0	2.1	2.2
Sulphur	wt%	0.0	0.0	0.0
Oxygen	wt%	17.6	19.3	19.6
Calorific Values				
Net calorific value	MJ/kg		31.7	32.2
Gross calorific value	MJ/kg	30.9	32.7	33.2
Density				
Density of single particle	kg/m^3			
Bulk density of pellets	kg/m^3			

INORGANIC CONTENT				
Major Elements		**WCA**	**EDX**	**XRF**
Na	ppm (dry)			
Mg	ppm (dry)			
Al	ppm (dry)			
Si	ppm (dry)			
P	ppm (dry)			
S	ppm (dry)			
Cl	ppm (dry)			
K	ppm (dry)			
Ca	ppm (dry)			
Ti	ppm (dry)			
Mn	ppm (dry)			
Fe	ppm (dry)			
Trace Elements		**ICP**		
Zn	ppm (dry)	7		
Pb	ppm (dry)	3		
Ash Composition		**WCA**	**EDX**	**XRF**
Na_2O	wt% (ash)	2.50%		
MgO	wt% (ash)	1.70%		
Al_2O_3	wt% (ash)	23.6%		
SiO_2	wt% (ash)	46.1%		
P_2O_5	wt% (ash)	0.30%		
K_2O	wt% (ash)	0.70%		
CaO	wt% (ash)	5.10%		
TiO_2	wt% (ash)	1.00%		
MnO	wt% (ash)	0.00%		
Fe_2O_3	wt% (ash)	14.3%		

COMBUSTION				
Single Particle Combustion Data				
$t = a.m^{b}$ (m = dry mass in mg)		**a**	**b**	**units**
Ignition delay				ms
Volatile flame				s
Char combustion				s
Total burn-out time				s
Combustion Kinetics				
$k = A.exp^{(-E/RT)}$	**ln(A)**	**units**	**E**	**units**
Devolatilisation	6.5	s^{-1}	75	J/kg
Char combustion	13.3	s^{-1}	120	J/kg

PHOTOGRAPHS

AS RECEIVED

PULVERIZED

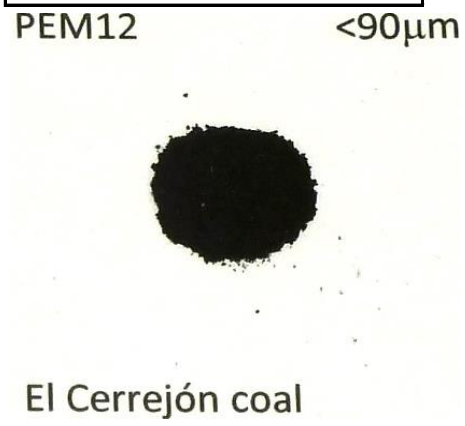

Coal C

Pittsburgh 8 coal	unit	ar	dry	daf
Proximate Analysis				
Moisture content	wt%	1.6	-	-
Ash content	wt%	7.5	7.6	-
Volatile matter	wt%	37.1	37.7	40.8
Fixed carbon	wt%	53.8	54.7	59.2
Ultimate Analysis				
Carbon	wt%	69.5	70.6	76.4
Hydrogen	wt%	5.2	5.1	5.5
Nitrogen	wt%	2.6	2.6	2.8
Sulphur	wt%	0.0	0.0	0.0
Oxygen	wt%	13.7	14.1	15.2
Calorific Values				
Net calorific value	MJ/kg		31.7	34.3
Gross calorific value	MJ/kg	32.2	32.7	35.4
Density				
Density of single particle	kg/m^3			
Bulk density of pellets	kg/m^3			

INORGANIC CONTENT				
Major Elements		**WCA**	**EDX**	**XRF**
Na	ppm (dry)			
Mg	ppm (dry)			
Al	ppm (dry)			
Si	ppm (dry)			
P	ppm (dry)			
S	ppm (dry)			
Cl	ppm (dry)			
K	ppm (dry)			
Ca	ppm (dry)			
Ti	ppm (dry)			
Mn	ppm (dry)			
Fe	ppm (dry)			
Trace Elements		**ICP**		
Zn	ppm (dry)	13		
Pb	ppm (dry)	5		
Ash Composition		**WCA**	**EDX**	**XRF**
Na_2O	wt% (ash)	0.60%		
MgO	wt% (ash)	0.70%		
Al_2O_3	wt% (ash)	22.1%		
SiO_2	wt% (ash)	40.0%		
P_2O_5	wt% (ash)	0.30%		
K_2O	wt% (ash)	1.20%		
CaO	wt% (ash)	3.30%		
TiO_2	wt% (ash)	0.90%		
MnO	wt% (ash)	0.10%		
Fe_2O_3	wt% (ash)	29.2%		

COMBUSTION				
Single Particle Combustion Data				
$t = a.m^{b}$ (m = dry mass in mg)		**a**	**b**	**units**
Ignition delay				ms
Volatile flame				s
Char combustion				s
Total burn-out time				s
Combustion Kinetics				
$k = A.exp^{(-E/RT)}$	**ln(A)**	**units**	**E**	**units**
Devolatilisation	4.4	s^{-1}	65	J/kg
Char combustion	18.7	s^{-1}	152	J/kg

PHOTOGRAPHS

AS RECEIVED

PULVERIZED

Appendix B

Single particle combustion model
FORTRAN code listing

```
!*****************************************************
!*****************************************************
!****  CONCENTRIC LAYER HEAT TRANSFER              ****
!****  BIOMASS SINGLE PARTICLE COMBUSTION MODEL    ****
!****  + POTASSIUM RELEASE MODELLING               ****
!****                                              ****
!****  PATRICK E. MASON                            ****
!****  UNIVERSITY OF LEEDS                         ****
!****  VERSION 26.2 JULY 2016                      ****
!*****************************************************
!*****************************************************
Program concentric_layer_SPC

!########### DEFINE VARIABLES ##########
implicit none
!particle
real :: Px,Py,Pz                                                          ! initial particle properties (input file)
real :: Volume, SurfaceArea, XSurfaceArea, Diameter, dr, shape             ! particle dimension variables (derived)
real :: Mass_gross, Mass_dry, dry_density                                  ! particle mass
real, dimension(100) :: Volume_layer,Mass_layer,SurfaceArea_layer          ! layer geometry variables
real, dimension(100) :: dr_layer,Volume_layer0,shrinkage                   ! layer geometry variables
!moisture
real :: moisture, Mw, Hevap, evap_coef                                     ! moisture properties
real, dimension(100) :: Mw_layer, dMw_layer, dQevap_layer                  ! layer moisture variables
!volatile matter
real :: volatile, Mvol, Hdevol, Hvolvap                                    ! volatiles properties
real, dimension(100) :: Mvol_layer, dMvol_layer, dQvol_layer               ! layer volatiles variables
!char
real :: char, Mchar, Hchar, char_density                                   !char properties
real, dimension(100) :: Mchar_layer, dMchar_layer, dQchar_layer            !layer char properties
!ash
real :: ash, Mash, ash_density                                             !ash properties
real, dimension(100) :: Mash_layer                                         !layer ash properties
!oxygen
real :: diff_oxy, diff_oxy_temp_fac, diff_oxy_temp_exp, Oxy_conc,dMoxy_surface  !oxygen properties
real, dimension(100) :: Oxy_conc_layer, Moxy_layer, dMoxy_layer            !layer oxygen properties
real :: air_density_fac,air_density, mass_air                              !air properties
!potassium
real :: potassium,MK,K_release,K_ent,diff_K,K_a                            !potassium properties
real :: MKOH,HKOH,BKOH,KOH_conc                                            !KOH properties
real :: MKCL,HKCL,BKCL,KCL_conc                                            !KCL species properties
real :: MKash,HKash,BKash,Kash_conc                                        !K in ash species properties
real, dimension(100) :: MKOH_layer, dMKOH_layer, KOHconc_layer             !layer KOH properties
real, dimension(100) :: MKCL_layer, dMKCL_layer, KCLconc_layer             !layer KCl properties
real, dimension(100) :: MKash_layer, dMKash_layer,Kashconc_layer           !layer mineral K properties
```

```
real, dimension(100) :: dmKOH_ent                                    !entrained K in layer
!chemical kinetics
real :: Avol,Evol,Achar,Echar,order                                  ! particle kinetics properties (input file)
!thermal properties
real :: Cp,Cpw,Cpv,Cpc,Cpa                                           ! specific heat capacities
real :: TC,TCw,TCv,TCc,TCa                                           ! particle thermal properties
real :: Ugas,TCgas,Vel_gas,Temp_gas,Re,Pr,Nu,R                       ! gas-flame thermodynamic properties
real :: Hconv, Em                                                    ! convective heat transfer coefficient & Emissivity
real :: dQconv,dQrad                                                 ! convective and radiative heat flux
real, dimension(100) :: dQcond,dQ_layer                              ! conductive heatflow
real, dimension(100) :: Cp_layer,TC_layer                            ! layer heat capacity and thermal conductivity
!temperature
real :: temp                                                         ! particle temperature
real, dimension(100):: Temp_layer,dTemp_layer                        ! layer heat temperature and temperature step
! calculation steps
real :: dt,time, time1,time2                                         ! calculation time step and duration
integer :: i,i2,idt,j,n,nlayers,volend,charburn,charend,data_out      ! loop iteration counters, layer indices, end-point markers

!########### INITIALISE VARIABLES AND CONSTANTS ##########
!Read properties from input file
real, dimension(12) :: property                                      ! file input property values
character(len=40), dimension(12) :: property_name                    ! file input property names
open(10,file='particle_data_input.txt')                              ! input property file name
do j=1,12                                                            ! number of properties to input
read(10,101) property_name(j)                                        ! property name from file
101 format(A40)
read(10,102) property(j)                                             ! property      value from file
102 format(F12.2)
end do                                                               ! end of inputs from file
! assign properties and convert to SI units
Px=property(1)/1000
Py=property(2)/1000
Pz=property(3)/1000
dry_density=property(4)
moisture=property(5)/100
ash=property(6)/100
volatile=property(7)/100
potassium=property(8)/1e6
Avol=property(9)
Evol=property(10)
Achar=property(11)
Echar=property(12)
! Derived particle dimension variables
Volume=Px*Py*Pz                                                      ! particle volume (m3)
Diameter=(Volume*1.91)**(0.3333333)                                  ! particle equivalent diameter (m)
```

```
XSurfaceArea=2.0*((Px*Py)+(Py*Pz)+(Pz*Px))
SurfaceArea=12.5664*((Diameter/2)**2)
Shape=0.7*(XSurfaceArea/SurfaceArea)
! Derived component mass variables
Mass_dry=dry_density*Volume
Mass_gross=Mass_dry/(1.0-moisture)
Mw=Mass_gross-Mass_dry
Mvol=Mass_dry*volatile
Mash=Mass_dry*ash
char=1-(volatile+ash)
Mchar=Mass_dry*char
ash_density=1000
char_density=Mchar/(volume -(Mash/ash_density))
evap_coef=0.0925
! Particle thermal properties
Cpw=4181
Cpv=1600
Cpc=1000
Cpa=800
Cp=((Cpw*Mw)+(Cpv*Mvol)+(Cpc*Mchar)+(Cpa*Mash))/Mass_gross
TCw=0.6
TCv=0.16
TCc=0.3
TCa=0.2
TC=((TCw*Mw)+(TCv*Mvol)+(TCc*Mchar)+(TCa*Mash))/Mass_gross
Temp=300
Em=0.85
! Enthalpy constants
Hevap=2.26e6
Hvolvap=0.5e6
Hdevol=0.2e6
Hchar=12.7e6
order=0.75
! Oxygen
diff_oxy_temp_fac=0.85e-10
diff_oxy_temp_exp=1.76
diff_oxy=diff_oxy_temp_fac*(temp**diff_oxy_temp_exp)
Oxy_conc=0.095
air_density_fac=353.18
air_density=air_density_fac/temp
! Gas thermal properties
R=8.314
Temp_gas=1600!1800
Vel_gas=3.0
Pr=0.71
```

```
! particle surface area (m2)
! surface area of equivalent spherical particle
! surface area shape correction factor

! particle dry mass (kg)
! particle wet/total mass (kg)
! mass of water in particle (kg)
! mass of volatiles in particle (kg) dry basis
! mass of ash in particle (kg) dry basis
! char content (dry basis)
! mass of fixed carbon in particle (kg) dry basis
! density of wood ash (kg/m3)
! density of char (kg/m3)
! evaporation coefficient

! Specific heat capacity of water (J/kg/K)
! Specific heat capacity of dry wood  (J/kg/K)
! Specific heat capacity of char  (J/kg/K)
! Specific heat capacity of ash  (J/kg/K)
! Specific heat capacity of particle(J/kg/K)
! Thermal conductivity of water  [W/m/K]
! Thermal conductivity of volatile part [W/m/K]
! Thermal conductivity of char part [W/m/K]
! Thermal conductivity of ash part [W/m/K]
! Thermal conductivity of particle (~wood) [W/m/K]
! particle initial temperature (K)
! Emissivity of particle

! Enthalpy of vapourisation of water (J/kg)
! Enthalpy of vapourisation of volatiles (J/kg)
! Enthalpy of devolatilisation (J/kg)
! Enthalpy of char oxidation (J per kg of C)
! Order of char reaction w.r.t. oxygen

! oxygen diffusion-temperature factor
! oxygen diffusion-temperature factor
! oxygen diffusion coefficient
! oxygen volumetric concentration
! factor x 1/Temp = density of air [kg/m3]
! density of air [kg/m3]

! gas Constant (J/mol/K)
! gas (flame) temperature (K)
! gas (flame) velocity (m/s)
! Prandtl number for gas (~air)
```

```
Ugas=(5.0e-11*(Temp_gas**2))+(8.6e-8*Temp_gas)-1.8e-5                                   ! Kinematic viscosity of gas (~air) [m2/s]
TCgas=1.25*(6.33e-5)*Temp_gas+0.00808                                                   ! Thermal conductivity of gas (~air) [W/m/K]
! Potassium
MK=Mass_dry*potassium                                                                   ! mass of potassium in particle (kg) dry basis
K_release=0                                                                             ! initial release value
K_ent=1.0e-4                                                                            ! coefficient of entrainment of K species
diff_K=diff_oxy*0.88                                                                    ! coefficient of diffusion of K species
K_a=0.065
KOH_conc=0                                                                              ! initial gas phase concentration
MKOH=MK*1.0                                                                             ! proportion of MK in MKOH
BKOH=6.44e6                                                                             ! coefficient of vapourisation (Pa)
HKOH=1.47e5                                                                             ! Enthalpy of vapourisation of KOH (J/mol)
KCL_conc=0                                                                              ! initial gas phase concentration
MKCL=MK*0.0                                                                             ! proportion of MK in MKCl
BKCl=1.16e8                                                                             ! coefficient of vapourisation (Pa)
HKCL=1.64e5                                                                             ! Enthalpy of vapourisation of KCl (J/mol)
Kash_conc=0                                                                             ! initial gas phase concentration
MKash=MK*0.0                                                                            ! proportion of MK in MKash
BKash=1.0e5                                                                             ! coefficient of vapourisation (Pa)
HKash=1.4e5                                                                             ! Enthalpy of vapourisation of Kash (J/mol)
! Set initial layer values
  dr=0.1e-3                                                                             !layer radial thickness [m]
  nlayers = (Diameter/(2*dr))-MOD(Diameter,(2*dr))                                      number of layers of [dr] radial thickness
  !outer layers
  do n=1,(nlayers)                                                                      !layer calculation loop
    if (n/=nlayers) then
    Volume_layer(n) = 4.18879*((((Diameter/2.0)-((n-1)*dr))**3)-(((Diameter/2.0)-((n)*dr))**3))   !volume of layer n [m3]
    dr_layer(n)=dr                                                                      !initial radius of layer n [m]
    else
    Volume_layer(n) = Volume-SUM(Volume_layer)                                          volume of central layer [m3]
    dr_layer(n)=(0.238732*Volume_layer(n))**(0.333333)                                  !initial radius of central layer [m]
    end if
    SurfaceArea_layer(n) = 12.5664*((Diameter/2.0)-((n-1)*dr))**2                       !surface area of outer surface of layer n [m2]
    Volume_layer0(n)=Volume_layer(n)                                                    !initial volume of layer n [m3]
    Mw_layer(n) = Mw*(Volume_layer(n)/Volume)                                           !mass of water in layer n [kg]
    Mvol_layer(n)=Mvol*(Volume_layer(n)/Volume)                                         !mass of volatiles in layer n [kg]
    Mchar_layer(n)=Mchar*(Volume_layer(n)/Volume)                                       !mass of char in layer n [kg]
    Mash_layer(n)=Mash*(Volume_layer(n)/Volume)                                         !mass of ash in layer n [kg]
    Mass_layer(n)=Mw_layer(n)+Mvol_layer(n)+Mchar_layer(n)+Mash_layer(n)                !gross mass of layer n [kg]
    Oxy_conc_layer(n)=Oxy_conc                                                          !oxygen concentration in layer n [%]
    Moxy_layer(n)= Oxy_conc_layer(n)*Volume_layer(n)*air_density                        !mass of oxygen in layer n [kg]
    Cp_layer(n)=Cp                                                                      specific heat capacity of layer n [J/kg/K]
    TC_layer(n)=TC                                                                      !thermal conductivity of layer n [W/m/k]
    MKOH_layer(n)=MKOH*(Volume_layer(n)/Volume)                                         !mass of KOH in layer n [kg]
    dmKOH_layer(n)=0                                                                    mass transfer of KOH in layer n [kg]
```

```
    Temp_layer(n)=Temp                                                                  temperature of layer(n)
  end do
! Print initial values
        103 format(A40,F12.2)
         do j=1,12
        print 103,property_name(j),property(j)
         end do
        print 103,'char content [%]                        ',char*100
        print 103,'particle dry mass [mg]                  ',Mass_dry*1e6
        print 103,'particle wet mass [mg]                  ',Mass_gross*1e6
        print 103,'char mass [mg]                          ',Mchar*1e6
        print 103,'equivalent diameter [mm]                ',Diameter*1000
        print 103,'particle volume [mm3]                   ',Volume*1e9
        print 103,'particle surface area  [mm2]            ',SurfaceArea*1e6
        print 103,'shape factor [ratio_of_area]            ',shape
        print 103,'gas temperature [K]                     ',Temp_gas
        print 103,'particle emissivity [ratio]             ',Em
        print 103,'thermal conductivity [W/m/K]            ',TC
        print 103,'specific heat capacity[J/kg/K]          ',Cp
        print 103,'Oxygen concentration [%vol]             ',Oxy_conc
! OUTPUT FILES
        open(11,file='SPC_mass_output_file.txt')                                        !mass transfer output file
        open(12,file='SPC_heat_output_file.txt')                                        !heat transfer output file
        open(13,file='SPC_layer_file.txt')                                !properties of internal layers: oxygen conc, thermal conductivity, heat capacity
! Text file header information
  do j=1,12                                                                             !header information
        write(11,110)property_name(j),property(j)
        write(12,110)property_name(j),property(j)
        write(13,110)property_name(j),property(j)
  end do                                                                                !from properties list
  do j=11,13
        write(j,110)'char content [%]              ',char*100
        write(j,110)'char mass [mg]                ',Mchar*1e6
        write(j,110)'particle dry-mass [mg]        ',Mass_dry*1e6
        write(j,110)'particle wet-mass [mg]        ',Mass_gross*1e6
        write(j,110)'equivalent diameter [mm]      ',Diameter*1000
        write(j,110)'particle volume [mm3]         ',Volume*1e9
        write(j,110)'particle surface-area [mm2]   ',SurfaceArea*1e6
        write(j,110)'shape factor [ratio_of_area]  ',shape
        write(j,110)'gas temperature [K]           ',Temp_gas
        write(j,110)'particle emissivity [ratio]   ',Em
        write(j,110)'thermal conductivity [W/m/K]  ',TC
        write(j,110)'specific heat capacity[J/kg/K]',Cp
        write(j,110)'Oxygen concentration [%vol]   ',Oxy_conc
        write(j,110)'_____________________________________________'
```

```
  end do
        110 format ( 1X,A40,T48,ES10.3)
        write(11,111)'time[s]','Temp','Mass','Mw','Mvol','Mchar','volume','K-rel','K-conc','K-mass'               !mass transfer file column headers
        write(11,111)'[s]','[K]','[mg]','[mg]','[mg]','[mg]','[mm3]','[ug/s]','[kg/m3]','[ug]'                   !mass transfer file column headers
        111 format ( 1X,A10,T12,A10,T24,A10,T36,A10,T48,A10,T60,A10,T72,A10,T84,A10,T96,A10,T108,A10)
        write(12,121)'layer','time[s]','Temp[K]','TC','Cp','dQconv','dQrad','dQcond','dQvol','dQchar'           !heat transfer file column headers
        121 format ( 1X,A10,T12,A10,T24,A10,T36,A10,T48,A10,T60,A10,T72,A10,T84,A10,T96,A10,T108,A10)
        write(13,131)'layer[n]','time[s]','Temp[K]','mass','Moxy','airden','Vol','oxy-conc','Mash','-'           !layer properties file column headers
        131 format ( 1X,A10,T12,A10,T24,A10,T36,A10,T48,A10,T60,A10,T72,A10,T84,A10,T96,A10,T108,A10)

!###################################
!########## CALCULATIONS ##########
!###################################
! Calculation loop parameters
dt=1.0e-6                                                                                 !define time step (seconds)
volend=0                                                                                  !reset devolatilisation end-point marker
charburn=0                                                                                reset char burn start marker
charend=0                                                                                 !reset char burn-out end-point marker
time=0                                                                                    !initialise time counter
time1=0
time2=0
data_out=10000                                                                            !data output
i=0                                                                                       !time step counter
i2=0
!>>>>>>>>>>>>>>>>>>>>>>>>>>>>>>>>>>>>>>>>>>>>>>>>>>>>>>>>>>>>>>>>>>>>>>>>>>>>>>>>>>----------------------------------- -----------------------|
!>>>>>>>>>>>>>>>>>>>  START OF TIME_STEP CALCULATION LOOP >>>>>>>>>>>>>>>>>>>>>>>                                                           |
!>>>>>>>>>>>>>>>>>>>>>>>>>>>>>>>>>>>>>>>>>>>>>>>>>>>>>>>>>>>>>>>>>>>>>>>>>>>>>>>>>                                                           V
  do                                                                                                                !time-step calculation loop
 !########## CONCENTRIC LAYER CALCULATIONS ##########
 !>>>>>>>>>>>>>>>>>>>>>>>>>>>>>>>>>>>>>>>>>>>>>>>>>>>>>>>>>>>>>>>>>>>>>>>>>>>>>>>>>------------------------------------------------------------|
 !>>>>>>>>>>>>>>>>>>>  START OF LAYER CALCULATION LOOP >>>>>>>>>>>>>>>>>>>>>>>>>>>                                                           |
 !>>>>>>>>>>>>>>>>>>>>>>>>>>>>>>>>>>>>>>>>>>>>>>>>>>>>>>>>>>>>>>>>>>>>>>>>>>>>>>>>>                                                           V
  do n=1,(nlayers)                                                                        !layer calculation loop
    if (n==1) then
   !Convective thermodynamics
    Re=(Vel_gas*(Diameter))/Ugas                                                          !Reynolds number
    Nu=2+(0.6*((Re**(0.5))*(Pr**(0.333333))))                                             !Nusselt number (Ranz Marshall approximation)
    Hconv=Nu*TCgas/(Diameter)                                                             !convective heat transfer coefficient (W/m2/K)
   !External heat transfer external layer
    dQconv=dt*SurfaceArea_layer(n)*Hconv*(Temp_gas-Temp_layer(n))                         !convective heat flux to surface layer(layer 1 only)
    dQrad=dt*shape*SurfaceArea_layer(n)*Em*5.67e-8*((300**4)-(Temp_layer(n)**4))          !radiative heat flux to surface  (layer 1 only)
    end if

  !Internal heat transfer inner surface of layer n
    if (n==nlayers) then
```

```
      dQcond(nlayers)=0                                                                    !conductive heat flow to interior layer: boundary condition
   else
      dQcond(n)=dt*TC_layer(n)*((SurfaceArea_layer(n+1)/dr_layer(n))*(Temp_layer(n)-Temp_layer(n+1)))   !conductive heat flow to interior layer
      end if

 !Evaporation of moisture
   if (Temp_layer(n)>310.0) then                                                       !evaporation only above threshold temperature
   dMw_layer(n)=dt*(Temp_layer(n)-310.0)*(Mw_layer(n))*evap_coef                       !evaporation mass loss
   dQevap_layer(n)=SUM(dMw_layer)*Hevap                                                !evaporation heat energy balance
   Mw_layer(n)=Mw_layer(n)-dMw_layer(n)                                                !moisture mass adjustment
   else                                                                                !no evaporation below threshold temperature
   dQevap_layer(n)=0
   dMw_layer(n)=0
   end if

!Devolatilisation
   dMvol_layer(n)=dt*Mvol_layer(n)*Avol*EXP((-1*Evol)/(R*Temp_layer(n)))               !mass loss from devolatilisation
   dQvol_layer(n)=     dMvol_layer(n)*Hdevol                                           !heat energy balance from devolatilisation
   if (n==1) then
   dQvol_layer(1)=dQvol_layer(1)+(SUM(dMvol_layer)*Hvolvap)                            !heat energy balance from vapourisation of volatiles at surface
       end if
   Mvol_layer(n)=Mvol_layer(n)-dMvol_layer(n)                                          !volatile mass adjustment

  !Oxygen concentration
   diff_oxy=diff_oxy_temp_fac*(Temp_layer(n)**diff_oxy_temp_exp)                       !oxygen diffusion coefficient
   air_density=(air_density_fac/(Temp_layer(n)))                                       !density of air in layer [kg/m3]
   Moxy_layer(n)= Oxy_conc_layer(n)*Volume_layer(n)*air_density                        !mass of oxygen in layer [kg]
   if (n==nlayers) then
   dMoxy_layer(nlayers)=0                                                              !oxygen diffusion at centre of particle: boundary condiditon
   else
   dMoxy_layer(n)=dt*diff_oxy*(SurfaceArea_layer(n+1)/dr_layer(n))*(Oxy_conc_layer(n)-Oxy_conc_layer(n+1))*air_density
                                                                                       !diffusion of oxygen in to interior layer [kg]
   end if
   if (n==1) then
   dMoxy_surface=dt*diff_oxy*(SurfaceArea_layer(n)/dr_layer(n))*(Oxy_conc-Oxy_conc_layer(n))*air_density  !diffusion of oxygen from surface [kg]
   end if

   !Char combustion
   dMchar_layer(n)=dt*Mchar_layer(n)*((Oxy_conc_layer(n)/0.21)**(order))*Achar*EXP((-1*Echar)/(R*Temp_layer(n)))!char mass loss from oxidisation
   dQchar_layer(n)=dMchar_layer(n)*Hchar                                               !heat energy balance from char combustion
   Mchar_layer(n)=Mchar_layer(n)-dMchar_layer(n)                                       !char mass adjustment
   if (Mchar_layer(n)<0.0) then
    Mchar_layer(n)=0.0
   end if
```

```
 !Oxygen consumption
 if (n==1) then
 Moxy_layer(n)=Moxy_layer(n)+dMoxy_surface-dMoxy_layer(n)-(1.5*dMchar_layer(n))        !consumption of oxygen in external layer [kg]
 else
 Moxy_layer(n)=Moxy_layer(n)+dMoxy_layer(n-1)-dMoxy_layer(n)-(1.5*dMchar_layer(n))     !consumption of oxygen in internal layers [kg]
     end if
 if (Moxy_layer(n)<1.0e-20) then
 Moxy_layer(n)=0.0
 end if
 mass_air=1e9*(Volume_layer(n)*air_density)                                            !mass of air in layer
 Oxy_conc_layer(n)=Moxy_layer(n)/mass_air                                              !oxygen concentration recalc
 Oxy_conc_layer(n)=Oxy_conc_layer(n)*1e9

 !Temperature change
 if (n==1) then
 dQ_layer(n)=dQconv+dQrad-dQcond(n)-dQevap_layer(n)-dQvol_layer(n)+dQchar_layer(n)     !net heat flux external layer
 Temp= Temp_layer(1)                                                                   !Temperature of external surface of particle
 else
 dQ_layer(n)=dQcond(n-1)-dQcond(n)-dQevap_layer(n)-dQvol_layer(n)+dQchar_layer(n)      !net heat flux internal layers
 end if
 dTemp_layer(n)= dQ_layer(n)/((Cp_layer(n))*(Mass_layer(n)))                           !Temperature change on external layer
 Temp_layer(n)=Temp_layer(n)+dTemp_layer(n)                                            !Temperature adjustment external layer

 !Potassium gas-phase diffusion and entrainment
diff_K=diff_oxy*0.88
if (MKOH_layer(n)>0) then
KOHconc_layer(n)=(K_a*MKOH_layer(n))*BKOH*EXP((-1.0*HKOH)/(R*Temp_layer(n)))/Volume_layer(n)   !gas phase K concentration in particle
dmKOH_ent(n)=(K_ent*dMvol_layer(n)*(MKOH_layer(n)/Volume_layer(n)))                    !entrained K
 if (n==1) then
 dmKOH_layer(n)=(dt*diff_K*(SurfaceArea_layer(n))*KOHconc_layer(n))                    !potassium diffusion to surface
     else
 dmKOH_layer(n)=(dt*diff_K*(SurfaceArea_layer(n)/dr_layer(n))*(KOHconc_layer(n)-KOHconc_layer(n-1)))   !potassium diffusion between layers
 end if
else
dmKOH_layer(n)=0
MKOH_layer(n)=0
end if
if (n==nlayers) then
MKOH_layer(n)=MKOH_layer(n)-dmKOH_layer(n)-dmKOH_ent(n)
else
MKOH_layer(n)=MKOH_layer(n)-dmKOH_layer(n)+dmKOH_layer(n+1)-dmKOH_ent(n)
end if

!Mass step all layers
Mass_layer(n)=Mw_layer(n)+Mvol_layer(n)+Mchar_layer(n)+Mash_layer(n)                                    !Mass change
```

```
   Cp_layer(n)=((Cpw*Mw_layer(n))+(Cpv*Mvol_layer(n))+(Cpc*Mchar_layer(n))+(Cpa*Mash_layer(n)))/Mass_layer(n)      !Specific heat capacity of layer(J/kg/K)
   TC_layer(n)=((TCw*Mw_layer(n))+(TCv*Mvol_layer(n))+(TCc*Mchar_layer(n))+(TCa*Mash_layer(n)))/Mass_layer(n)      !Thermal conductivity of layer
   Volume_layer(n)=(Mchar_layer(n)/char_density)+(Mash_layer(n)/ash_density)              !Volume of char particle (shrinking related to char mass loss)
   shrinkage(n)=(Volume_layer(n)/volume_layer0(n))**(0.3333333)
    if (shrinkage(n)<0.0001) then
    shrinkage(n)=0.0001
    end if
   dr_layer(n)=dr*shrinkage(n)                                                            !adjustment of radial thickness of layer from volume shrinkage

  ! OUTPUTS from layer calculations
  if (MOD(i,data_out)==0) then
   write(12,122) (n),time,Temp_layer(n),TC_layer(n),Cp_layer(n),dQconv,dQrad,dQcond(n),dQvol_layer(n),dQchar_layer(n)              !heat transfer file output
   write(13,132) (n),time,Temp_layer(n),Mass_layer(n),Moxy_layer(n),air_density,Volume_layer(n),Oxy_conc_layer(n),Mash_layer(n)    !layer properties file
   122 format (' ',1I11,2F11.4,7ES11.3)
   132 format (' ',1I11,2F11.4,6ES11.3)
  end if
 end do

!<<<<<<<<<<<<<<<<<<<<<<<<<<<<<<<<<<<<<<<<<<<<<<<<<<<<<<<<<<<<<<<<<<<<<<<<<<<<<<<<<<                                                           ^
!<<<<<<<<<<<<<<<   END OF LAYER CALCULATION LOOP <<<<<<<<<<<<<<<<<<<<<<<<<<<<<<<<<<                                                           |
!<<<<<<<<<<<<<<<<<<<<<<<<<<<<<<<<<<<<<<<<<<<<<<<<<<<<<<<<<<<<<<<<<<<<<<<<<<<<<<<<<-----------------------------------------------------------|
!########## WHOLE PARTICLE CALCULATIONS ##########
  !Particle dimensions and mass step
  Volume=SUM(Volume_layer)
  Diameter=(Volume*1.909872)                                                              ! particle equivalent diameter (m) - based on volume of char only
  Diameter=Diameter**(0.333333)                                                           ! particle equivalent diameter (m) - based on volume of char only
  SurfaceArea=12.5664*((Diameter/2.0)**2)                                                 ! surface area of equivalent spherical particle
  Mass_gross=SUM(Mass_layer)                                                              ! total mass of particle
  Mw=SUM(Mw_layer)                                                                        ! total mass of moisture in particle
  Mvol=SUM(Mvol_layer)                                                                    ! total mass of volatiles in particle
  Mchar=SUM(Mchar_layer)                                                                  ! total mass of char in particle
  Mash=SUM(Mash_layer)                                                                    ! total mass of ash in particle
  Volume=(Mchar+Mash)/char_density                                                        ! volume based on mass of char+ash only
  MKOH=SUM(MKOH_layer)                                                                    ! Total mass of K in particle
  KOH_conc=SUM(MKOH_layer)/Volume                                                         ! overall concentration of in particle
  K_release=dMKOH_layer(1)+SUM(dMKOH_ent)                                                 ! K released from surface: diffused + entrained

  ! OUTPUTS from whole particle calculations
  if (MOD(i,data_out)==0) then
  write(11,112) time,Temp,(Mass_gross*1e6),(Mw*1e6),(Mvol*1e6),Mchar*1e6,(Volume*1e9),((K_release*1e9)/dt),KOH_conc,(MKOH*1e9)!mass transfer data file output
  112 format (' ',2f11.4,8ES11.3)
  end if
!Time step
  i=i+1
if (charburn==0) then
```

```fortran
time1=dt*(i*1.0)
else
time2=(i-i2)*dt
end if
time=time1+time2
idt=INT(1.0/dt)
if (MOD(i,idt)==0) then                                                                   !progress monitoring
   print *,'calculating  ',NINT(time),' seconds'
end if
if ((Mvol<5e-9).AND.(volend==0)) then
  print *,'devol time = ',time
  volend=1
  !exit
end if
if ((Mchar<5e-7).AND.(charburn==0)) then
  charburn=1
  dt=dt*0.1
  i2=i
end if
if ((Mchar<5e-9).AND.(charend==0)) then
  print *,'end of char burn-out= ',time
  charend=1
  !exit
end if
if ((MKOH<1e-12).AND.(charend==1)) then
  print *,'end K release= ',time
  exit
end if
end do
!<<<<<<<<<<<<<<<<<<<<<<<<<<<<<<<<<<<<<<<<<<<<<<<<<<<<<<<<<<<<<<<<<<<<<<<<<<<<<<<<<<<<<<<<<<<<<<<<<END OF TIME_STEP CALCULATION LOOP
!Print final values of particle dimensions and mass
                    print 103,'final particle temperature [K]          ',Temp
                    print 103,'final particle mass [mg]                ',Mass_gross*1e6
                    print 103,'final diameter [mm]                     ',Diameter*1000
                    print 103,'final diameter check [mm]               ',(SUM(dr_layer))*2000
                    print 103,'final volume [mm3]                      ',Volume*1e9
                    print 103,'final Mw [mg]                           ',Mw*1e6
                    print 103,'final Mvol [mg]                         ',Mvol*1e6
                    print 103,'final Mchar [mg]                        ',Mchar*1e6
                    print 103,'total iterations                        ',(i*1.0)

!################## THE END ####################
end program concentric_layer_SPC
```

Too many flames with too much to burn
And life's only made of paper
Oh how I need to be free of this pain
But it goes over
and over
and over
and over again

Ronnie James Dio 1981.